



Provided by the author(s) and University of Galway in accordance with publisher policies. Please cite the published version when available.

Title	Carbon fibre reinforced PEEK laminated as a material for orthopaedic devices: An experimental and computational investigation
Author(s)	Gallagher, Elizabeth Anne
Publication Date	2018-11-27
Publisher	NUI Galway
Item record	<a href="http://hdl.handle.net/10379/14665">http://hdl.handle.net/10379/14665</a>

Downloaded 2024-05-14T07:31:48Z

Some rights reserved. For more information, please see the item record link above.



# **Carbon Fibre Reinforced PEEK Laminates as a Material for Orthopaedic Devices: An Experimental and Computational Investigation**

**Elizabeth Anne Gallagher B.E.**



A thesis submitted to the National University of Ireland as fulfilment  
of the requirements for the Degree of Doctor of Philosophy

**2018**

Discipline of Biomedical Engineering  
College of Engineering and Informatics  
National University of Ireland, Galway

Supervisor of Research: Dr. Patrick McGarry



## **Abstract**

The overall objective of this thesis is to investigate carbon fibre reinforced poly-ether-ether-ketone (PEEK) laminates as a material for fracture fixation devices through a combination of experimental testing and computational modelling.

Orthopaedic devices using unidirectional carbon fibre reinforced PEEK laminates potentially offer several benefits over metallic implants including: anisotropic material properties; radiolucency and strength to weight ratio. However, despite FDA clearance of PEEK-OPTIMA™ Ultra-Reinforced, no investigation of the mechanical properties or failure mechanisms of a medical grade unidirectional laminate material has been published to date, thus hindering the development of first-generation laminated orthopaedic devices. This study presents the first investigation of the mechanical behaviour and failure mechanisms of PEEK-OPTIMA™ Ultra-Reinforced. This thesis presents a multi-axial suite of experimental tests are presented: 0° and 90° tension and compression, in-plane shear, mode I and mode II fracture toughness, compression of ±45° laminates and flexure of 0°, 90° and ±45° laminates. Three damage mechanisms are uncovered: (1) inter-laminar delamination, (2) intra-laminar cracking and (3) anisotropic plasticity. A computational damage and failure model that incorporates all three damage mechanisms is developed. The model accurately predicts the complex multi-mode failure mechanisms observed experimentally. The ability of a model to predict diverse damage mechanisms under multiple loading directions conditions is critical for the safe design of fibre reinforced laminated orthopaedic devices subjected to complex physiological loading conditions.

Laminated fracture fixation plates can be designed with custom anisotropic material properties, thus enabling the engineer to tailor the overall stiffness of the implant to the specific loading conditions it will experience in vivo. In this work a multi-scale computational investigation of idealised distal radius fracture fixation plate (DRP) is conducted. Physiological loading conditions are applied to macro-scale finite element models of DRPs. The mechanical response is compared for several carbon fibre reinforced PEEK (CF/PEEK) laminate layups to examine the effect of ply layup design. The importance of ply orientation in laminated DRPs is highlighted. A high number of 0° plies near the outer surfaces results in a greater bending strength while the addition of 45° plies increases the torsional strength of

the laminates. Intra-laminar transverse tensile failure is predicted as the primary mode of failure. A micro-mechanical analysis of the CF/PEEK microstructure uncovers the precise mechanism under-lying intra-laminar transverse tensile crack to be debonding of the PEEK matrix from carbon fibres. Plastic strains in the matrix material are not sufficiently high to result in ductile failure of the matrix. The findings of this study demonstrate the significant challenge in the design and optimisation of fibre reinforced laminated composites for orthopaedic applications, highlighting the importance of multi-scale modelling for identification of failure mechanisms.

A common feature of all such fixation devices is that screws are used to anchor the plates to the fractured bone. However, drilling holes in fibre reinforced laminates has a direct effect on the laminate strength. Therefore, fully characterising the open and filled hole failure mechanics of fibre reinforced laminates is essential. Additionally, it is imperative that the computational modelling framework developed in this thesis can accurately predict the damage and failure progression at screw holes. Experimental testing of both open hole and filled hole configurations in tension and compression reveal extensive intra-laminar cracking initiating on the transverse side of the hole in the open hole tests and on the axial side of the hole in the filled hole experiments. Failure mechanisms for open and filled hole tests are correctly predicted by the computational model.

When holes are machined in fibre reinforced laminates the continuous fibres are broken, promoting inter-laminar delamination and cracking at screw hole sites. An alternative approach is to mould the screw holes into the implant during processing, eliminating the requirement of drilling holes following fabrication of the laminate structure. In this approach carbon fibres are moulded around the holes during processing, so that fibres remain continuous in the laminate without broken exposed fibre ends at the site of the hole. This thesis presents, for the first time, a computational methodology for creating finite element models of moulded holes in continuous fibre reinforced laminated devices. Models of fracture fixation devices with moulded and drilled holes are constructed and their mechanical performance is compared. The drilled implant is predicted to have considerably greater failure strength in compression and bending but a slightly lower failure strength in torsion.

The findings of this thesis have important implications for the development of next-generation laminated fibre reinforced fracture fixation plates. The experimental

results represent the first full material characterisation of medical grade unidirectional carbon fibre reinforced PEEK and uncovers the complex failure mechanisms present. The novel damage and failure computational model presented provides the ability to predict diverse damage mechanisms under multiple loading directions conditions is critical for the safe design of fibre reinforced laminated orthopaedic devices.

## Acknowledgements

First and foremost, I need to express my deepest gratitude to my supervisor Dr. Patrick McGarry, for his invaluable support, encouragement and direction throughout my studies. Without his expertise, guidance and generous time I could not have completed this PhD.

I would also like to thank Invibio Ltd. for kindly providing test materials, and Dr. Steven Lamorinière for sharing his knowledge and enthusiasm which contributed greatly to the project. I must also acknowledge ÉireComposites Teo. and CTL for the use of their manufacturing facilities and technical support- a huge thanks to all the guys who welcomed me in Inverin, especially Bryan who gave up so much of his time to help me. The experimental studies in this PhD could not have succeeded without the help and support everyone in both Invbio and ÉireComposites/CTL.

I wish to thank the Irish Research Council and the College of Engineering and Informatics in NUIG for funding this research. The Irish Centre for High End Computing (ICHEC) also provided me with invaluable support over the past years. Further, I wish to extend my sincere appreciation to the technical staff in the Engineering Department, in particular to Colm Wash, Pat Kelly, Boni Kennedy and William Kelly for their assistance and support throughout the experimental testing.

Next to those, who helped me maintain a full and vibrant life outside of this PhD; To all of the gang on the 2<sup>nd</sup> and 3<sup>rd</sup> floors (past and present), thanks for making sure there was never a dull moment, for the constant supply of baked goods and the scintillating lunchtime conversations! To the ‘McGarry row’; Eoin Mc, Catherine, Brían, Jamie, Brian, Diarmuid, Ryan, Enda and honorary member Ciara- thank you for always providing welcome distractions from uncooperative models. A big thanks to my ‘composites friends’, Ted, Emer, and Dave G, for being so generous with your RVE/PEEK/XFEM knowledge. To my PhD brothers, Dave and Noel, thank you for all the wise words, rare moods, adventures and phrasings. Thanks to ‘the girls’ for all the hilariously random snaps and chats, and the unwanted but appreciated birthday cakes (Fiona!!). Sinéad, thank you for all the holidays, celebratory Moets and Taylor concerts, keeping me motivated when the end was neither near nor in sight.

To my family, whose love and support has taken me through not just this PhD, but everything else too. Joe and Ro, thank you for always reminding me about what’s really important, like who is Rosco’s favourite and who actually owned the blue plate. To my dear and greatly missed Mum, thank you for showing me what it is to be kind and brave and strong; I miss your beautiful smile. And finally, to my Dad, my best bud and constant cheerleader, I do not possess adequate words to express the depth of gratitude I owe to you. Without your unending support and belief in me, I could not have gotten this far; echoes of ‘*giv’em hell*’ will forever follow me wherever I go.

# Table of Contents

## Chapter 1

<b>Introduction .....</b>	<b>1</b>
1.1 Overview of Thesis .....	1
1.2 Objectives .....	5
1.3 Thesis Structure .....	7
1.4 Publications and conference proceedings.....	9
1.1 References .....	11

## Chapter 2

<b>Background.....</b>	<b>15</b>
2.1 Bone mechanics.....	16
2.1.1 Bone composition .....	16
2.1.2 Mechanical properties of cortical and trabecular bone .....	18
2.2 Fracture fixation .....	19
2.2.1 Tension band wiring.....	20
2.2.2 Intramedullary nails .....	21
2.2.3 Fracture fixation plates.....	23
2.3 Orthopaedic biomaterials .....	26
2.3.1 Bio-metals .....	26
2.3.2 Poly-ether-ether-ketone (PEEK) .....	27
2.3.3 Fibre reinforced laminates.....	30
2.4 Failure of composite materials .....	36
2.4.1 World wide failure exercise (WWFE) .....	37
2.4.2 Failure theories.....	41
2.4.3 Modelling inter-and intra-laminar failure .....	46
2.4.4 Micro-scale modelling .....	48
2.5 References .....	52

## Chapter 3

<b>Theory .....</b>	<b>64</b>
3.1 Notation .....	65
3.2 Continuum mechanics .....	66

3.2.1	Deformation and strain measures .....	66
3.2.2	Stress measures .....	71
3.3	Mechanical behaviour of composites .....	74
3.4	The finite element (FE) method .....	83
3.4.1	Implicit FE method solution .....	84
3.5	Damage modelling .....	88
3.5.1	The Extended Finite Element Method (XFEM) .....	88
3.5.2	The Cohesive Zone Model (CZM).....	92
3.6	Digital Image Correlation (DIC) theory .....	94
3.7	References .....	96

## Chapter 4

### **Multi-axial damage and failure of CF/PEEK laminates:**

#### **Experimental testing and computational modelling.....97**

4.1	Introduction .....	97
4.2	Experimental methods .....	101
4.2.1	Specimen preparation.....	101
4.2.2	Experimental testing.....	102
4.3	Computational model development.....	103
4.3.1	Simulating anisotropic plasticity of composite structures .....	103
4.3.2	Simulating inter-laminar delamination .....	104
4.3.3	Simulation intra-laminar failure.....	106
4.4	Experimental results and computational model calibration .....	107
4.5	Model validation.....	123
4.6	Preliminary device design .....	131
4.7	Discussion .....	137
4.8	References .....	141
	Appendix 4A .....	146
	Appendix 4B.....	147
	Appendix 4C.....	149

## Chapter 5

### **Finite element investigation into CF/PEEK laminates for distal radius fracture fixation plates.....154**

5.1	Introduction .....	154
5.2	Model development .....	155
5.2.1	Macro-scale model of distal radius fracture fixation .....	156
5.2.2	Laminate computational damage and failure model .....	158
5.3	Micro-mechanical model of CF/PEEK micro-structure.....	159
5.4	Results .....	163
5.4.1	Macro-scale model of composite fracture fixation plate.....	163
5.4.2	Micro-scale model of fibre-matrix debonding in RVE .....	173
5.5	Discussion .....	177
5.6	References .....	181
	Appendix 5A .....	183
	Appendix 5B.....	185

## **Chapter 6**

### **Mechanical response of CF/PEEK laminates with open holes and filled holes .....186**

6.1	Introduction .....	186
6.2	Materials and methods.....	188
6.2.1	Experimental methods.....	188
6.2.2	Digital Image Correlation (DIC) method.....	190
6.2.3	Computational model .....	192
6.3	Results .....	194
6.3.1	Open hole and filled hole compression: Experimental test results ....	194
6.3.2	Open hole and filled hole compression: Experimental and computational failure modes.....	195
6.3.3	Longitudinal compressive strength .....	201
6.3.4	Open hole tension.....	203
6.4	Discussion .....	205
6.5	References .....	209

## **Chapter 7**

### **Computational Modelling of Moulded Screw Holes.....212**

7.1	Introduction .....	212
7.2	Development of the moulded fibre model.....	214

7.2.1	Fibre bending model .....	215
7.2.2	Discretisation of spatially dependent fibre orientations.....	218
7.3	Computational analysis of fixation plate with moulded and drilled holes	221
7.4	Results .....	222
7.5	Discussion .....	225
7.6	References .....	229
	Appendix 7 A .....	231

## **Chapter 8**

	<b>Concluding remarks and future perspectives .....</b>	<b>232</b>
8.1	Summary of key contributions .....	232
8.2	Future perspectives .....	235
8.3	References .....	238

# Chapter 1

## Introduction

---

### **1.1 Overview of Thesis**

When bone is diseased or injured, orthopaedic implants are inserted into the body to either replace the damaged bone or support the bone while it heals (Bachmeier et al., 2001; Feerick et al., 2013a; Fortin et al., 2002; Long and Rack, 1998; Trampuz and Zimmerli, 2006). Direct trauma, typically through a fall or accident, is the most common cause of orthopaedic fractures (Olson et al., 1982; Stevens and Rudd, 2010), but fractures can also occur under physiological loading conditions in patients with diseases that cause reduced bone mineral density, such as osteoporosis (Aubry-Rozier et al., 2016; Cosman et al., 2014). The global trauma fixation device market has been steadily expanding in recent years and is projected to reach \$9.4 billion by the end of 2020 (Heimbach and Wei, 2017).

Currently, metals such as titanium alloys and steel alloys are the material of choice for orthopaedic implants (Long and Rack, 1998; Manivasagam et al., 2010). Metal has many favourable qualities, including material strength, withstanding the high loading environment of the body, while inducing minimal immune reaction. However, rigid metal implants have been shown to cause stress shielding effects in the peri-prosthetic bone. Stress shielding leads to resorption of the bone surrounding the implant, resulting aseptic loosening of the implant, a common cause of implant failure (Gross and Abel, 2001; Huiskes et al., 1992; Scannell and Prendergast, 2009; Wan et al., 1999).

Polyetheretherketone (PEEK) is becoming increasingly more attractive as a biomaterial for use in orthopaedic applications, including trauma and spinal implants (Chen et al., 2013; Cho et al., 2002; Kurtz and Devine, 2007; Ponnappan et al., 2009; Sagomonyants et al., 2008). It has been shown that carbon fibre PEEK composites, that is PEEK reinforced with short unaligned carbon fibres, has a comparable elastic modulus, strength and density to cortical bone (Scholz et al., 2011; Steinberg et al., 2012; Williams et al., 1987). However it is well established that bone has anisotropic material properties (Ashman et al., 1984; Fan et al., 2002; Feerick et al., 2013b; Turner et al., 1999), therefore in order to get a true match for the material properties of the peri-prosthetic bone a device that is also anisotropic should be considered.

The addition of continuous unidirectional carbon fibres to PEEK allows a reinforced ply to be manufactured. Stacking several plies on top of one another creates what is known as a reinforced laminate. The orientation of the plies with respect to the global axis of the laminate will determine the strength and stiffness of the laminate in different loading directions. The anisotropic material properties of a laminate can be

customised by the designer to fit specific applications. In the case of orthopaedic implants the material properties can be designed to withstand the specific loading environment of the surrounding anatomy. Therefore, different laminates would be designed for different regions in the body, depending on the physiological and external loading experienced in those areas. This will provide superior performance in terms of reducing bone resorption and reducing the thickness of the plate, while maintaining the structural support currently provided by metallic implants. The use of fibre reinforced composites in orthopaedics is a novel application for composite laminates, whose use has been well established in the automotive and aerospace industries for many years.

To date PEEK-OPTIMA™ Ultra-Reinforced (Invibio Ltd., Thornton-Cleveleys, UK), hereafter referred to as CF/PEEK, is the only unidirectional fibre reinforced thermoplastic material that has been cleared by the FDA for implantation in humans. However, no experimental or computational characterisation of the material has been published and the failure mechanisms have not been uncovered. This represents a significant blockage to the widespread development and implantation of carbon fibre reinforced laminates. This thesis aims to perform the first in depth mechanical characterisation of CF/PEEK. As described in Chapter 4, the author was provided with two spools of unidirectional CF/PEEK by Invibio Ltd. to fabricate a range of laminates and perform a series of advanced experimental characterisation.

Fundamental failure theories for fibre reinforced composites are very well established in the literature (Chang and Chang, 1987; Hashin, 1980; Puck and Schürmann, 2002; Rotem and Hashin, 1975; Tsai and Wu, 1971). More recently implementing finite element modelling in conjunction with experimentation has

proven to be an extremely valuable tool in laminate failure analysis (Hinton et al., 2004; Hsu et al., 1999; Liu and Zheng, 2010; Pinho et al., 2006a, 2006b; Vogler and Kyriakides, 1999; Zhang and Yang, 2009), as the complexity of composite laminate failure mechanisms in the experimental results can be better interpreted through computational models that incorporate all composite failure modes. One focus of this research is to develop a novel finite element modelling framework for the case of medical grade carbon fibre reinforced PEEK (CF/PEEK) laminates. To generate macro- and microscale models that will simulate crack propagation through the PEEK matrix, fibre-matrix debonding, delamination and fibre breakage while accurately captures the progressive failure of CF/PEEK laminates under complex external loading, analogous to the loading environment of the human body.

Biomechanical analysis will be performed on an area of the skeleton that is most frequently injured and requires fixation plates to be implanted to aid healing of the fractured bones, i.e. the distal radius (Christen et al., 2013; Davidson et al., 2006; Hirahara et al., 2003; Lochmüller et al., 2002). Laminated fixation plates will be designed and compared with existing homogeneous metallic fixation plates to determine if CF/PEEK plates can be designed to be comparable with materials already on the market.

Screw pull out is a common failure that occurs in current orthopaedic implants (Feerick and McGarry, 2012; Heller et al., 1995; Reitman et al., 2004). Analyses of laminated fracture fixation plates reveals that cracks often propagate from the screw holes. Before CF/PEEK can be considered as an alternative material to metal for the fabrication of fracture fixation devices, it is necessary to fully characterise the mechanisms of failure in the region of the screw hole. Experimental tests of

laminates containing open and filled holes will be carried out to observe and define the failure mechanisms at the screw hole. The experimental results will be used to further validate the computational damage model.

Drilling of holes in unidirectional carbon fibre reinforced laminates is not a trivial task and ultimately causes the destruction of the reinforcing fibres in the hole. Incorrect drilling parameters can also induce, delaminations, fibre pull-outs and matrix cracking among others (Panchagnula and Palaniyandi, 2017). One proposed alternative to drilling unidirectional laminates is to mould the holes into the part during laminate processing. Moulded holes in this fashion results in holes with little to no process induced damage and no fibre breakages (Fujihara et al., 2003; Huang and Fujihara, 2005; Rohner et al., 2005). To date no computational simulations have been performed on moulded fibre reinforced laminates. A computational methodology is developed to generate finite element models of moulded holes. Simulations are performed on a generic fracture fixation device to compare computationally the drilled and moulded holes.

This thesis represents an important contribution to the development of next-generation fibre reinforced laminated composite orthopaedic implants.

### **1.2 Objectives**

The overall objective of this thesis is to determine if carbon fibre reinforced PEEK laminates are a suitable material for the next generation of orthopaedic implants. To investigate if laminated implants may be superior to their metallic equivalent for certain applications e.g. fracture fixation plates, through a combination of experimental tests and computational simulations. This section provides motivations

for the specific objectives of this thesis. A comprehensive background and motivation for each objective is provided in the corresponding technical chapter.

- Experimental characterisation of the elastic material properties of medical grade unidirectional carbon fibre reinforced PEEK. To date no experimental data has been published for medical grade carbon fibre reinforced PEEK. Previous experiments, largely performed in the 1980s, to determine the unidirectional material properties have been performed on generic carbon fibre reinforced PEEK. Hence there is a need to determine experimentally the unidirectional material properties of medical grade CF/PEEK.
- Develop a computational damage model to accurately simulate the failure point, location and mechanism of CF/PEEK laminates and subsequent validation with experimental data. A detailed and robust methodology for simulating the formation of random 3D crack paths and the amassing of sub critical damage areas, in addition to inter-ply delamination achieved through a novel combined extended finite element method and cohesive zone model (XFEM/CZM).
- Computational investigation of the effect of multi-axial loading on laminated distal radius fracture fixation plates on a macro- and micro-scale. The macroscopic stress/strain state of composite implants under physiological loads must be first be analysed. Macro-scale characterisation will then be used as inputs for an investigation of micro-structural failure mechanisms. A fundamental understanding of the failure mechanisms of CF/PEEK is essential for the safe design of laminated implants.
- Experimental investigation of the damage propagation and failure behaviour of multi-ply laminates containing open and filled drilled holes. Digital image

correlation is used to visualise the crack propagation and compute the strain field in the region of the drilled hole. Determine if the previously developed computational damage model can simulate the complex crack propagation in the experimental tests.

- Develop a novel computational technique to simulate moulded screw holes and compare their mechanical behaviour under uni- and multi-axial loading to drilled screw holes. An alternative to drilling holes in laminates is to mould the holes prior to the curing process however it is not clear how much damage is caused by forcing the fibres around the pins. It is believed that composite flow moulding (CFM), the process used to manufacture moulded screws, results in holes that have greater reinforcement compared to drilled holes, however to date no studies have been performed to simulate the CFM process.

### 1.3 Thesis Structure

The following is an outline of each chapter in this thesis.

**Chapter 2** gives a general literature review on carbon fibre reinforced poly-ether-ether-ketone (PEEK). With a focus on computational modelling of carbon fibre reinforced polymers (CFRPs), including micro-mechanical modelling techniques and failure and damage models for CFRPs. The use of PEEK in orthopaedic devices, bone structure and material properties. Included in each of the subsequent technical studies (Chapters 4-7) is a critical literature review directly pertinent to each study, while Chapter 2 give a more general background to the literature.

In **Chapter 3**, a background to the theoretical and numerical methods implemented in the computational work of this thesis is provided.

In **Chapter 4**, the material characterisation of carbon fibre reinforced PEEK laminates is fully obtained through various experimental measurements. A computational study is also performed to validate the XFEM damage initiation and evolution criteria of unidirectional CF/PEEK lamina, which is implemented in all subsequent computational models in Chapters 5-7 of this thesis.

**Chapter 5** presents a computational investigation of CF/PEEK laminates for use in distal radius fracture fixation plates. The response of several laminate layups to physiologically relevant multi-axial loading conditions is examined. An optimum layup for the loading conditions of the distal radius is established and its stress/strain response is compared with similar homogeneous PEEK and titanium alloy devices. Micro-mechanical representative volume elements (RVEs) are also generated to simulate the micro-scale damage occurring in the laminate under physiologically relevant loading conditions.

In **Chapter 6**, the mechanical response of CF/PEEK laminates containing damaged sections, in the form of drilled holes, is examined experimentally. Open and filled hole tensile and compression tests are performed on two common laminate layups. It is demonstrated that the computational damage model can accurately simulate damage and failure in larger laminates containing more angled plies.

In **Chapter 7**, moulded holes, a proposed alternative to drilling holes in laminates during post-processing which results in high levels of micro- and macro-damage, are investigated. A novel method of modelling moulded screw holes in laminates is

developed. It is demonstrated that a fibre reinforced laminate with moulded holes does not guarantee greater strength in the laminate compared with a drilled hole.

**Chapter 8** outlines the key findings of this thesis and summarises the implications of these results for the future design, development and use of fibre reinforced laminates in orthopaedic devices. Suggestions for future experimental and computational work are also presented.

### 1.4 Publications and conference proceedings

#### Peer reviewed journal publications

**Chapter 4:** Published in *Journal of the Mechanical Behaviour of Biomedical Materials*:

Gallagher, EA, Lamorinière, S, McGarry, JP. Multi-axial damage and failure of medical grade carbon fibre reinforced PEEK laminates: experimental testing and computational modelling.

**Chapter 5:** Submitted to *Journal of Biomaterials applications*:

Gallagher, EA, Lamorinière, S, McGarry, JP. Finite Element Investigation into the use of Carbon Fibre Reinforced PEEK Composite Laminates for Distal Radius Fracture Fixation Implants.

**Chapter 6:** Under preparation for publication in *Journal of Biomechanical Engineering*:

Gallagher, EA, Lamorinière, S, McGarry, JP. Experimental characterisation of carbon fibre reinforced PEEK laminates containing open and filled holes.

**Chapter 7:** Under preparation for publication in '*Composites Science and Technology*'

Gallagher, EA, Lamorinière, S, McGarry, JP. Computational methodology for the generation of finite element models of moulded holes in fibre reinforced laminates.

**International conference proceedings**

Gallagher, E.A., Lamorinière, S., McGarry, J.P., 'Failure of carbon fibre PEEK laminated composites', 3<sup>rd</sup> International PEEK Meeting, April 2017, Washington, D.C., USA.

Gallagher, E.A., Ó Brádaigh, C.M., McGarry, J.P., 'A computational investigation into the use of carbon fibre reinforced PEEK laminates for orthopaedic applications, 2<sup>nd</sup> International PEEK Meeting, April 2015, Washington, D.C., USA.

Gallagher, E.A., Ó Brádaigh, C.M., McGarry, J.P., 'Identification of microstructural failure mechanisms of laminated composite orthopaedic implants', 7<sup>th</sup> World Congress of Biomechanics, July 2014, Boston, MA, USA.

Gallagher, E.A., Ó Brádaigh, C.M., McGarry, J.P., 'Comparison of carbon fibre PEEK laminated, titanium and unreinforced PEEK as materials for distal radius fracture fixation plates', 19th Congress of the European Society of Biomechanics, August 2013, Patras, Greece.

## 1.1 References

- Ashman, R.B., Cowin, S.C., Van Buskirk, W.C., Rice, J.C., 1984. A continuous wave technique for the measurement of the elastic properties of cortical bone. *J. Biomech.* 17, 349–361. [https://doi.org/10.1016/0021-9290\(84\)90029-0](https://doi.org/10.1016/0021-9290(84)90029-0)
- Aubry-Rozier, B., Gonzalez-Rodriguez, E., Stoll, D., Lamy, O., 2016. Severe spontaneous vertebral fractures after denosumab discontinuation: three case reports. *Osteoporos. Int.* 27, 1923–1925. <https://doi.org/10.1007/s00198-015-3380-y>
- Bachmeier, C.J., March, L.M., Cross, M.J., Lapsley, H.M., Tribe, K.L., Courtenay, B.G., Brooks, P.M., 2001. A comparison of outcomes in osteoarthritis patients undergoing total hip and knee replacement surgery. *Osteoarthr. Cartil.* 9, 137–146.
- Chang, F., Chang, K.-Y., 1987. Laminated Composites Containing Stress Concentrations. *J. Compos. Mater.* 21, 834–855.
- Chen, Y., Wang, X., Lu, X., Yang, L., Yang, H., Yuan, W., Chen, D., 2013. Comparison of titanium and polyetheretherketone (PEEK) cages in the surgical treatment of multilevel cervical spondylotic myelopathy: A prospective, randomized, control study with over 7-year follow-up. *Eur. Spine J.* 22, 1539–1546. <https://doi.org/10.1007/s00586-013-2772-y>
- Cho, D.Y., Liau, W.R., Lee, W.Y., Liu, J.T., Chiu, C.L., Sheu, P.C., 2002. Preliminary experience using a polyetheretherketone (PEEK) cage in the treatment of cervical disc disease.[Erratum appears in *Neurosurgery*. 2003 Mar;52(3):693]. *Neurosurgery* 51, 1343–1350.
- Christen, P., Ito, K., Knippels, I., Müller, R., van Lenthe, G.H., van Rietbergen, B., 2013. Subject-specific bone loading estimation in the human distal radius. *J. Biomech.* 46, 759–66. <https://doi.org/10.1016/j.jbiomech.2012.11.016>
- Cosman, F., de Beur, S.J., LeBoff, M.S., Lewiecki, E.M., Tanner, B., Randall, S., Lindsay, R., National Osteoporosis Foundation, 2014. Clinician’s Guide to Prevention and Treatment of Osteoporosis. *Osteoporos. Int.* 25, 2359–81. <https://doi.org/10.1007/s00198-014-2794-2>
- Davidson, P.L., Chalmers, D.J., Stephenson, S.C., 2006. Prediction of distal radius fracture in children, using a biomechanical impact model and case-control data on playground free falls. *J. Biomech.* 39, 503–509. <https://doi.org/10.1016/j.jbiomech.2004.11.028>
- Fan, Z., Swadener, J.G., Rho, J.Y., Roy, M.E., Pharr, G.M., 2002. Anisotropic properties of human tibial cortical bone as measured by nanoindentation. *J. Orthop. Res.* 20, 806–810. [https://doi.org/10.1016/S0736-0266\(01\)00186-3](https://doi.org/10.1016/S0736-0266(01)00186-3)
- Feerick, E.M., Kennedy, J., Mullett, H., FitzPatrick, D., McGarry, P., 2013a. Investigation of metallic and carbon fibre PEEK fracture fixation devices for three-part proximal humeral fractures. *Med. Eng. Phys.* 35, 712–722. <https://doi.org/10.1016/j.medengphy.2012.07.016>
- Feerick, E.M., Liu, X.C., McGarry, P., 2013b. Anisotropic mode-dependent damage of cortical bone using the extended finite element method (XFEM). *J. Mech. Behav. Biomed. Mater.* 20, 77–89. <https://doi.org/10.1016/j.jmbbm.2012.12.004>
- Feerick, E.M., McGarry, J.P., 2012. Cortical bone failure mechanisms during screw pullout.

- J. Biomech. 45, 1666–1672. <https://doi.org/10.1016/j.jbiomech.2012.03.023>
- Fortin, P.R., Penrod, J.R., Clarke, A.E., St-Pierre, Y., Joseph, L., Belisle, P., Liang, M.H., Ferland, D., Phillips, C.B., Mahomed, N., Tanzer, M., Sledge, C., Fossel, A.H., Katz, J.N., 2002. Timing of total joint replacement affects clinical outcomes among patients with osteoarthritis of the hip or knee. *Arthritis Rheum.* 46, 3327–3330. <https://doi.org/10.1002/art.10631>
- Fujihara, K., Huang, Z.M., Ramakrishna, S., Satknanantham, K., Hamada, H., 2003. Performance study of braided carbon/PEEK composite compression bone plates. *Biomaterials* 24, 2661–2667. [https://doi.org/10.1016/S0142-9612\(03\)00065-6](https://doi.org/10.1016/S0142-9612(03)00065-6)
- Gross, S., Abel, E.W., 2001. A finite element analysis of hollow stemmed hip prostheses as a means of reducing stress shielding of the femur. *J. Biomech.* 34, 995–1003. [https://doi.org/10.1016/S0021-9290\(01\)00072-0](https://doi.org/10.1016/S0021-9290(01)00072-0)
- Hashin, Z., 1980. Failure Criteria for Unidirectional Fiber Composites. *J. Appl. Mech.* 47, 329. <https://doi.org/10.1115/1.3153664>
- Heimbach, B., Wei, M., 2017. Composite Orthopedic Fixation Devices, in: *Orthopedic Biomaterials*. Springer International Publishing, Cham, pp. 399–425. [https://doi.org/10.1007/978-3-319-73664-8\\_15](https://doi.org/10.1007/978-3-319-73664-8_15)
- Heller, J.G., Silcox, D.H., Sutterlin, C.E., 1995. Complications of posterior cervical plating. *Spine (Phila. Pa. 1976)*. 20, 2442–8. <https://doi.org/10.1097/00007632-199511001-00013>
- Hinton, M.J., Kaddour, A.S., Soden, P.D., 2004. Failure Criteria in Fibre-Reinforced-Polymer Composites, Failure Criteria in Fibre-Reinforced-Polymer Composites. <https://doi.org/10.1016/B978-0-080-44475-8.X5000-8>
- Hirahara, H., Neale, P.G., Lin, Y. Te, Cooney, W.P., An, K.N., 2003. Kinematic and torque-related effects of dorsally angulated distal radius fractures and the distal radial ulnar joint. *J. Hand Surg. Am.* 28, 614–621. [https://doi.org/10.1016/S0363-5023\(03\)00249-1](https://doi.org/10.1016/S0363-5023(03)00249-1)
- Hsu, S., Vogler, T., Kyriakides, S., 1999. Inelastic behavior of an AS4/PEEK composite under combined transverse compression and shear. Part II: modeling. *Int. J. Plast.* 15.
- Huang, Z.M., Fujihara, K., 2005. Stiffness and strength design of composite bone plates. *Compos. Sci. Technol.* 65, 73–85. <https://doi.org/10.1016/j.compscitech.2004.06.006>
- Huiskes, R., Weinans, H., van Rietbergen, B., 1992. The relationship between stress shielding and bone resorption around total hip stems and the effects of flexible materials. *Clin. Orthop. Relat. Res.* 124–134. <https://doi.org/10.1097/00003086-199201000-00014>
- Kurtz, S.M., Devine, J.N., 2007. PEEK biomaterials in trauma, orthopedic, and spinal implants. *Biomaterials* 28, 4845–69. <https://doi.org/10.1016/j.biomaterials.2007.07.013>
- Liu, P.F., Zheng, J.Y., 2010. Recent developments on damage modeling and finite element analysis for composite laminates: A review. *Mater. Des.* 31, 3825–3834. <https://doi.org/10.1016/j.matdes.2010.03.031>
- Lochmüller, E.-M., Lill, C.A., Kuhn, V., Schneider, E., Eckstein, F., 2002. Radius Bone Strength in Bending, Compression, and Falling and Its Correlation With Clinical Densitometry at Multiple Sites. *J. Bone Miner. Res.* 17, 1629–1638. <https://doi.org/10.1359/jbmr.2002.17.9.1629>

- Long, M., Rack, H.J., 1998. Titanium alloys in total joint replacement--a materials science perspective. *Biomaterials* 19, 1621–1639. [https://doi.org/10.1016/S0142-9612\(97\)00146-4](https://doi.org/10.1016/S0142-9612(97)00146-4)
- Manivasagam, G., Dhinasekaran, D., Rajamanickam, A., 2010. Biomedical Implants: Corrosion and its Prevention - A Review. *Recent Patents Corros. Sci.* 2, 40–54. <https://doi.org/10.2174/1877610801002010040>
- Olson, R.A., Fonseca, R.J., Zeitler, D.L., Osbon, D.B., 1982. Fractures of the mandible: A review of 580 cases. *J. Oral Maxillofac. Surg.* 40, 23–28. [https://doi.org/10.1016/S0278-2391\(82\)80011-6](https://doi.org/10.1016/S0278-2391(82)80011-6)
- Panchagnula, K.K., Palaniyandi, K., 2017. Drilling on fiber reinforced polymer/nanopolymer composite laminates: A review. *J. Mater. Res. Technol.* <https://doi.org/10.1016/j.jmrt.2017.06.003>
- Pinho, S.T., Iannucci, L., Robinson, P., 2006a. Physically based failure models and criteria for laminated fibre-reinforced composites with emphasis on fibre kinking. Part II: FE implementation. *Compos. Part A Appl. Sci. Manuf.* 37, 766–777. <https://doi.org/10.1016/j.compositesa.2005.06.008>
- Pinho, S.T., Iannucci, L., Robinson, P., 2006b. Physically based failure models and criteria for laminated fibre-reinforced composites with emphasis on fibre kinking: Part I: Development. *Compos. Part A Appl. Sci. Manuf.* 37, 63–73. <https://doi.org/10.1016/j.compositesa.2005.06.008>
- Ponnappan, R.K., Serhan, H., Zarda, B., Patel, R., Albert, T., Vaccaro, A.R., 2009. Biomechanical evaluation and comparison of polyetheretherketone rod system to traditional titanium rod fixation. *Spine J.* <https://doi.org/10.1016/j.spinee.2008.08.002>
- Puck, A., Schürmann, H., 2002. Failure Analysis of FRP Laminates By Means of Physically Based Phenomenological Models. *Compos. Sci. Technol.* 62, 1633–1662. [https://doi.org/10.1016/S0266-3538\(96\)00140-6](https://doi.org/10.1016/S0266-3538(96)00140-6)
- Reitman, C.A., Nguyen, L., Fogel, G.R., 2004. Biomechanical evaluation of relationship of screw pullout strength, insertional torque, and bone mineral density in the cervical spine. *J. Spinal Disord. Tech.* 17, 306–311. <https://doi.org/10.1097/01.bsd.0000090575.08296.9d>
- Rohner, B., Wieling, R., Magerl, F., Schneider, E., Steiner, A., 2005. Performance of a composite flow moulded carbon fibre reinforced osteosynthesis plate. *Vet. Comp. Orthop. Traumatol.* 18, 175–182.
- Rotem, A., Hashin, Z., 1975. Failure Modes of Angle Ply Laminates. *J. Compos. Mater.* 9. <https://doi.org/10.1177/002199837500900209>
- Sagomyants, K.B., Jarman-Smith, M.L., Devine, J.N., Aronow, M.S., Gronowicz, G.A., 2008. The in vitro response of human osteoblasts to polyetheretherketone (PEEK) substrates compared to commercially pure titanium. *Biomaterials* 29, 1563–1572. <https://doi.org/10.1016/j.biomaterials.2007.12.001>
- Scannell, P.T., Prendergast, P.J., 2009. Cortical and interfacial bone changes around a non-cemented hip implant: Simulations using a combined strain/damage remodelling algorithm. *Med. Eng. Phys.* 31, 477–488. <https://doi.org/10.1016/j.medengphy.2008.11.007>
- Scholz, M.S., Blanchfield, J.P., Bloom, L.D., Coburn, B.H., Elkington, M., Fuller, J.D.,

- Gilbert, M.E., Muflahi, S.A., Pernice, M.F., Rae, S.I., Trevarthen, J.A., White, S.C., Weaver, P.M., Bond, I.P., 2011. The use of composite materials in modern orthopaedic medicine and prosthetic devices: A review. *Compos. Sci. Technol.* <https://doi.org/10.1016/j.compscitech.2011.08.017>
- Steinberg, E.L., Rath, E., Shlaifer, A., Chechik, O., Maman, E., Salai, M., 2012. Carbon fiber reinforced PEEK Optima-A composite material biomechanical properties and wear/debris characteristics of CF-PEEK composites for orthopedic trauma implants. *J. Mech. Behav. Biomed. Mater.* 17, 221–228. <https://doi.org/10.1016/j.jmbbm.2012.09.013>
- Stevens, J.A., Rudd, R.A., 2010. Declining hip fracture rates in the United States. *Age Ageing.* <https://doi.org/10.1093/ageing/afq044>
- Trampuz, A., Zimmerli, W., 2006. Diagnosis and treatment of infections associated with fracture-fixation devices. *Injury Suppl* 2, S59-66. <https://doi.org/10.1016/j.injury.2006.04.010>
- Tsai, S.W., Wu, E.M., 1971. A General Theory of Strength for Anisotropic Materials. *J. Compos. Mater.* 5, 58–80. <https://doi.org/10.1177/002199837100500106>
- Turner, C.H., Rho, J., Takano, Y., Tsui, T.Y., Pharr, G.M., 1999. The elastic properties of trabecular and cortical bone tissues are similar: Results from two microscopic measurement techniques. *J. Biomech.* 32, 437–441. [https://doi.org/10.1016/S0021-9290\(98\)00177-8](https://doi.org/10.1016/S0021-9290(98)00177-8)
- Vogler, T., Kyriakides, S., 1999. Inelastic behavior of an AS4/PEEK composite under combined transverse compression and shear. Part I: experiments. *Int. J. Plast.* 15, 783–806. [https://doi.org/10.1016/S0749-6419\(99\)00011-X](https://doi.org/10.1016/S0749-6419(99)00011-X)
- Wan, Z., Dorr, L.D., Woodsome, T., Ranawat, A., Song, M., 1999. Effect of stem stiffness and bone stiffness on bone remodeling in cemented total hip replacement. *J. Arthroplasty* 14, 149–158. [https://doi.org/10.1016/S0883-5403\(99\)90118-3](https://doi.org/10.1016/S0883-5403(99)90118-3)
- Williams, D.F., McNamara, A., Turner, R.M., 1987. Potential of polyetheretherketone (PEEK) and carbon-fibre-reinforced PEEK in medical applications. *J. Mater. Sci. Lett.* 6, 188–190. <https://doi.org/10.1007/BF01728981>
- Zhang, Y.X., Yang, C.H., 2009. Recent developments in finite element analysis for laminated composite plates. *Compos. Struct.* 88, 147–157. <https://doi.org/10.1016/j.compstruct.2008.02.014>

# Chapter 2

## Background

---

This chapter provides an overview of the literature and background theory relevant to the subject areas of this thesis. In Section 2.1 a background to bone structure, mechanics and the anatomy of the wrist is given, with a focus on the distal radius. In Section 2.2 an overview of current orthopaedic fracture fixation devices is presented. In Section 2.3 the relevant biomaterials currently in use for orthopaedic devices are outlined, including the use of poly-ether-ether-ketone (PEEK) as a biomaterial, experimentally reported properties, along with a detailed overview of carbon fibre reinforced PEEK. In Section 2.4 composite failure modes and previously developed failure theories are outlined, along with commonly utilised computational techniques for micromechanical modelling and failure of fibre reinforced composites are presented. While this chapter provides a general overview of the literature relevant to this body of work, it should be noted that each technical chapter of this thesis (Chapters 4-7) provides a focused discussion of the critical literature in the context of the key results and findings. Furthermore, Chapter 3 provides a detailed

presentation of the theoretical and numerical techniques that are implemented and developed in this thesis.

### **2.1 Bone mechanics**

The skeletal system provides the bony framework that supports and protects the internal organs of the body. Movement of the body is facilitated through the contraction of muscles that are anchored to the bones of the skeletal system. Bone undergoes a range of complex multi-axial static and cyclic loading configurations while performing these movements and functions. Bone tissue has a complex structure and material properties; it is lightweight whilst also providing strength, support, and stiffness. This unique mechanical behaviour is imparted by a composite material of organic proteins and mineral crystals, which are intricately organized, across many scales, to create the material properties that allow bone to serve these functions under the variety of loading conditions experienced during everyday activities (Jee, 2001; Rho et al., 1998).

#### **2.1.1 Bone composition**

The complex hierarchical structure and organisation of bone is outlined in Figure 2.1. The mechanical properties of bone are determined by its nano-structural, sub-micro-structural (lamellar), micro-structural (trabecular/osteons) and structural (compact/cancellous) organisation as well as its composition (Zysset et al., 1999). At the macro-scale two distinct types of bone tissue are present, cortical and trabecular bone. As shown in Figure 2.1(e), a hard outer shell of cortical bone surrounds a core of less dense trabecular bone.

Cortical bone, also referred to as compact bone, is a naturally occurring composite composed of organic and inorganic compounds. The inorganic phase comprises

mainly of collagen type I (90%), and the organic phase is composed of impure hydroxyapatite (Reilly and Burstein, 1975). At the micro-scale, the functional units of cortical bone are the concentric stacks of collagen sheets that make up osteons (Weiner et al., 1999), see Figure 2.1(c). Osteons have been shown to act as microstructural barriers to crack growth in bones and have been likened to fibre reinforcements in composite materials (Martin and Burr, 1989; O'Brien et al., 2007; Taylor and Prendergast, 1997). Cylindrical osteons, also known as Haversian systems, are embedded in an interstitial matrix of hydroxyapatite. In the long bones of the body, e.g. femur, tibia, humerus, radius etc., the osteons run parallel to the central axis of the bone. It is thought that the osteon organisation provides structural support to the bone.

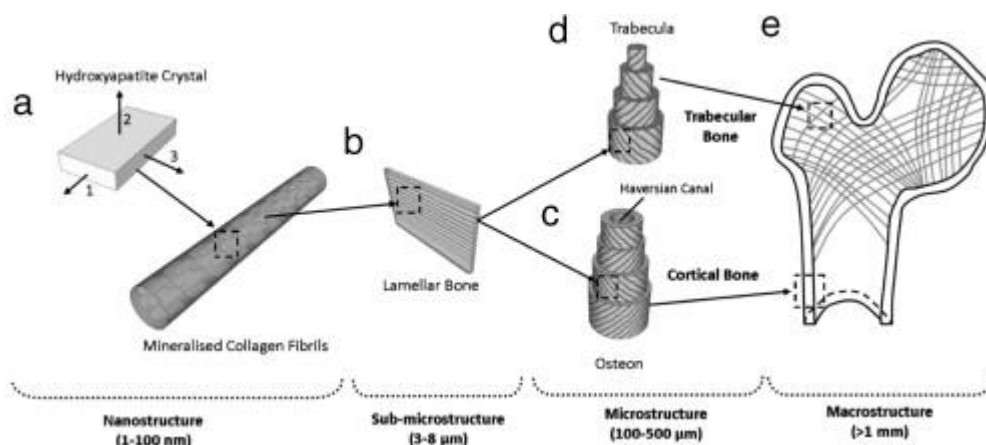


Figure 2.1: Illustration of the hierarchical structure of bone from the nano- to the macro-level, highlight bone's inherent composite structure; (a) Bone mineral crystals and mineralised collagen fibrils; (b) Lamellar bone in the sub-microscale; (c) An osteon with a Haversian system; (d) A trabecula; and (e) cortical and trabecular bone (Vaughan et al., 2012).

Trabecular or cancellous bone is an irregular porous material comprised of a three-dimensional network of trabecular bone struts surrounded by bone marrow. The struts are observed to orient themselves in the direction of maximum force in order to provide some degree of enhanced structural support to the highly porous material.

Although trabecular bone has an almost identical composition to cortical bone they differ greatly in terms of their structure. The porosity of trabecular bone is in the region of 30 - >90%, compared to 5 - 30% for cortical bone (Carter and Spengler, 1978). The mechanical properties of bone are greatly influenced by its hierarchal structure and as such can vary greatly at the different structural levels.

### 2.1.2 Mechanical properties of cortical and trabecular bone

The mechanical properties of cortical bone have been investigated experimentally on several scales using a range of experimental methods by several research groups. A summary of the reported mechanical properties are reported in Table 2.1 below.

Table 2.1: Reported experimentally measured values for the elastic modulus of cortical bone

Study	Type of loading	Elastic modulus $\pm$ standard deviation (GPa)	Ultimate strength $\pm$ standard deviation (MPa)	Bone
Ascenzi and Bonucci (1968)	Longitudinal Compression	$6.3 \pm 1.8$	$109.8 \pm 10.1$	Femoral osteon
Ascenzi and Bonucci (1968)	Transverse Compression	$9.3 \pm 1.6$	$163 \pm 11.7$	Femoral osteon
Reilly and Burstein (1975)	Longitudinal Tension	$17.9 \pm 3.92$	$135 \pm 15.6$	Femur
Reilly and Burstein (1975)	Transverse Tension	$10.1 \pm 2.35$	$53 \pm 10.7$	Femur
Reilly and Burstein (1975)	Longitudinal Compression	$18.2 \pm 0.85$	$205 \pm 17.3$	Femur
Reilly and Burstein (1975)	Transverse Compression	$11.7 \pm 1.01$	$131 \pm 20.7$	Femur
Keller et al. (1990)	4-point bend	$12.1 \pm 4.14$	$174 \pm 84.1$	Femur
Snyder and Schneider (1991)	3-point bend	$17.5 \pm 1.62$	$214 \pm 21.1$	Tibia
Rho et al. (1993)	Tension	$18.6 \pm 3.5$	-	Microtibial specimens
Rho et al. (1997)	Indentation	$22.5 \pm 1.3$	-	Tibial osteon

The reported values for cortical bone presented in Table 2.1 show that the elastic behaviour and strength of cortical bone are anisotropic, with a higher modulus and strength in the longitudinal direction. A wide range of elastic moduli and ultimate strengths are also reported for trabecular bone. A summary of the reported values are presented in Table 2.2 below. The stiffness and strength of trabecular bone is generally much lower than that of cortical bone.

Table 2.2: Reported experimentally measured values for the elastic modulus of trabecular bone

Study	Elastic modulus $\pm$ standard deviation (MPa)	Ultimate strength $\pm$ standard deviation (MPa)	Bone
Linde et al. (1989)	445 $\pm$ 257	5.3 $\pm$ 2.9	Tibia (proximal)
Martens et al. (1983)	900 $\pm$ 710	9.3 $\pm$ 4.5	Femur (head)
Martens et al. (1983)	616 $\pm$ 707	6.6 $\pm$ 6.3	Femur (proximal)
Kuhn et al. (1989)	298 $\pm$ 224	5.6 $\pm$ 3.8	Femur (distal)

## 2.2 Fracture fixation

Bone fractures are the most common large-organ traumatic injuries that occur in humans, (Kerr-Valentic et al., 2003; Lavini et al., 2014; Pogue et al., 1990). Despite this, approximately 10% of all fractures do not heal properly (Einhorn and Gerstenfeld, 2015). Fracture healing involves a complicated sequence of biophysical processes that are believed to mimic the events that take place during embryonic development of the skeleton (Bolander, 1992; Einhorn, 1998; Ferguson et al., 1999; Freeman and McNamara, 2017; Gerstenfeld et al., 2003). In depth analyses of these complex processes are beyond the scope of this work, and the following section will

instead focus on medical interventions to stabilise long bones during fracture healing.

The aim of fracture treatment is the complete recovery of limb function and a solid union of the fractured bones as early as possible (Schatzker et al., 2005). When fractures are too severe or complex to heal with external casting alone, surgery is performed to internally fix the fracture site (Bradway et al., 1989; Roh et al., 2015). Approximately 20% of all proximal humerus fractures require operative reduction and fixation (Gerber et al., 2004). In the United States alone, 2 million fracture fixation devices are implanted each year (Darouiche, 2004). Among the most commonly used internal orthopaedic fracture fixation devices are fracture fixation plates; however, several other methods of internal fixation exist, including tension band wiring and intramedullary nails. The technical chapters of this thesis are focused solely on laminated fracture fixation plates but tension band wiring and intramedullary nails will also be discussed below for completeness.

### **2.2.1 Tension band wiring**

Tension band wiring (TBW) is the most common operating technique for the internal fixation of displaced olecranon fractures (a fracture of the bony portion of the elbow), see Figure 2.2. The tension band method was first described by Pauwels, and was later introduced by Weber and Vasey for olecranon fracture fixation (Chalidis et al., 2008; Mullett et al., 2000).



Figure 2.2: X-Ray images of a severe olecranon fracture (A) pre- and (B) post- TBW insertion (Chalidis et al., 2008)

Open reduction and internal fixation is performed using two parallel Kirschner wires (K-wires) and a tension band wire loop. This method ensures that the forces produced by the pulling motion of the triceps are transferred into a compression of the fracture (Mullett et al., 2000); therefore, allowing early motion of the elbow and preventing elbow stiffness (van der Linden et al., 2012). A number of long-term TBW studies have reported good outcomes (Finsen et al., 2000; Holdsworth and Mossad, 1984; Karlsson et al., 2002), particularly in transverse and oblique fractures (Kozin et al., 1996). Although the procedure is associated with a high union rate complication rates as high as 82% (Helm et al., 1987; Macko and Szabo, 1985). K-wire instability and prominence of the K-wires at the insertion site causes pain and, in some cases, skin breakages, are the most common causes of complication (Chalidis et al., 2008; Kuo et al., 2011; Mullett et al., 2000; Schneider et al., 2014).

### 2.2.2 Intramedullary nails

The treatment of long bone fractures was revolutionised in 1939 when intramedullary (IM) nails were introduced by Küntscher (Pfeifer et al., 2010). To this day IM nailing remains the treatment of choice for closed midshaft long bone fractures. Complications such as wound infection and non-union are decreased

compared to open reduction techniques (Wähnert and Gehweiler, 2017). Stability of the IM nails is increased through interlocking nailing, whereby screws are placed through fenestrations in the IM (Rommens and Hessmann, 2015; Stedtfeld, 2015; Winquist et al., 1984). Stable fractures are fixated using dynamic interlocking IM nails while static interlocking IM nails are used to fix unstable fractures of the long bones. In dynamic fixation interlocking is performed at only either the proximal or distal end of the nail. In stable fixation, a secondary screw is inserted at the opposite end of the IM nail to enhance callus formation (see Figure 2.3) (Rommens and Hessmann, 2015).

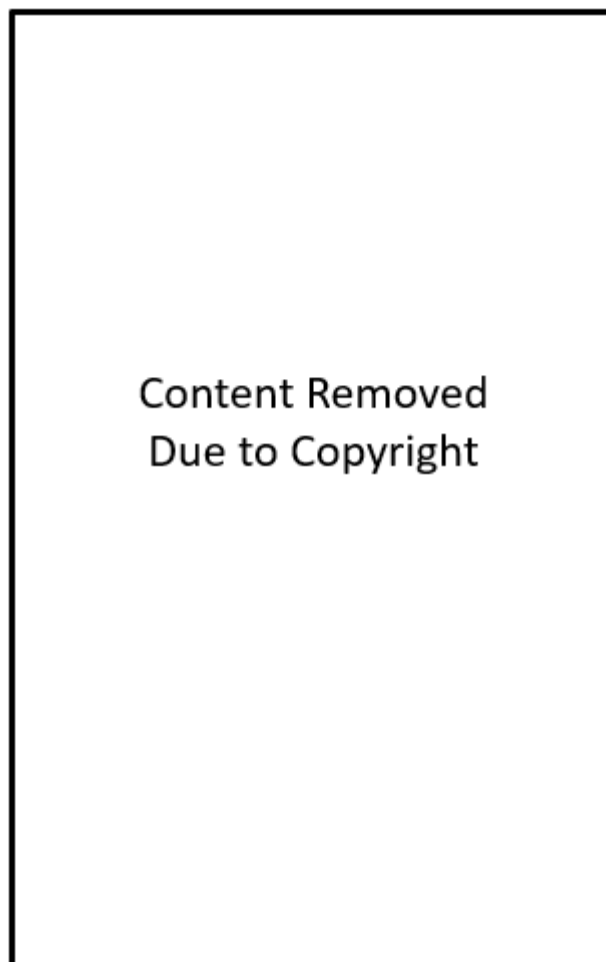


Figure 2.3: (A) Illustration of static interlocking of an unstable fracture. (B) Illustration of dynamic fixation of a stable long bone fracture (Rommens and Hessmann, 2015)

Several studies show that fracture plating results in lower instances of delayed union, mal-union and secondary procedures compared to intramedullary nailing (Kwok et al., 2014; Mao et al., 2015; Markolf et al., 2016; Vallier et al., 2008). Fracture fixation plates are next discussed.

### 2.2.3 Fracture fixation plates

Implanting metal plates for fracture fixation was first introduced in the late 1800s (Cronier et al., 2010; Uthoff et al., 2006). Several advancements to both the materials and geometric design of fixation plates have occurred in recent decades. Typically fracture plates are categorised as either dynamic compression plates or locking compression plates.

A characteristic feature of dynamic compression plates (DCPs) is the incorporation of the screw holes that operate on the spherical gliding principle (Allgüwer et al., 1973). The screw hole resembles two cylinders intersecting at an obtuse angle, Figure 2.4.



Figure 2.4: Longitudinal section through a non-symmetric DCP screw hole (Allgüwer et al., 1973)

The effect of this hole geometry is that the downward movement of the screw into the hole results in the generation of strain in the fracture plate that causes a compression of the fracture site, see Figure 2.5.



Figure 2.5: Illustration of the mechanics of screw insertion in the DCP (Gold and Gilley, 2006)

An analysis of the clinical outcomes of 25,000 DCP implantations reports that non-unions occur in only 2.2% of cases, with and implant breakages occurring in only 1.4% of cases (Matter and Burch, 1990). A more recent study reports higher instances (22.5%) of non-unions following DCP insertion (Kabak et al., 2004).

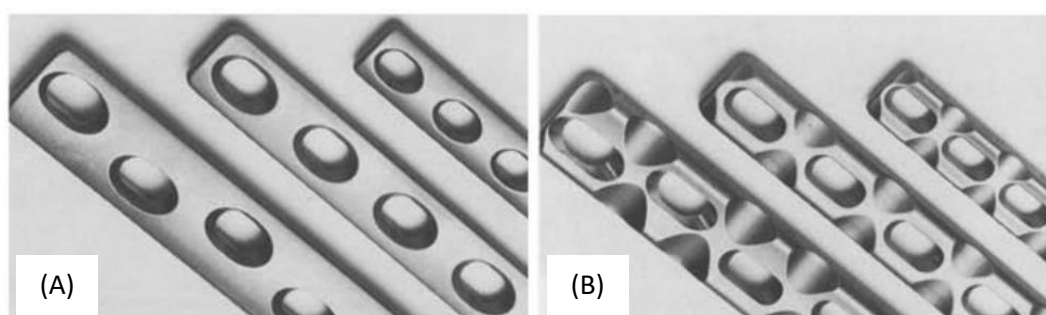


Figure 2.6: Under surface of the (A) a DCP implant and (B) a LC-DCP implant (Perren et al., 1990)

The low-contact DCP (LC-DCP) was designed to reduce the area of plate in direct contact with the bone, thereby increasing the blood supply to the bone and potentially decreasing healing time (McKee et al., 1995; Perren et al., 1990). Kabak et al, report on clinical outcomes of LC-DCPs, finding that time to union in patients

treated with LC-DCPs was shorter than those treated with DCP ( $p < 0.001$ ) (Kabak et al., 2004).

The locking compression plate (LCP), so called because in combination with the conventional holes previously described in the DCP section, the LCP holes contain a threaded section (Figure 2.7). The locking screw hole allows the option of locking the plate in place, in addition to generation of compression at the fracture site (Frigg, 2003; Sommer et al., 2003).



Figure 2.7: Image of the screw hole in the locking compression plate (DePuy Synthes, 2018)

Using screws that are locked in the plate gives angular stability to the construct, therefore the need for the plate to be in direct contact with the bone is removed (Ahmad et al., 2007; Fulkerson et al., 2006). Another advantage of the LCP not having to be in direct contact with the bone is that the implant can be anatomically pre-shaped to ease fixation of more anatomically complex areas of the skeleton, e.g. tibial plateau, proximal ulna, clavicle etc. among others (Ehlinger et al., 2015; Siebenlist et al., 2010; Sommer et al., 2003; Woltz et al., 2016).



Figure 2.8: X-Ray image of an implanted proximal ulna LCP fixing a comminuted olecranon fracture (Siebenlist et al., 2010)

Currently, LCPs and all of the other devices discussed in this section are typically manufactured from biomedical grade titanium (Ti-6Al-4V) or stainless steel (Camarda et al., 2016; Ehlinger et al., 2009; Flynn et al., 2001; Hayes and Richards, 2010; Miller and Goswami, 2007).

## 2.3 Orthopaedic biomaterials

### 2.3.1 Bio-metals

The introduction of stainless steel and titanium in the early-to mid-20<sup>th</sup> century revolutionised the fracture fixation device industry (Hayes and Richards, 2010). Generally, fixation devices must be ductile, strong, stiff and have a high fatigue resistance. However, despite fulfilling all of the aforementioned requirements, and despite their widespread use for orthopaedic implants, titanium and stainless-steel devices present a number of drawbacks.

Stainless steel provides good corrosion resistance. However it has been shown to have poor resistance to wear (Navarro et al., 2008). Titanium has a lower stiffness than stainless steel, but a higher fatigue resistance (Hayes and Richards, 2010). As previously stated, the Young's modulus of cortical bone has been reported as

~18GPa. The Young's moduli of stainless steel and titanium are ~186GPa and 110GPa, respectively. This material stiffness mismatch between the fixation plate and the adjacent bone can lead to a phenomenon known as stress shielding, whereby an applied load is largely supported by the implant and the stress in the peri-prosthetic bone is significantly reduced (Uthoff et al., 2006). Stress shielding results in resorption of the peri-prosthetic bone and can eventually lead to implant failure or bone breakage. Carbon fibre reinforced polymers with a Young's modulus closer to that of bone (20GPa) (Kurtz and Devine, 2007) have been proposed as an alternative to homogenous metal implants. Constituent materials for such non-metallic composite implants will be discussed in the following sections.

### 2.3.2 Poly-ether-ether-ketone (PEEK)

Poly-ether-ether-ketone (PEEK) is a high performance polyaromatic semi-crystalline thermoplastic polymer that was first available commercially for use in orthopaedic, trauma and spinal implants in the 1990s by Invivo Ltd. (Thorton Cleveleys, UK) (Kurtz and Devine, 2007; Panayotov et al., 2016). The chemical formula of PEEK is  $(-C_6H_4 - CO - C_6H_4 - O - C_6H_4 - O -)_n$ , shown in Figure 2.9 below.

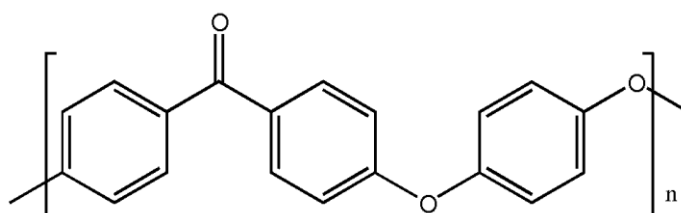


Figure 2.9: Illustration of the chemical composition of PEEK (Kurtz and Devine, 2007)

Its resistance to chemical and radiation damage, thermal stability, radiolucency, biocompatibility and mechanical properties have made PEEK a very attractive candidate for orthopaedic devices (Kurtz and Devine, 2007). Compared to medical grade titanium, with an elastic modulus of 101-110GPa (Niinomi, 1998), the

Young's modulus of unreinforced neat PEEK is 4GPa (Kurtz and Devine, 2007; Panayotov et al., 2016) providing a closer match to the Young's modulus of cortical bone (18-20GPa) (Bayraktar et al., 2004; Rho et al., 1993). Rae et al. (2007) carried out experimental tests to capture the full elastic plastic response of neat/unreinforced PEEK during fracture from  $-50^{\circ}\text{C}$  to  $150^{\circ}\text{C}$ . Results show an increase in compressive yield strength of 30%, from 128MPa to 184MPa, when the strain rate is increased by seven orders of magnitude (Figure 2.10(a)). Similarly, the tensile yield point also increases with increasing strain rate, from  $\sim 102\text{MPa}$  to  $\sim 118\text{MPa}$  over approximately three order of strain rate magnitude (Figure 2.10(b)). Additionally, the yield stress of PEEK is lower in tension than compression.

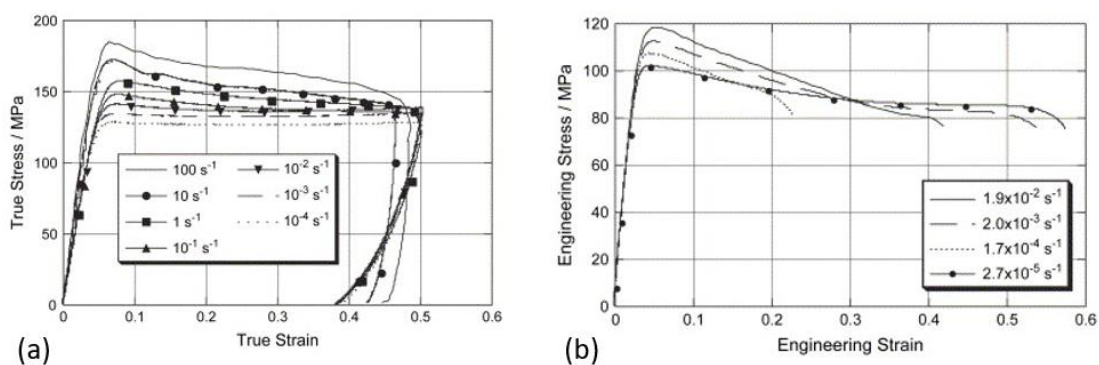


Figure 2.10: Effect of strain rate at  $23^{\circ}\text{C}$  on (a) compressive properties of PEEK and (b) tensile properties of PEEK (Rae et al., 2007).

Several structural and chemical changes can be made to neat PEEK (unfilled) to improve its biological and mechanical properties. Varying amounts of hydroxyapatite (HA) and  $\beta$ -tricalcium phosphate have been added to different unfilled PEEK to increase its bioactivity levels for different clinical applications (Walsh et al., 2016). The mechanical properties unfilled PEEK, specifically its strength and stiffness, can be significantly increased with the addition of reinforcing carbon fibres. Including 30% w/w chopped carbon fibre reinforcement in neat PEEK

results in an increased modulus of 20GPa (Green and Schlegel, 2001; Kurtz and Devine, 2007), see Figure 2.11.

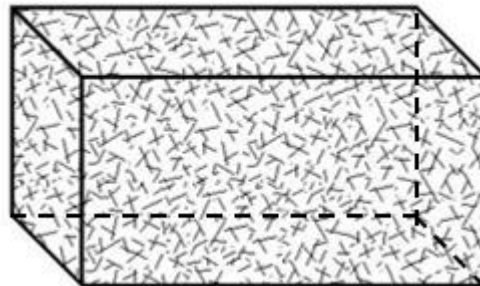


Figure 2.11: Illustration of chopped carbon fibres within the PEEK matrix material

Considering the close match between the Young's modulus of reinforced PEEK and cortical bone, it is clear to see why reinforced PEEK is considered a promising alternative to metallic and ceramic orthopaedic devices. Since its commercialisation, the use of unfilled and short fibre reinforced PEEK devices has become commonplace in several surgical procedures, some examples are outlined below:

- Dental Implants: Implant Fixtures: Dental Implants e.g. Perso-C (SisoMM), Dental Crowns (Najeeb et al., 2016)
- Trauma Implants: Fracture Plates, Intramedullary Rods (Kurtz and Devine, 2007; Steinberg et al., 2012)
- Spinal Implants: Interbody Fusion Devices: Posterior Stabilisation Rods, Anterior Plates, Vertebral cages e.g. Concorde (DePuy Synthes Spine) (Kabir et al., 2010)
- Orthopaedic Implants: Arthroplasty, Arthroscopy: Suture anchors e.g. PEEK IntraLine (Stryker) (Hak et al., 2014)

Unidirectional fibres can also be added to PEEK to create anisotropic lamina that form laminates when stacked on top of one another at various orientations, outlined in the following section.

### 2.3.3 Fibre reinforced laminates

Fibre reinforced laminates are composed of a number of lamina or plies (Figure 2.12). Each ply is made up of unidirectional fibres embedded in a matrix material. A wide range of amorphous and crystalline materials can be used as reinforcing fibres, including, but not limited to, carbon, glass, basalt, silica, Kevlar and aramid (Crawford, 1998). Similarly, a large number of thermoplastic and thermosetting matrix materials are available for use, for example; PEEK, epoxy, unsaturated polyester, nylon, polycarbonate etc. (Crawford, 1998).

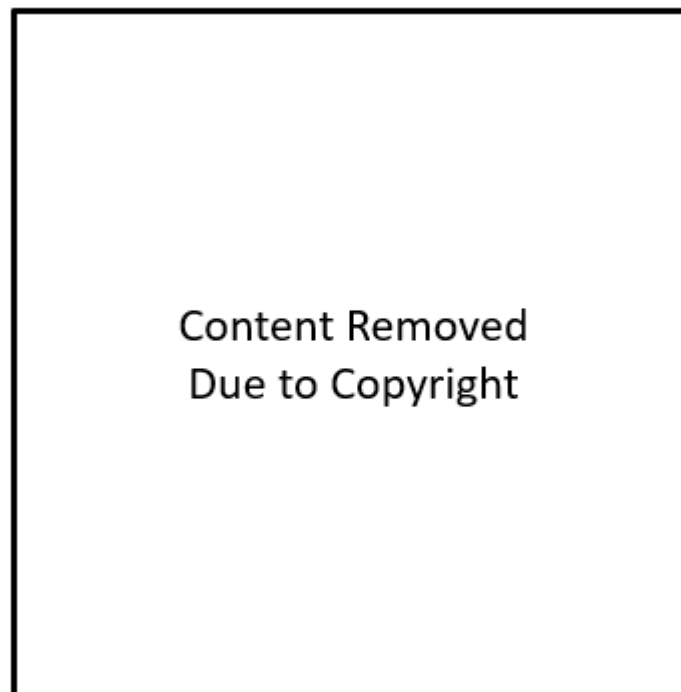


Figure 2.12: Illustration of how unidirectional plies can be stacked to form different laminate layups (Campbell, 2010)

Along with the choice of matrix material and the reinforcing fibre material, there are a number of other variables that can be adjusted during the manufacture of fibre

reinforced laminates, including: (i) the volume of fibres in the matrix material (fibre volume fraction), (ii) the thickness of each ply, (iii) the number of plies in the laminate and (iv) the orientation of each ply in the laminate layup.

Manufacturing laminated plates is a labour-intensive process; a brief outline of the major steps in the procedure to assemble laminates are listed below. All of the experimental specimens tested in Chapters 4 and 6 of this thesis were fabricated by the author using the compression moulding technique. A detailed description of the compression moulding procedure is provided by (Crawford, 1998). In summary:

- The unidirectional prepreg tape is cut to the desired length (Figure 2.13(a)).
- To create a ply, the individual cuts are tacked together using a solder iron (Figure 2.13(b)).
- The plies are next stacked in the desired layup (Figure 2.13(c)).
- The laminate is placed in hot compression press to be consolidated (Figure 2.13(d)).
- A diamond coated laminate saw is used to cut the laminated panel to the desired size (Figure 2.13(e)).

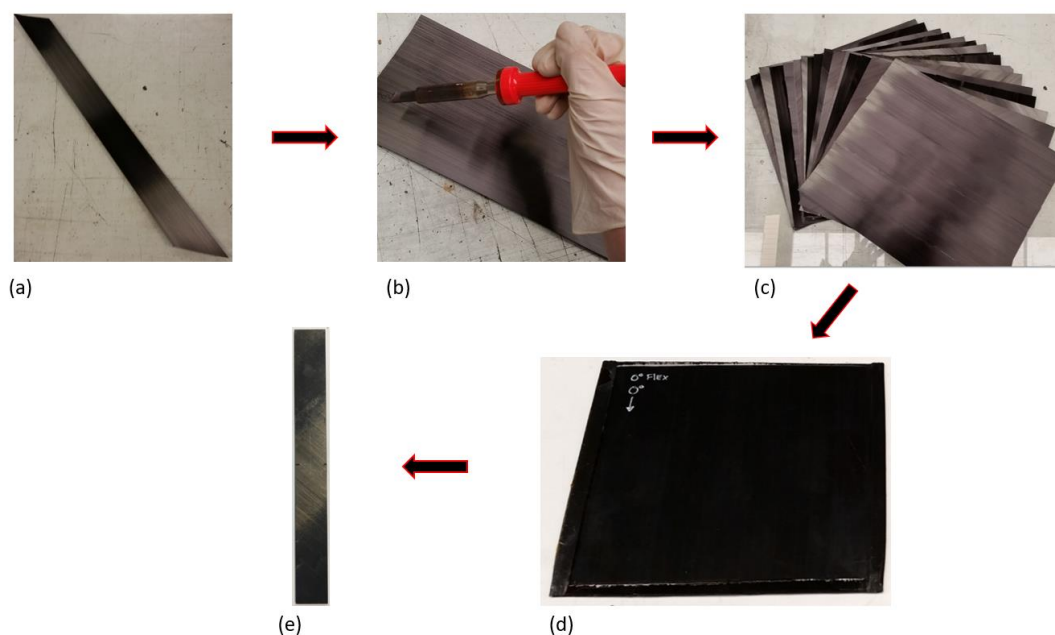


Figure 2.13: Process for manufacturing fibre reinforced thermoplastic composite layups; (a) a cut is taken from the spool of unidirectional composite material, (b) cuts are tacked together to form a ply, (c) plys are stacked to form the laminate layup, (d) laminate panel is consolidated in autoclave or compression press, and (e) diamond tipped laminate saw is used to cut panel to size.

The work in this thesis focuses on medical grade carbon fibre reinforced PEEK. To date PEEK-OPTIMA™ Ultra-Reinforced (Invibio Ltd., Thornton-Cleveleys, UK) is the only unidirectional long fibre reinforced thermoplastic material that has been cleared by the FDA for implantation in humans. A limited number of continuous unidirectional fibre reinforced implants are available on the market (Carbofix Orthopedic Ltd, Herzeliya, Israel) (Pinter et al., 2017; Steinberg et al., 2012; Zoccali et al., 2016). However, while the mechanical properties of unidirectional continuous carbon fibre reinforced PEEK must have been characterised prior to FDA clearance, they are not available in the public domain. No experimental characterisation of the material has been published to date and the failure mechanisms have not been fully uncovered.

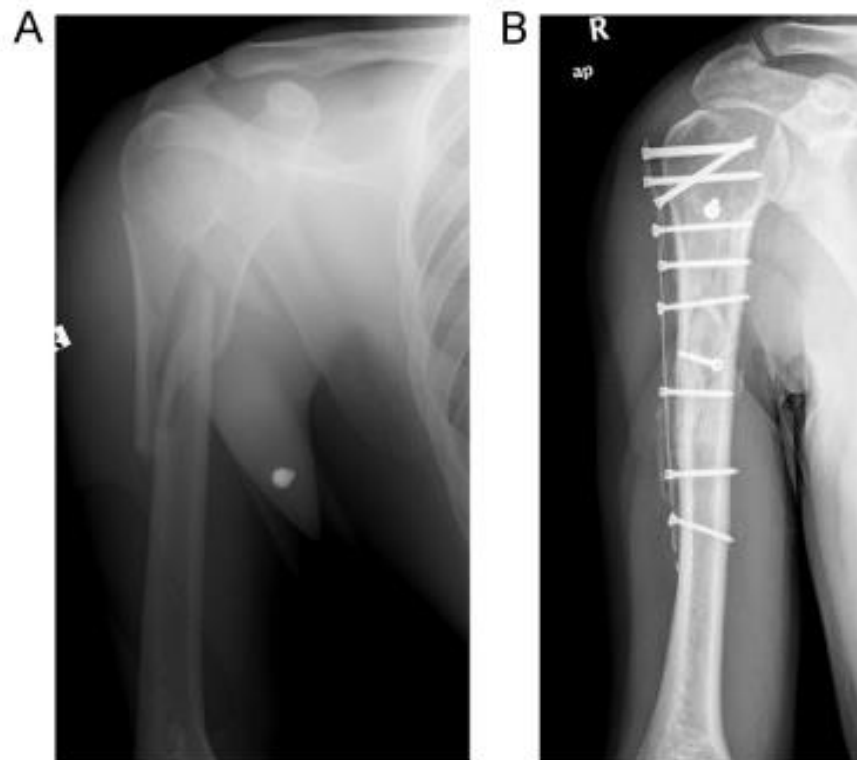


Figure 2.14: (A) Preoperative x-ray of a proximal humeral fracture. (B) Postoperative x-ray of the fracture stabilised by a humeral Piccola CF/PEEK implant (Steinberg et al., 2012).

Steinberg et al. (Steinberg et al., 2012) performed an evaluation of the Carbofix Piccolo nail and plates, which are manufactured from continuous carbon fibre reinforced PEEK. It was reported that the Carbofix implants satisfied the requirements for strength and wear for new devices and are safe to be implanted into humans. However, as details of laminate layups used in the study were not provided, it is unclear whether these implants are unidirectional or if stacked plies with multiple orientations are used. To the author's knowledge, very few studies have investigated the mechanical behaviour of multi-directional laminated orthopaedic devices. An experimental and computational study on the multiaxial fatigue behaviour of laminated hip prosthesis was reported by Liao and Reifsnider (1993). Laminated hip prostheses were manufactured from the plate-cut process, whereby a laminated panel was assembled and cured and the prosthesis was cut from the panel

in post processing (Figure 2.15). All experimental samples were cyclically loaded to failure.



Figure 2.15: Schematic diagram of the plate-cut process (Liao and Reifsnider, 1993).

A life prediction model based on the critical-element model (Reifsnider et al., 1986) was developed for the composite prosthesis. The model determines the critical element, i.e. the element with the highest stress in the fibre direction. As the number of cycles increases, damage in the subcritical elements increases, resulting in degradation of materials properties.

Yildiz et al developed a three-dimensional finite element code for analysing composite hip prosthesis (Yildiz et al., 1998b, 1998a). These studies conclude that standard hip prosthesis geometries are problematic if fabricated as a laminated composite due to the high number of plies (~150) and the significant difference in cross-sectional area from the proximal to distal end of the implant which can only be accommodated by neighbouring plies terminating at different locations. These uneven ply terminations are referred to as ply drop-offs. To simulate such a device an 8-node ply drop-off element was proposed, which accommodated more than one direction of ply orientation while also allowing ply drop-offs within the element (Figure 2.16). The element requires that the corner edges of the element must remain parallel to the ply interface, thereby allowing the relationship between the element

coordinates and the ply coordinates to be established by shape functions. The finite element predictions showed good agreement with experimental results.

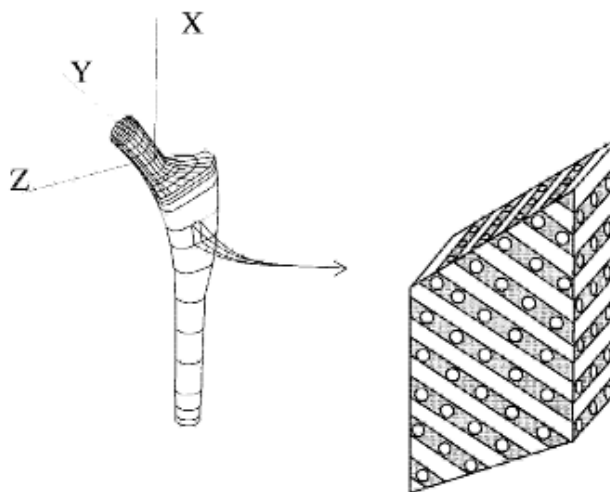


Figure 2.16: Composite hip implant with 3D 8-node composite elements (Yildiz et al., 1998b)

Li et al. also carried out combined experimental and computational studies on the progressive failure of laminated femoral stem components of total hip prosthesis (Li et al., 2003, 2002). The results of the experiments, similar to those described by Liao and Reifsnider (1993), showed the fatigue strength of the laminated stems is influenced by the ply stacking sequence. The failure criterion and material degradation models integrated into the computational model were, the Tasi-Wu criterion (discussed below in Section 2.4.2), the independent failure criterion (similar to the criterion proposed by Hashin and Rotem (1973)) and the interlaminar and intralaminar criterion. The study reports a good agreement with the experimental results using the independent failure criterion. However, a detailed comparison of the results of the three damage models was not provided. A composite laminate hip stem may decrease stress-shielding effects present with metallic prostheses. However, they may also induce other issues such as increased shear stress at the bone-stem

interface. Therefore, analytical models capable of accurately predicting damage are a necessity.

Clearly there is a need for extensive experimental and computational characterisation of these CF/PEEK laminated orthopaedic devices to establish their suitability for widespread clinical implantation.

### 2.4 Failure of composite materials

The failure mechanisms of fibre reinforced composite materials depend greatly on the mode of loading, e.g. tensile, compressive or shear. and on the fibre orientation in each ply. Composite failure is generally categorised into six primary failure modes, outline below (Hashin, 1980; Maimí et al., 2007; Talreja, 2016):

- 1) *Fibre failure in tension*, characterised by small numbers of fibre breakages (one or two fibres at a time) occurring at low load levels, increasing to larger clusters of fibre breakages (four or more fibres at a time) at higher loads. Ultimate failure is caused by an accumulation of fibre breaks at random locations (Figure 2.17(a)).
- 2) *Fibre failure in compression*, while characterised as fibre failure the failure mechanisms involved depend significantly on the behaviour of the matrix material. Fibre misalignment (fibre kinking) in the laminate causes localised shear deformation of the matrix. This allows shear bands to form, resulting in bending of the fibres and eventual breakage (Figure 2.17(b)).
- 3) *Matrix failure in transverse tension*, typically believed to occur as a result of fibre-matrix debonding or failure of the fibre-matrix interface (Figure 2.17(c)). Although there may be evidence to suggest that brittle failure of the matrix or coalescing of inclusions causes matrix failure in transverse tension.

- 4) Matrix failure in transverse compression, failure occurs on planes parallel to the fibres but otherwise inclined to the loading direction, suggesting that shear stress in the matrix influences the failure process (Figure 2.17(d)).
- 5) Matrix failure in in-plane shear, characterised by microcracks developing in the matrix along plane inclined to the fibres. The cracks tend to turn and grow in the fibre directions, merging to form axial cracks (Figure 2.17(e)).
- 6) Failure modes in combined loading. The individual failure mechanisms described above are governed by the appropriate local conditions. For instance, fibre failure in combined tension and transverse or in-plane shear, will aid or hinder the formation of failed fibre clusters depending on the local load transfer from a failed fibre to its neighbouring fibre.

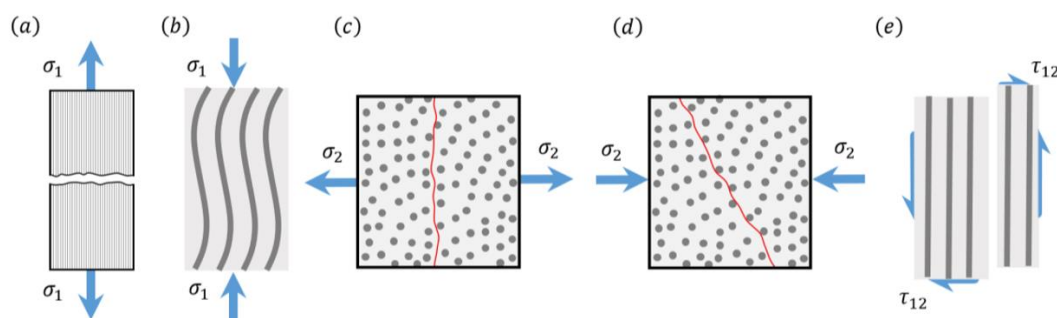


Figure 2.17: Schematic diagram of fibre reinforced composite failure modes; (a) fibre failure in tension, (b) fibre failure in compression, (c) matrix failure in transverse tension, (d) matrix failure in transverse compression, and (e) matrix in-plane shear failure (Image courtesy of E.M. Fagan)

#### 2.4.1 World-wide failure exercise (WWFE)

In the general field of composites mechanics, the ‘World-Wide Failure Exercise’ (WWFE), (conceived in 1991) has the specific aim of determining the level of confidence in the current failure prediction methods for fibre reinforced composites. An overview of the WWFE is given by Hinton et al. (Hinton et al., 2004a). Since the middle of the last century a large body of research into composite materials has been

published. Despite extensive investigation, accurate and reliable methodologies for prediction of strength of laminates remained elusive, leading to the establishment of the WWFE. To complicate matters further, there was also no universal definition of what constitutes failure of a composite. Prior to the WWFE the global design allowables of composite structures were typically set to 30% of the ultimate load, which is considered a conservative factor of safety for large scale structural composites. However, if laminated composites are to be implanted into the human body a factor of safety of 30% would be rather low, especially when damage accumulation under fatigue loading as well as load uncertainty are taken into consideration. The WWFE was developed (Hinton et al., 2004a; Kaddour and Hinton, 2012a). The goal of phase one of the exercise was to compare the existing mature theories, determine the strengths and limitations of each one, and provide this information to designers. The 19 failure criteria examined in phase one of the WWFE are outlined by Kaddour and Hinton (Hinton et al., 2004a) and the results are presented in two papers (Hinton et al., 2002, 2004b). The overall rankings of the examined failure theories are shown in Figure 2.18. The following scoring system was utilised, whereby:

- Grade A: The prediction lies within  $\pm 10\%$  of the experimental value
- Grade B: The prediction lies between  $\pm 10\%$  and  $\pm 50\%$  of the experimental value
- Grade C: The prediction lies between  $\pm 50\%$  and  $\pm 150\%$  of the experimental value
- Not Attempted: no solution was offered

The results show that the theories who achieve the highest grades are Cuntze and Bogetti with Zinoviev and Puck.

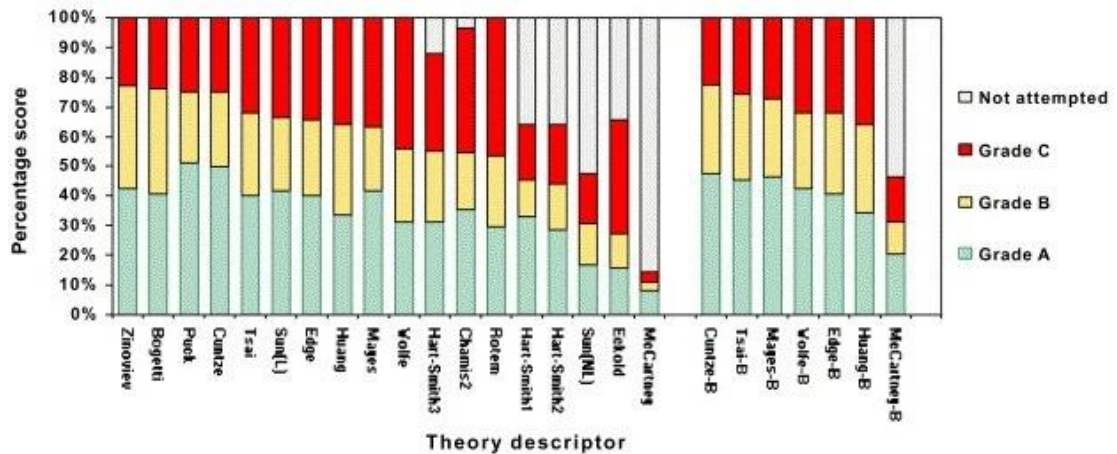


Figure 2.18: Overall ranking of the failure theories according to their capability to fulfil the five ranking categories examined; biaxial failure stress of unidirectional and multi-directional lamina, initial failure characteristics and deformation of multi-directional lamina and general features of the experimental results (Hinton et al., 2004b)

The 19 criteria examined in the first phase of the WWFE are for two-dimensional (2D) stress analysis of composite laminates and will hereafter be referred to as WWFE-I. The results of WWFE exposed the strengths and weaknesses of current theories and also highlighted gaps in the experimental data (Kaddour and Hinton, 2012a).

An extension to WWFE-I is currently being undertaken, assessing the understanding of the failure behaviour of fibre reinforced laminates under triaxial loads (Kaddour and Hinton, 2012a). This new activity is known as the WWFE-II. As part of the WWFE-II, Kress (Kress, 2012) is taking part to employ Hashin's failure criteria. The results of the WWFE-II are presented in two papers (Kaddour and Hinton, 2012b) and (Kaddour and Hinton, 2013).

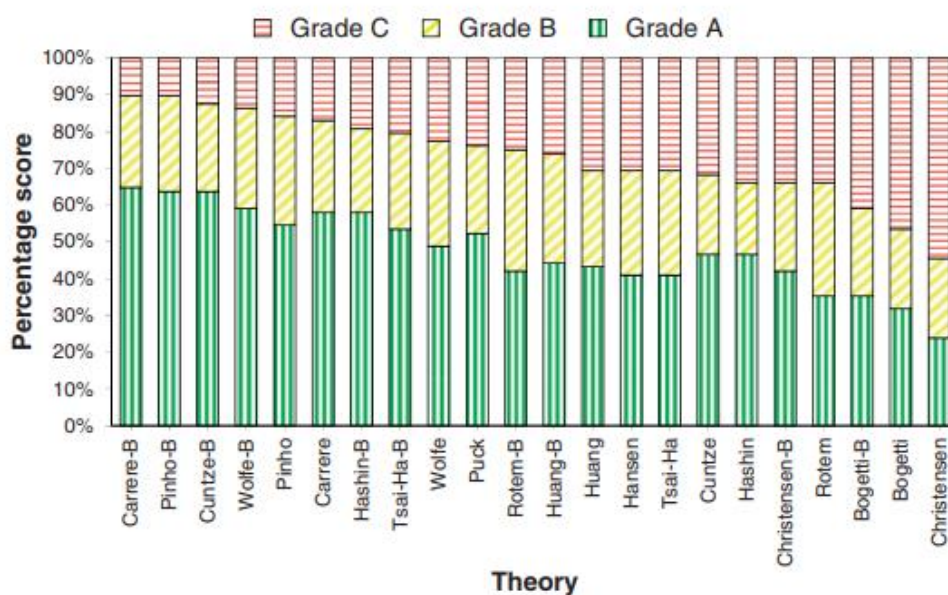


Figure 2.19: WWFE-II ranking of the theories for combined quantitative and qualitative assessment (Kaddour and Hinton, 2013)

The percentage of A, B and C grades for the combined quantitative and qualitative assessment of the individual WWFE-II theories are presented in Figure 2.19. The results include both the blind predictions and the revised predictions (denoted by *theory\_name-B*). The blind predictions were conducted without access to experimental data, whereas upon receiving the data pack some participants chose to revise their theories and predictions (Kaddour and Hinton, 2013, 2012b). The results show that the revised theories of Carrere-B and Pinho-B highest grades, with A and B grades of ~90% of ranked cases. The original Hashin theory scored A and B grades in ~67% of ranked cases. The revised Hashin model proposed by Kress (Kress, 2012) scored higher than the blind predictions, with ~80% of cases scoring in the A and B grades.

The results of the WWFE-I revealed the Puck model as the best predictor of experimental data. The Puck model has a micromechanical basis that is credited to the Hashin model. Both failure theories, along with the popular Tsai-Wu theory are discussed below in further detail.

## 2.4.2 Failure theories

### Tsai-Wu failure theory

The Tsai and Wu (1971) (Tsai-Wu) failure criterion is one of the earliest developed anisotropic failure theories. The criterion was originally proposed in the general context of anisotropic materials by using a quadratic polynomial expression of the stresses with tensorial coefficients. The orthotropic form of the criterion is described below:

$$F = F_{11}\sigma_1^2 + F_{22}\sigma_2^2 + F_{33}\sigma_3^2 + 2F_{23}\sigma_2\sigma_3 + 2F_{13}\sigma_1\sigma_3 + 2F_{12}\sigma_1\sigma_2 + F_1\sigma_1 + F_2\sigma_2 + F_3\sigma_3 + F_{44}\tau_{23}^2 + F_{55}\tau_{13}^2 + F_{66}\tau_{12}^2 \quad 2.1$$

where,  $F_i$  and  $F_{ij}$  ( $i, j = 1-6$ ) are contracted forms of the 4<sup>th</sup> and 2<sup>nd</sup> ranked tensors and failure occurs at  $F \geq 1$ . A criticism of the Tsai-Wu theory is that underlying failure mechanisms are not explicitly represented, with a single quadratic function being used to account for all possible failure modes observed in experiments (Li et al., 2017).

### Puck failure theory

The failure theory developed by Puck and Schürmann (2002) (the Puck failure theory) is a phenomenologically based theory that distinguished between fibre failure (FF) and inter-fibre failure (IFF) from the following set of five failure criteria:

$$f_E(FF)^+ = \frac{1}{\varepsilon_{1T}} \left( \varepsilon_1 + \frac{\nu_{12}}{E_1} m_{\sigma f} \sigma_2 \right) \quad 2.2$$

$$f_E(FF)^- = \frac{1}{\varepsilon_{1C}} \left| \left( \varepsilon_1 + \frac{\nu_{12}}{E_1} m_{\sigma f} \sigma_2 \right) \right| + (10\gamma_{12})^2 \quad 2.3$$

$$f_E(IFF)_A = \sqrt{\left( \frac{\tau_{12}}{S_{12}} \right)^2 + \left( 1 - p_{\perp}^{(+)} \frac{Y_T}{S_{12}} \right)^2 \left( \frac{\sigma_2}{Y_T} \right)^2} + p_{\perp}^{(+)} \frac{\sigma_2}{S_{12}} \quad 2.4$$

$$f_E(IFF)_B = \frac{1}{S_{12}} \left( \sqrt{\tau_{12}^2 + \left( p_{\perp}^{(+)} \sigma_2 \right)^2} + p_{\perp}^{(-)} \sigma_2 \right) \quad 2.5$$

$$f_E(IFF)_C = \left[ \left( \frac{\tau_{12}}{2(1 + p_{\perp\perp}^{(-)})S_{12}} \right)^2 + \left( \frac{\sigma_2}{Y_C} \right)^2 \right] \frac{Y_C}{(-\sigma_2)} \quad 2.6$$

where  $f_E(FF)^+$  and  $f_E(FF)^-$  are the tensile and compressive stress exposure for FF, respectively,  $f_E(IFF)_A$ ,  $f_E(IFF)_B$ ,  $f_E(IFF)_C$  are the stress exposure for IFF in modes A, B and C respectively,  $\varepsilon_{1T}$  and  $\varepsilon_{1C}$  are the tensile and compressive failure strains, respectively,  $m_{\sigma f}$  is the mean stress magnification factor and  $p$  is a parameter that controls the shape function.

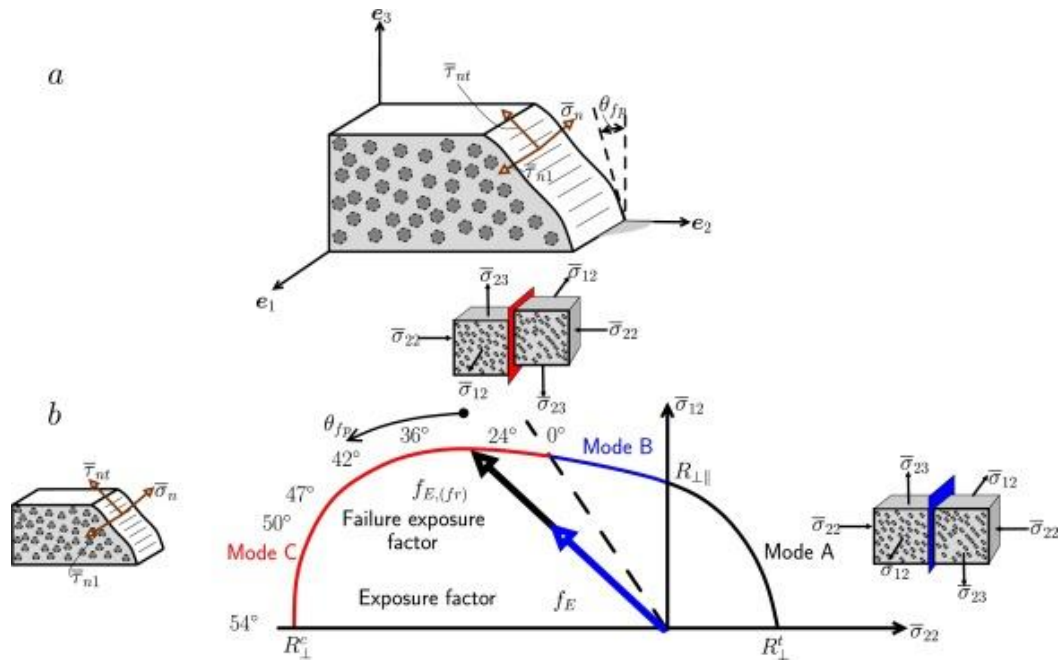


Figure 2.20: (a) Definition of acting stresses on the fracture plane. (b) Visualisation of the exposure factor ( $f_E$ ) at the failure point (Reinoso et al., 2017)

The occurrence of some failure modes is not considered critical, for example matrix cracking in modes A and B will affect the laminates overall stiffness but may not result in a loss of function. However, mode C failure corresponds to an immediate failure of the entire laminate. The Puck criteria have been widely utilised in the literature for a variety of applications (Deveci et al., 2016; Fagan et al., 2016; Kennedy et al., 2013; Lee et al., 2015; Reinoso et al., 2017).

### Hashin failure theory

The Hashin (1980) failure criteria was developed to predict anisotropic failure in fibre reinforced laminates. The failure criteria are typically composed of four separate failure modes related to fibre failure or matrix failure in tension or compression. The failure criteria are interactive, such that more than one stress component is used to evaluate the different failure modes. The Hashin criteria have been widely utilised in the literature for a variety of applications (Feerick et al., 2013; Grogan et al., 2015b; Guo-qing et al., 2018; Luo et al., 2016; Warren et al., 2016) and as discussed in Section 2.4.1 the Hashin theory also inspired other composite failure models.

The failure modes included in Hashins criteria are as follows:

Tensile fibre failure for  $\sigma_{11} \geq 0$

$$\left(\frac{\sigma_{11}}{X_T}\right)^2 + \frac{\sigma_{12}^2 + \sigma_{13}^2}{S_{12}^2} = \begin{cases} \geq 1 & \text{failure} \\ < 1 & \text{no failure} \end{cases} \quad 2.7$$

Compressive fibre failure for  $\sigma_{11} < 0$

$$\left(\frac{\sigma_{11}}{X_C}\right)^2 = \begin{cases} \geq 1 & \text{failure} \\ < 1 & \text{no failure} \end{cases} \quad 2.8$$

Tensile matrix failure for  $\sigma_{22} + \sigma_{33} > 0$

$$\frac{(\sigma_{22} + \sigma_{33})^2}{Y_T^2} + \frac{\sigma_{23}^2 - \sigma_{22}\sigma_{33}}{S_{23}^2} + \frac{\sigma_{12}^2 + \sigma_{13}^2}{S_{12}^2} = \begin{cases} \geq 1 & \text{failure} \\ < 1 & \text{no failure} \end{cases} \quad 2.9$$

Compressive matrix failure for  $\sigma_{22} + \sigma_{33} < 0$

$$\left[\left(\frac{Y_C}{2S_{23}}\right)^2 - 1\right] \left(\frac{\sigma_{22} + \sigma_{33}}{Y_C}\right) + \frac{(\sigma_{22} + \sigma_{33})^2}{4S_{23}^2} + \frac{\sigma_{23}^2 - \sigma_{22}\sigma_{33}}{S_{23}^2} + \frac{\sigma_{12}^2 + \sigma_{13}^2}{S_{12}^2} = \begin{cases} \geq 1 & \text{failure} \\ < 1 & \text{no failure} \end{cases} \quad 2.10$$

where,  $\sigma_{ij}$  denotes the stress components,  $X_T, Y_T$  are the tensile strengths in the fibre and matrix direction, respectively,  $X_C, Y_C$  are the compressive strengths in the fibre and matrix direction, respectively,  $S_{ij}$  denotes the shear strengths in the respective ply directions.

The Hashin criteria do not always fit experimental results well, especially in the case of matrix compression (Gu and Chen, 2017). The damage and failure model developed in this thesis implements Hashin-type (Hashin, 1980) failure criteria and is explained in further detail in Chapter 4.

### 2.4.3 Continuum damage modelling

Composite structures often accumulate damage, including micro-delaminations and micro-cracks, before catastrophic structural collapse of the composite. Continuum based criteria have been developed to relate the onset of composite failure to stresses and experimental measures of strength (Davila et al., 2005; Pinho et al., 2005; Soden et al., 1998). However, failure based continuum approaches do not always predict the stiffness degradation of fibre reinforced composites that can be considered the macroscopic representation of micro-scale damage accumulation (Liu and Zheng, 2008; Maimí et al., 2007).

Kachanov, (1958), was the first to implement progressive failure analysis using continuum damage mechanics (CDM), describing damage using a single scalar variable. The CDM replaces the mechanical properties of the damaged materials by associating the damage mechanism with their effect on the elastic constants of the material (Liu and Zheng, 2008). However, implementing CDM in transverse orthotropic fibre reinforced composites presents a computational challenge. The

alignment of the continuous fibres within the material naturally induces preferred directions for crack growth, i.e. matrix cracks propagating parallel to the fibre direction. Furthermore, the fibre-matrix interface is weaker than the surrounding material and can often be the point of initial failure in the composite (Maimí et al., 2007). Despite these difficulties several damage models have been established for fibre reinforced composites (Barbero and Lonetti, 2001; Car et al., 2002; Chaboche et al., 2001; Fish and Yu, 2001; Matzenmiller et al., 1995; Oller et al., 2005; Williams et al., 2003)

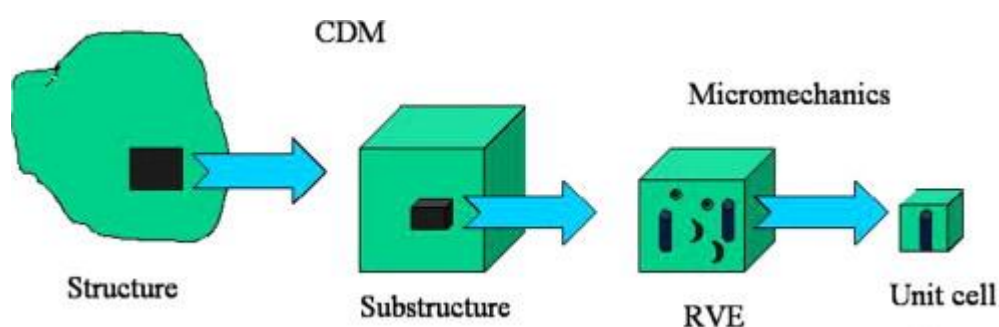


Figure 2.21: Multi-scale modelling of damage in composites from a structural level to a unit cell level (Talreja, 2008).

Two approaches used to evaluate the elastic and inelastic response of fibre reinforced composite materials are multi-scale modelling and meso-scale modelling. Multi-scale models define responses between a meso-scale, where a material is homogeneous, and a micro-scale, where the individual constituents are modelled as separate entities, using homogenization laws. Analysing the composite material as a homogeneous continuum and implementing a constitutive law to predict the anisotropic material behaviour is well suited to numerical models of large scale laminated structures, where modelling individual microscopic features would be very computationally expensive. It is often useful to model the laminates as individual

plies and implement cohesive zone models at the interface of each ply to predict inter-laminar delaminations. This approach is outlined in further detail in the following section (Section 2.4.4).

### **2.4.4 Modelling inter-and intra-laminar failure**

As discussed previously in Section 2.4, failure of fibre reinforced laminates can be driven by intra-laminar failures in the fibres or matrix; failure can also be caused by extensive inter-laminar delaminations.

During macro-scale analysis of laminated composites, each ply can be considered as a homogenous material with anisotropic material properties, which depend on the fibre and matrix material properties. Several studies have successfully considered the ply as the basic entity of the laminated structure. A detailed overview of laminate failure modelling is presented by van der Meer (2012). When the plies are individually modelled in macro-scale simulations, interface elements or cohesive zone models (CZMs) are often implemented to model the ply-to-ply interaction/interface (Allix and Ladevèze, 1992; Balzani and Wagner, 2008; Heidari-Rarani et al., 2013; Turon et al., 2010; Wisnom, 2010; Zhao et al., 2014), thereby making it possible to model/predict inter-laminar delaminations. A theoretical overview of CZMs is outlined in Chapter 3, Section 3.5.2 of this thesis.

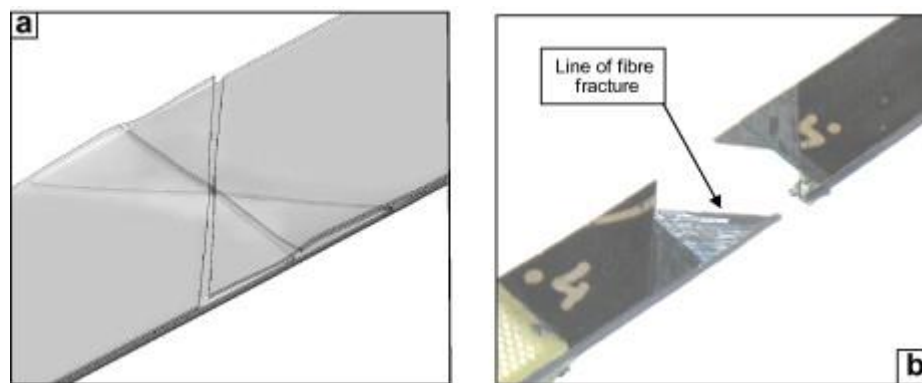


Figure 2.22: (a) Computational predictions of inter-laminar delaminations and (b) a failed experimental specimen (Wisnom, 2010).

Predicting inter-laminar delaminations in laminates is simplified by the fact that the crack path is generally constrained to the interface between the plies. Simulating fibre or matrix crack initiation is made more complex due to its random nature and that multiple cracks may grow in different directions through the laminate. However, the introduction of partition of unity methods such as the extended finite element method (XFEM) have removed the need for a crack initiation point, thus alleviating some of the issues inherent with modelling of intra-laminar cracks. The ability of the XFEM technique to model crack propagation along an arbitrary path without requiring remeshing has led to more realistic and sophisticated simulations of intra-laminar cracking than those requiring initial cracks and/or remeshing to allow the cracks to propagate (Campilho et al., 2011; Feerick et al., 2014, 2013; Hettich et al., 2008). The XFEM theory is described in detail in Section 3.5.1 of this thesis.

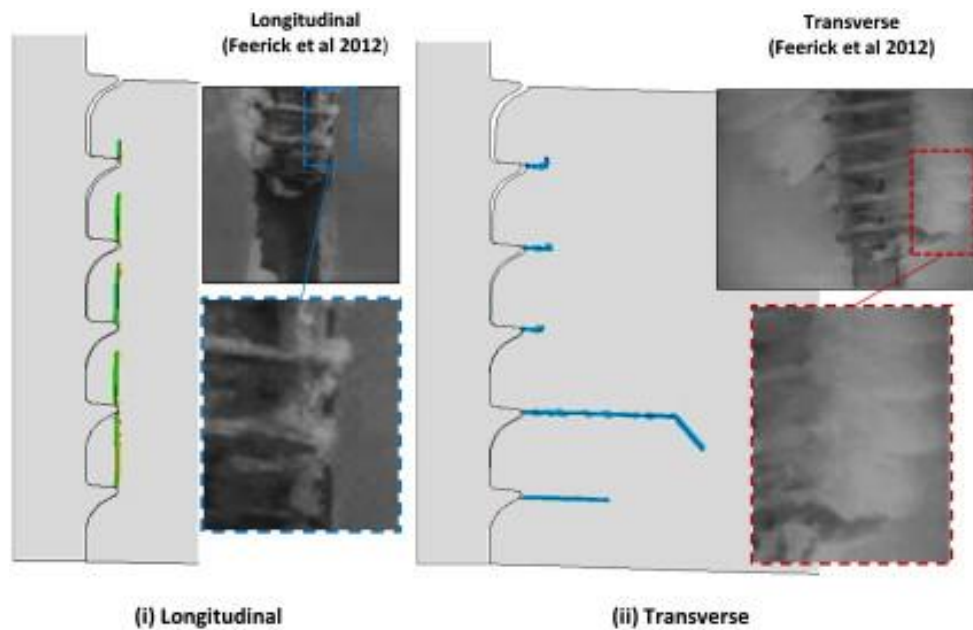


Figure 2.23: Fracture pattern predicted by 2D screw pull-out simulation compared to the experimental failure mechanisms observed for (i) longitudinal and (ii) transversely orientated cortical bone (Feerick et al., 2013).

Most recently combined inter- and intra-laminar failure models, that implement both CZM at the ply-to-ply interface and XFEM, have been introduced that show very good agreement with experimentally observed failure modes (Bieniaś et al., 2012; Bouhala et al., 2015; Grogan et al., 2015a; van der Meer et al., 2011; Viguera et al., 2015; Vogler et al., 2013). In this thesis a combined extended finite element method and cohesive zone model (XFEM/CZM) is developed to simulate the formation of random 3D crack paths, the growth inter-ply delaminations and anisotropic plasticity of the fibre reinforced laminates, described in detail in Chapter 4.

#### 2.4.5 Micro-scale modelling

Although macro-mechanical models (such as that developed in Chapter 4 of this thesis) offer accurate predictions of damage and failure in fibre reinforced laminates, they do not allow for any insight into the underlying failure mechanisms at the individual fibre level. For this reason, micro-mechanical models have been developed to predict/determine damage and failure to the fibre-matrix interface

region. The expansive and notable work of Llorca et al., (2011) on multi-scale modelling strategies for fibre reinforced composites has paved the way for modern techniques of virtual testing. This micro-mechanical approach is undertaken in Chapter 5 of this thesis to uncover the failure mechanism of the  $90^\circ$  laminate under tensile loading.

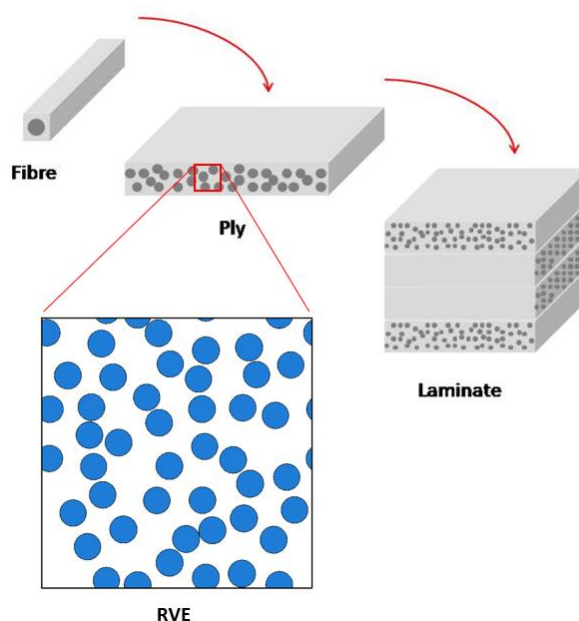


Figure 2.24: Schematic illustrating the representative volume element within a unidirectional ply.

The periodic homogenisation approach is utilised in the micro-mechanics study in Chapter 5, therefore a brief background is now provided. It is assumed that the macro-scale structure is made up of an infinite array of repeating units; hereafter referred to as representative volume elements (RVEs) (Figure 2.24), first proposed by Hill (1963). Hill defined an RVE as a region that must be (a) structurally entirely typical of the whole part on average, and (b) contain a sufficient number of inclusions for the apparent overall moduli to be effectively independent of the surface values of traction and displacement. Periodic boundary conditions must be

applied in order to maintain periodicity, outlined in Chapter 5 of this thesis and described in detail by (Dowling et al., 2013; Vaughan and McCarthy, 2011a, 2010).

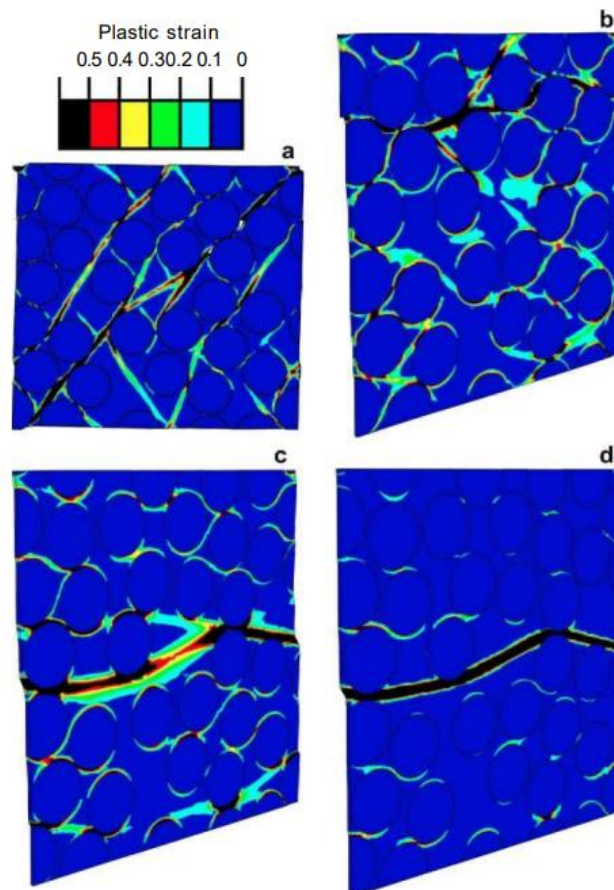


Figure 2.25: Contour plot of the accumulated plastic strain in a CF/PEEK lamina subjected to: (a) uniaxial compression, (b) biaxial compression and shear, (c) biaxial compression and shear, and (d) longitudinal shear (Totry et al., 2008)

The boundary between the fibre and the matrix material is known as the fibre-matrix interface. The interface region takes up a relatively small amount of the total volume of the RVE however it is the region that determines the composites ability to transfer load. Failure of fibre-matrix interface strength is understood to be the primary failure mode in transverse tensile failure (Talreja, 2016). Previous studies have implemented cohesive elements to model the fibre-matrix interface (Figure 2.25) (O'Dwyer et al., 2013; Totry et al., 2008; Vaughan and McCarthy, 2011b). The CZM described in

Chapter 4 of this thesis is implemented as a cohesive surface in the micromechanical model described in Chapter 5 of this thesis.

## 2.5 References

- Ahmad, M., Nanda, R., Bajwa, A.S., Candal-Couto, J., Green, S., Hui, A.C., 2007. Biomechanical testing of the locking compression plate: When does the distance between bone and implant significantly reduce construct stability? *Injury* 38, 358–364. <https://doi.org/10.1016/j.injury.2006.08.058>
- Allgüwer, D., Matter, P., Perren, S., Ruedi, T., 1973. *The Dynamic Compression Plate DCP*. Springer Berlin Heidelberg.
- Allix, O., Ladevèze, P., 1992. Interlaminar interface modelling for the prediction of delamination. *Compos. Struct.* 22, 235–242. [https://doi.org/10.1016/0263-8223\(92\)90060-P](https://doi.org/10.1016/0263-8223(92)90060-P)
- Ascenzi, A., Bonucci, E., 1968. The compressive properties of single osteons. *Anat. Rec.* 161, 377–391. <https://doi.org/10.1002/ar.1091610309>
- Balzani, C., Wagner, W., 2008. An interface element for the simulation of delamination in unidirectional fiber-reinforced composite laminates. *Eng. Fract. Mech.* 75, 2597–2615. <https://doi.org/10.1016/j.engfracmech.2007.03.013>
- Barbero, E.J., Lonetti, P., 2001. Damage model for composites defined in terms of available data. *Mech. Compos. Mater. Struct.* <https://doi.org/10.1080/107594101753172539>
- Bayraktar, H.H., Morgan, E.F., Niebur, G.L., Morris, G.E., Wong, E.K., Keaveny, T.M., 2004. Comparison of the elastic and yield properties of human femoral trabecular and cortical bone tissue. *J. Biomech.* 37, 27–35. [https://doi.org/10.1016/S0021-9290\(03\)00257-4](https://doi.org/10.1016/S0021-9290(03)00257-4)
- Bieniaś, J., Dębski, H., Surowska, B., Sadowski, T., 2012. Analysis of microstructure damage in carbon/epoxy composites using FEM, in: *Computational Materials Science*. pp. 168–172. <https://doi.org/10.1016/j.commatsci.2012.03.033>
- Bolander, M.E., 1992. Regulation of Fracture Repair by Growth Factors. *Exp. Biol. Med.* 200, 165–170. <https://doi.org/10.3181/00379727-200-43410A>
- Bouhala, L., Makradi, A., Belouettar, S., Younes, A., Natarajan, S., 2015. An XFEM/CZM based inverse method for identification of composite failure parameters. *Comput. Struct.* 153, 91–97. <https://doi.org/10.1016/j.compstruc.2015.02.035>
- Bradway, J.K., Amadio, P.C., Cooney, W.P., 1989. Open reduction and internal fixation of displaced, comminuted intra-articular fractures of the distal end of the radius. *J. Bone Joint Surg. Am.* 71, 839–47. <https://doi.org/10.1002/14651858>
- Camarda, L., La Gattuta, A., Butera, M., Siragusa, F., D'Arienzo, M., 2016. FiberWire tension band for patellar fractures. *J. Orthop. Traumatol.* 17, 75–80. <https://doi.org/10.1007/s10195-015-0359-6>
- Campbell, F.C. (Flake C., 2010. *Structural composite materials*, 1st ed. ASM International, Materials Park.
- Campilho, R.D.S.G., Banea, M.D., Pinto, A.M.G., Da Silva, L.F.M., De Jesus, A.M.P., 2011. Strength prediction of single- and double-lap joints by standard and extended finite element modelling. *Int. J. Adhes. Adhes.* 31, 363–372. <https://doi.org/10.1016/j.ijadhadh.2010.09.008>

- Car, E., Zalamea, F., Oller, S., Miquel, J., Oñate, E., 2002. Numerical simulation of fiber reinforced composite materials—two procedures. *Int. J. Solids Struct.* [https://doi.org/10.1016/S0020-7683\(01\)00240-2](https://doi.org/10.1016/S0020-7683(01)00240-2)
- Carter, D.R., Spengler, D.M., 1978. Mechanical properties and composition of cortical bone. *Clin. Orthop. Relat. Res.* 192–217. <https://doi.org/10.1097/00003086-197809000-00041>
- Chaboche, J.L., Kruch, S., Maire, J.F., Pottier, T., 2001. Towards a micromechanics based inelastic and damage modeling of composites, in: *International Journal of Plasticity*. [https://doi.org/10.1016/S0749-6419\(00\)00056-5](https://doi.org/10.1016/S0749-6419(00)00056-5)
- Chalidis, B.E., Sachinis, N.C., Samoladas, E.P., Dimitriou, C.G., Pournaras, J.D., 2008. Is tension band wiring technique the “gold standard” for the treatment of olecranon fractures? A long term functional outcome study. *J. Orthop. Surg. Res.* 3. <https://doi.org/10.1186/1749-799X-3-9>
- Crawford, R.J., 1998. *Plastics engineering*. Butterworth-Heinemann.
- Cronier, P., Pietu, G., Dujardin, C., Bigorre, N., Ducellier, F., Gerard, R., 2010. The concept of locking plates. *Orthop. Traumatol. Surg. Res.* <https://doi.org/10.1016/j.otsr.2010.03.008>
- Darouiche, R.O., 2004. Treatment of infections associated with surgical implants. *N. Engl. J. Med.* 350, 1422–1429. <https://doi.org/10.1056/NEJMra035415>
- Davila, C.G., Camanho, P.P., Rose, C.A., 2005. Failure Criteria for FRP Laminates. *J. Compos. Mater.* <https://doi.org/10.1177/0021998305046452>
- DePuy Synthes, 2018. LCP™ Locking Compression Plate [WWW Document]. URL <https://emea.depuysynthes.com/hcp/trauma/products/qs/lcp-locking-compression-plate> (accessed 7.16.18).
- Deveci, H.A., Aydin, L., Secil Artem, H., 2016. Buckling optimization of composite laminates using a hybrid algorithm under Puck failure criterion constraint. *J. Reinf. Plast. Compos.* 35, 1233–1247. <https://doi.org/10.1177/0731684416646860>
- Dowling, E.P., Ronan, W., McGarry, J.P., 2013. Computational investigation of in situ chondrocyte deformation and actin cytoskeleton remodelling under physiological loading. *Acta Biomater.* 9, 5943–55. <https://doi.org/10.1016/j.actbio.2012.12.021>
- Ehlinger, M., Adam, P., Simon, P., Bonnomet, F., 2009. Technical difficulties in hardware removal in titanium compression plates with locking screws. *Orthop. Traumatol. Surg. Res.* 95, 373–376. <https://doi.org/10.1016/j.otsr.2009.03.020>
- Ehlinger, M., Adamczewski, B., Rahmé, M., Adam, P., Bonnomet, F., 2015. Comparison of the pre-shaped anatomical locking plate of 3.5 mm versus 4.5 mm for the treatment of tibial plateau fractures. *Int. Orthop.* 39, 2465–2471. <https://doi.org/10.1007/s00264-015-2713-y>
- Einhorn, T.A., 1998. The cell and molecular biology of fracture healing. *Clin. Orthop. Relat. Res.* S7-21. <https://doi.org/10.1097/00003086-199810001-00003>
- Einhorn, T.A., Gerstenfeld, L.C., 2015. Fracture healing: Mechanisms and interventions. *Nat. Rev. Rheumatol.* <https://doi.org/10.1038/nrrheum.2014.164>
- Fagan, E.M., Kennedy, C.R., Leen, S.B., Goggins, J., 2016. Damage mechanics based

- design methodology for tidal current turbine composite blades. *Renew. Energy* 97, 358–372. <https://doi.org/10.1016/j.renene.2016.05.093>
- Feerick, E.M., Liu, X.C., McGarry, P., 2013. Anisotropic mode-dependent damage of cortical bone using the extended finite element method (XFEM). *J. Mech. Behav. Biomed. Mater.* 20, 77–89. <https://doi.org/10.1016/j.jmbbm.2012.12.004>
- Feerick, E.M., Wilson, J., Jarman-Smith, M., Ó’Brádaigh, C.M., McGarry, J.P., 2014. Self-tapping ability of carbon fibre reinforced polyetheretherketone suture anchors. *J. Biomater. Appl.* 29, 502–513. <https://doi.org/10.1177/0885328214535274>
- Ferguson, C., Alpern, E., Miclau, T., Helms, J.A., 1999. Does adult fracture repair recapitulate embryonic skeletal formation? *Mech. Dev.* 87, 57–66. [https://doi.org/10.1016/S0925-4773\(99\)00142-2](https://doi.org/10.1016/S0925-4773(99)00142-2)
- Finsen, V., Lingaas, P.S., Storrø, S., 2000. AO tension-band osteosynthesis of displaced olecranon fractures. *Orthopedics* 23, 1069–72.
- Fish, J., Yu, Q., 2001. Two-scale damage modeling of brittle composites. *Compos. Sci. Technol.* [https://doi.org/10.1016/S0266-3538\(01\)00115-4](https://doi.org/10.1016/S0266-3538(01)00115-4)
- Flynn, J., Hresko, T., Reynolds, R., Blasier, R., Davidson, R., Kasser, J., 2001. Titanium elastic nails for pediatric femur fractures: a multicenter study of early results with analysis of complications. *J. Pediatr. Orthop.* 21, 4–8. <https://doi.org/10.1097/01241398-200101000-00003>
- Freeman, F.E., McNamara, L.M., 2017. Endochondral Priming: A Developmental Engineering Strategy for Bone Tissue Regeneration. *Tissue Eng. Part B Rev.* 23, 128–141. <https://doi.org/10.1089/ten.teb.2016.0197>
- Frigg, R., 2003. Development of the locking compression plate. *Injury.* <https://doi.org/10.1016/j.injury.2003.09.020>
- Fulkerson, E., Egol, K.A., Kubiak, E.N., Liporace, F., Kummer, F.J., Koval, K.J., 2006. Fixation of diaphyseal fractures with a segmental defect: A biomechanical comparison of locked and conventional plating techniques. *J. Trauma - Inj. Infect. Crit. Care* 60, 830–835. <https://doi.org/10.1097/01.ta.0000195462.53525.0c>
- Gerber, C., Werner, C.M.L., Vienne, P., 2004. Internal fixation of complex fractures of the proximal humerus. *J. Bone Joint Surg. Br.* 86, 848–55. <https://doi.org/10.1302/0301-620X.86B6.14577>
- Gerstenfeld, L.C., Cullinane, D.M., Barnes, G.L., Graves, D.T., Einhorn, T.A., 2003. Fracture healing as a post-natal developmental process: Molecular, spatial, and temporal aspects of its regulation. *J. Cell. Biochem.* 88, 873–884. <https://doi.org/10.1002/jcb.10435>
- Gold, R., Gilley, R., 2006. Screw Insertion (DCP vs LC-DCP) [WWW Document]. URL <http://cal.vet.upenn.edu/projects/orthopod/csfr/terms/screwinsertion.htm> (accessed 7.16.18).
- Green, S., Schlegel, J., 2001. A polyaryletherketone biomaterial for use in medical implant applications. *Polym. Med. Ind. Proc. a Conf. held Brussels* 1–7.
- Grogan, D.M., Ó Brádaigh, C.M., Leen, S.B., 2015a. A combined XFEM and cohesive zone model for composite laminate microcracking and permeability. *Compos. Struct.* 120, 246–261. <https://doi.org/10.1016/j.compstruct.2014.09.068>

- Grogan, D.M., Ó Brádaigh, C.M., McGarry, J.P., Leen, S.B., 2015b. Damage and permeability in tape-laid thermoplastic composite cryogenic tanks. *Compos. Part A Appl. Sci. Manuf.* 78, 390–402. <https://doi.org/10.1016/j.compositesa.2015.08.037>
- Gu, J., Chen, P., 2017. Some modifications of Hashin's failure criteria for unidirectional composite materials. *Compos. Struct.* 182, 143–152. <https://doi.org/10.1016/j.compstruct.2017.09.011>
- Guo-qing, Y., Yi-ru, R., Tian-tian, Z., Wan-shen, X., Hong-yong, J., 2018. Hashin Failure Theory Based Damage Assessment Methodology of Composite Tidal Turbine Blades and Implications for the Blade Design. *China Ocean Eng.* 32, 216–225. <https://doi.org/10.1007/s13344-018-0023-z>
- Hak, D.J., Mauffrey, C., Seligson, D., Lindeque, B., 2014. Use of Carbon-Fiber-Reinforced Composite Implants in Orthopedic Surgery. *Orthopedics.* <https://doi.org/10.3928/01477447-20141124-05>
- Hashin, Z., 1980. Failure Criteria for Unidirectional Fiber Composites. *J. Appl. Mech.* 47, 329. <https://doi.org/10.1115/1.3153664>
- Hashin, Z., Rotem, A., 1973. A Fatigue Failure Criterion for Fiber Reinforced Materials. *J. Compos. Mater.* 7, 448–464. <https://doi.org/10.1177/002199837300700404>
- Hayes, J.S., Richards, R.G., 2010. The use of titanium and stainless steel in fracture fixation. *Expert Rev. Med. Devices.* <https://doi.org/10.1586/erd.10.53>
- Heidari-Rarani, M., Shokrieh, M.M., Camanho, P.P., 2013. Finite element modeling of mode I delamination growth in laminated DCB specimens with R-curve effects. *Compos. Part B Eng.* 45, 897–903. <https://doi.org/10.1016/j.compositesb.2012.09.051>
- Helm, R.H., Hornby, R., Miller, S.W., 1987. The complications of surgical treatment of displaced fractures of the olecranon. *Injury* 18, 48–50.
- Hettich, T., Hund, A., Ramm, E., 2008. Modeling of failure in composites by X-FEM and level sets within a multiscale framework. *Comput. Methods Appl. Mech. Eng.* 197, 414–424. <https://doi.org/10.1016/j.cma.2007.07.017>
- Hill, R., 1963. Elastic properties of reinforced solids: Some theoretical principles. *J. Mech. Phys. Solids* 11, 357–372. [https://doi.org/10.1016/0022-5096\(63\)90036-X](https://doi.org/10.1016/0022-5096(63)90036-X)
- Hinton, M., Kaddour, A., Soden, P., 2002. A comparison of the predictive capabilities of current failure theories for composite laminates, judged against experimental evidence. *Compos. Sci. Technol.* 62, 1725–1797. [https://doi.org/10.1016/S0266-3538\(02\)00125-2](https://doi.org/10.1016/S0266-3538(02)00125-2)
- Hinton, M.J., Kaddour, A.S., Soden, P.D., 2004a. The world-wide failure exercise. Its origin, concept and content, in: *Failure Criteria in Fibre-Reinforced-Polymer Composites.* pp. 2–28. <https://doi.org/10.1016/B978-008044475-8/50002-0>
- Hinton, M.J., Kaddour, A.S., Soden, P.D., 2004b. A Further Assessment of the Predictive Capabilities of Current Failure Theories for Composites Laminates: Comparison with Experimental Evidence. *Compos. Sci. Technol.* 64, 549–588. [https://doi.org/10.1016/S0266-3538\(02\)00125-2](https://doi.org/10.1016/S0266-3538(02)00125-2)
- Holdsworth, B.J., Mossad, M.M., 1984. Elbow function following tension band fixation of displaced fractures of the olecranon. *Injury* 16, 182–187. [https://doi.org/10.1016/0020-1383\(84\)90156-6](https://doi.org/10.1016/0020-1383(84)90156-6)

- Jee, W.S.S., 2001. Integrated Bone Tissue Physiology: Anatomy and Physiology, in: Cowin, S.C. (Ed.), *Bone Mechanics Handbook*. CRC Press LLC, pp. 1–68. [https://doi.org/10.1016/0268-0033\(90\)90036-6](https://doi.org/10.1016/0268-0033(90)90036-6)
- Kabak, S., Halici, M., Tuncel, M., Avsarogullari, L., Karaoglu, S., 2004. Treatment of midclavicular nonunion: Comparison of dynamic compression plating and low-contact dynamic compression plating techniques. *J. Shoulder Elb. Surg.* 13, 396–403. <https://doi.org/10.1016/j.jse.2004.01.033>
- Kabir, S.M.R., Alabi, J., Rezajooi, K., Casey, A.T.H., 2010. Anterior cervical corpectomy: Review and comparison of results using titanium mesh cages and carbon fibre reinforced polymer cages. *Br. J. Neurosurg.* <https://doi.org/10.3109/02688697.2010.503819>
- Kachanov, L.M., 1958. Time of the rupture process under creep conditions. *Izv Akad Nauk S S R Otd Tech Nauk.* <https://doi.org/citeulike-article-id:5466815>
- Kaddour, A.S., Hinton, M.J., 2013. Maturity of 3D failure criteria for fibre-reinforced composites: Comparison between theories and experiments: Part B of WWFE-II. *J. Compos. Mater.* 47, 925–966. <https://doi.org/10.1177/0021998313478710>
- Kaddour, A.S., Hinton, M.J., 2012a. Progress in failure criteria for polymer matrix composites: A view from the first World-Wide Failure Exercise (WWFE), in: *Failure Mechanisms in Polymer Matrix Composites: Criteria, Testing and Industrial Applications*. pp. 3–25. <https://doi.org/10.1016/B978-1-84569-750-1.50001-X>
- Kaddour, A.S., Hinton, M.J., 2012b. Benchmarking of triaxial failure criteria for composite laminates: Comparison between models of “Part (A)” of “WWFE-II.” *J. Compos. Mater.* 46, 2595–2634. <https://doi.org/10.1177/0021998312449887>
- Karlsson, M.K., Hasserius, R., Besjakov, J., Karlsson, C., Josefsson, P.O., 2002. Comparison of tension-band and figure-of-eight wiring techniques for treatment of olecranon fractures. *J. Shoulder Elb. Surg.* 11, 377–382. <https://doi.org/10.1067/mse.2002.124548>
- Keller, T.S., Mao, Z., Spengler, D.M., 1990. Young’s modulus, bending strength, and tissue physical properties of human compact bone. *J. Orthop. Res.* 8, 592–603. <https://doi.org/10.1002/jor.1100080416>
- Kennedy, C.R., Brádaigh, C.M.Ó., Leen, S.B., 2013. A multiaxial fatigue damage model for fibre reinforced polymer composites. *Compos. Struct.* 106, 201–210. <https://doi.org/10.1016/j.compstruct.2013.05.024>
- Kerr-Valentic, M.A., Arthur, M., Mullins, R.J., Pearson, T.E., Mayberry, J.C., 2003. Rib fracture pain and disability: Can we do better? *J. Trauma* 54, 1058–1064. <https://doi.org/10.1097/01.TA.0000060262.76267.EF>
- Kozin, S.H., Berglund, L.J., Cooney, W.P., Morrey, B.F., An, K.N., 1996. Biomechanical analysis of tension band fixation for olecranon fracture treatment. *J. Shoulder Elbow Surg.* 5, 442–448. [https://doi.org/10.1016/S1058-2746\(96\)80016-4](https://doi.org/10.1016/S1058-2746(96)80016-4)
- Kress, G., 2012. Examination of Hashin’s failure criteria for the second world-wide failure exercise. *J. Compos. Mater.* 46, 2539–2561. <https://doi.org/10.1177/0021998312449892>
- Kuhn, J.L., Goldstein, S.A., Ciarelli, M.J., Matthews, L.S., 1989. The limitations of canine trabecular bone as a model for human: A biomechanical study. *J. Biomech.* 22, 95–

107. [https://doi.org/10.1016/0021-9290\(89\)90032-8](https://doi.org/10.1016/0021-9290(89)90032-8)
- Kuo, C.-C., Hsu, H.-C., Hong, S.-W., Lu, T.-W., 2011. BIOMECHANICAL ASSESSMENT OF TENSION-BAND WIRING FOR OLECRANON FRACTURES. *Biomed. Eng. Appl. Basis Commun.* 23, 83–87. <https://doi.org/10.4015/S1016237211002402>
- Kurtz, S.M., Devine, J.N., 2007. PEEK biomaterials in trauma, orthopedic, and spinal implants. *Biomaterials* 28, 4845–69. <https://doi.org/10.1016/j.biomaterials.2007.07.013>
- Kwok, C.S., Crossman, P.T., Loizou, C.L., 2014. Plate versus nail for distal tibial fractures: A systematic review and meta-analysis. *J. Orthop. Trauma.* <https://doi.org/10.1097/BOT.0000000000000068>
- Lavini, F., Dall’Oca, C., Mezzari, S., Maluta, T., Luminari, E., Perusi, F., Vecchini, E., Magnan, B., 2014. Temporary bridging external fixation in distal tibial fracture. *Injury* 45, S58–S63. <https://doi.org/10.1016/j.injury.2014.10.025>
- Lee, C.S., Kim, J.H., Kim, S.K., Ryu, D.M., Lee, J.M., 2015. Initial and progressive failure analyses for composite laminates using Puck failure criterion and damage-coupled finite element method. *Compos. Struct.* 121, 406–419. <https://doi.org/10.1016/j.compstruct.2014.11.011>
- Li, C., Granger, C., Del Schutte, H., Biggers, S.B., Kennedy, J.M., Latour, R. a, 2002. Progressive failure analysis of laminated composite femoral prostheses for total hip arthroplasty. *Biomaterials* 23, 4249–62.
- Li, C., Granger, C., Schutte Jr., H. Del, Biggers Jr., S.B., Kennedy, J.M., Latour Jr., R. a., 2003. Failure analysis of composite femoral components for hip arthroplasty. *J. Rehabil. Res. Dev.* 40, 133. <https://doi.org/10.1682/JRRD.2003.03.0133>
- Li, S., Sitnikova, E., Liang, Y., Kaddour, A.S., 2017. The Tsai-Wu failure criterion rationalised in the context of UD composites. *Compos. Part A Appl. Sci. Manuf.* 102, 207–217. <https://doi.org/10.1016/j.compositesa.2017.08.007>
- Liao, K., Reifsnider, K.L., 1993. A Life Prediction Model for Fatigue Composite Femoral Prosthesis Loaded. *ASTM Int.*
- Linde, F., Hvid, I., Pongsoipetch, B., 1989. Energy absorptive properties of human trabecular bone specimens during axial compression. *J. Orthop. Res.* 7, 432–439. <https://doi.org/10.1002/jor.1100070316>
- Liu, P.F., Zheng, J.Y., 2008. Progressive failure analysis of carbon fiber/epoxy composite laminates using continuum damage mechanics. *Mater. Sci. Eng. A* 485, 711–717. <https://doi.org/10.1016/J.MSEA.2008.02.023>
- Llorca, J., González, C., Molina-Aldareguía, J.M., Segurado, J., Seltzer, R., Sket, F., Rodríguez, M., Sádaba, S., Muñoz, R., Canal, L.P., 2011. Multiscale modeling of composite materials: A roadmap towards virtual testing. *Adv. Mater.* <https://doi.org/10.1002/adma.201101683>
- Luo, H., Yan, Y., Meng, X., Jin, C., 2016. Progressive failure analysis and energy-absorbing experiment of composite tubes under axial dynamic impact. *Compos. Part B Eng.* 87, 1–11. <https://doi.org/10.1016/j.compositesb.2015.10.016>
- Macko, D., Szabo, R.M., 1985. Complications of tension-band wiring of olecranon fractures. *J. Bone Joint Surg. Am.* 67, 1396–401.

- Maimí, P., Camanho, P.P., Mayugo, J. a., Dávila, C.G., 2007. A continuum damage model for composite laminates: Part I – Constitutive model. *Mech. Mater.* 39, 897–908. <https://doi.org/10.1016/j.mechmat.2007.03.005>
- Mao, Z., Wang, G., Zhang, L., Zhang, L., Chen, S., Du, H., Zhao, Y., Tang, P., 2015. Intramedullary nailing versus plating for distal tibia fractures without articular involvement: A meta-analysis. *J. Orthop. Surg. Res.* 10. <https://doi.org/10.1186/s13018-015-0217-5>
- Markolf, K.L., Cheung, E., Joshi, N.B., Boguszewski, D. V., Petrigliano, F.A., McAllister, D.R., 2016. Plate versus intramedullary nail fixation of anterior tibial stress fractures: A biomechanical study. *Am. J. Sports Med.* 44, 1590–1596. <https://doi.org/10.1177/0363546516631745>
- Martens, M., Van Audekercke, R., Delpont, P., De Meester, P., Mulier, J.C., 1983. The mechanical characteristics of cancellous bone at the upper femoral region. *J. Biomech.* 16, 971–983. [https://doi.org/10.1016/0021-9290\(83\)90098-2](https://doi.org/10.1016/0021-9290(83)90098-2)
- Martin, R., Burr, D., 1989. The microscopic structure of bone, in: *Structure, Function and Adaptation of Bone*. p. 18–56b. <https://doi.org/Structure, function, and adaptation of compact bone>
- Matter, P., Burch, H.B., 1990. Clinical experience with titanium implants, especially with the limited contact dynamic compression plate system. *Arch. Orthop. Trauma Surg.* 109, 311–313. <https://doi.org/10.1007/BF00636167>
- Matzenmiller, a., Lubliner, J., Taylor, R.L., 1995. A constitutive model for anisotropic damage in fiber-composites. *Mech. Mater.* 20, 125–152. [https://doi.org/10.1016/0167-6636\(94\)00053-0](https://doi.org/10.1016/0167-6636(94)00053-0)
- McKee, M.D., Seiler, J.G., Jupiter, J.B., 1995. The application of the limited contact dynamic compression plate in the upper extremity: an analysis of 114 consecutive cases. *Injury* 26, 661–666. [https://doi.org/10.1016/0020-1383\(95\)00148-4](https://doi.org/10.1016/0020-1383(95)00148-4)
- Miller, D.L., Goswami, T., 2007. A review of locking compression plate biomechanics and their advantages as internal fixators in fracture healing. *Clin. Biomech.* <https://doi.org/10.1016/j.clinbiomech.2007.08.004>
- Mullett, J.H., Shannon, F., Noël, J., Lawlor, G., Lee, T.C., O'Rourke, S.K., 2000. K-Wire position in tension band wiring of the Olecranon - A comparison of two techniques. *Injury* 31, 427–431. [https://doi.org/10.1016/S0020-1383\(00\)00014-0](https://doi.org/10.1016/S0020-1383(00)00014-0)
- Najeeb, S., Zafar, M.S., Khurshid, Z., Siddiqui, F., 2016. Applications of polyetheretherketone (PEEK) in oral implantology and prosthodontics. *J. Prosthodont. Res.* <https://doi.org/10.1016/j.jprior.2015.10.001>
- Navarro, M., Michiardi, A., Castan, O., Planell, J.A., 2008. Review. Biomaterials in orthopaedics. *J. R. Soc. Interface* 5, 1137–1158. <https://doi.org/10.1098/rsif.2008.0151>
- Niinomi, M., 1998. Mechanical properties of biomedical titanium alloys. *Mater. Sci. Eng. A* 243, 231–236. [https://doi.org/10.1016/S0921-5093\(97\)00806-X](https://doi.org/10.1016/S0921-5093(97)00806-X)
- O'Brien, F.J., Taylor, D., Clive Lee, T., 2007. Bone as a composite material: The role of osteons as barriers to crack growth in compact bone. *Int. J. Fatigue* 29, 1051–1056. <https://doi.org/10.1016/j.ijfatigue.2006.09.017>
- O'Dwyer, D., O'Dowd, N., McCarthy, C., 2013. Numerical micromechanical investigation

- of interfacial strength parameters in a carbon fibre composite material. *J. Compos. Mater.* 48, 749–760. <https://doi.org/10.1177/0021998313477172>
- Oller, S., Canet, J.M., Zalamea, F., 2005. Composite material behavior using a homogenization double scale method. *J. Eng. Mech.* [https://doi.org/10.1061/\(ASCE\)0733-9399\(2005\)131:1\(65\)](https://doi.org/10.1061/(ASCE)0733-9399(2005)131:1(65))
- Panayotov, I.V., Orti, V., Cuisinier, F., Yachouh, J., 2016. Polyetheretherketone (PEEK) for medical applications. *J. Mater. Sci. Mater. Med.* <https://doi.org/10.1007/s10856-016-5731-4>
- Perren, S.M., Mane, K., Pohler, O., Predieri, M., Steinemann, S., Gautier, E., 1990. The limited contact dynamic compression plate (LC-DCP). *Arch. Orthop. Trauma Surg.* 109, 304–310. <https://doi.org/10.1007/BF00636166>
- Pfeifer, R., Sellei, R., Pape, H.C., 2010. The biology of intramedullary reaming. *Injury.* [https://doi.org/10.1016/S0020-1383\(10\)70002-4](https://doi.org/10.1016/S0020-1383(10)70002-4)
- Pinho, S.T., Dávila, C.G., Camanho, P.P., Iannucci, L., Robinson, P., 2005. Failure Models and Criteria for FRP Under In-Plane or Three-Dimensional Stress States Including Shear Non-linearity. *Nasa/Tm-2005-213530.* <https://doi.org/NASA/TM-2005-213530>
- Pinter, Z., Smith, K., Hudson, P., Jones, C., Hadden, R., Elattar, O., Shah, A., 2017. A Retrospective Case Series of Carbon Fiber Plate Fixation of Ankle Fractures. *Foot Ankle Specialist* 11, 223–229. <https://doi.org/10.1177/1938640017718343>
- Pogue, D.J., Viegas, S.F., Patterson, R.M., Peterson, P.D., Jenkins, D.K., Sweo, T.D., Hokanson, J.A., 1990. Effects of distal radius fracture malunion on wrist joint mechanics. *J. Hand Surg. Am.* 15, 721–7. [https://doi.org/10.1016/0363-5023\(90\)90143-F](https://doi.org/10.1016/0363-5023(90)90143-F)
- Puck, A., Schürmann, H., 2002. Failure Analysis of FRP Laminates By Means of Physically Based Phenomenological Models. *Compos. Sci. Technol.* 62, 1633–1662. [https://doi.org/10.1016/S0266-3538\(96\)00140-6](https://doi.org/10.1016/S0266-3538(96)00140-6)
- Rae, P.J., Brown, E.N., Orler, E.B., 2007. The mechanical properties of poly(ether-etherketone) (PEEK) with emphasis on the large compressive strain response. *Polymer (Guildf)*. 48, 598–615. <https://doi.org/10.1016/j.polymer.2006.11.032>
- Reifsnider, K.L., Stinchcomb, W.W., Hahn, H.T., 1986. A Critical-Element Model of the Residual Strength and Life of Fatigue-Loaded Composite Coupons, in: Hahn, H.T. (Ed.), *Composite Materials: Fatigue and Fracture*, ASTM STP 907. American Society for Testing and Materials, Philadelphia, pp. 298–313.
- Reilly, D.T., Burstein, A.H., 1975. The Elastic and Ultimate Properties of Compact Bone Tissue. *J. Biomech.* 8, 393–405. [https://doi.org/10.1016/0021-9290\(75\)90075-5](https://doi.org/10.1016/0021-9290(75)90075-5)
- Reinoso, J., Catalanotti, G., Blázquez, A., Areias, P., Camanho, P.P., París, F., 2017. A consistent anisotropic damage model for laminated fiber-reinforced composites using the 3D-version of the Puck failure criterion. *Int. J. Solids Struct.* 126–127, 37–53. <https://doi.org/10.1016/j.ijsolstr.2017.07.023>
- Rho, J.Y., Ashman, R.B., Turner, C.H., 1993. Young's modulus of trabecular and cortical bone material: Ultrasonic and microtensile measurements. *J. Biomech.* 26, 111–119. [https://doi.org/10.1016/0021-9290\(93\)90042-D](https://doi.org/10.1016/0021-9290(93)90042-D)
- Rho, J.Y., Kuhn-Spearing, L., Zioupos, P., 1998. Mechanical properties and the hierarchical

- structure of bone. *Med. Eng. Phys.* 20, 92–102. [https://doi.org/10.1016/S1350-4533\(98\)00007-1](https://doi.org/10.1016/S1350-4533(98)00007-1)
- Rho, J.Y., Tsui, T.Y., Pharr, G.M., 1997. Elastic properties of human cortical and trabecular lamellar bone measured by nanoindentation. *Biomaterials* 18, 1325–1330. [https://doi.org/10.1016/S0142-9612\(97\)00073-2](https://doi.org/10.1016/S0142-9612(97)00073-2)
- Roh, Y.H., Lee, B.K., Baek, J.R., Noh, J.H., Gong, H.S., Baek, G.H., 2015. A randomized comparison of volar plate and external fixation for intra-articular distal radius fractures. *J. Hand Surg. Am.* 40, 34–41. <https://doi.org/10.1016/j.jhsa.2014.09.025>
- Rommens, P.M., Hessmann, M.H., 2015. *Intramedullary nailing: a comprehensive guide*. Springer-Verlag, London.
- Schatzker, J., Tile, M., Axelrod, T., Hu, R., Stephen, D., 2005. *The rationale of operative fracture care: Third edition, The Rationale of Operative Fracture Care: Third Edition*. <https://doi.org/10.1007/3-540-27708-0>
- Schneider, M.M., Nowak, T.E., Bastian, L., Katthagen, J.C., Isenberg, J., Rommens, P.M., Müller, L.P., Burkhart, K.J., 2014. Tension band wiring in olecranon fractures: The myth of technical simplicity and osteosynthetic perfection. *Int. Orthop.* 38, 847–855. <https://doi.org/10.1007/s00264-013-2208-7>
- Siebenlist, S., Torsiglieri, T., Kraus, T., Burghardt, R.D., Stöckle, U., Lucke, M., 2010. Comminuted fractures of the proximal ulna - Preliminary results with an anatomically preshaped locking compression plate (LCP) system. *Injury* 41, 1306–1311. <https://doi.org/10.1016/j.injury.2010.08.008>
- Snyder, S.M., Schneider, E., 1991. Estimation of mechanical properties of cortical bone by computed tomography. *J. Orthop. Res.* 9, 422–431. <https://doi.org/10.1002/jor.1100090315>
- Soden, P.D., Hinton, M.J., Kaddour, A.S., 1998. A comparison of the predictive capabilities of current failure theories for composite laminates. *Compos. Sci. Technol.* 58, 1225–1254. [https://doi.org/10.1016/S0266-3538\(98\)00077-3](https://doi.org/10.1016/S0266-3538(98)00077-3)
- Sommer, C., Gautier, E., Müller, M., Helfet, D.L., Wagner, M., 2003. First clinical results of the Locking Compression Plate (LCP). *Injury* 34. <https://doi.org/10.1016/j.injury.2003.09.024>
- Stedtfeld, H.-W., 2015. Rationale of Intramedullary Nailing, in: *Intramedullary Nailing*. Springer London, London, pp. 13–25. [https://doi.org/10.1007/978-1-4471-6612-2\\_2](https://doi.org/10.1007/978-1-4471-6612-2_2)
- Steinberg, E.L., Rath, E., Shlaifer, A., Chechik, O., Maman, E., Salai, M., 2012. Carbon fiber reinforced PEEK Optima-A composite material biomechanical properties and wear/debris characteristics of CF-PEEK composites for orthopedic trauma implants. *J. Mech. Behav. Biomed. Mater.* 17, 221–228. <https://doi.org/10.1016/j.jmbbm.2012.09.013>
- Talreja, R., 2016. Physical modelling of failure in composites, in: *Philosophical Transactions of the Royal Society A: Mathematical, Physical and Engineering Sciences*. <https://doi.org/10.1098/rsta.2015.0280>
- Talreja, R., 2008. Damage and fatigue in composites – A personal account. *Compos. Sci. Technol.* 68, 2585–2591. <https://doi.org/10.1016/J.COMPSCITECH.2008.04.042>
- Taylor, D., Prendergast, P.J., 1997. Model for fatigue crack propagation and remodelling in

- compact bone. *Proc. Inst. Mech. Eng. Part H J. Eng. Med.* 211, 369.
- Totry, E., González, C., LLorca, J., 2008. Prediction of the failure locus of C/PEEK composites under transverse compression and longitudinal shear through computational micromechanics. *Compos. Sci. Technol.* 68, 3128–3136. <https://doi.org/10.1016/j.compscitech.2008.07.011>
- Tsai, S.W., Wu, E.M., 1971. A General Theory of Strength for Anisotropic Materials. *J. Compos. Mater.* 5, 58–80. <https://doi.org/10.1177/002199837100500106>
- Turon, A., Camanho, P.P., Costa, J., Renart, J., 2010. Accurate simulation of delamination growth under mixed-mode loading using cohesive elements: Definition of interlaminar strengths and elastic stiffness. *Compos. Struct.* 92, 1857–1864. <https://doi.org/10.1016/j.compstruct.2010.01.012>
- Uthoff, H.K., Poitras, P., Backman, D.S., 2006. Internal plate fixation of fractures: Short history and recent developments. *J. Orthop. Sci.* <https://doi.org/10.1007/s00776-005-0984-7>
- Vallier, H.A., Le, T.T., Bedi, A., 2008. Radiographic and clinical comparisons of distal tibia shaft fractures (4 to 11 cm proximal to the plafond): Plating versus intramedullary nailing. *J. Orthop. Trauma* 22, 307–311. <https://doi.org/10.1097/BOT.0b013e31816ed974>
- van der Linden, S.C., van Kampen, A., Jaarsma, R.L., 2012. K-wire position in tension-band wiring technique affects stability of wires and long-term outcome in surgical treatment of olecranon fractures. *J. Shoulder Elb. Surg.* 21, 405–411. <https://doi.org/10.1016/j.jse.2011.07.022>
- van der Meer, F., Sluys, L., Hallett, S., Wisnom, M., 2011. Computational modeling of complex failure mechanisms in laminates. *J. Compos. Mater.* 46, 603–623. <https://doi.org/10.1177/0021998311410473>
- van der Meer, F.P., 2012. Mesolevel Modeling of Failure in Composite Laminates: Constitutive, Kinematic and Algorithmic Aspects. *Arch. Comput. Methods Eng.* 19, 381–425. <https://doi.org/10.1007/s11831-012-9076-y>
- Vaughan, T.J., McCarthy, C.T., 2011a. A micromechanical study on the effect of intra-ply properties on transverse shear fracture in fibre reinforced composites. *Compos. Part A Appl. Sci. Manuf.* 42, 1217–1228. <https://doi.org/10.1016/j.compositesa.2011.05.004>
- Vaughan, T.J., McCarthy, C.T., 2011b. Micromechanical modelling of the transverse damage behaviour in fibre reinforced composites. *Compos. Sci. Technol.* 71, 388–396. <https://doi.org/10.1016/j.compscitech.2010.12.006>
- Vaughan, T.J., McCarthy, C.T., 2010. A combined experimental–numerical approach for generating statistically equivalent fibre distributions for high strength laminated composite materials. *Compos. Sci. Technol.* 70, 291–297. <https://doi.org/10.1016/j.compscitech.2009.10.020>
- Vaughan, T.J., McCarthy, C.T., McNamara, L.M., 2012. A three-scale finite element investigation into the effects of tissue mineralisation and lamellar organisation in human cortical and trabecular bone. *J. Mech. Behav. Biomed. Mater.* 12, 50–62. <https://doi.org/10.1016/j.jmbbm.2012.03.003>
- Vigueras, G., Sket, F., Samaniego, C., Wu, L., Noels, L., Tjahjanto, D., Casoni, E., Houzeaux, G., Makradi, A., Molina-Aldareguia, J.M., Vázquez, M., Jérusalem, A.,

2015. An XFEM/CZM implementation for massively parallel simulations of composites fracture. *Compos. Struct.* 125, 542–557. <https://doi.org/10.1016/j.compstruct.2015.01.053>
- Vogler, M., Rolfes, R., Camanho, P.P., 2013. Modeling the inelastic deformation and fracture of polymer composites-Part I: Plasticity model. *Mech. Mater.* 59, 50–64. <https://doi.org/10.1016/j.mechmat.2012.12.002>
- Wähnert, D., Gehweiler, D., 2017. Complications of intramedullary nailing—Evolution of treatment. *Injury* 48, S59–S63. <https://doi.org/10.1016/j.injury.2017.04.032>
- Walsh, W.R., Pelletier, M.H., Bertollo, N., Christou, C., Tan, C., 2016. Does PEEK/HA Enhance Bone Formation Compared With PEEK in a Sheep Cervical Fusion Model? *Clin. Orthop. Relat. Res.* 474, 2364–2372. <https://doi.org/10.1007/s11999-016-4994-x>
- Warren, K.C., Lopez-Anido, R.A., Vel, S.S., Bayraktar, H.H., 2016. Progressive failure analysis of three-dimensional woven carbon composites in single-bolt, double-shear bearing. *Compos. Part B Eng.* 84, 266–276. <https://doi.org/10.1016/j.compositesb.2015.08.082>
- Weiner, S., Traub, W., Wagner, H.D., 1999. Lamellar bone: structure-function relations. *J. Struct. Biol.* 126, 241–255. <https://doi.org/10.1006/jsbi.1999.4107>
- Williams, K. V., Vaziri, R., Poursartip, A., 2003. A physically based continuum damage mechanics model for thin laminated composite structures. *Int. J. Solids Struct.* [https://doi.org/10.1016/S0020-7683\(03\)00016-7](https://doi.org/10.1016/S0020-7683(03)00016-7)
- Winqvist, R.A., Hansen, S.T., Clawson, D.K., 1984. Closed intramedullary nailing of femoral fractures. A report of five hundred and twenty cases. *J. Bone Joint Surg. Am.* 66, 529–39.
- Wisnom, M.R., 2010. Modelling discrete failures in composites with interface elements. *Compos. Part A Appl. Sci. Manuf.* <https://doi.org/10.1016/j.compositesa.2010.02.011>
- Woltz, S., Duijff, J.W., Hoogendoorn, J.M., Rhemrev, S.J., Breederveld, R.S., Schipper, I.B., Beeres, F.J.P., 2016. Reconstruction plates for midshaft clavicular fractures: A retrospective cohort study. *Orthop. Traumatol. Surg. Res.* 102, 25–29. <https://doi.org/10.1016/J.OTSR.2015.11.008>
- Yildiz, H., Chang, F.K., Goodman, S., 1998a. Composite hip prosthesis design. II. Simulation. *J. Biomed. Mater. Res.* 39, 102–119. [https://doi.org/10.1002/\(SICI\)1097-4636\(199801\)39:1](https://doi.org/10.1002/(SICI)1097-4636(199801)39:1)
- Yildiz, H., Ha, S.K., Chang, F.K., 1998b. Composite hip prosthesis design. I. Analysis. *J. Biomed. Mater. Res.* 39, 92–101. [https://doi.org/10.1002/\(SICI\)1097-4636\(199801\)39:1<92::AID-JBM12>3.0.CO;2-Q](https://doi.org/10.1002/(SICI)1097-4636(199801)39:1<92::AID-JBM12>3.0.CO;2-Q)
- Zhao, L., Gong, Y., Zhang, J., Chen, Y., Fei, B., 2014. Simulation of delamination growth in multidirectional laminates under mode I and mixed mode I/II loadings using cohesive elements. *Compos. Struct.* 116, 509–522. <https://doi.org/10.1016/j.compstruct.2014.05.042>
- Zoccali, C., Soriani, A., Rossi, B., Salducca, N., Biagini, R., 2016. The Carbofix™ “Piccolo Proximal femur nail”: A new perspective for treating proximal femur lesion. A technique report. *J. Orthop.* 13, 343–346. <https://doi.org/10.1016/j.jor.2016.07.001>
- Zysset, P.K., Edward Guo, X., Edward Hoffler, C., Moore, K.E., Goldstein, S.A., 1999.

Elastic modulus and hardness of cortical and trabecular bone lamellae measured by nanoindentation in the human femur. *J. Biomech.* 32, 1005–1012. [https://doi.org/10.1016/S0021-9290\(99\)00111-6](https://doi.org/10.1016/S0021-9290(99)00111-6)

# Chapter 3

## Theory

---

This chapter outlines the theoretical basis and the finite element theory for the work presented in Chapters 4, 5, 6 and 7 in the current work. Firstly, an overview of continuum mechanics is outlined in Section 3.2. Secondly, the theoretical basis for the mechanics of composite materials is presented in Section 3.4. The governing equations and theoretical framework for the finite element theory for the computational models presented in this work are summarized in Section 3.5. Modelling techniques for two computational methods of failure are outlined, namely the extended finite element (XFEM) theory and cohesive zone models (CZM) are considered in Section 3.6. The digital image correlation theory applied in Chapter 6 is described in Section 3.7.

### 3.1 Notation

An introduction to the notation used within this thesis is presented for clarity; a summary is presented in Table 3.1.

Table 3.1: Summary of the notation used hereafter in the present thesis

<b>Type</b>	<b>Notation</b>	<b>Example</b>
Scalar values	Written in italics	<i>a</i>
Vectors	Written in bold or unbold within square brackets	<b>a</b> or [a]
Transpose vectors	A vector with a superscript capital T	<b>a<sup>T</sup></b>
Second order Tensors	Written in bold	<b>a</b>

For example the dot product of two 3D components ( $\mathbf{u}, \mathbf{v}$ ), which is the summation of its component parts, is written as follows:

$$\mathbf{u} \cdot \mathbf{v} = u_i v_i = u_1 v_1 + u_2 v_2 + u_3 v_3 = \sum_i^3 u_i v_i \quad 3.1$$

Each component is denoted by two subscripts,  $i$  and  $j$ , that define its location in the tensor, where  $i, j = 1, 2, 3$ . For example, a component of the second order tensor  $\mathbf{A}$ , denoted  $A_{ij}$ , defines the value in the  $i^{th}$  row and the  $j^{th}$  column of the tensor.

## 3.2 Continuum mechanics

### 3.2.1 Deformation and strain measures

A representation of deformation and motion of a body is illustrated in Figure 3.1. Here, an undeformed body in its reference configuration,  $\Omega_0$ , at a time  $t=0$  undergoes a motion,  $\chi$ , to the deformed configuration,  $\Omega$ . When describing deformation and motion the equations are stated with respect to a reference configuration. Therefore, if a body is subjected to a deformation or displacement, a particle in that body,  $p$ , may move from an original position in space ( $\mathbf{X}$ ) to a new position in space ( $\mathbf{x}$ ), such that:

$$\mathbf{x} = \chi(\mathbf{X}, t) \quad 3.2$$

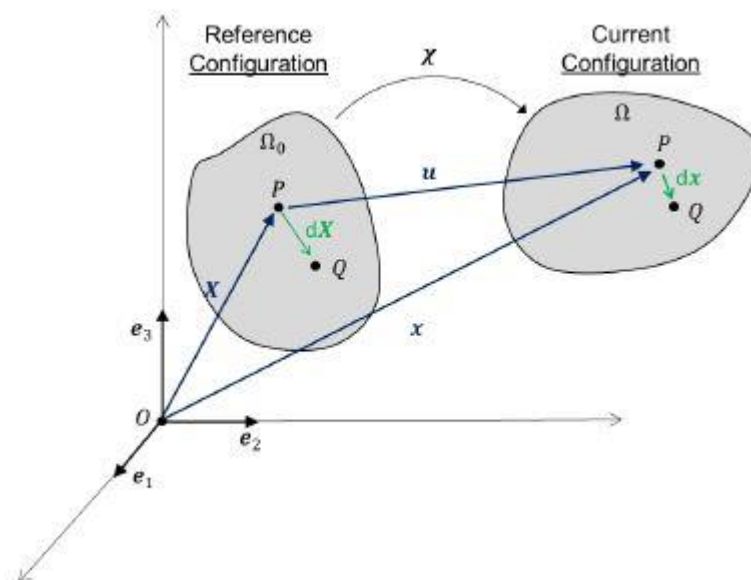


Figure 3.1: Reference (undeformed) and current (deformed) configurations and the associated vectors. (Image courtesy of J.A. Grogan)

Essentially, for the point,  $p$ ,  $\mathbf{X}$  defines the material coordinates and  $\mathbf{x}$  describes the spatial coordinates. The displacement vector,  $\mathbf{u}$ , defining the movement of the

material point between the reference configuration and the current configuration is given as:

$$\mathbf{u}(\mathbf{x}, t) = \mathbf{x} - \mathbf{X} \quad 3.3$$

Next consider two neighbouring material points,  $p$  and  $q$ , in the reference configuration joined by an infinitesimal line element,  $\partial\mathbf{X}$ . The deformation gradient tensor,  $\mathbf{F}$ , defines the transformation of  $\partial\mathbf{X}$  to  $\partial\mathbf{x}$  in the current configuration such that:

$$\mathbf{F} = \frac{\partial\mathbf{x}}{\partial\mathbf{X}} \quad \text{or} \quad F_{ij} = \frac{\partial x_i}{\partial X_j} \quad 3.4$$

The deformation gradient tensor,  $\mathbf{F}$ , is used to define strain measures such as the Green-Lagrange strain,  $\mathbf{E}$ , given by:

$$\mathbf{E} = \frac{1}{2}(\mathbf{F}^T \cdot \mathbf{F} - \mathbf{I}) \quad \text{or} \quad E_{ij} = \frac{1}{2} \left( \frac{\partial u_i}{\partial X_j} + \frac{\partial u_j}{\partial X_i} + \frac{\partial u_k}{\partial X_i} \frac{\partial u_k}{\partial X_j} \right) \quad 3.5$$

where  $\mathbf{F}^T$  is the transpose of  $\mathbf{F}$ ,  $(\mathbf{F}^T \cdot \mathbf{F})_{ij} = \mathbf{F}_{ik}^T \mathbf{F}_{kj}$  and  $\mathbf{I}$  is the identity tensor, where  $\mathbf{F} \cdot \mathbf{I} = \mathbf{F}$ . By assuming that the product of the infinitesimal (small) strain is negligible  $\left( \frac{\partial u_k}{\partial X_i} \frac{\partial u_k}{\partial X_j} \approx 0 \right)$ , the Green-Lagrange strain can be used to find the infinitesimal strain tensor ( $\boldsymbol{\varepsilon}$ ), giving:

$$\varepsilon_{ij} = \frac{1}{2} \left( \frac{\partial u_i}{\partial X_j} + \frac{\partial u_j}{\partial X_i} \right) \quad 3.6$$

Two useful measures of stretch are the left and right Cauchy-Green tensors,  $\mathbf{B}$  and  $\mathbf{C}$  respectively, which are:

$$\mathbf{B} = \mathbf{F} \cdot \mathbf{F}^T \quad \text{and} \quad \mathbf{C} = \mathbf{F}^T \cdot \mathbf{F} \quad 3.7$$

Invariants 1, 2 and 3 of the left and right Cauchy tensors are equivalent for both tensors and are given by:

$$I_1 = \text{tr}(\mathbf{C}) = \lambda_1^2 + \lambda_2^2 + \lambda_3^2 \quad 3.8$$

$$I_2 = \frac{1}{2} [I_1^2 - \text{tr}(\mathbf{C}^2)] = \lambda_1^2 \lambda_2^2 + \lambda_2^2 \lambda_3^2 + \lambda_3^2 \lambda_1^2 \quad 3.9$$

$$I_3 = \det(\mathbf{C}) = [\det(\mathbf{F})]^2 = \lambda_1^2 \lambda_2^2 \lambda_3^2 \quad 3.10$$

where  $\lambda$  is the stretch.

Given that the deformation gradient tensor,  $\mathbf{F}$ , is a well-defined second order tensor, the polar decomposition theorem can be implemented to decompose the tensor into an orthogonal rotation tensor  $\mathbf{R}$  and symmetric spatial and material stretch tensors,  $\mathbf{V}$  and  $\mathbf{U}$ , respectively, as follows:

$$\mathbf{F} = \mathbf{R} \cdot \mathbf{U} = \mathbf{V} \cdot \mathbf{R} \quad 3.11$$

Consequently, deformation can be considered as a stretch followed by a rotation ( $\mathbf{F} = \mathbf{V} \cdot \mathbf{R}$ ) or vice versa ( $\mathbf{F} = \mathbf{R} \cdot \mathbf{U}$ ). The principal stretches,  $\hat{\lambda}_{i=1,2,3}$ , are the eigenvalues of  $\mathbf{U}$ , and the logarithmic (true) strain,  $\boldsymbol{\varepsilon}$ , can be found from  $\mathbf{V}$ , the symmetric spatial tensor:

$$\boldsymbol{\varepsilon} = \ln \mathbf{V} \quad 3.12$$

The eigenvalues of  $\varepsilon$  are the principal logarithmic strains and the results in this thesis are presented in terms of the maximum principal logarithmic strain, unless otherwise stated.

The velocity of the material point P (see Figure 3.1) is defined as the rate of change of spatial position  $\mathbf{x}$  as a function of time as follows:

$$\mathbf{v} = \frac{\partial \mathbf{x}}{\partial t} \quad 3.13$$

The difference in velocity between two neighbouring material points is given in equation 3.14

$$d\mathbf{v} = \frac{\partial \mathbf{v}}{\partial \mathbf{x}} \cdot d\mathbf{x} = \mathbf{L} \cdot d\mathbf{x} \quad 3.14$$

where,  $\mathbf{L}$  is the spatial velocity gradient tensor, which relates to the deformation gradient,  $\mathbf{F}$ , as follows:

$$d\mathbf{v} = \mathbf{L} \cdot d\mathbf{x} = \mathbf{L} \cdot \mathbf{F} \cdot d\mathbf{X} \quad 3.15$$

$$d\mathbf{v} = \frac{\partial}{\partial t} (\mathbf{F} \cdot d\mathbf{X}) = \dot{\mathbf{F}} \cdot d\mathbf{X} \quad 3.16$$

Comparing the two equations for the velocity difference in terms of the distance between the material points ( $d\mathbf{X}$ ) gives the following equations for the velocity gradient,  $\mathbf{L}$ :

$$\mathbf{L} = \frac{\partial \mathbf{v}}{\partial \mathbf{x}} = \frac{\partial \mathbf{v}}{\partial \mathbf{X}} \cdot \frac{\partial \mathbf{X}}{\partial \mathbf{x}} = \frac{\partial \mathbf{F}}{\partial t} \cdot \mathbf{F}^{-1} = \dot{\mathbf{F}} \cdot \mathbf{F}^{-1} \quad 3.17$$

where,  $\dot{\mathbf{F}}$  is the time derivative of the deformation gradient, and  $\mathbf{F}^{-1}$  is the inverse of  $\mathbf{F}$ . The velocity gradient is often decomposed into its two symmetric and skew-symmetric component parts,

$$\mathbf{D} = \frac{1}{2}(\mathbf{L} + \mathbf{L}^T) = \text{sym}(\mathbf{L}) \quad 3.18$$

$$\mathbf{W} = \frac{1}{2}(\mathbf{L} - \mathbf{L}^T) = \text{asym}(\mathbf{L}) \quad 3.19$$

$\mathbf{D}$  is the symmetric strain rate tensor and  $\mathbf{W}$  is the anti-symmetric rotation or spin tensor. Under conditions where the principal referential axes remain fixed with respect to the material coordinates the rate of deformation tensor,  $\mathbf{D}$ , can be integrated to derive the logarithmic strain tension,  $\boldsymbol{\varepsilon}$ , given by:

$$\boldsymbol{\varepsilon}(t) = \int_0^t \mathbf{D} dt \quad 3.20$$

which for this case is equivalent to the logarithmic strain Abaqus Theory Manual, (DS SIMULIA, RI, USA).

## 3.2.2 Stress measures

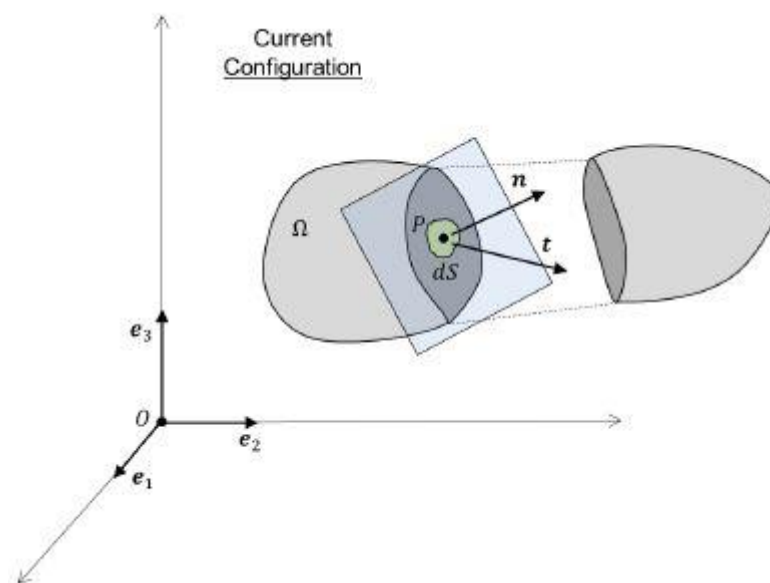


Figure 3.2: Traction,  $\mathbf{t}$ , acting on an infinitesimal surface,  $dS$ , and  $\mathbf{n}$  is the normal vector to the surface (Image courtesy of J.A. Grogan)

With reference to a volume,  $V$ , (see Figure 3.2) the traction,  $\mathbf{t}$ , is the force per unit area that acts on an infinitesimal surface element  $dS$  in the vicinity of a point  $P$  in the current configuration. The surface element  $dS$  is described by its unit normal,  $\mathbf{n}$ . The Cauchy (true) stress,  $\boldsymbol{\sigma}$ , relates the unit normal to the traction vector by:

$$\mathbf{t} = \boldsymbol{\sigma} \cdot \mathbf{n} \quad 3.21$$

The symmetric Cauchy stress tensor can be expressed in terms of a hydrostatic pressure stress  $p$  and a deviatoric stress  $\mathbf{S}$  given by:

$$\boldsymbol{\sigma} = \mathbf{S} - p\mathbf{I} \quad 3.22$$

with

$$p = \frac{-\text{tr}(\boldsymbol{\sigma})}{3} \quad 3.23$$

where  $tr(\boldsymbol{\sigma}) = \sum_{i=1}^3 \sigma_{ii}$ .

The Kirchhoff stress,  $\boldsymbol{\tau}$ , is a symmetric tensor defined as:

$$\boldsymbol{\tau} = J\boldsymbol{\sigma} \tag{3.24}$$

where  $J = \frac{d\Gamma}{d\Gamma_0}$  is the ratio of infinitesimal volume of the current and reference configurations in the vicinity of a point  $P$ . The first Piola-Kirchhoff stress,  $\mathbf{P}$ , is a non-symmetric tensor is given by:

$$\mathbf{P} = \mathbf{N}^T = \boldsymbol{\tau} \cdot \mathbf{F}^{-T} \tag{3.25}$$

where  $\mathbf{N}^T$  is the transpose of the nominal stress.

Mean von Mises equivalent stresses,  $\boldsymbol{\sigma}_e$ , are defined as follows:

$$\boldsymbol{\sigma}_e = \sqrt{\frac{3}{2} S_{ij} S_{ij}} \tag{3.26}$$

A brief overview of the fundamental principles of deformation kinematics has been presented.

### **3.3 Plasticity**

Continuum constitutive plasticity formulations are required for neat unreinforced PEEK and continuous fibre reinforced PEEK laminates that can predict the inelastic deformation. In the present work it is assumed that neat PEEK is a rate dependent, homogeneous and elastic plastic and the Drucker-Prager plasticity model is implemented to capture this. The Drucker-Prager is described in further detail in

Chapter 5 of this thesis. To provide a continuum representation of the anisotropic plasticity observed in the experimental results of fibre reinforced PEEK, Chapter 4, the Hill potential function is implemented, presented in greater detail in Chapter 4.

Both the Drucker-Prager and the Hill plasticity formulation are elastic-plastic constitutive models, and in general the common assumptions with elastic-plastic formulations, is that the deformation can be split into a reversible elastic part and a irreversible plastic part. Therefore, the total deformation gradient,  $\mathbf{F}$ , previously defined in eqn. 1.4 can now be defined as follows:

$$\mathbf{F} = \mathbf{F}^e \cdot \mathbf{F}^{pl} \quad 3.27$$

where  $\mathbf{F}^e$  is the recoverable elastic part of the deformations and  $\mathbf{F}^{pl}$  is the non-recoverable plastic part of deformation. The deformation gradient can be approximated in terms of mechanical strain rates in the system, which can also be broken into elastic and plastic parts

$$d\boldsymbol{\varepsilon} = d\boldsymbol{\varepsilon}^e \cdot d\boldsymbol{\varepsilon}^{pl} \quad 3.28$$

where  $d\boldsymbol{\varepsilon}$  is the total strain rate, made up of the elastic strain rate,  $d\boldsymbol{\varepsilon}^e$ , and the plastic strain rate,  $d\boldsymbol{\varepsilon}^{pl}$ . Integrating eqn. 1.28 with respect to time gives the total strain tensor,  $\boldsymbol{\varepsilon}$ ,

$$\boldsymbol{\varepsilon} = \boldsymbol{\varepsilon}^e \cdot \boldsymbol{\varepsilon}^{pl} \quad 3.29$$

Rae et al., (2007) has shown that unreinforced PEEK is a rate sensitive material, and Ferguson et al., (2006) has shown that PEEK is also susceptible to non-recoverable time dependent creep, however, all of the experiments and simulations in the current thesis are carried out under quasi-static loading conditions at similar strain rates.

Future work should investigate the rate dependence and viscoelasticity in carbon fibre reinforced PEEK which was outside the scope of the current thesis.

### 3.4 Mechanical behaviour of composites

A laminate is a stack of organised unidirectional composite plies. The stack or layup of the laminate is defined by the fibre directions of each ply in the composite stack. The following section outlines basic mechanics of composite laminate plate theory (Crawford, 1998).

#### Rule of Mixtures

The longitudinal and transverse moduli of a unidirectional composite correlate directly to the proportion of the matrix and fibre volume fractions of that composite. Calculating the moduli using the proportions of the fibres and matrix in the composite is known as the rule of mixtures.

Longitudinal modulus in the fibre direction:

$$E_1 = E_f V_f + E_m V_m \quad 3.30$$

Transverse modulus:

$$E_2 = \frac{E_f E_m}{E_f V_m + E_m V_f} \quad 3.31$$

where,  $E_m$  is the elastic modulus of the matrix material and  $E_f$  is the modulus of the fibres.

With this simplistic mechanics of material analyses the in-plane shear modulus can be similarly calculated:

$$G_{12} = \frac{G_f G_m}{G_f V_m + G_m V_f} \quad 3.32$$

Where,  $G_m$  and  $G_f$  are the shear moduli of the matrix and the fibres respectively.

The rule of mixtures provides a simplistic approach to the calculation of the elastic properties for a single unidirectional lamina.

### Deformation behaviour of a single ply

When considering a single unidirectional reinforced ply it is commonplace for a 1-2-3 orthogonal coordinate system to be used, where the 1-axis is aligned with the fibres, the 2-axis is aligned perpendicular to the fibres but in the same plane as the fibres and the 3-axis is perpendicular to the plane of the fibres. The laminate has some alignment in the global x-y-z- coordinate system. The linear elastic stress strain relations for fibre reinforced composite materials are easily derived.

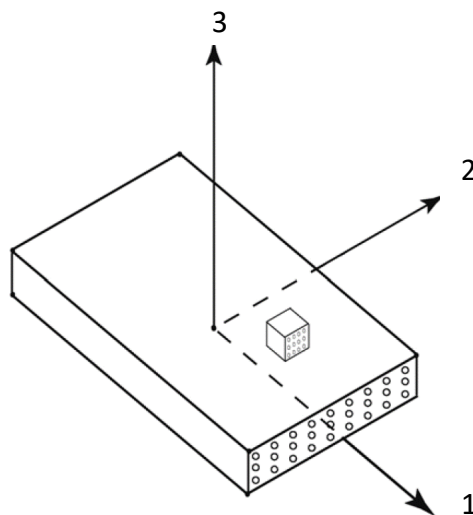


Figure 3.3: An illustration of the principle material coordinate system

Considering a thin unidirectional lamina in a state of plane stress, with no out of plane stresses, a reduced form of the compliance matrix can be used as shown in equation 3.33. As previously established, the material properties of lamina are anisotropic and have modulus values of  $E_1$  and  $E_2$  in fibre and transverse directions, respectively.

$$\begin{Bmatrix} \varepsilon_x \\ \varepsilon_y \\ \gamma_{xy} \end{Bmatrix} = \begin{bmatrix} \frac{1}{E_1} & \frac{-\nu_{21}}{E_2} & 0 \\ \frac{-\nu_{12}}{E_1} & \frac{1}{E_2} & 0 \\ 0 & 0 & \frac{1}{G_{12}} \end{bmatrix} \begin{Bmatrix} \sigma_x \\ \sigma_y \\ \tau_{xy} \end{Bmatrix} \quad 3.33$$

Abbreviated to:

$$\{\varepsilon\} = [S]\{\sigma\}$$

Where:

$$[S] = \begin{bmatrix} S_{11} & S_{12} & 0 \\ S_{12} & S_{22} & 0 \\ 0 & 0 & S_{66} \end{bmatrix}$$

3.23 can be inverted as follows:

$$\begin{Bmatrix} \sigma_x \\ \sigma_y \\ \tau_{xy} \end{Bmatrix} = \begin{bmatrix} Q_{11} & Q_{12} & 0 \\ Q_{12} & Q_{22} & 0 \\ 0 & 0 & Q_{66} \end{bmatrix} \begin{Bmatrix} \varepsilon_x \\ \varepsilon_y \\ \gamma_{xy} \end{Bmatrix} \quad 3.34$$

where [Q] is the reduced stiffness matrix. If the lamina (local) 1-2 coordinate system is aligned with the global x-y coordinate system, the fibres of the lamina are aligned in the global x-direction and the terms in the [Q] matrix are as follows:

$$Q_{11} = \frac{E_1}{1 - \nu_{12}\nu_{21}} \qquad Q_{11} = \frac{E_2}{1 - \nu_{21}\nu_{12}}$$

$$Q_{12} = \nu_{21}Q_{22} \qquad Q_{66} = G_{12}$$

For angled plies, where the local coordinate system of the ply does not align exactly with the global system, the applied global stresses must be transformed onto the local axis. To do this the stress transformation matrix [T] is implemented as follows:

$$\begin{Bmatrix} \sigma_1 \\ \sigma_2 \\ \tau_{12} \end{Bmatrix} = \begin{bmatrix} m^2 & n^2 & 2mn \\ n^2 & m^2 & -2mn \\ -mn & mn & (m^2 - n^2) \end{bmatrix} \begin{Bmatrix} \sigma_x \\ \sigma_y \\ \tau_{xy} \end{Bmatrix} \qquad 3.35$$

where,  $m = \cos \theta$ ,  $n = \sin \theta$  and  $\theta$  is the angle of the lamina with respect to the global axis (see Figure 3.4).

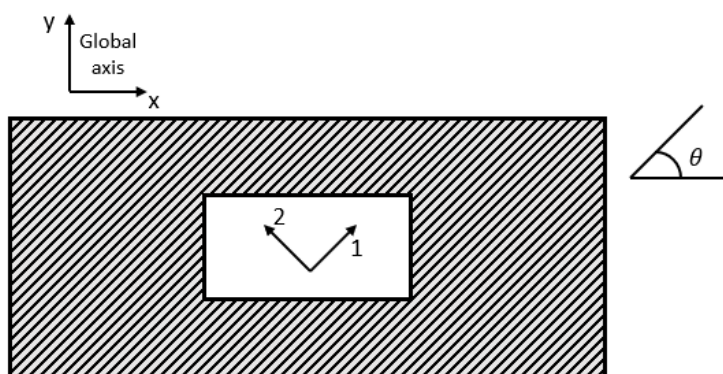


Figure 3.4: Ply oriented at an angle  $\theta$  to the global axis.

Similarly, the transformation matrix is also employed for the transformation of strains from global coordinate system to the lamina coordinate system.

$$\begin{Bmatrix} \varepsilon_1 \\ \varepsilon_2 \\ \frac{1}{2}\gamma_{12} \end{Bmatrix} = [T] \begin{Bmatrix} \varepsilon_x \\ \varepsilon_y \\ \frac{1}{2}\gamma_{xy} \end{Bmatrix} \qquad 3.36$$

For both cases the global x-y stresses and strains may also be expressed in terms of the local lamina stresses and strains by inverting equations 3.35 and 3.36. The inverted transformation matrix is given as:

$$[T]^{-1} = \begin{bmatrix} m^2 & n^2 & -2mn \\ n^2 & m^2 & 2mn \\ mn & -mn & (m^2 - n^2) \end{bmatrix}$$

Therefore, to determine the global stiffness in the x-y directions of a ply whose fibres are aligned at an angle  $\theta$  to the x-axis, the following steps must be taken:

- Determine the strains in the local 1-2 directions by transforming the applied global strains, equation 3.36
- Calculate the local stresses using the local stiffness matrix  $[Q]$  derived earlier
- Transform the local stresses to the global directions using  $[T]^{-1}$

Combining these steps an equation for the global stresses in terms of the global strains can be written as follows:

$$\begin{Bmatrix} \sigma_x \\ \sigma_y \\ \tau_{xy} \end{Bmatrix} = [\bar{Q}] \begin{Bmatrix} \varepsilon_x \\ \varepsilon_y \\ \gamma_{xy} \end{Bmatrix} \quad 3.37$$

Providing an overall stiffness matrix  $[\bar{Q}]$  for the ply where,

$$\bar{Q}_{11} = Q_{11}m^4 + 2m^2n^2(Q_{12} + 2Q_{66}) + Q_{22}n^4$$

$$\bar{Q}_{22} = Q_{22}m^4 + 2m^2n^2(Q_{12} + 2Q_{66}) + Q_{11}n^4$$

$$\bar{Q}_{12} = (Q_{11} + Q_{22} - 4Q_{66})m^2n^2 + Q_{12}(m^4 + n^4)$$

$$\bar{Q}_{66} = (Q_{11} + Q_{22} - 2Q_{12})m^2n^2 + Q_{66}(m^2 + n^2)^2$$

$$\bar{Q}_{16} = \bar{Q}_{61} = [(Q_{11} - Q_{12} - 2Q_{66})m^2 - (Q_{22} - Q_{12} - 2Q_{66})n^2]mn$$

$$\bar{Q}_{26} = \bar{Q}_{62} = [(Q_{22} - Q_{12} - 2Q_{66})m^2 - (Q_{11} - Q_{12} - 2Q_{66})n^2]mn$$

Similarly, the overall compliance matrix,  $[\bar{S}]$ , can be used to analyse strains in the global direction, where  $[\bar{S}] = [\bar{Q}]^{-1}$ .

$$\begin{pmatrix} \varepsilon_x \\ \varepsilon_y \\ \gamma_{xy} \end{pmatrix} = [\bar{S}] \begin{pmatrix} \sigma_x \\ \sigma_y \\ \tau_{xy} \end{pmatrix} \quad 3.38$$

Combining equation 3.38 with terms in the unidirectional ply compliance matrix derived earlier, equation 3.33, the stiffness of a unidirectional ply loaded at any angle  $\theta$  to the fibre direction can be expressed as:

$$\frac{1}{E_x} = \bar{S}_{11} \qquad \frac{1}{E_y} = \bar{S}_{22} \qquad \frac{1}{G_{xy}} = \bar{S}_{66}$$

### **Mechanics of Laminated Composites**

It is assumed that the laminate thickness is very small compared to its other dimensions and that the plies in the laminate are securely bonded together. When a force is applied to the laminate all of the plies deform by the same amount. Hence the strain is the same in each ply but due to the different angulations of the plies, the stresses are discontinuous from ply to ply.

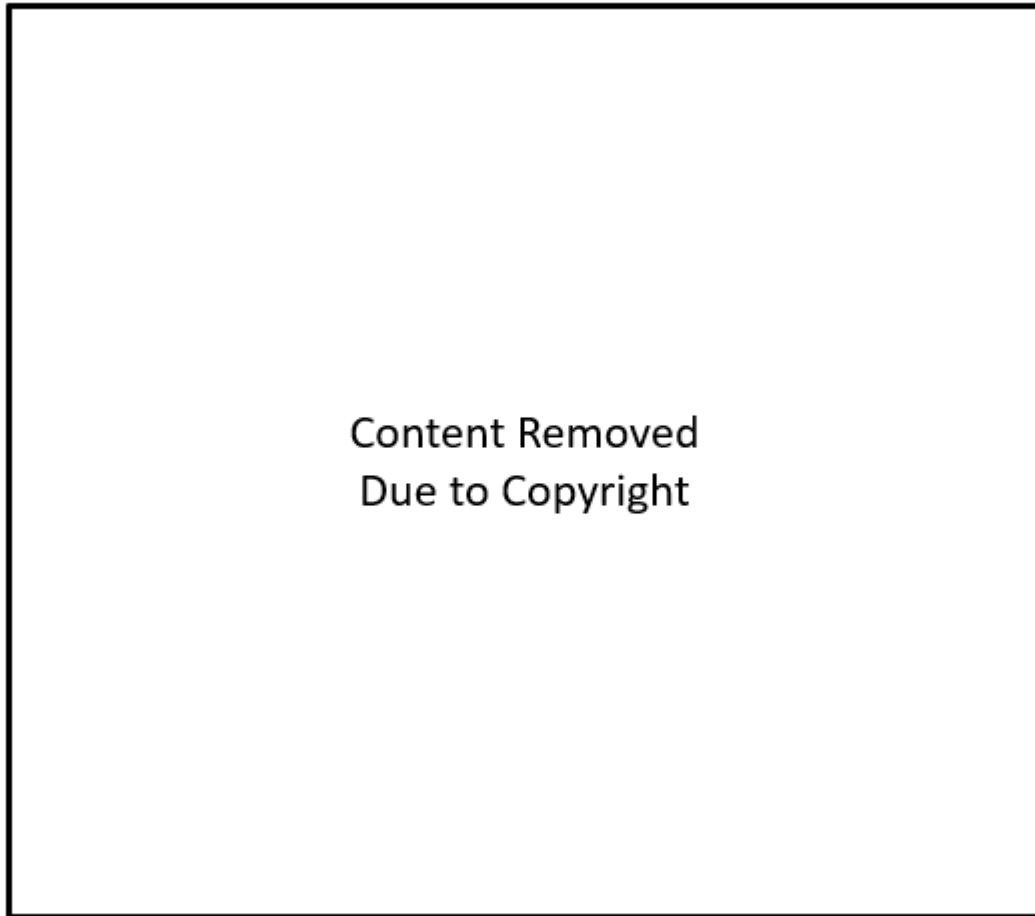


Figure 3.5: Diagram of the displacements in a laminate along the z axis during to an applied bending load (Nettles, 1994)

Figure 3.5 shows an example of displacements in a laminate undergoing bending, where displacements in the x-direction are denoted u, y-direction displacements are designated v and w for displacements in the z-direction. The strains in the laminate can be described as follows:

$$\begin{bmatrix} \varepsilon_x \\ \varepsilon_y \\ \gamma_{xy} \end{bmatrix} = \begin{bmatrix} \varepsilon_x^0 \\ \varepsilon_y^0 \\ \gamma_{xy}^0 \end{bmatrix} + z \begin{bmatrix} \kappa_x \\ \kappa_y \\ \kappa_{xy} \end{bmatrix} \quad 3.39$$

where  $\varepsilon_x^0$ ,  $\varepsilon_y^0$  and  $\gamma_{xy}^0$  are the mid-plane strains,  $\kappa_x$ ,  $\kappa_y$  and  $\kappa_{xy}$  are the laminate curvatures and z is the distance from the neutral axis. Therefore, the strain,  $\varepsilon$ , at any

point in the ply is a function of the bending curvature,  $\kappa$ , and an in-plane strain component,  $\varepsilon_o$ .

From equation 3.37 the stresses in each ply can then be determined as follows:

$$\begin{bmatrix} \sigma_x \\ \sigma_y \\ \tau_{xy} \end{bmatrix} = [\bar{Q}] \begin{bmatrix} \varepsilon_x^0 \\ \varepsilon_y^0 \\ \gamma_{xy}^0 \end{bmatrix} + z[\bar{Q}] \begin{bmatrix} \kappa_x \\ \kappa_y \\ \kappa_{xy} \end{bmatrix} \quad 3.40$$

Since the stresses are discontinuous from ply to ply, they are defined in terms of equivalent forces acting at the mid-surface for convenience. The resulting integral is defined as the stress resultant and is denoted  $N$  with units of force per unit length and is given as:

$$\begin{bmatrix} N_x \\ N_y \\ N_{xy} \end{bmatrix} = \int_{-h/2}^{h/2} \begin{bmatrix} \sigma_x \\ \sigma_y \\ \tau_{xy} \end{bmatrix} dz \quad 3.41$$

The bending moments can be similarly expressed:

$$\begin{bmatrix} M_x \\ M_y \\ M_{xy} \end{bmatrix} = \int_{-h/2}^{h/2} \begin{bmatrix} \sigma_x \\ \sigma_y \\ \tau_{xy} \end{bmatrix} z dz \quad 3.42$$

The integrals in equations 3.41 and 3.42 must be performed over each ply in the laminate and summed. Combining with equation 3.40 and integrating gives:

$$\begin{bmatrix} N_x \\ N_y \\ N_{xy} \end{bmatrix} = \sum_{k=1}^n \left\{ [\bar{Q}]_k \begin{bmatrix} \varepsilon_x^0 \\ \varepsilon_y^0 \\ \gamma_{xy}^0 \end{bmatrix} (h_k - h_{k-1}) + [\bar{Q}]_k \begin{bmatrix} \kappa_x \\ \kappa_y \\ \kappa_{xy} \end{bmatrix} \frac{1}{2} (h_k^2 - h_{k-1}^2) \right\} \quad 3.43$$

and

$$\begin{aligned} \begin{bmatrix} M_x \\ M_y \\ M_{xy} \end{bmatrix} &= \sum_{k=1}^n \left\{ [\bar{Q}]_k \begin{bmatrix} \varepsilon_x^0 \\ \varepsilon_y^0 \\ \gamma_{xy}^0 \end{bmatrix} \frac{1}{2} (h_k^2 - h_{k-1}^2) \right. \\ &\quad \left. + [\bar{Q}]_k \begin{bmatrix} \kappa_x \\ \kappa_y \\ \kappa_{xy} \end{bmatrix} \frac{1}{3} (h_k^3 - h_{k-1}^3) \right\} \end{aligned} \quad 3.44$$

The constitutive equations can thus be defined as:

$$\begin{bmatrix} N \\ M \end{bmatrix} = \begin{bmatrix} A & B \\ B & D \end{bmatrix} \begin{bmatrix} \varepsilon^0 \\ \kappa \end{bmatrix} \quad 3.45$$

where

$$[A] = A_{ij} = \sum_{k=1}^n (\bar{Q}_{ij})_k [h_k - h_{k-1}] \quad 3.46$$

$$[B] = B_{ij} = \frac{1}{2} \sum_{k=1}^n (\bar{Q}_{ij})_k [h_k^2 - h_{k-1}^2] \quad 3.47$$

$$[D] = D_{ij} = \frac{1}{3} \sum_{k=1}^n (\bar{Q}_{ij})_k [h_k^3 - h_{k-1}^3] \quad 3.48$$

$[A]$  is the extensional stiffness matrix and  $[B]$  is the coupling matrix and  $[D]$  is the bending stiffness matrix. For symmetric laminates, the geometric mid-plane of the laminate is also the neutral plane of the laminate. Therefore the  $[B]$  matrix reduces to zero and there is no coupling between the bending strains and the normal stresses. All of the laminates examined in this thesis are symmetric laminates. However, while it is essential to understand these simplistic analytical approaches, they are not implemented in the finite element simulations presented in the technical chapters of this thesis (Chapters 4-7). Each ply is modelled as an individual homogeneous

anisotropic material. Predictions of damage and failure of the carbon fibre reinforced laminates, including delamination, plasticity and cracking, under complex loading conditions requires the use of numerical solution schemes, outlined in the next section (Section 3.5) of this chapter.

**Laminate notation**

Laminates consist of several unidirectional plies stacked on top of one another at different angles. The plies are listed from top to bottom and an s denotes that the laminate is symmetric, i.e. a laminate in which the plies above the centre plane are a mirror image of those below it. Examples of laminate notation are outlined in Table 3.2 for convenience.

Table 3.2: Summary of the laminate layup notation used in this body of work

Laminate Layup	Notation
$0^\circ / 0^\circ / 0^\circ / 0^\circ$	$[0^\circ_2]_s$
$+45^\circ / -45^\circ / +45^\circ / -45^\circ$	$[\pm 45^\circ]_s$
$0^\circ / 90^\circ / 90^\circ / 0^\circ$	$[0^\circ / 90^\circ]_s$
$0^\circ / +45^\circ / -45^\circ / 90^\circ / 90^\circ / -45^\circ / +45^\circ / 0^\circ$	$[0^\circ / \pm 45^\circ / 90^\circ]_s$

**3.5 The finite element (FE) method**

The numerical solutions of continuum mechanics problems presented in this thesis are achieved using the FE method, as implemented in the commercial FE code, Abaqus (DS SIMULIA, RI, USA). In the present work the Abaqus/Standard or Implicit form is used to solve boundary value problems. A brief overview of

fundamental equations of the implicit FE solution is presented in the following section. A more details discussion of the FE method is available in the Abaqus Theory Manual (DS SIMULIA, RI, USA).

The FE method divides a body into an assembly of subsections called elements which are connected together at points called nodes. The elements and nodes which represent the material body ( $V$ ), on which the boundary value problems are solved, is known as the FE mesh. Quantities such as displacements can be interpolated throughout the body based on discrete values calculated and the element nodes according to the element shape functions. For each discrete element, the governing constitutive equations are assembled to form a system equation, which describe the behaviour in the body as a whole. Stress and strain in the material body is calculated in an incremental fashion once boundary conditions are applied to the system equations

### 3.5.1 Implicit FE method solution

In the context of Abaqus/Standard, the word ‘implicit’ refers to the method of updating the state of a FE model from time  $t$  to  $t + \Delta t$ . Displacements are applied incrementally over each of the time steps  $\Delta t$  and in a fully implicit solution the state at  $t + \Delta t$  is determined based on the information at  $t + \Delta t$ . The implicit FE method in Abaqus/Standard implements a form of the Newton-Raphson (N-R). During the iterative N-R method a tangent function,  $f(x)$ , of the current solution is used to approximate a more accurate solution:

$$x_{i+1} = x_i - \frac{f(x_i)}{f'(x_i)} \quad 3.49$$

The process continues iteratively until such a time as the solution converges and an accurate approximation is achieved.

Consider again Figure 3.2 and the principal of virtual work, which is the fundamental equation upon which the FE method is based:

$$\int_V \delta \boldsymbol{\varepsilon}^T \boldsymbol{\sigma} dV = \int_S \delta \mathbf{u}^T \mathbf{t} dS \quad 3.50$$

Where equilibrium is enforced on a reference volume,  $V$ , bounded by a surface,  $S$ .  $\delta \boldsymbol{\varepsilon}$  and  $\delta \mathbf{u}$  are the virtual strain and virtual displacement vectors, respectively, while  $\boldsymbol{\sigma}$  is the stress vector and  $\mathbf{t}$  is the traction vector. The integrals of equation 3.50 are taken over each element (e) of volume  $V_e$  and surface  $S_e$  in the FE mesh:

$$\delta \boldsymbol{\varepsilon} = \widehat{\mathbf{B}}_e \delta \mathbf{u}_e \quad 3.51$$

$$\delta \mathbf{u} = \widehat{\mathbf{N}}_e \delta \mathbf{u}_e \quad 3.52$$

$\widehat{\mathbf{B}}_e$  is the element shape function gradient matrix and  $\widehat{\mathbf{N}}_e$  is the element shape function matrix. Substituting these equations into equation 3.50 and rearranging, the following expression for the principal of virtual work is obtained:

$$\sum_e \int_{V_e} \delta \mathbf{u}_e^T \widehat{\mathbf{B}}_e^T \boldsymbol{\sigma}(\mathbf{u}_e) dV = \sum_e \int_{S_e} \delta \mathbf{u}_e^T \widehat{\mathbf{N}}_e^T \mathbf{t} dS \quad 3.53$$

Which summates to:

$$\delta \mathbf{u}^T \left( \int_V \widehat{\mathbf{B}}^T \boldsymbol{\sigma}(\mathbf{u}) dV - \int_S \widehat{\mathbf{N}}^T \mathbf{t} dS \right) = 0$$

Eliminating the arbitrary virtual displacements,  $\delta \mathbf{u}$ , yields:

$$\int_V \widehat{\mathbf{B}}^T \boldsymbol{\sigma}(\mathbf{u}) dV - \int_S \widehat{\mathbf{N}}^T \mathbf{t} dS = 0 \quad 3.54$$

A set of global equations in  $\mathbf{u}$  for the out of balance residual force,  $\mathbf{G}$ , can then be assembled (equation 3.55), where  $\mathbf{u}$  is the global nodal displacement.

$$\mathbf{G}(\mathbf{u}) = \int_V \widehat{\mathbf{B}}^T \boldsymbol{\sigma}(\mathbf{u}) dV - \int_S \widehat{\mathbf{N}}^T \mathbf{t} dS \quad 3.55$$

To achieve an equilibrium stress state such that,  $\mathbf{G}(\mathbf{u}) = 0$ , the non-linear set of equations must be solved. In general, non-linear problems involving non-linear constitutive laws and/or non-linear boundary conditions are solved incrementally, where loads/displacements are applied in time steps,  $\Delta t$ , up to the ultimate time,  $t_{final}$ . At time  $t + \Delta t$ , the loads/displacements may have caused geometry deviations and equation 3.53 must be updated to reflect this.

Within each increment of the implicit FE Abaqus/Standard solution, the N-R scheme updates all nodal displacements iteratively from  $t$  to  $t + \Delta t$ , to solve for  $\mathbf{u}_{i+1}^{t+\Delta t}$ , until stable equilibrium between the internal forces and the externally applied displacement/loads is reached. An estimation of the roots of equation 3.53 is made using the N-R formula such that, for the  $i^{th}$  iteration:

$$\partial \mathbf{u}_{i+1} = \mathbf{u}_{i+1}^{t+\Delta t} - \mathbf{u}_i^{t+\Delta t} = - \left[ \frac{\partial \mathbf{G}(\mathbf{u}_i^{t+\Delta t})}{\partial \mathbf{u}} \right]^{-1} \mathbf{G}(\mathbf{u}_i^{t+\Delta t}) \quad 3.56$$

which can be written in terms of the tangent stiffness matrix,  $\bar{\mathbf{K}}$ , where the partial derivative of the right-hand side of the equation is also referred to as the Jacobian matrix:

$$\bar{\mathbf{K}}(\mathbf{u}_i^{t+\Delta t}) = \frac{\partial \mathbf{G}(\mathbf{u}_i^{t+\Delta t})}{\partial \mathbf{u}}$$

$$\bar{\mathbf{K}}(\mathbf{u}_i^{t+\Delta t}) \partial \mathbf{u}_{i+1} = -\mathbf{G}(\mathbf{u}_i^{t+\Delta t}) \quad 3.57$$

where  $\mathbf{u}_i^{t+\Delta t}$  is the vector nodal displacements for the  $i^{th}$  iteration at time  $t + \Delta t$ , and  $\mathbf{u}_{i+1}^{t+\Delta t}$  is the improved estimation of the nodal displacements relative to  $\mathbf{u}_i^{t+\Delta t}$ . These FE equations must be solved, for each iteration, for the change in incremental displacements,  $\partial \mathbf{u}_{i+1}$ , in the process until the solution converges or a tolerance is reached, such that:

$$|\mathbf{G}(\mathbf{u}_{i+1}^{t+\Delta t})| < Tolerance \quad 3.58$$

Finally, the tangent stiffness matrix,  $\bar{\mathbf{K}}$ , can be expressed as:

$$\begin{aligned} \bar{\mathbf{K}}(\mathbf{u}) &= \frac{\partial \mathbf{G}(\mathbf{u})}{\partial \mathbf{u}} = \frac{\partial}{\partial \mathbf{u}} \left( \int_V \hat{\mathbf{B}}^T \boldsymbol{\sigma}(\mathbf{u}) dV - \mathbf{F} \right) \\ &= \frac{\partial}{\partial \mathbf{u}} \left( \int_V \hat{\mathbf{B}}^T \boldsymbol{\sigma}(\mathbf{u}) dV \right) = \int_V \hat{\mathbf{B}}^T \frac{\partial \boldsymbol{\sigma}(\mathbf{u})}{\partial \mathbf{u}} dV \\ &= \int_V \hat{\mathbf{B}}^T \frac{\partial \boldsymbol{\sigma}(\mathbf{u})}{\partial \boldsymbol{\varepsilon}} \frac{\partial \boldsymbol{\varepsilon}}{\partial \mathbf{u}} dV = \int_V \hat{\mathbf{B}}^T \frac{\partial \boldsymbol{\sigma}(\boldsymbol{\varepsilon})}{\partial \boldsymbol{\varepsilon}} \hat{\mathbf{B}} dV \\ \bar{\mathbf{K}}(\mathbf{u}) &= \int_V \hat{\mathbf{B}}^T \mathbf{D}^{Tan} \hat{\mathbf{B}} dV \quad 3.59 \end{aligned}$$

where  $\mathbf{D}^{Tan}$  is the consistent tangent matrix of the Jacobian constitutive law:

$$\mathbf{D}^{Tan} = \frac{\partial \boldsymbol{\sigma}(\boldsymbol{\varepsilon})}{\partial \boldsymbol{\varepsilon}} \quad 3.60$$

The tangent stiffness matrix,  $\bar{\mathbf{K}}(\mathbf{u})$ , is solved for each iteration, but in order to solve for  $\partial \mathbf{u}_{i+1}$  the stiffness matrix must be inverted, resulting in a significant computation expense. However, iteration ensures that relatively large time increments can be used while maintaining the accuracy of the solution, unlike other solution techniques, such as the Abaqus/Explicit method, which does not facilitate the use of large time steps. The FE simulations presented in this thesis are performed using the Implicit method. User defined subroutines developed to accurately predicted damage, delamination and failure in the fibre reinforced laminates. These damage modelling methodologies are introduced in the following section.

### 3.6 Damage modelling

The FE method described in the previous section delivers a way to predict the failure behaviour of materials once the appropriate continuum mechanics failure models are implemented. A plethora of damage and failure models are available to this end. The extended finite element method (XFEM) and cohesive zone models (CZM) are used extensively in this body of work and are thus presented in more detail in the following sections.

#### 3.6.1 The Extended Finite Element Method (XFEM)

The extended finite element method (XFEM) was developed as a method to computationally model crack initiation and propagation without the need for computationally expensive adaptive re-meshing of the model (Feerick et al., 2013;

Grogan et al., 2014; Sukumar et al., 2004). XFEM can be used to model stationary and moving cracks; the work presented in this thesis focuses on modelling moving cracks. Distinct from cohesive zone modelling, described in Section 0, where predefined crack paths are implemented, XFEM can predict crack initiation and propagation along solution dependant paths. Furthermore, unlike the element deletion method, crack propagation results from the splitting of elements using the XFEM method as opposed to removing elements from the mesh. XFEM is an extension of the conventional finite element code that allocates additional degrees of freedom to enriched elements in the presence of discontinuities. The failure mechanism consists of two parts: a damage initiation criterion and a damage evolution law. Damage initiation is predicted using user defined damage initiation subroutines that are defined in Chapter 4 of this thesis. Energy based damage evolution functions inbuilt in Abaqus 6.13 (DS SIMULIA, RI, USA) are used to simulate the damage evolution of the XFEM cracks.

Nodal enrichment functions are applied to the conventional nodal displacement vector for the purpose of fracture analysis in the XFEM model. Typically, the enrichments consist of a discontinuous function that represents the jump in the displacement across the crack and asymptotic functions that capture the singularity at the crack tip. The enriched displacement vector is outlined in equation 3.61. The first term in the equation is applied to all of the nodes in the model, the second term is only valid for those nodes whose shape function has been cut by the crack and the third term is used for the nodes whose shape function supports the crack tip.

$$\mathbf{u} = \sum_{I=1}^N N_I(x) [\mathbf{u}_I + H(x)\mathbf{a}_I + \sum_{\alpha=1}^4 F_{\alpha}(x)\mathbf{b}_I^{\alpha}] \quad 3.61$$

Where  $N_I(x)$  are the usual nodal shape functions,  $\mathbf{u}_I$  is the usual nodal displacement vector associated with the continuous part of the finite element solution,  $H(x)$  is the discontinuous jump function,  $\mathbf{a}_I$  is the enriched degree of freedom vector,  $F_\alpha(x)$  are the associated asymptotic crack functions and  $\mathbf{b}_I^\alpha$  is the nodal enriched degree of freedom vector. When modelling moving cracks, the crack propagation is not tied to the element boundary conditions of the mesh and the crack is free to move along any arbitrary path. The asymptotic function at the crack tip is not required as the crack propagates across entire elements at a time to avoid modelling the stress singularity, thus equation 1.36 can be reduced to:

$$\mathbf{u} = \sum_{I=1}^N N_I(x) [\mathbf{u}_I + H(x) \mathbf{a}_I] \quad 3.62$$

Phantom nodes are superimposed on the original real nodes and a combination of these phantom nodes and a predefined fracture energy release rate is used to simulate the propagation of cracks through the model. When an element is intact the phantom nodes are constrained to their corresponding real nodes. When a crack occurs, the element splits into two parts, the phantom nodes, no longer constrained to the real nodes, are free to move apart, allowing the crack to propagate.

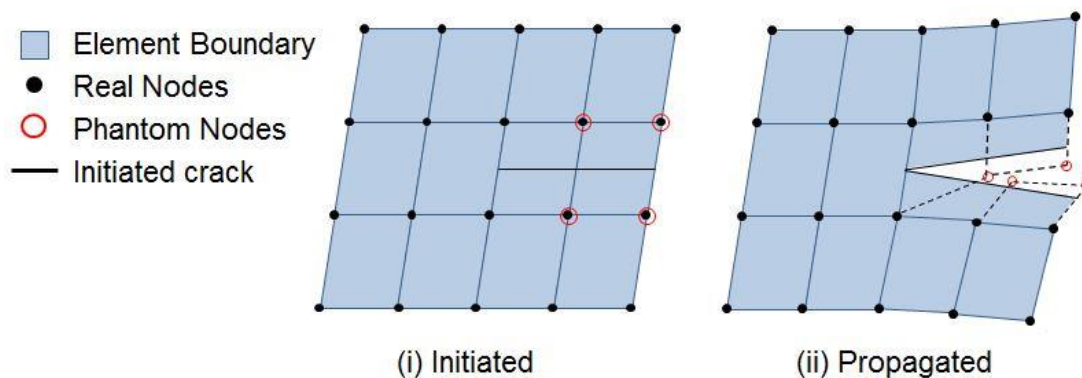


Figure 3.6: (i) Illustration of the point of damage initiation, crack has formed but phantom nodes remain in the same location as the real nodes; (ii) The critical point of energy dissipation is exceeded and the phantom and real nodes are free to move independently of one another, causing the crack to open.

As shown in Figure 3.6 above, nodes with additional degrees of freedom (phantom nodes) are coincident with the real node locations at the onset of damage. The phantom node will separate from the real node when the critical strain energy release rate at the crack tip is reached. The traction ( $T$ ) initially holds the two cracked surfaces together by equal and opposite forces. The traction degrades over the separation of the two cracked surfaces and the dissipated energy will allow the crack to grow.

Once the initiation criterion is met, damage can occur according to a predefined damage evolution law. The evolution law describes the rate at which the stiffness of the element degrades once the damage initiation criterion has been reached, described further in Chapter 4 of this thesis. The traction strength ( $T_{max}$ ) of a cracked element is defined by the critical fracture energy ( $G_c$ ) required to break the crack and the maximum separation ( $\delta_{max}$ ) of the cracked surfaces.

$$T_{max} = \frac{2G_c}{\delta_{max}} \quad 3.63$$

When implementing XFEM in the commercial software Abaqus (DS SIMULIA, RI, USA), it is important to note that crack initiation and propagation is extremely mesh sensitive and it is therefore imperative that mesh sensitivity studies be performed for every new simulation. XFEM crack initiation and subsequent propagation can result in a localised instability in the finite element model. Abaqus/Standard provides automatic mechanism for stabilising unstable quasi-static problems with the introduction of volume proportional damping in the model, which for all of the XFEM models presented in this thesis is implemented through a static stabilisation in the step function (further information regarding automatic stabilisation in Abaqus is available in the Abaqus User Documentation).

### **3.6.2 The Cohesive Zone Model (CZM)**

Cohesive zone models consider fracture in terms of a gradual separation that takes place across a cohesive zone, or crack tip, between two adjacent surfaces. The separation is resisted by cohesive tractions. Therefore, a cohesive zone does not represent any physical material, it merely describes the forces which occur when two materials are separating or being pulled apart. A traction-separation law governs the constitutive behaviour of the crack opening. Once the chosen traction-separation law is defined, no additional criteria are required for fracture to occur. As with the XFEM described above, the presence of an initial crack is not necessary. Additionally, the CZM is able to compute the toughness at the crack tip together with describing the entire fracture process including initiation and propagation. Particular to this body of work, a modified traction-separation law is proposed and used to simulate the inter-ply failure (delamination) of the laminated composites, described in detail in Chapter 4 (Máirtín et al., 2014; McGarry et al., 2014).

Consider a solid specimen with a cracked surface. Along the crack path a pair of virtual cracked surfaces is assumed. The surfaces are subjected to a separating force called cohesive traction. In the form of the principle of virtual work, the mechanical equilibrium equation considering the contribution of the cohesive tractions can be written as follows:

$$\int_V \mathbf{s} \delta \mathbf{F} dV - \int_{S_{int}} \mathbf{T}_{cz} \delta \mathbf{\Delta} dS = \int_{S_{ext}} \mathbf{T}_{ext} \delta \mathbf{u} dS \quad 3.64$$

Where,  $V$ ,  $S_{int}$ ,  $S_{ext}$  are the specimen volume, the internal/cohesive surface and the external surface of the solid, respectively.  $\mathbf{s}$  is the nominal stress tensor and  $\mathbf{F}$  denotes the deformation gradient.  $\mathbf{T}_{cz}$  and  $\mathbf{T}_{ext}$  are the cohesive and external traction vectors, respectively.  $\mathbf{\Delta}$  is the separation vector and  $\mathbf{u}$  is the displacement vector. The integration of the cohesive traction vector over the internal cohesive surface,  $\int_{S_{int}} \mathbf{T}_{cz} \delta \mathbf{\Delta} dS$ , describes the cohesive surface contributions of the crack and the cohesive zone at the front of the crack tip. In this way the evolution of the local traction-separation behaviour at the crack tip is defined by the constitutive law, analogous to conventional stress-strain relations describing the deformation behaviour of bulk materials.

Under isothermal conditions, the traction vector acting on the cohesive surfaces,  $\mathbf{T}_{cz}$ , can be derived from an interface potential  $\phi(\mathbf{\Delta})$ . Where,  $\phi(\mathbf{\Delta})$  represents the free energy density function. Thus, with the correct potential function,  $\phi$ , the constitutive equation between the cohesive traction and the relative separation can be formulated.

$$\mathbf{T}_{cz} = \frac{\partial \phi(\mathbf{\Delta})}{\partial \mathbf{\Delta}} \quad 3.65$$

The CZM can be implemented into FE analysis as mixed boundary conditions, relating to displacements at boundaries/interfaces or embedded into the FE model as cohesive elements. This work will focus on mixed boundary condition CZM, to which an in-depth background to the current literature was presented in Chapter 2. More information on the cohesive element approach can be found in the Abaqus User Documentation (DS SIMULIA, RI, USA).

### 3.7 Digital Image Correlation (DIC) theory

Digital image correlation (DIC) is an optical method used to experimentally measure deformation and strain is implemented in Chapter 6 of this thesis. The DIC technique combines image registration and tracking methods for accurate measurements of change in the images (Pan et al., 2009b, 2009a). Through a combination of the pixel intensity array subsets and extracting the deformation mapping functions that relate a series of corresponding images a correlation coefficient can be determined. DIC is based upon the calculation of this correlation coefficient.

DIC involves the tracking of the same points through a series of images take while the body is being deformed. The displacements of a single point  $Q$  are calculated by creating a square reference subset of  $(2m + 1) \times (2m + 1)$  centred around the point  $Q(x_0, y_0)$  or  $Q_0$  in the reference/undeformed configuration, see Figure 3.7. This will be used to track the points corresponding location through the series of deformed images. The cross correlation coefficient is used to calculate the degree of similarity between the reference/undeformed subset and the deformed subset. The position of the deformed subset is determined once the peak value of the correlation has been

found. The in-plane displacement vector at the point for each image can be calculated from the change in position of the subset in each image.

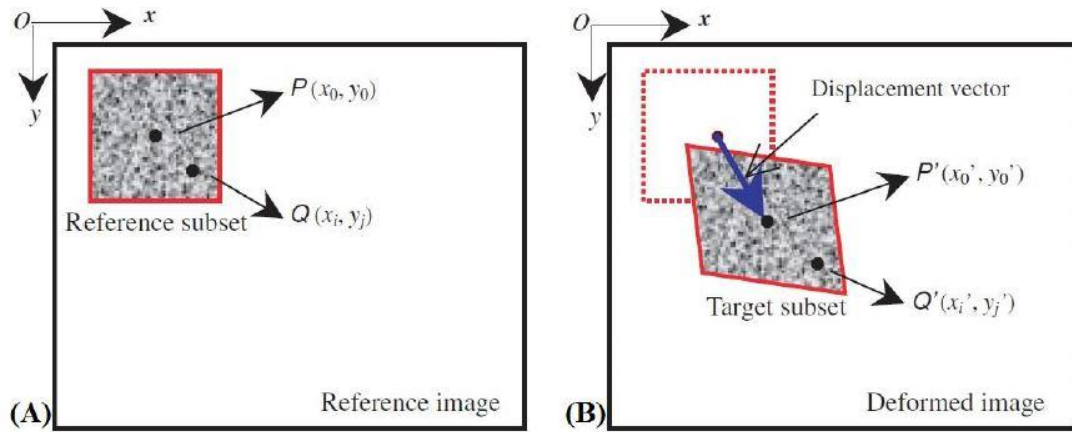


Figure 3.7: Illustration of (A) the reference subset prior to any deformation and (B) the deformed reference subset after deformation (Pan et al., 2009b)

To distinguish between displacement and deformation a second point, R, within the reference subset is also chosen. Similarly, this point is mapped from the reference configuration,  $R(x_i, y_j)$  or  $R_0$ , to the deformed,  $R'(x'_i, y'_j)$  or  $R'$ , in the series of images, according to the shape function:

$$x'_i = x_i + \xi(x_i, y_j) \quad (i, j = -M:M)$$

$$y'_i = y_i + \eta(x_i, y_j) \quad 3.66$$

Rigid body translation is assumed, where displacement of all points is the same, allowing displacements to be determined using a zero-order shape function as follows:

$$\xi_0(x_i, y_i) = u \quad \eta_0(x_i, y_i) = v \quad 3.67$$

### 3.8 References

- Crawford, R.J., 1998. *Plastics engineering*. Butterworth-Heinemann.
- Feerick, E.M., Liu, X.C., McGarry, P., 2013. Anisotropic mode-dependent damage of cortical bone using the extended finite element method (XFEM). *J. Mech. Behav. Biomed. Mater.* 20, 77–89. <https://doi.org/10.1016/j.jmbbm.2012.12.004>
- Ferguson, S.J., Visser, J.M.A., Polikeit, A., 2006. The long-term mechanical integrity of non-reinforced PEEK-OPTIMA polymer for demanding spinal applications: experimental and finite-element analysis. *Eur. Spine J.* 15, 149–56. <https://doi.org/10.1007/s00586-005-0915-5>
- Grogan, D.M., Leen, S.B., Ó Brádaigh, C.M., 2014. An XFEM-based methodology for fatigue delamination and permeability of composites. *Compos. Struct.* 107, 205–218. <https://doi.org/10.1016/j.compstruct.2013.07.050>
- Máirtín, É.Ó., Parry, G., Beltz, G.E., McGarry, J.P., 2014. Potential-based and non-potential-based cohesive zone formulations under mixed-mode separation and over-closure—Part II: Finite element applications. *J. Mech. Phys. Solids* 63, 363–385. <https://doi.org/10.1016/J.JMPS.2013.08.019>
- McGarry, J.P., Ó Máirtín, É., Parry, G., Beltz, G.E., 2014. Potential-based and non-potential-based cohesive zone formulations under mixed-mode separation and over-closure. Part I: Theoretical analysis. *J. Mech. Phys. Solids* 63, 336–362. <https://doi.org/10.1016/j.jmps.2013.08.020>
- Nettles, A.T., 1994. *Basic Mechanics of Laminated Composite Plates*. NASA Ref. publication 107.
- Pan, B., Asundi, A., Xie, H., Gao, J., 2009a. Digital image correlation using iterative least squares and pointwise least squares for displacement field and strain field measurements. *Opt. Lasers Eng.* 47, 865–874. <https://doi.org/10.1016/j.optlaseng.2008.10.014>
- Pan, B., Qian, K., Xie, H., Asundi, A., 2009b. Two-dimensional digital image correlation for in-plane displacement and strain measurement: a review. *Meas. Sci. Technol.* 20, 062001. <https://doi.org/10.1088/0957-0233/20/6/062001>
- Rae, P.J., Brown, E.N., Orlor, E.B., 2007. The mechanical properties of poly(ether-etherketone) (PEEK) with emphasis on the large compressive strain response. *Polymer (Guildf)*. 48, 598–615. <https://doi.org/10.1016/j.polymer.2006.11.032>
- Sukumar, N., Huang, Z.Y., Prévost, J.H., Suo, Z., 2004. Partition of unity enrichment for bimaterial interface cracks. *Int. J. Numer. Methods Eng.* 59, 1075–1102. <https://doi.org/10.1002/nme.902>

# Chapter 4

## Multi-Axial Damage and Failure of CF/PEEK Laminates: Experimental Testing and Computational Modelling

---

### 4.1 Introduction

To date PEEK-OPTIMA™ Ultra-Reinforced (Invibio Ltd., Thornton-Cleveleys, UK) is the only unidirectional fibre reinforced thermoplastic material that has been cleared by the FDA for implantation in humans. However, no experimental characterisation of the material has been published and the failure mechanisms have not been uncovered. This presents a significant obstacle to the development of first-generation long unidirectional carbon fibre PEEK medical implants. This chapter aims to address this key deficiency by presenting the first extensive experimental and

computational investigation of the material behaviour and failure mechanisms of PEEK-OPTIMA™ Ultra-Reinforced.

Only a limited number of fibre reinforced composite medical implants are currently available. Short fibre and weaved glass fibre reinforced composites are being used in dental implants and craniofacial implants (Aitasalo et al., 2014; Ballo et al., 2007; Piitulainen et al., 2015), and neat PEEK and unaligned short fibre reinforced PEEK materials are currently used for a limited number of spinal and trauma implants, such as vertebral cages and suture anchors (Brantigan and Steffee, 1993; Feerick et al., 2014, 2013a; Kurtz and Devine, 2007). However such neat PEEK and short carbon fibre reinforced PEEK composites are not suitable for fracture fixation devices due to low strength and stiffness (Gallagher et al., 2015). In contrast, laminated fracture fixation devices constructed from unidirectional long carbon fibre reinforced PEEK plies provide increased stiffness and strength along with tailorable anisotropic material properties. Development of first-generation orthopaedic fracture fixation devices using carbon fibre reinforced laminates potentially offer several benefits: (1) The effective anisotropic stiffness of a device can be designed to match that of the peri-prosthetic bone, reducing instances of bone resorption, which is a leading cause of metallic implant failure (Huiskes et al., 1992); (2) Unlike traditional materials, carbon fibre reinforced poly-ether-ether-ketone (PEEK) is radiolucent, thus avoiding the artefact caused by metal implants during CT imaging and X-rays and improving post-operative medical imaging (Kurtz and Devine, 2007); (3) The high strength to weight ratio of laminated devices will result in lighter and thinner implants compared to metallic equivalents, resulting in considerable improvement of patient functionality and comfort; (4) Fibre reinforced composites implants will not induce

patient pain and discomfort in cold weather, in contrast to metallic implants (Der Tavitian et al., 2002; Lanzetta and Foucher, 1995).

Identification of the complex failure mechanisms of laminated composites presents a significant challenge to the design and development of first-generation fibre reinforced laminated medical implants. A comprehensive characterisation of such failure mechanisms is particularly important for orthopaedic fracture fixation devices, given the complex multi-axial physiological loading environment post-implantation. Depending on the mode of loading, a combination of fibre failure, matrix failure, ply debonding and/or plasticity may occur. A number of well-established damage models have been proposed for failure of fibre reinforced laminates that take into account fibre and matrix failure in compression and tension, including Hashin (Hashin, 1980a), Tsai-Wu (Tsai and Wu, 1971) and Puck (Puck and Schürmann, 2002). Recent finite element (FE) implementations incorporate the extended finite element method (XFEM) to predict crack propagation in conjunction with Hashin-type damage initiation criteria (Ahmad et al., 2014; Duarte et al., 2017; Feerick et al., 2013b). These modelling approaches focus solely on intra-laminar failure and do not consider inter-laminar delamination. Several experimental studies have shown that certain loading modes result in failure due to delamination, most notably tensile and compressive testing of laminates containing holes or arbitrarily angled plies (Lessard and Chang, 1991; O'Brien, 1982; Wisnom and Hallett, 2009). Various computational methodologies that include cohesive zone models (CZM) at the interface between the plies have been presented to predict inter-laminar failure (Heidari-Rarani et al., 2013; Turon et al., 2010; Zhao et al., 2014). Most recently, models have been proposed that implement both inter- and intra- laminar failure in a combined XFEM/CZM modelling methodology (Bienias et al., 2012; Bouhala et al., 2015; Grogan et al.,

2015a; Viguera et al., 2015). Finally inelastic permanent plastic deformation has been observed in several experimental studies of fibre reinforced laminates (Soden et al., 2004; Van Paepegem et al., 2006). However, the plastic deformation of fibre reinforced laminates has seldom been considered computationally. Vogler et al. (Vogler et al., 2013) identified the need for a constitutive model that is capable of predicting non-linearities under multi-axial and tri-axial stress states. van der Meer et al. (van der Meer et al., 2011) has presented an implicit XFEM\CZM methodology that includes plasticity but only considers the off-axis non-linear responses in one loading direction and does not make reference to the anisotropic nature of the plasticity response of fibre reinforced laminates. In the current study a combined extended finite element method and cohesive zone model (XFEM/CZM) is developed to simulate the formation of random 3D crack paths, the growth inter-ply delaminations and anisotropic plasticity of the fibre reinforced laminates.

The current chapter presents the first comprehensive experimental characterisation of the mechanical behaviour and failure mechanisms of a medical grade unidirectional carbon fibre reinforced PEEK material, PEEK-OPTIMA™ Ultra-Reinforced, hereafter referred to as *CF/PEEK*. Based on experimental data, a computation framework is developed so that material failure due to intra-laminar cracking, inter-laminar delamination, and anisotropic plasticity is predicted. Finally, a preliminary device design study is carried out to demonstrate the potential of the computational framework, developed in this chapter, as a design tool for future laminated. Such comprehensive experimental data and multi-mode damage modelling is essential for the development of first-generation laminated fracture fixation devices due to the complex multi-axial physiological loading environment encountered post-implantation. The chapter is structured as follows: Section 4.2 - Experimental

methods; Section 4.3 - Computational model development; Section 4.4 - Experimental results and model calibration; Section 4.5 - Analysis of failure modes and model validation; and Section 6 - Preliminary laminated device design.

### 4.2 Experimental methods

*CF/PEEK* is a medical grade poly-ether-ether-ketone (PEEK) polymer reinforced with continuous unidirectional carbon fibres, with a 62% fibre volume fraction. As mentioned in the introduction, to date no experimental data has been published for *CF/PEEK*. In order to determine the orthotropic moduli and failure strengths of the *CF/PEEK* material, uniaxial tension and compression tests were performed on  $0^\circ$ ,  $90^\circ$  and  $\pm 45^\circ$  specimens. All the experiments performed in this study comply with the ASTM or ISO standards. The authors are not aware of other works that provide such extensive experimental testings.

#### 4.2.1 Specimen preparation

*CF/PEEK* prepreg, which has a thickness of 0.2mm, was consolidated into a number of laminated panels with angled plies according to ASTM D5687. Compression moulding was used to consolidate the  $\pm 45^\circ$  laminates, while the  $0^\circ$  and  $90^\circ$  laminated panels were consolidated in an autoclave. The resulting thickness of the laminated plates was dependent on the number of plies in the layup.

Test specimens were cut from the laminated panels using a composite cutting machine with a diamond-coated cutting blade. The specimen geometries were in accordance with their respective test standards (Tensile: ASTM D3039-07 (ASTM International, 2014), Compression: ASTM D6641-14 (ASTM International, 2012), Flexure: ISO 14125-98 (ISO, 1998), In-Plane Shear: ASTM D3518-13 (ASTM International, 2013), Mode I and II fracture toughness tests: EN6033-95 and

EN6034-95 (AECMA Standard, 1995a, 1995b). The exact specimen dimensions for each experiment are listed in Table 4A1 in Appendix 4A. For each mode of loading 5 test specimens were tested in accordance with the standards, in total 75 test specimens were prepared.

For the tension, compression and in-plane-strain experiments, cross gauges were attached to the specimens to measure strains in the longitudinal and transverse directions. In accordance with the standards a linear gauge was also attached to the opposite face of the specimen to simultaneously measure the longitudinal strain on both faces and allow for detection of any bending that may occur during testing. A camera system was used to measure deformation in the flexure tests (1.31 MPa, 25 fps; uEye, IDS, Obersulm, Germany; videoXtens software, Zwick, Ulm, Germany).

### 4.2.2 Experimental testing

The loading rates and machines used for each experiment are next presented. The 0° tensile specimens and the in-plane-shear  $\pm 45^\circ$  specimens were monotonically loaded in a Denison Meyer T.24.B.4 machine (with a 500kN load cell). The 90° tensile tests were performed on a 4467 Screw Driven Instron (30kN load cell). A displacement rate of 2mm/min was implemented for all tests. The four-point-bend flexure tests were also carried out on a 4467 Screw Driven Instron at a rate of 2mm/min. All the compression specimens were mounted in a combined loading compression test fixture and loaded to failure on a Zwick Z250 testing machine (with a 250kN load cell) at a nominal rate of 1.3mm/min. The fracture toughness tests were performed on a Zwick Z010 testing machine (10kN load cell) with crosshead displacement rates of 10mm/min and 1mm/min for the  $G_{ic}$  and  $G_{iic}$  tests, respectively. The technical drawings for each of the experimental specimens are presented in Appendix 4C of this thesis.

### 4.3 Computational model development

Due to the complex multi-axial loading environment encountered by fracture fixation devices a predictive modelling framework must be developed that incorporates inter-laminate failure, intra-laminate failure and laminate plasticity. As will be shown in the experimental results in section 4.4 and 4.5 of this chapter, a combination of all three failure mechanisms may occur in *CF/PEEK*. Furthermore, a study of neat PEEK (Rae et al., 2007) shows that the matrix material exhibits inelastic plastic material behaviour under compressive and tensile loading. In Section 4.3.1 we outline a plasticity formulation to simulate permanent anisotropic deformation of the unidirectional fibre reinforced material. In Section 4.3.2 we outline the mixed mode traction separation relations governing delamination in the laminates. Finally, in Section 4.3.3 the Hashin-type intra-laminar damage initiation criteria are outlined. To the best of the author's knowledge the modelling framework presents the first combination of anisotropic plastic laminar deformation, mode dependent inter-laminar failure and intra-laminar failure.

#### 4.3.1 Simulating anisotropic plasticity of composite structures

Previous models have implemented isotropic plasticity in their computational damage model but the experimental results in this study clearly point to an anisotropic inelastic plastic response of the laminates. The yield behaviour of the laminate is simulated using Hill's potential function. The yield criterion is expressed below in terms of Cauchy stress components.

$$f(\sigma) = \left( \sqrt{F(\sigma_{22} - \sigma_{33})^2 + G(\sigma_{33} - \sigma_{11})^2 + H(\sigma_{11} - \sigma_{22})^2 + 2L\sigma_{23}^2 + 2M\sigma_{31}^2 + 2N\sigma_{12}^2} \right) - \sigma_{yield} = 0 \quad 4.1$$

where,  $F$ ,  $G$ ,  $H$ ,  $L$ ,  $M$ , and  $N$  are constants obtained from experimental testing of the material. They are defined as follows:

$$F = \frac{(\sigma_{yield})^2}{2} \left( \frac{1}{\sigma_{22}^2} + \frac{1}{\sigma_{33}^2} - \frac{1}{\sigma_{11}^2} \right) = \frac{1}{2} \left( \frac{1}{R_{22}^2} + \frac{1}{R_{33}^2} - \frac{1}{R_{11}^2} \right) \quad 4.2$$

$$G = \frac{(\sigma_{yield})^2}{2} \left( \frac{1}{\sigma_{33}^2} + \frac{1}{\sigma_{11}^2} - \frac{1}{\sigma_{22}^2} \right) = \frac{1}{2} \left( \frac{1}{R_{33}^2} + \frac{1}{R_{11}^2} - \frac{1}{R_{22}^2} \right) \quad 4.3$$

$$H = \frac{(\sigma_{yield})^2}{2} \left( \frac{1}{\sigma_{11}^2} + \frac{1}{\sigma_{22}^2} - \frac{1}{\sigma_{33}^2} \right) = \frac{1}{2} \left( \frac{1}{R_{11}^2} + \frac{1}{R_{22}^2} - \frac{1}{R_{33}^2} \right) \quad 4.4$$

$$L = \frac{3}{2} \left( \frac{\tau_{yield}}{\sigma_{23}} \right)^2 = \frac{3}{2R_{23}^2} \quad 4.5$$

$$M = \frac{3}{2} \left( \frac{\tau_{yield}}{\sigma_{13}} \right)^2 = \frac{3}{2R_{13}^2} \quad 4.6$$

$$N = \frac{3}{2} \left( \frac{\tau_{yield}}{\sigma_{12}} \right)^2 = \frac{3}{2R_{12}^2} \quad 4.7$$

where each  $\sigma_{ij}$  is the measured yield stress value under a uniaxial load in the  $ij$  direction;  $\sigma_{yield}$  is the reference yield stress;  $R_{ij}$  are the anisotropic yield stress ratios and  $\tau_{yield} = \frac{\sigma_{yield}}{\sqrt{3}}$ . A parameter study is carried out to determine each of the anisotropic yield ratios using the results of the experimental in-plane shear test and the uniaxial tension and compression tests performed on the  $0^\circ$  and  $90^\circ$  laminates.

### 4.3.2 Simulating inter-laminar delamination

The results of the  $G_{iC}$  and  $G_{iiC}$  fracture toughness tests presented in Section 4.4 provide motivation for a mode dependent CZM formulation. Inter-laminar failure is governed by the traction separation relations defined in Eqns. 4.8-4.11 below. Delaminations can occur in the laminate if the interface traction exceeds a critical value of  $\sigma_{max}$  in mode I and  $\tau_{max}$  in mode II.

when  $\Delta_n > 0$ ,

$$T_n(\Delta_n, \Delta_t) = \sigma_{max} \exp(1) \left( \frac{\Delta_n}{\delta_n} \right) \exp \left( - \sqrt{\frac{\Delta_n^2}{\delta_n^2} + \frac{\Delta_t^2}{\delta_t^2}} \right) \quad 4.8$$

$$T_t(\Delta_n, \Delta_t) = \tau_{max} \exp(1) \left( \frac{\Delta_t}{\delta_t} \right) \exp \left( - \sqrt{\frac{\Delta_n^2}{\delta_n^2} + \frac{\Delta_t^2}{\delta_t^2}} \right) \quad 4.9$$

when  $\Delta_n < 0$ ,

$$T_n(\Delta_n, \Delta_t) = \sigma_{max} \exp(1) \left( \frac{\Delta_n}{\delta_n} \right) \exp \left( - \sqrt{\frac{\Delta_n^2}{\delta_n^2}} \right) \quad 4.10$$

$$T_t(\Delta_n, \Delta_t) = \tau_{max} \exp(1) \left( \frac{\Delta_t}{\delta_t} \right) \exp \left( - \sqrt{\frac{\Delta_t^2}{\delta_t^2}} \right) \quad 4.11$$

where,  $\sigma_{max}$  is the maximum normal traction (referred to hereafter as the “mode I interface strength”),  $\tau_{max}$  is the maximum tangential traction (referred to hereafter as the “mode II interface strength”),  $\Delta_n$  and  $\Delta_t$  are the normal and tangential components of the interface separation vector  $\underline{\Delta}$ , respectively and  $\delta_n$  and  $\delta_t$  are the normal and tangential interface characteristic lengths, respectively (McGarry et al., 2014). The normal (mode I) work of separation is given as  $\phi_n = \sigma_{max} \Delta_n \exp(1)$  and the tangential (mode II) work of separation is given as  $\phi_t = \tau_{max} \Delta_t \exp(1)$ .

Two sets of normal and tangential traction equations are presented. When the model undergoes normal tensile separation Eqns. 4.8 and 4.9 are implemented, where both the normal and the tangential interface tractions,  $T_n$  and  $T_t$ , are coupled by the effective separation parameter  $(\Delta_n^2/\delta_n^2 + \Delta_t^2/\delta_t^2)$ . Eqns. 4.10 and 4.11 prevent

overclosure during normal compression of the interface, while allowing shear delamination. This CZM is a modified version of the SMC model developed by McGarry *et al.* (McGarry et al., 2014) and a Fortran code is written to implement the CZM through a user defined interface subroutine (UINTER). A parametric study was performed to determine the required element length to provide a converged solution of crack propagation rate and fracture toughness. Convergence is achieved using an element length of 33 $\mu\text{m}$ .

### 4.3.3 Simulation intra-laminar failure

A multi-axial failure criterion with a continuum representation of intra-laminar failure that may result from fibre rupture and/or matrix cracking is presented. Here two failure mechanisms are considered when modelling the intra-laminar failure of fibre reinforced laminates, failure of the fibres and failure of the matrix material. The Hashin-type damage initiation criteria (Hashin, 1980b) are outlined in Eqs. 4.12-4.15 below. The equations describe both fibre ( $f^f$ ) and matrix ( $f^m$ ) failure of the laminate in tension ( $f_T$ ) and compression ( $f_C$ ). Once any of the failure criteria reaches a value of 1, damage is initiated for that criterion and a crack will occur. The four anisotropic damage initiation criteria used in this model are described as follows:

$$f_T^m = \left( \frac{(\sigma_{22} + \sigma_{33})^2}{Y_T^2} \right) + \left( \frac{\sigma_{23}^2 - \sigma_{22}\sigma_{33}}{S^2} \right) + \left( \frac{\sigma_{12}^2 - \sigma_{13}^2}{S^2} \right) \quad 4.12$$

$$f_C^m = \left[ \left( \frac{Y_C}{2S_{23}} \right)^2 - 1 \right] \left( \frac{\sigma_{22} + \sigma_{33}}{Y_C} \right) + \frac{(\sigma_{22} + \sigma_{33})^2}{4S^2} + \frac{\sigma_{23}^2 - \sigma_{22}\sigma_{33}}{S^2} + \frac{\sigma_{12}^2 + \sigma_{13}^2}{S^2} \quad 4.13$$

$$f_T^f = \left( \frac{\sigma_{11}}{X_T} \right)^2 + \left( \frac{\sigma_{12}}{S} \right)^2 + \left( \frac{\sigma_{13}}{S} \right)^2 \quad 4.14$$

$$f_C^f = \left( \frac{\sigma_{11}}{X_C} \right)^2 + \left( \frac{\sigma_{12}}{S} \right)^2 + \left( \frac{\sigma_{13}}{S} \right)^2 \quad 4.15$$

where,  $X_T$  and  $X_C$  are the longitudinal tensile and compressive strengths, respectively, and  $Y_T$  and  $Y_C$  are the transverse tensile and compressive strengths, respectively and  $S$  is the shear strength of the laminate. A Fortran code is written to implement the fibre and matrix failure criteria through a user defined damage initiation subroutine (UDMGINI). Following initiation, XFEM (Feerick et al., 2013b) is used to simulate the propagation of the crack through the laminate. An energy-based damage evolution parameter is chosen, the mode I fracture toughness is implemented as the evolution parameter for tensile fibre failures while the mode II fracture toughness is implemented for the other three intra-laminar failure criteria. Once the prescribed fracture criterion has been reached the real nodes and corresponding phantom nodes will separate and allow the crack to propagate.

### 4.4 Experimental results and computational model calibration

The following section presents the results for the experimental tests that are performed on the *CF/PEEK* laminates that are used to calibrate the computational damage and failure model. The experiments that are used to validate that computational model (i.e. the flexure tests and the 45° compression test) are presented at the end of this section. Importantly experimental observations are used to develop and calibrate our computational model. Compression tests are performed on 90° laminates to measure the transverse ultimate compressive strength. Tensile tests are performed on 0° and 90° laminates in order to determine the longitudinal modulus and ultimate tensile strength and the transverse modulus and ultimate tensile strength, respectively. The mode I and mode II inter-laminar strengths are determined through fracture toughness test carried out on a 0° laminate manufactured with a pre-crack. Compression tests are also carried out on 0° laminates to measure the

longitudinal ultimate compressive strengths. Flexure tests are performed on  $0^\circ$ ,  $90^\circ$  and  $\pm 45^\circ$  laminates and compression tests are performed on  $\pm 45^\circ$  laminates. In-plane shear tests performed on  $\pm 45^\circ$  are used to measure the shear modulus and shear strength of the *CF/PEEK* composite material. All of the tests are modelled in the commercial finite element software Abaqus 6.13 (SIMULIA, Providence, RI, USA) and calibrated using the results of the experiments. General purpose linear eight noded brick elements (C3D8) are implemented for all FE models. Mesh sensitivity studies were carried out for each simulation as the XFEM crack initiation is extremely mesh sensitive. Convergence was found using one element through the thickness of each ply and an element length of approximately 0.5mm.

### **Experimental measurement of elastic constants and failure strengths and fracture toughness**

The orthotropic properties of unidirectional *CF/PEEK* that are determined experimentally through tensile tests performed on  $0^\circ$ ,  $90^\circ$  and  $\pm 45^\circ$  specimens are presented in Table 4.1 below.

Table 4.1: CF/PEEK tensile material properties (mean  $\pm$  standard deviation).

$E_{11}$ (GPa)	$175.37 \pm 5.61$
$E_{22}$ (GPa)	$9.40 \pm 0.16$
$G_{12}$ (GPa)	$5.21 \pm 0.19$
$\nu_{12}$	$0.38 \pm 0.04$

The measured longitudinal modulus  $E_{11}$ , i.e. the modulus in fibre direction, is an order of magnitude greater than the transverse modulus  $E_{22}$ , i.e the modulus in the matrix direction. The longitudinal modulus is slightly higher than typical values for non-medical grades of carbon fibre reinforced PEEK laminates, which are reported to

be in the range of 135 – 155 GPa. Similarly, the measured Poisson’s ratio value of 0.38 is higher than other reported values, 0.32-0.34. However, both the transverse modulus and the shear modulus for *CF/PEEK* are in good agreement with the values reported for other grades of *CF/PEEK* laminates (Grogan et al., 2015b; Li et al., 2002).

The failure strengths for *CF/PEEK* are given in Table 4.2, where  $X_T$  and  $X_C$  are the longitudinal tensile and compressive strengths, respectively,  $Y_T$  and  $Y_C$  are the transverse tensile and compressive strengths, respectively and  $S$  is the shear strength.

Table 4.2: *CF/PEEK* tensile, compressive and shear strengths and mode I and mode II fracture toughness (mean  $\pm$  standard deviation).

$X_T$ (MPa)	2882.09 $\pm$ 98.25
$Y_T$ (MPa)	49.60 $\pm$ 3.92
$X_C$ (MPa)	1182.26 $\pm$ 67.99
$Y_C$ (MPa)	185.69 $\pm$ 8.92
$S$ (MPa)	95.83 $\pm$ 7.44
$G_{ic}$ (kJ/m <sup>2</sup> )	1.44 $\pm$ 0.10
$G_{iic}$ (kJ/m <sup>2</sup> )	1.01 $\pm$ 0.03

The measured longitudinal tensile strength,  $X_T$ , of 2882 MPa is greater than values for other grade of unidirectional *CF/PEEK* reported in the literature (2068 MPa (Li et al., 2002)). Both the transverse tensile strength,  $Y_T$ , and the transverse compressive strength,  $Y_C$ , 50 MPa and 213 MPa respectively, are similar to other grades of *CF/PEEK* materials (Grogan et al., 2015b) but at the lower end of the range of transverse strengths for other carbon fibre reinforced polymers (O’Higgins et al., 2008). It should be noted that there is no polymer sizing on the fibres in the

*CF/PEEK* material tested, as there is no known sizing that is fully compatible with PEEK. Sizing is a coating added to the carbon fibres to improve fibre-matrix interface strength (Pozegic et al., 2016), which would significantly increase the laminates transverse strengths. The shear strength,  $S$ , of *CF/PEEK*, measured as 96 MPa falls within the range of values reported for other grades of *CF/PEEK* unidirectional laminates (Grogan et al., 2015b; Li et al., 2002).

### *Analysis of compressive failure of 90° laminates*

Experimental results and computational analysis for compression tests performed on 90° laminates are presented in Figure 4.1. The experimental and computational stress-strain diagrams are shown in Figure 4.1(A).

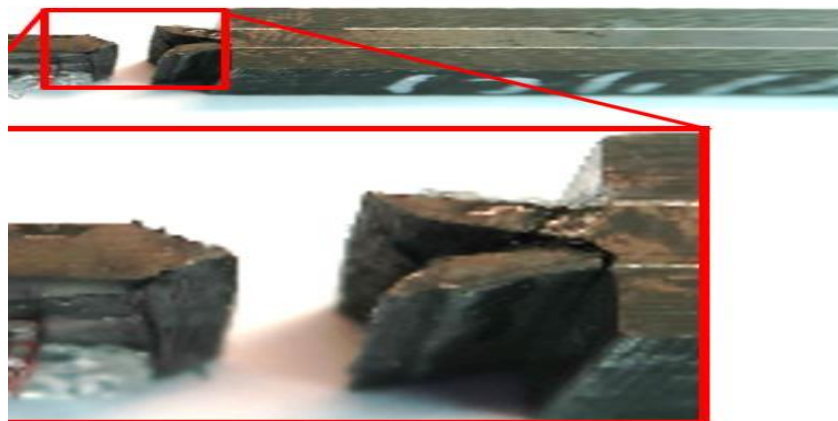
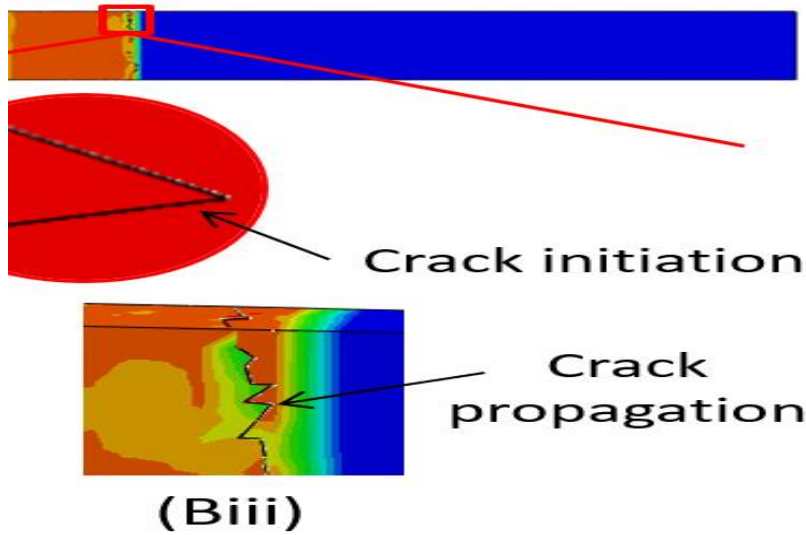
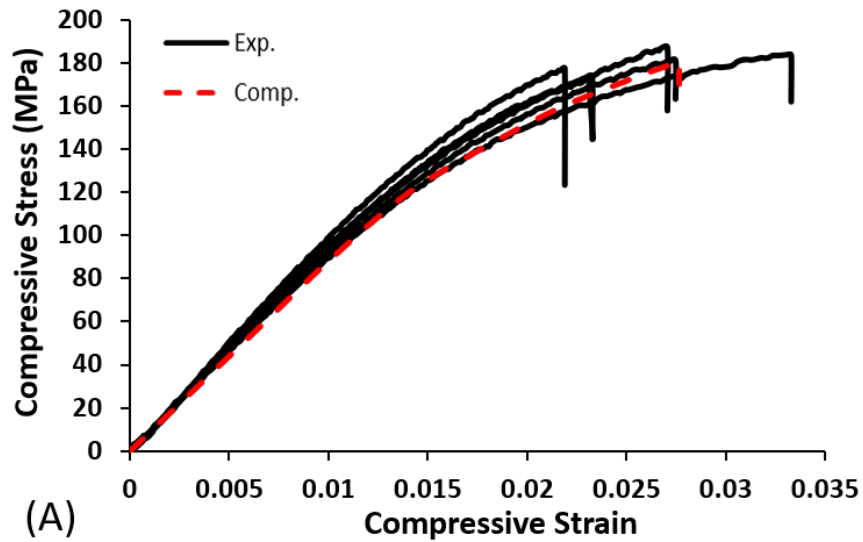


Figure 4.1: (A) Experimental and computational nominal stress - nominal strain curves for compression of  $90^\circ$  laminates. (Bi) Von Mises stress ( $\sigma$ ) distribution in the  $90^\circ$  laminate at failure. (Bii) Predicted crack at the point of initiation. (Biii) Propagated crack at the point of failure. (C) Experimental image of a failed specimen highlighting shear crack failure surfaces.

The experimental stress-strain curves exhibit an initial linear-elastic region up to a yield stress of 110 MPa. Following the initial yield point the specimens undergo strain hardening up to the ultimate compressive failure stress. Our computational model provides an accurate prediction of the initial elastic behaviour, post yield hardening and ultimate failure. The computed stress (176.6 MPa) and strain (0.028) at failure are similar to the experimentally observed values of  $185.69 \pm 8.92$  MPa and  $0.0266 \pm 0.0044$ , respectively. This suggests that the transverse compressive strength,  $Y_C$ , represents a ductile failure of the matrix.

The computed compressive failure mode of the  $90^\circ$  laminate is shown in Figure 4.1 (B). The crack initiates on the x-z face of the specimen. As shown in the inset of Figure 4.1 (Bii) ‘V-shaped’ shear cracks are computed. The cracks propagate through the laminate in the y-direction until ultimate failure, as shown in Figure 4.1 (Biii). The  $\pm 45^\circ$  shear cracks on the xz-plane are observed experimentally, as shown in Figure 4.1 (C). The crack propagation through the specimen in the y-direction is also evident. The predicted stress concentrations at the grips in the finite element simulations captures the experimental stress concentrations, and thus the experimental cracks are correctly predicted, even when close to the grips.

#### **Analysis of tensile failure of 0 and 90 laminates**

The experimental results and computational predictions for tensile tests performed on  $0^\circ$  and  $90^\circ$  laminates are presented in Figure 4.2 and Figure 4.3 below, respectively.

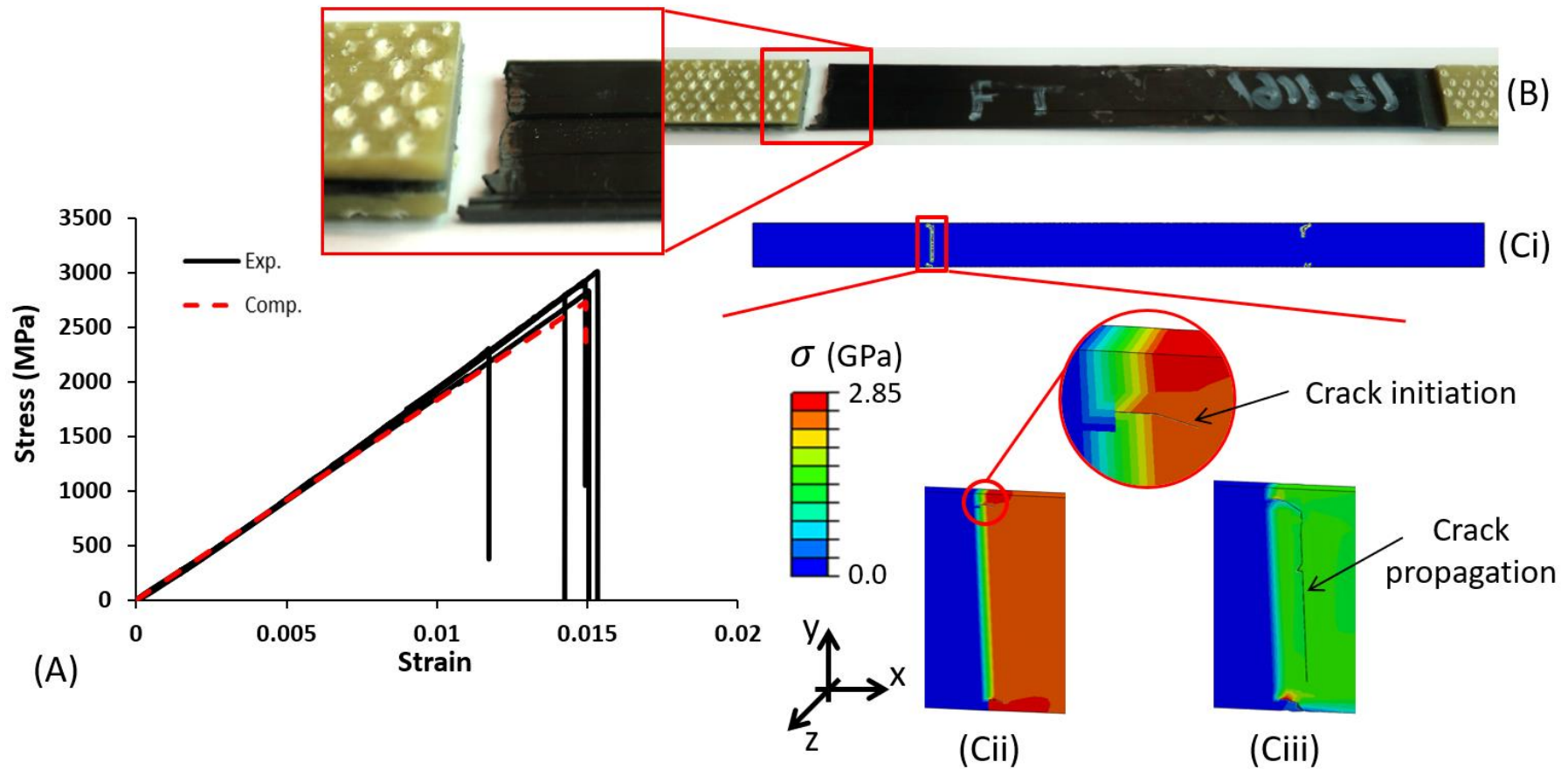


Figure 4.2: (A) Experimental and computational nominal stress - nominal strain curves for the tensile tests of  $0^\circ$  laminates. (B) Experimental image of a  $0^\circ$  tensile specimen. (Ci) Predicted von Mises stress ( $\sigma$ ) distribution in a  $0^\circ$  laminate. (Cii) Von Mises stress ( $\sigma$ ) distribution in the  $0^\circ$  laminate at the point of crack initiation. (Ciii) Propagated crack in the  $0^\circ$  laminate at failure.

Figure 4.2(A) shows the stress-strain diagram for the 0° tensile test. A linear elastic regime is observed up to the point of longitudinal tensile strength,  $X_T$ , of  $2765.14 \pm 274.98$  MPa at a strain of  $0.012 \pm 0.001$ . The computational model provides a good prediction of the experimental stress-strain behaviour. The absence of plastic deformation is correctly predicted by the computational model due to the high value of  $R_{11}$  in the Hill model, resulting in ultimate longitudinal tensile failure before yielding is predicted. This demonstrates the importance of anisotropic plasticity when modelling fibre reinforced laminates because, if for example the 90° Hill ratio,  $R_{22} = 1$ , was applied to the 0° laminate the model would predict nonlinear behaviour in the 0° tension prior to ultimate failure, which is not observed experimentally. The crack predicted by the computational model initiates at 45° due to stress concentrations caused by the constraint of the tabs, shown in Figure 4.2(Cii). Following initiation, the crack is computed to ‘kink’ and propagate through the laminate in the y-direction (Figure 4.2(Ciii)). Comparing with the experimental image (Figure 4.2(B)) it is clear that the computational model predicts the propagated crack very accurately.

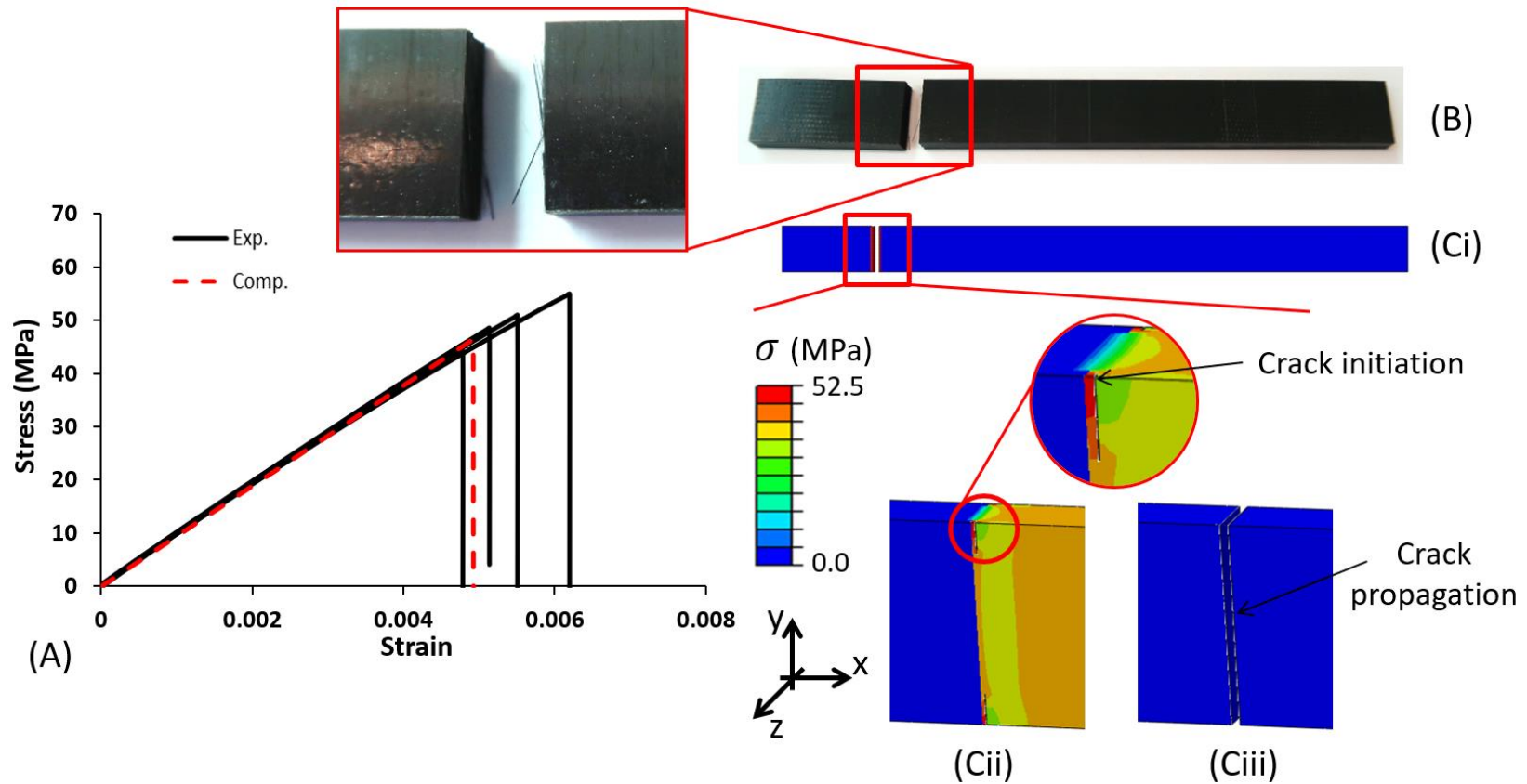


Figure 4.3: (A) Experimental and computational nominal stress - nominal strain curves for the tensile tests of 90° laminates. (B) Experimental image of a 90° specimen following failure. (Ci) Predicted von Mises stress ( $\sigma$ ) distribution in the 90° laminate at failure. (Cii) Predicted stress state following crack initiation. (Ciii) Predicted crack propagation at ultimate failure.

Figure 4.3(C) shows the stress-strain diagram for tensile testing of 90° laminates. The experimental results exhibit linear elastic behaviour up to the transverse tensile strength,  $Y_T$ , of  $49.60 \pm 3.95$  MPa at a strain of  $0.0054 \pm 0.0005$ . Unlike the compressive testing of 90° laminates, shown in Figure 4.3(A) above, plasticity is not observed in the tensile test. This is correctly predicted by the computational model, in which the transverse failure strength,  $Y_T$ , is reached before plastic yielding can occur. This result suggests that failure during transverse tensile tests, characterised by  $Y_T$ , is due to debonding of the fibre-matrix interface rather than plastic yielding and ductile failure of the matrix. In the experimental image (Figure 4.3 (B)) there is no evidence of fibrillation on the crack surface further supporting the proposed failure mechanism of fibre-matrix debonding. Figure 4.3(Ci) shows the predicted stress distribution at failure in the computational simulation. The model accurately predicts the crack location and the propagation through the laminate in the y-direction.

#### **Analysis of the $G_{Ic}$ and $G_{IIc}$ fracture toughness tests**

Results for the mode I (Figure 4.4) and the mode II (Figure 4.5) fracture toughness tests are presented.

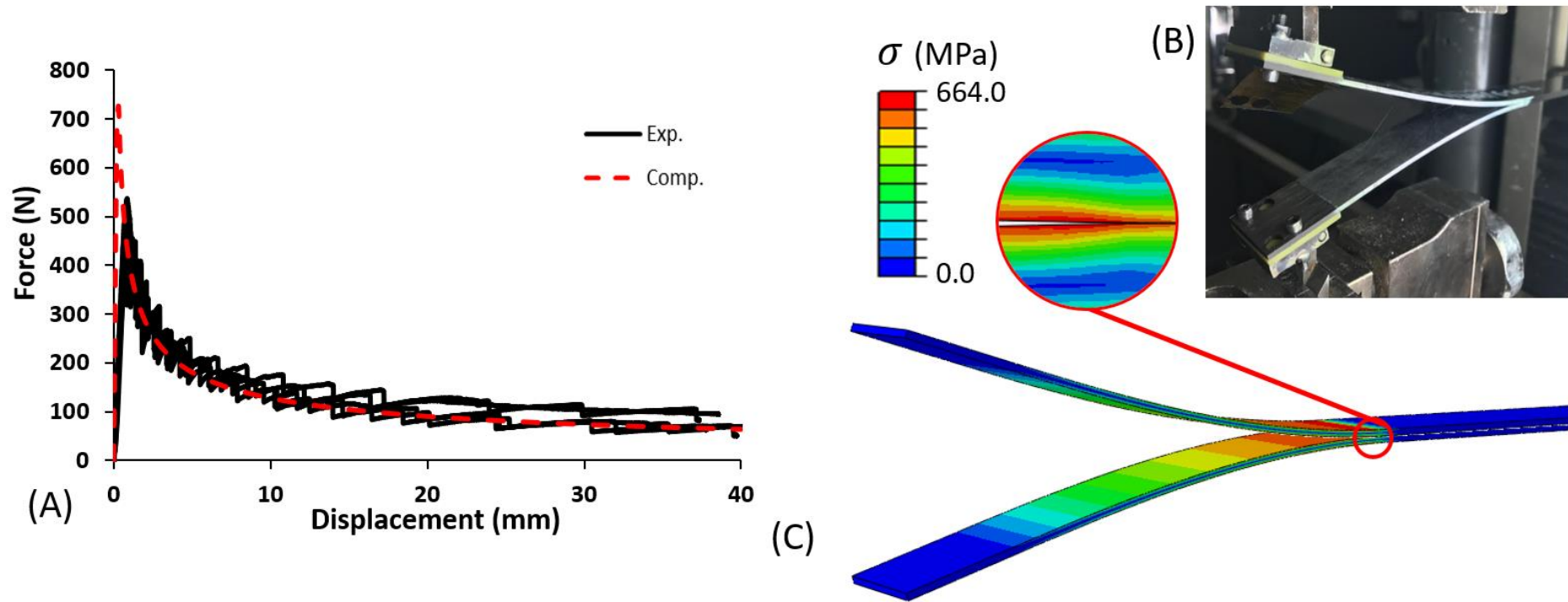


Figure 4.4: (A) Experimental and predicted force-displacement curves for mode I fracture toughness tests. (B) Experimental image of the mode I crack propagation. (C) Predicted crack propagation and von Mises stress ( $\sigma$ ) distribution in the mode I fracture toughness tests.

Figure 4.4(A) shows the measured force-displacement curves for the mode I fracture toughness tests, from which a  $G_{ic}$  value of  $1299.13 \pm 92.77 \text{ J/m}^2$  is determined. Computational simulation of this mode I fracture tests accurately predicts the force-displacement behaviour and  $G_{ic}$  value when a cohesive zone mode I strength of  $\sigma_{max} = 49.5 \text{ MPa}$  is used with a characteristic interface length of  $\Delta_n = 10 \text{ }\mu\text{m}$ , so that  $\phi_n = 1341 \text{ J/m}^2$ . A parametric investigation of the influence of cohesive zone model parameters and inter-laminar delamination is presented in Appendix B. The CZM simulation of delamination propagation provides an accurate prediction of the measured force-displacement relationship with an initial drop in force followed by a plateau during steady state crack propagation. The experimental results reveal that a propagated crack of 100mm is achieved for an applied crosshead displacement of  $38.77 \pm 1.34 \text{ mm}$ . Such crack propagation is accurately predicted by the computational model with a crack of 100mm computed at an applied end displacement of 37.6mm. Figure 4.4(B) shows an experimentally deformed specimen at a crack propagation of 100mm. Figure 4.4(C) shows the stress distribution in the computed deformed specimen. Finally, it is interesting to note that the calibrated mode I inter-laminar strength,  $\sigma_{max}$ , is equal in value to the transverse tensile strength,  $Y_T$ , measure in tensile tests of  $90^\circ$  laminates. In both cases the failure stress is lower than the calibrated yield stress (110 MPa), see Figure 4.1(A), suggesting that fibre-matrix debonding is the underlying failure mechanism in both mode I inter-laminar delamination and intra-laminar transverse tensile failure.

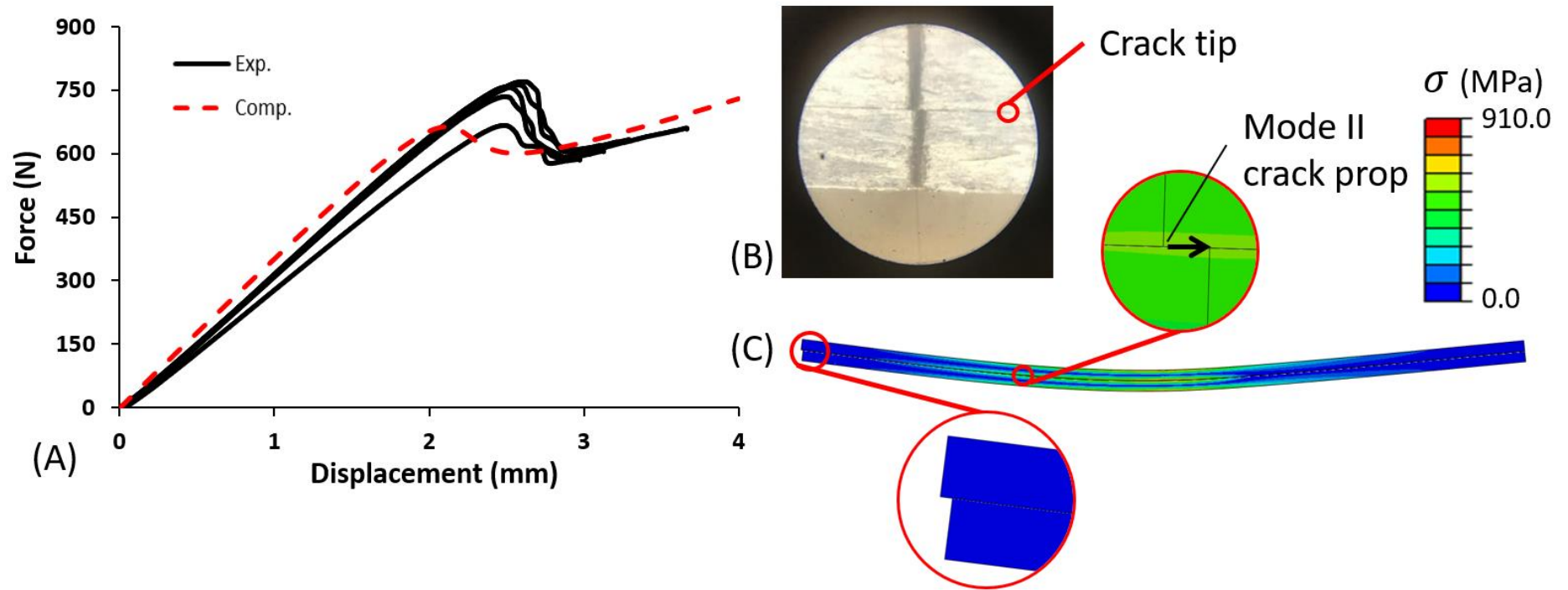


Figure 4.5: (A) Experimental and predicted force-displacement curves for mode II fracture toughness tests. (B) Experimental image of the mode II crack propagation. (C) Predicted crack propagation and von Mises stress ( $\sigma$ ) distribution in the mode II fracture toughness tests.

Figure 4.5(A) shows the experimental force-displacement curves for the mode II fracture toughness tests. The experimental  $G_{iic}$  is determined as  $1007.01 \pm 71.43 J/m^2$ . Computational simulation of this mode II fracture tests accurately predicts the  $G_{iic}$  value when a cohesive zone mode II strength of  $\tau_{max} = 37$  MPa is used with a characteristic interface length of  $\Delta_t = 10 \mu m$ , so that  $\phi_t = 1003 J/m^2$  (results of the parametric investigation are presented in Appendix B). These values give a reasonable replication of the experimentally observed force-displacement curve (Figure 4.5(A)) with an initial linear region followed by a drop in the force as the crack propagation begins. Figure 4.5(B) shows an experimental image of the mode II crack viewed through a microscope. The tip of the crack is highlighted. The vertical line (thick black line) used to mark the tip of the crack prior to testing is visible. Crack propagation is taken to initiate once a discontinuity appears in this marker. Figure 4.5(C) shows the predicted stress distribution in the  $G_{iic}$  fracture toughness test. The propagation of the mode II crack is highlighted.

#### **Analysis of the compression failure of 0° laminates**

The results for the compression tests performed on the 0° laminates are outlined in Figure 4.6.

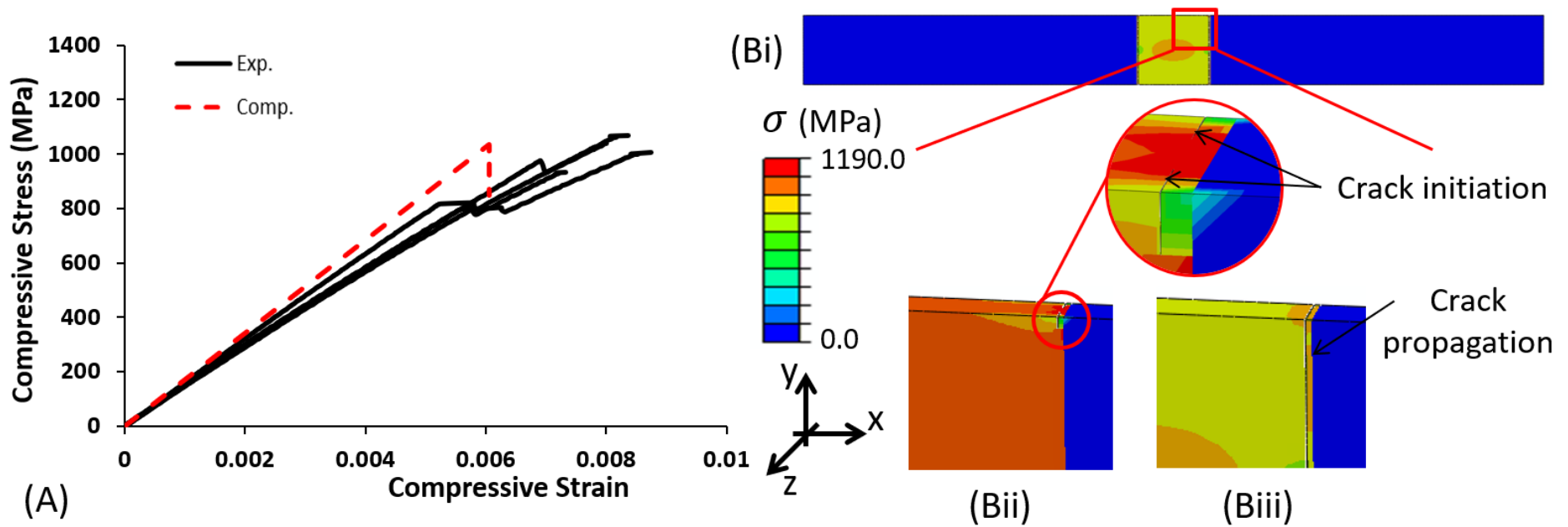


Figure 4.6: (A) Experimental and computational nominal stress - nominal strain curves for the compression of  $0^\circ$  laminates. (Bi) Predicted von Mises ( $\sigma$ ) stress distribution in failed  $0^\circ$  laminate. (Bii) Stress distribution at the point of crack initiation. (Biii) Von Mises stress ( $\sigma$ ) distribution at the point of compressive failure following crack propagation.

Figure 4.6(A) shows the stress-strain diagram for the 0° compression tests. Linear-elastic behaviour up to a nominal axial compressive strain of 0.0055 is observed. At strains in the region of 0.005-0.006, all experimental specimens experience a small drop in force before continuing to deform linearly up to a longitudinal compressive strength,  $X_Y$ , of  $1182.26 \pm 67.99$  MPa. The slight drop in stress coincides with the point of tab detachment. The computational model predicts a linear stress-strain response up to the ultimate compressive strength of the 0° laminate at 1036.4 MPa at a strain of 0.0061. Tab detachment is not included in the model the discontinuity in the stress response is not predicted prior to ultimate failure. Figure 4.6(Bii) shows the location for the predicted crack initiation on the edge of the laminate. The crack propagates through the laminate in the y-direction until ultimate failure, Figure 4.6(Biii).

**Summary of calibrated model parameters**

Plasticity and damage model parameters for *CF/PEEK* are listed in Table 4.3 below. Additionally, intra-laminar failure model parameters are taken directly from experimental results in Table 4.2 and material and elastic properties are taken from experimental values listed in Table 4.1

Table 4.3: Calibrated material parameters for CF/PEEK

Hill's potential function	$R_{11}$	250
	$R_{22}, R_{33}$	1.0
	$R_{12}, R_{13}$	0.64
	$R_{23}$	1.0
Cohesive Zone Model	$\sigma_{max}$ (MPa)	49.5
	$\tau_{max}$ (MPa)	37
	$\delta_n$ ( $\mu\text{m}$ )	10
	$\delta_t$ ( $\mu\text{m}$ )	10

## 4.5 Model validation

Using the model parameters calibrated in the previous section we next assess the ability of the model to predict a variety of failure patterns. Specifically, we consider flexure tests of  $0^\circ$  and  $90^\circ$  laminates, compression and flexure tests of  $\pm 45^\circ$  laminates and in-plane shear tests of  $\pm 45^\circ$  laminates.

### *Predicting failure in $0^\circ$ and $90^\circ$ laminates under flexure loads*

The flexural modulus and strength measured from four-point-bend tests performed on  $0^\circ$  and  $90^\circ$  laminates are presented in Table 4.4 below.

Table 4.4: Flexural modulus and strength of the  $0^\circ$  and  $90^\circ$  laminates (mean  $\pm$  standard deviation).

	$0^\circ$	$90^\circ$
Modulus (GPa)	$182.19 \pm 3.195$	$11.30 \pm 0.485$
Strength (MPa)	$1623.27 \pm 66.255$	$107.37 \pm 8.942$

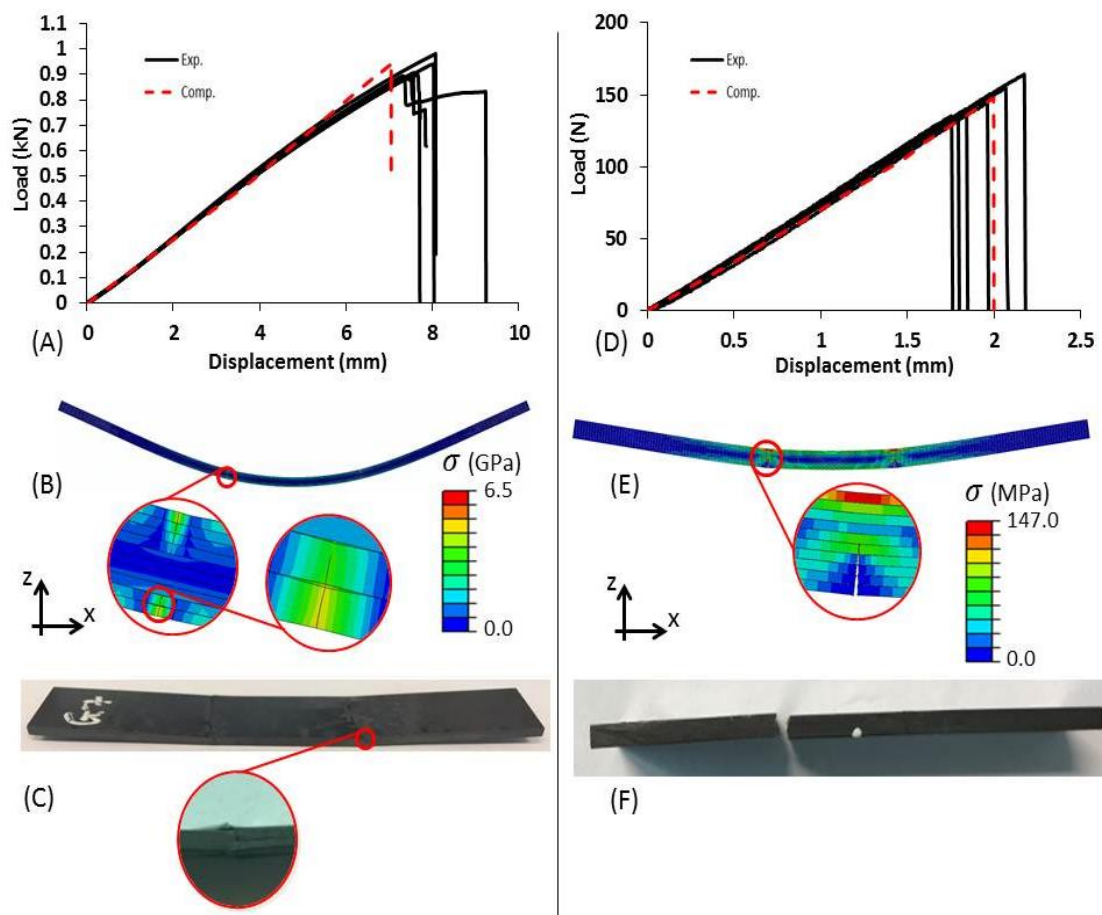


Figure 4.7: (A) Experimental and computational force - displacement curves for flexure tests on 0° laminates. (B) Computational prediction of flexural failure in 0° laminates. (C) Experimental image of the failed 0° specimen. (D) Experimental and computational force - displacement curves for the 90° laminate. (E) Predicted von Mises stress ( $\sigma$ ) distribution at failure. (F) Experimental image of a 90° flexure specimen following failure.

Figure 4.7(A) shows the force-displacement curves for 0° flexure tests. The force increases linearly to a failure load of  $918.11 \pm 36.71$  N at an applied displacement of  $7.61 \pm 0.92$  mm. The computational model provides a good prediction of the force-displacement relationship with a computed failure load of 940.99 N at a displacement of 7.05 mm. An experimental image of the 0° flexure specimen in Figure 4.7(C), exhibits inter-laminar delamination in addition to crack propagation in the vicinity of the load points on both the compressive and tensile sides of the specimen. The

computational model correctly predicts the simultaneous evolution of these three modes of damage as shown in Figure 4.7(B).

Figure 4.7(D) shows a linear force-displacement relationship for the 90° flexure tests up to an ultimate failure load of  $145.37 \pm 11.79$  N at an applied displacement of  $1.93 \pm 0.17$  mm. The computational model accurately predicts this linear behaviour, with a computed failure load of 147.77 N at 1.99 mm displacement. As shown in Figure 4.7(E) the model predicts crack initiation on the tensile surface of the laminate and propagation through the laminate in the z-direction. The computed crack predictions are in good agreement with experimentally observed failure modes (Figure 4.7(F)). It should be noted that inter-laminar delamination is not observed experimentally in 90° flexure tests. Again, this is correctly simulated by the model; computed inter-ply tractions are below the critical values, therefore cohesive zone delamination is not predicted to occur.

### **Predicting failure in compression tests of $\pm 45^\circ$ laminates**

Experimental results and computational predictions for compression tests performed on  $\pm 45^\circ$  laminates are presented in Figure 4.8 below.

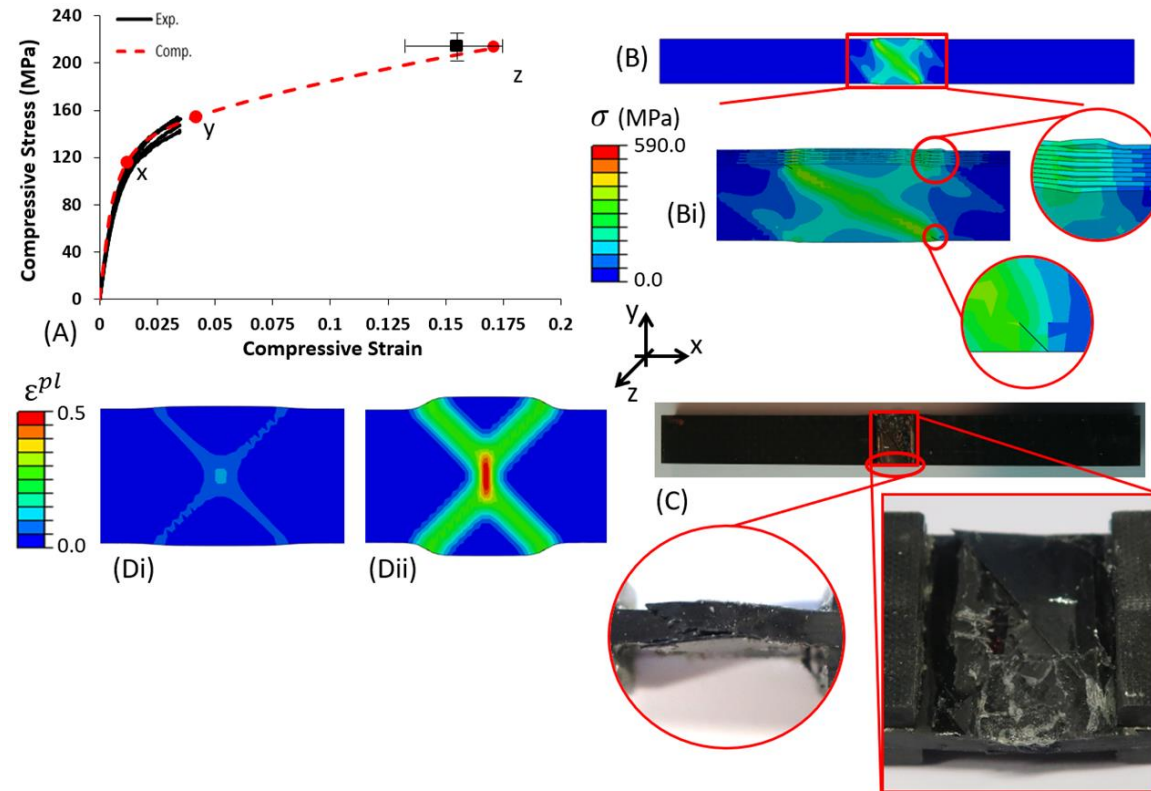


Figure 4.8: A) Experimental and computational compressive stress – compressive strain curve for  $\pm 45^\circ$  laminates where (x) is the computed point of localised crack initiation in the outermost plies, (y) is the computed point of inter-laminar delamination onset and (z) is the point of ductile failure in all plies. B) Von Mises stress ( $\sigma$ ) distribution in the computational model at the initiation of inter-laminar delamination. (Bi) Predicted locations for intra-laminar cracking and inter-laminar delamination. C) Experimental image of the  $\pm 45^\circ$  compression specimen at failure. (Di) Computed plastic strain distribution in the middle ply at the onset of delamination (at point y). (Dii) Predicted plastic strain distribution in the middle ply at failure.

The experimentally measured stress-strain relationship is shown in Figure 4.8(A). The  $\pm 45^\circ$  laminates exhibit a linear elastic response followed by initial plastic yielding at a 0.2% proof stress of 92.5 MPa. Following initial yielding, the specimen undergoes strain hardening up to a compressive strain of 0.034; beyond this point the specified working limit of the strain gauges is exceeded and subsequent experimental strain data is not recorded. However, the ultimate compressive strength of the laminate is measured as  $213.19 \pm 10.90$  MPa, indicating that strain hardening continues beyond a strain of 0.034. A failure strain of  $0.133 \pm 0.016$  is estimated from the test machine cross-head position, as indicated in Figure 4.8(A). The computational model provides an accurate prediction for the initial elastic behaviour and the post yield hardening behaviour. The yield point is strongly influenced by the  $R_{12}$  value in the Hill model (Eqn. 4.1), again highlighting the importance of anisotropic plasticity for laminate structures. The model predicts that a crack initiates in the outermost plies at an applied nominal strain of 0.015 (Figure 4.8(Bi)) with crack propagation parallel to the fibre direction. Further loading does not result in crack propagation in the inner plies. The model also predicts that buckling and delamination of the outer plies occurs at an applied nominal strain of 0.04 (Figure 4.8(Bi)). Again, further loading does not result in delamination of inner plies and the laminate is predicted to support an increasing applied load until the equivalent plastic strain in the matrix exceeds the material ductility limit (0.48 (Rae et al., 2007)) in all ten plies (Figure 4.8(Dii)) at an applied strain of 0.17 with a predicted ultimate failure load of 218 MPa.

The predicted damage and failure mechanisms are supported by experimental test data (Figure 4.8(C)). Buckling and delamination are observed only in outer plies, in addition to crack growth parallel to the fibre direction. Additionally, experimental

tests demonstrate that the laminate structure maintains its load bearing capacity up to an applied strain of 0.155; our model predicts that at such a high applied strain ductile failure due to excessive plastic deformation occurs in all plies.

**Predicting failure in flexure tests of  $\pm 45^\circ$  laminates**

Experimental results and computational predictions for flexure tests performed on  $\pm 45^\circ$  laminates are presented in Figure 4.9 below.

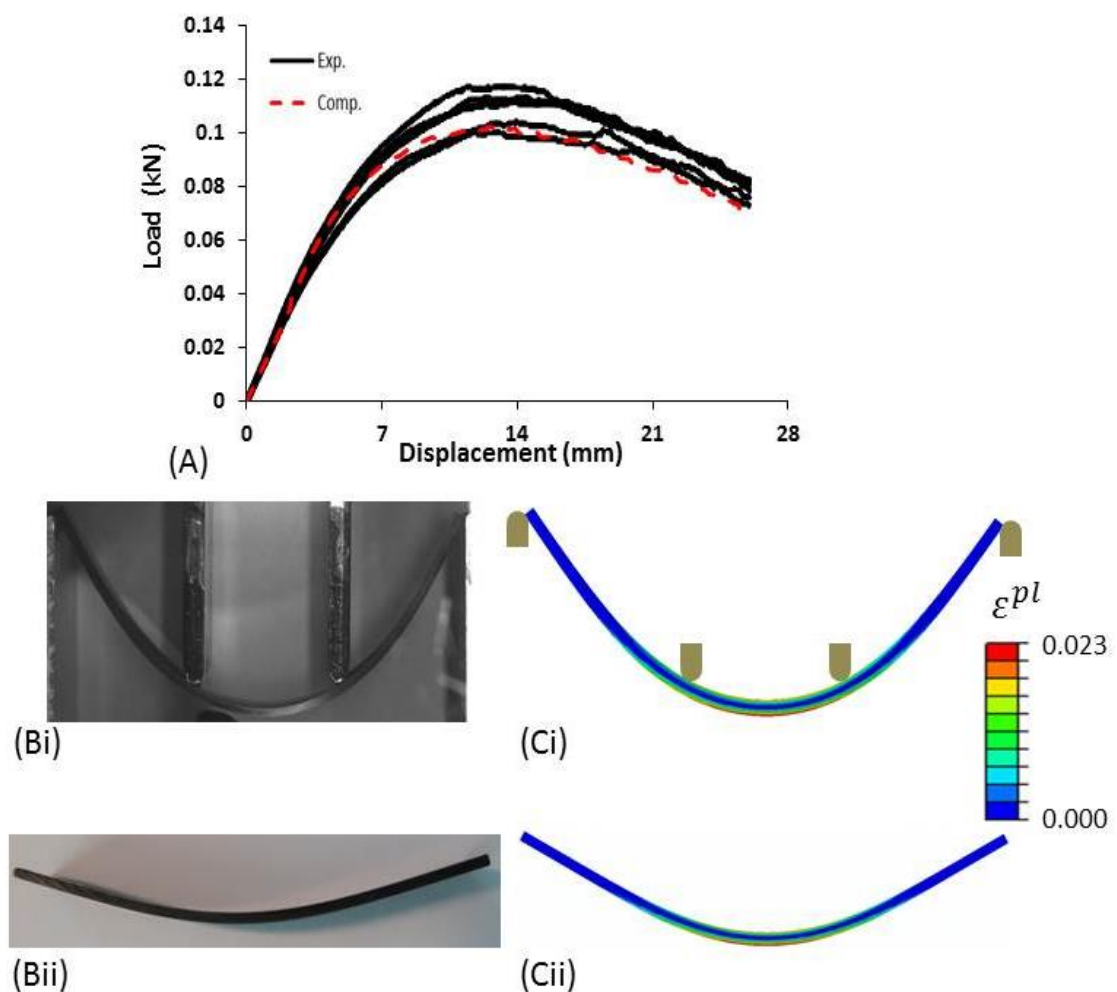


Figure 4.9: (A) Experimental and computational force-displacement curve for the flexure test of  $\pm 45^\circ$  laminates. (Bi) Experimental image of  $\pm 45^\circ$  laminate at maximum deformation. (Bii) Experimental image of  $\pm 45^\circ$  laminate after unloading. (Ci) Predicted plastic strain ( $\epsilon^{pl}$ ) distribution at maximum deformation. (Cii) Predicted plastic deformation after unloading.

Figure 4.9(A) shows the force-displacement diagram for  $\pm 45^\circ$  flexure test. The laminate exhibits linear-elastic behaviour up to initial plastic yielding at a 0.2% proof load of 70 N. After initial yielding, the specimen undergoes strain hardening up to a maximum force of  $110.34 \pm 0.63$  N at an applied displacement of  $13.07 \pm 1.29$  mm. The  $\pm 45^\circ$  laminates do not experience ultimate failure during the flexure tests. Rather, the samples continue to bend until the ends slide between the fixed supports, as shown in Figure 4.9(Bi). No intra-laminar cracking or inter-laminar delamination is observed in the specimen. However permanent plastic deformation is observed upon removal of the applied load, as shown in Figure 4.9(Bii). The computational model accurately predicts the observed load-displacement behaviour (Figure 4.9(A)). The maximum load predicted by the computational model is 102.2 N at an applied displacement of 12.61 mm. Consistent with experimental observations, the model does not predict any delamination or cracking. Finally, the model predicts significant plastic deformation upon load removal as shown in Figure 4.9(Cii), although it is slightly more than the plastic deformation observed experimentally (Figure 4.9(Bii)). The effects of a geometric non-linearity is visible in the experimental results where there is a gradual drop in load towards the end of the experiment. This is as a result of the sample slipping on the support grips, effectively causing the length of the test specimen during the test. This non-linearity is correctly predicted by the computational model, where the test specimen also slips on the support grips.

### **Predicting failure in in-plane shear tests of $\pm 45^\circ$ laminates**

Results for in-plane shear (IPS) tests on  $\pm 45^\circ$  laminates are shown in Figure 4.10.

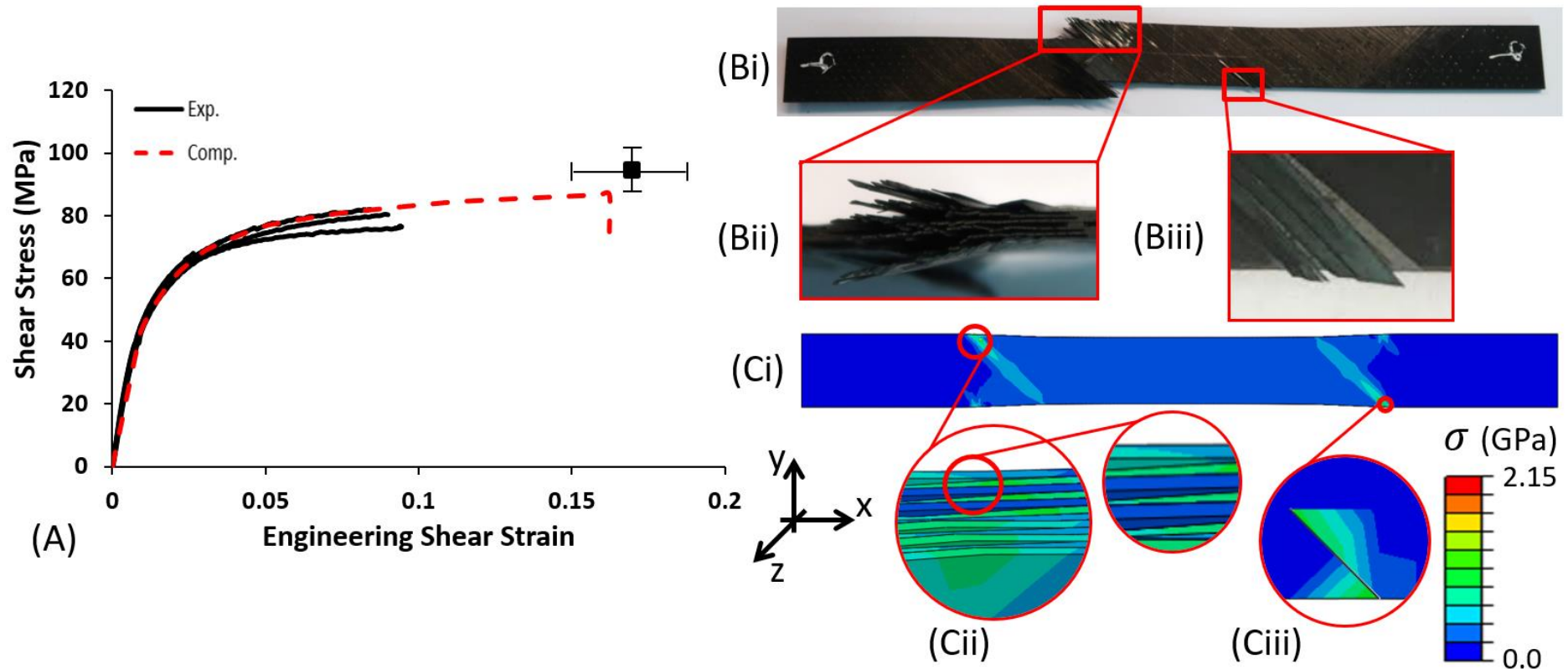


Figure 4.10: (A) Experimental and computational shear stress - shear strain curves for the in-plane shear tests carried out on  $45^\circ$  laminates. (Bi) Experimental image of the  $\pm 45^\circ$  laminate at failure. (Bii) Experimental image of the delamination at failure. (Biii) Experimental image of matrix cracks propagating at  $45^\circ$  at failure. (Ci) Predicted von Mises stress ( $\sigma$ ) distribution in the  $\pm 45^\circ$  laminate at failure. (Cii) Predicted inter-laminar delamination at failure. (Ciii) Predicted location of crack initiation.

Figure 4.10(A) shows the experimentally measured shear stress-shear strain relationship for the  $\pm 45^\circ$  laminate. A linear elastic region is observed up to a yield stress of 37.5 MPa, after which plastic deformation and strain hardening is observed. Measured strain data is plotted up to the specified limit of the strain gauges. Beyond this point, the specimen continues to undergo strain hardening up to a measured failure stress of  $95.83 \pm 7.44$  MPa. A failure strain of  $0.168 \pm 0.031$  is estimated from the crosshead displacement at failure, as indicated in Figure 4.10(A). The computational model provides an accurate prediction of the shear stress-shear strain behaviour, including the initial elastic region, initial plastic yielding and strain hardening. The model predicts that post yield hardening continues until failure at a shear stress of 86.9 MPa at an engineering shear strain of 0.162. Experimental images of a failed specimen (Figure 4.10(Bi)) reveal the complexity of failure in  $\pm 45^\circ$  laminates. Inter-laminar cracking parallel to the fibres (Figure 4.10(Biii)), in addition to inter-laminar delamination (Figure 4.10(Bii)), is observed. The model correctly predicts both the intra-laminar  $45^\circ$  cracks (Figure 4.10 (Ciii)) and inter-laminar delamination (Figure 4.10(Cii)) in the same regions observed experimentally.

## **4.6 Preliminary device design**

Next, we present an analysis of laminate plate performance under the physiological loading conditions of the femur. An adult femur (Isaza et al., 2013) is modelled with a mid-shaft fracture. The fracture is fixed with a locking compression plate (LCP) modelled on plates currently available in the market. The LCP (10 holes; length = 204mm; width = 10mm; thickness = 6.4mm) is attached to the femur with rigid screws (diameter= 5mm) in all 10 screw holes. The screws are modelled as rigid

analytical surfaces, a tie constraint is placed between the rigid surface and the inside surfaces of each hole. Physiological joint forces and abductor muscle forces are applied to the proximal end of the femur (Özkaya et al., 2016; Polgár et al., 2003; Radcliffe and Taylor, 2007; Speirs et al., 2007). We assume that body weight (BW) is 70kg, and during single leg stance the force acting through the femur head ( $F_J$ ) and the muscle attachment point ( $F_M$ ) is  $|F_J| = 3.4BW$  and  $|F_M| = 2.6BW$ , respectively. The fractured femur fixed with the LCP in plate is shown in Figure 4.11(A), the boundary conditions for the femur during single leg stance are also illustrated (A).

Three different laminate layups are compared:

Laminate 1:  $[0^\circ_{16}]_S$ , hereafter referred to as the  $0^\circ$  plate.

Laminate 2:  $[\pm 45^\circ_4/0^\circ_8]_S$ , hereafter referred to as the  $45^\circ/0^\circ$  plate.

Laminate 3:  $[\pm 45^\circ_8]_S$ , hereafter referred to as the  $45^\circ$  plate.

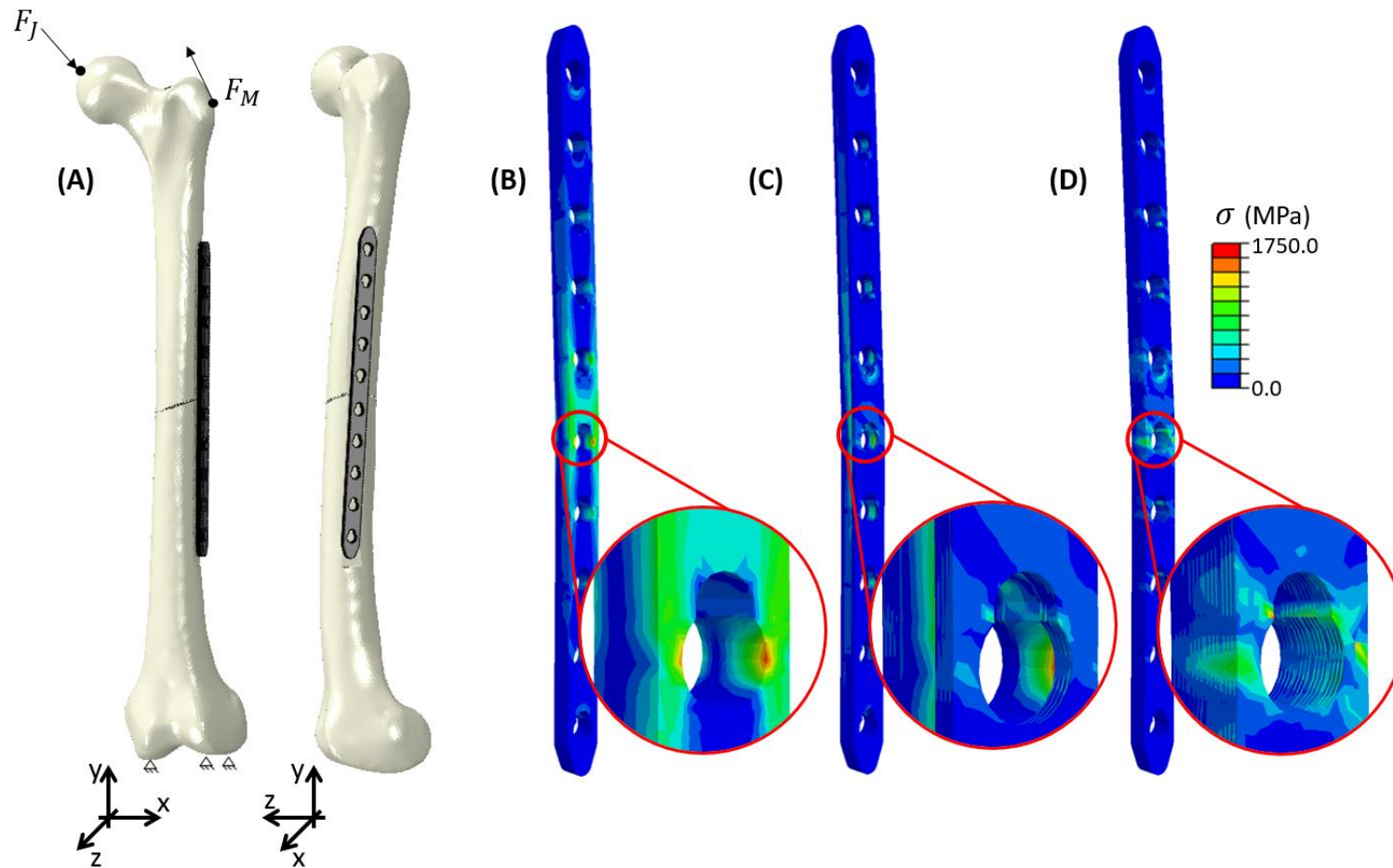


Figure 4.11: (A) Femur geometry and attached LCP plate geometry with boundary conditions indicated. Contour plot of von Mises ( $\sigma$ ) stress in the plate for single leg stance where  $|F_J| = 2.335kN$  and  $|F_M| = 1.785kN$  for; (B)  $0^\circ$  plate; (C)  $45^\circ/0^\circ$  plate and (D)  $45^\circ$  plate.

The stress distribution in the  $0^\circ$ ,  $45^\circ/0^\circ$  and  $45^\circ$  plates during single leg stance is shown in Figure 4.11(B), (C) and (D), respectively. In all three plates the areas of high stress are concentrated around the screw hole on the distal side of the fracture, with the highest stress predicted in the  $0^\circ$  plate. In the  $45^\circ/0^\circ$  plate (Figure 4.11(D)) it is clear that the  $0^\circ$  plies, located in the middle of the laminate and aligned with the femur shaft, are more highly stressed than the  $\pm 45^\circ$  plies located in the outermost plies of the laminate.

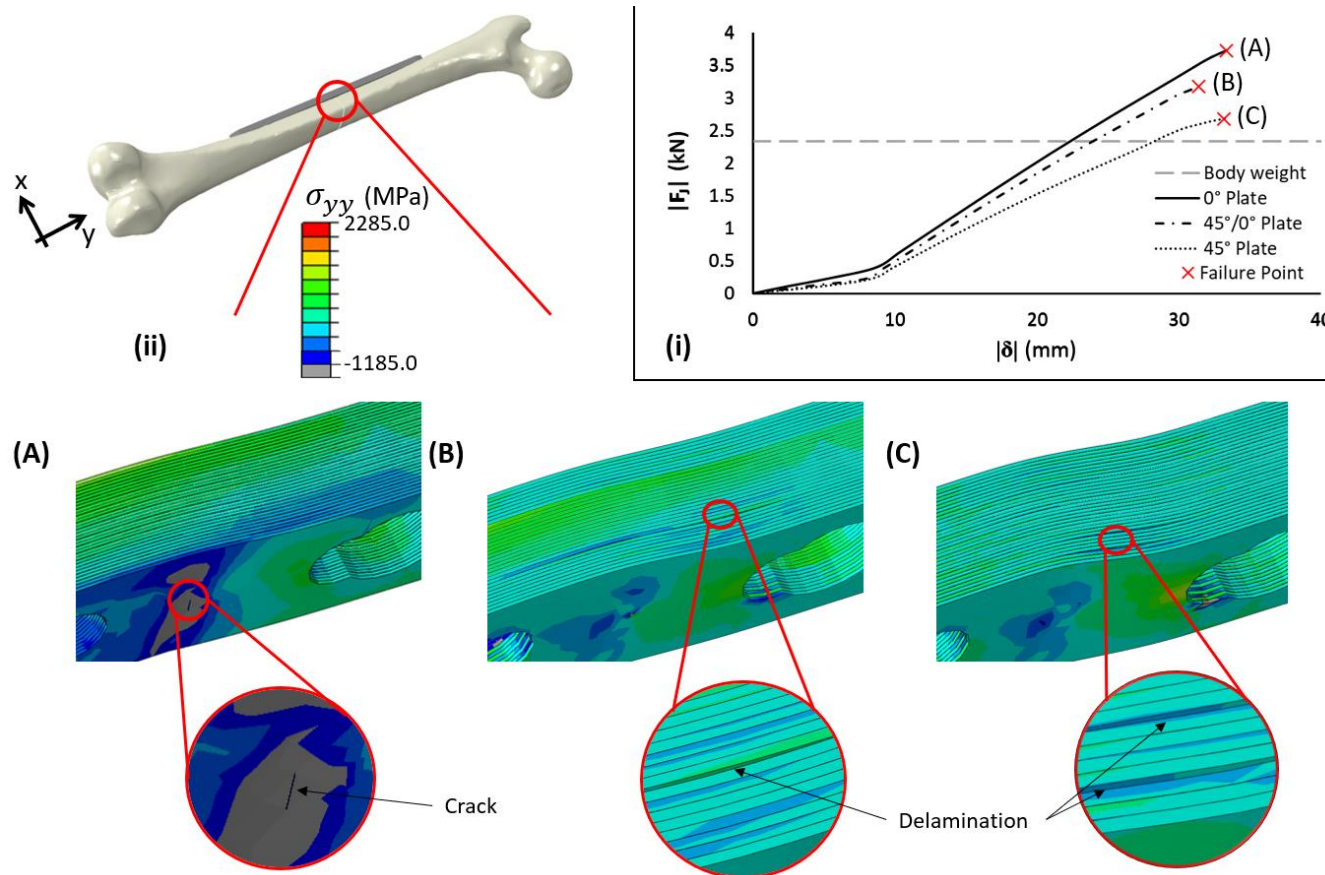


Figure 4.12: (i) Graph of applied joint force ( $|F_J|$ ) against displacement ( $|\delta|$ ) of the femur head at the point of the applied joint force  $F_J$ , relative to the fixed distal end of the femur. (ii) Location of the close-up images of the longitudinal stress ( $\sigma_{yy}$ ) distribution at failure for; (A) 0° plate; (B) 45°/0° plate and (C) 45° plate.

In Figure 4.12 the laminated plates are loaded to failure to determine the load bearing capacity of each plate under physiological loading conditions.  $|F_J|$  and  $|F_M|$  are increased up to the point of failure while keeping a constant ratio of  $|F_J| / |F_M|$ . Figure 4.12(i) shows the relationship between the magnitude of  $F_J$  and the magnitude of the displacement of the femoral head relative to the fixed distal end of the femur. Clearly all three plates fail at loads greater than those associated with single leg stance. The  $45^\circ$  plate is the most compliant of the three plates, it fails at an applied joint load of 2.7kN and a femur head displacement of 33.2mm. The addition of the  $0^\circ$  plies to the  $\pm 45^\circ$  plies in the  $45^\circ/0^\circ$  plate results in an increase in stiffness and an increase in the applied load at failure to 3.2kN which is 1.4 times greater than loading associated with single leg stance. The  $0^\circ$  plate is the stiffest of the three plates and fails at an applied joint load of 3.7kN, 1.6 times greater than applied loading during single leg stance, at a femur head displacement of 33.3mm.

As shown in Figure 4.12(A) the compressive strength (-1183 MPa) is reached in the outermost ply on the medial side of the  $0^\circ$  plate and a crack forms. The  $45^\circ/0^\circ$  plate (Figure 4.12(B)) fails due to delamination at the interface of the 8th and 9th plies, where the 8th ply is a  $45^\circ$  ply and the 9th ply is a  $0^\circ$  ply. The change in stress concentration between the  $0^\circ$  ply and the  $45^\circ$  ply at that location (as highlighted in insert Figure 4.12(B)) results in extensive inter-laminar failure at that location. Similarly, the  $45^\circ$  ply (Figure 4.12(C)) fails due to inter-laminar failure. Delaminations are predicted in multiple locations through the thickness of the laminate, as highlighted in the insert in Figure 4.12(C).

The preliminary results demonstrate the importance of ply layup design for fracture fixation plates. It also demonstrates that all the failure mechanisms uncovered in

Sections 4.4 and 4.5 of this chapter must be considered during the design of laminated fracture fixation plates.

### 4.7 Discussion

This chapter presents, for the first time, experimental material characterisation of the medical grade unidirectional carbon fibre reinforced PEEK laminates, PEEK-OPTIMA™ Ultra-Reinforced. Due to the complex loading conditions applied to fracture fixation plates in the human body, it is essential that a comprehensive multi-axial characterisation of material behaviour is performed in order to design reliable and safe implant devices. Our suite of multi-axial experimental tests uncovers three damage mechanisms: (1) inter-laminar delamination, (2) intra-laminar cracking and (3) anisotropic plasticity. A computational damage and failure model that incorporates all three modes of damage is developed and validated using our experimental data.

PEEK-OPTIMA™ Ultra-Reinforced has been cleared by the FDA for implantation in humans but to date no experimental test data has been published for the material. This presents a significant obstacle for safe design of first-generation laminated orthopaedic implants. In this study we present the first extensive material characterisation of PEEK-OPTIMA™ Ultra-Reinforced. In a previous study to determine the mechanical properties of a novel glass/flax/epoxy composite plate for long bone fracture fixation, tension, compression and three-point bend tests were performed (Bagheri et al., 2013; Manteghi et al., 2017). Studies on non-medical grade laminate materials have included compression and tension testing of 0° and 90° laminates and in-plane shear tests of  $\pm 45^\circ$  laminates (O'Higgins et al., 2008; Wonderly et al., 2005; Wu and Springer, 1988). In addition to such standard tests,

the current study also presents extensive flexure testing of  $0^\circ$ ,  $90^\circ$  and  $\pm 45^\circ$  laminates and mode I and mode II fracture toughness tests. Due to the complex multi-axial loading environment of orthopaedic implants, such an extensive suite of multi-axial experiments is necessary for safe device design. The preliminary device design presented in Section 4.6 of this study highlights the importance of ply layup design for the load bearing capacity of laminated fracture fixation plates. It also demonstrates how the computational framework developed in this study which combines anisotropic plasticity, inter-laminar and intra-laminar failure must be considered during the design of next generation laminated devices.

Experiments reveal the need for a complex multi-modal damage and failure model that includes: (1) inter-laminar delamination, (2) intra-laminar crack initiation and propagation and (3) anisotropic plasticity. Previous studies have developed computational damage models for non-medical grade laminate material. Such models have been limited to either the simulation of intra-laminar crack propagation (Ahmad et al., 2014; Duarte et al., 2017) or inter-laminar delamination (Heidari-Rarani et al., 2013; Turon et al., 2010; Zhao et al., 2014). Only the recent studies of Bouhala et al., Viguera et al. and Grogan et al. (Bouhala et al., 2015; Grogan et al., 2015a, 2015b; Viguera et al., 2015) have simulated combined intra-and inter-laminar failure. Furthermore only two studies that have included plasticity in their combined inter- intra-laminar failure models (Higuchi et al., 2017; van der Meer et al., 2011). A key deficiency of the van der Meer study is that only the off-axis non-linear responses in one loading direction are considered. Our suite of multi-axial experiments have shown that CF/PEEK has different yield points in different loading directions, it is impossible to accurately predict yielding in all directions if the yielding is only measured experimentally in one direction. In order to accurately

simulate our experimental results we establish that anisotropic plasticity must be incorporated. Our model accurately predicts plastic yielding and strain hardening during compression loading of  $90^\circ$  laminates, and also during tension and compression loading of  $\pm 45^\circ$  laminates. Moreover, the model correctly predicts that fracture occurs without any plastic deformation in the case of tension and flexure loading of  $0^\circ$  and  $90^\circ$  laminates. By incorporating anisotropic plasticity in conjunction with inter-laminar delamination and intra-laminar crack propagation we accurately predict highly complex patterns of delamination evolution and laminate failure for a wide range of loading conditions, as observed in our experiments. The prediction of multi-axial multi-mode failure mechanisms is critical for the design of fibre reinforced laminated orthopaedic fracture fixation devices. However, one limitation of the current chapter is that it is possible that yielding is due to micro-cracks and micro-damage within the laminate and not plasticity, in order to confirm that this, further experiments should be conducted where specimens are unloaded prior to failure. A further limitation of the current study is that the fracture toughness tests were carried out on  $0^\circ$  laminates alone, potential differences of fracture toughness in angled plies (i.e.  $45^\circ$  plies) are not considered. Future studies should consider performing a fracture toughness test similar to the  $G_{IC}$  test on a  $45^\circ$  laminate to confirm if the fibre orientation has an effect of the inter-laminar strength. It should be noted that the failure of the tabs in the  $0^\circ$  compression tests led to an underprediction of the longitudinal compressive strength ( $X_C$ ). Future studies should consider using open hole compression tests in order to calculate the longitudinal compressive strength of fibre reinforced materials as  $0^\circ$  compression tests are notoriously difficult to carry out. Follow-on studies will consider additional multi-axial loading modes, and the influence of pressure-dependent yielding and mode

dependent hardening (Vogler et al., 2013; Xue and Hutchinson, 2004) on laminate behaviour. Additionally, future studies should consider, cyclic loading, combined isotropic kinematic hardening plasticity formulation, fatigue failure and strain rate hardening.

In order to develop first-generation fibre reinforced laminated composite orthopaedic implants, the current chapter makes two key contributions: (1) The first comprehensive experimental material characterisation of FDA cleared material PEEK-OPTIMA™ Ultra-Reinforced is presented; (2) A finite element framework that incorporates anisotropic plasticity in addition to inter-laminar delamination and intra-laminar cracks in order to accurately predict the complex failure mechanisms observed experimentally is developed. Follow-on studies will investigate the failure modes of laminates containing holes, laminated fracture fixation plate designs, and device-bone interface failure (Feerick and McGarry, 2012). Additionally, a micro-mechanical model will be developed to further investigate the modes of failure at the matrix-fibre interface.

## 4.8 References

- AECMA Standard, 1995a. prEN 6033 Aerospace series Carbon fibre reinforced plastics Test method Determination of interlaminar fracture toughness energy Mode I.
- AECMA Standard, 1995b. prEN 6034 Aerospace series Carbon fibre reinforced plastics Test method Determination of interlaminar fracture toughness energy Mode II.
- Ahmad, H., Crocombe, A.D., Smith, P.A., 2014. Strength prediction in CFRP woven laminate bolted single-lap joints under quasi-static loading using XFEM. *Compos. Part A Appl. Sci. Manuf.* 66, 82–93. <https://doi.org/10.1016/j.compositesa.2014.07.013>
- Aitasalo, K.M.J., Piitulainen, J.M., Rekola, J., Vallittu, P.K., 2014. Craniofacial bone reconstruction with bioactive fiber-reinforced composite implant. *Head Neck* 36, 722–728. <https://doi.org/10.1002/hed.23370>
- ASTM International, 2014. ASTM D3039/D3039M: Standard test method for tensile properties of polymer matrix composite materials. *Annu. B. ASTM Stand.* <https://doi.org/10.1520/D3039>
- ASTM International, 2013. ASTM D3518/D3518M Standard Test Method for In-Plane Shear Response of Polymer Matrix Composite Materials by Tensile Test of a 45 ° Laminate. *Annu. B. ASTM Stand.* <https://doi.org/10.1520/D3518>
- ASTM International, 2012. ASTM D6641/D6641M Standard Test Method for Compressive Properties of Polymer Matrix Composite Materials Using a Combined Loading Compression (CLC). *Annu. B. ASTM Stand.* i, 1–11. <https://doi.org/10.1520/D6641>
- Bagheri, Z.S., El Sawi, I., Schemitsch, E.H., Zdero, R., Bougherara, H., 2013. Biomechanical properties of an advanced new carbon/flax/epoxy composite material for bone plate applications. *J. Mech. Behav. Biomed. Mater.* 20, 398–406. <https://doi.org/10.1016/j.jmbbm.2012.12.013>
- Ballo, A.M., Lassila, L. V., Vallittu, P.K., Närhi, T.O., 2007. Load bearing capacity of bone anchored fiber-reinforced composite device. *J. Mater. Sci. Mater. Med.* 18, 2025–2031. <https://doi.org/10.1007/s10856-007-3159-6>
- Bieniaś, J., Dębski, H., Surowska, B., Sadowski, T., 2012. Analysis of microstructure damage in carbon/epoxy composites using FEM, in: *Computational Materials Science*. pp. 168–172. <https://doi.org/10.1016/j.commatsci.2012.03.033>
- Bouhala, L., Makradi, A., Belouettar, S., Younes, A., Natarajan, S., 2015. An XFEM/CZM based inverse method for identification of composite failure parameters. *Comput. Struct.* 153, 91–97. <https://doi.org/10.1016/j.compstruc.2015.02.035>
- Brantigan, J.W., Steffee, A.D., 1993. A Carbon Fiber Implant to Aid Interbody Lumbar Fusion. *Spine (Phila. Pa. 1976)*. 18, 2106–2117. <https://doi.org/10.1097/00007632-199310001-00030>
- Der Tavitian, J., Davison, J.N.S., Dias, J.J., 2002. Clavicular fracture non-union surgical outcome and complications. *Injury* 33, 135–143. [https://doi.org/10.1016/S0020-1383\(01\)00069-9](https://doi.org/10.1016/S0020-1383(01)00069-9)

- Duarte, A.P.C., Díaz Sáez, A., Silvestre, N., 2017. Comparative study between XFEM and Hashin damage criterion applied to failure of composites. *Thin-Walled Struct.* 115, 277–288. <https://doi.org/10.1016/j.tws.2017.02.020>
- Feerick, E.M., Kennedy, J., Mullett, H., FitzPatrick, D., McGarry, P., 2013a. Investigation of metallic and carbon fibre PEEK fracture fixation devices for three-part proximal humeral fractures. *Med. Eng. Phys.* 35, 712–722. <https://doi.org/10.1016/j.medengphy.2012.07.016>
- Feerick, E.M., Liu, X.C., McGarry, P., 2013b. Anisotropic mode-dependent damage of cortical bone using the extended finite element method (XFEM). *J. Mech. Behav. Biomed. Mater.* 20, 77–89. <https://doi.org/10.1016/j.jmbbm.2012.12.004>
- Feerick, E.M., McGarry, J.P., 2012. Cortical bone failure mechanisms during screw pullout. *J. Biomech.* 45, 1666–1672. <https://doi.org/10.1016/j.jbiomech.2012.03.023>
- Feerick, E.M., Wilson, J., Jarman-Smith, M., Ó’Brádaigh, C.M., McGarry, J.P., 2014. Self-tapping ability of carbon fibre reinforced polyetheretherketone suture anchors. *J. Biomater. Appl.* 29, 502–513. <https://doi.org/10.1177/0885328214535274>
- Gallagher, E., Ó’Brádaigh, C.M., McGarry, J.P., 2015. A computational investigation into the use of carbon fibre reinforced PEEK laminates for orthopaedic applications, in: *Proceedings of the 2nd International PEEK Meeting*. Washinton D.C, p. 60.
- Grogan, D.M., Ó Brádaigh, C.M., Leen, S.B., 2015a. A combined XFEM and cohesive zone model for composite laminate microcracking and permeability. *Compos. Struct.* 120, 246–261. <https://doi.org/10.1016/j.compstruct.2014.09.068>
- Grogan, D.M., Ó Brádaigh, C.M., McGarry, J.P., Leen, S.B., 2015b. Damage and permeability in tape-laid thermoplastic composite cryogenic tanks. *Compos. Part A Appl. Sci. Manuf.* 78, 390–402. <https://doi.org/10.1016/j.compositesa.2015.08.037>
- Hashin, Z., 1980a. Failure Criteria for Unidirectional Fiber Composites. *J. Appl. Mech.* 47, 329. <https://doi.org/10.1115/1.3153664>
- Hashin, Z., 1980b. Failure Criteria for Unidirectional Fiber Composites. *J. Appl. Mech.* 47, 329. <https://doi.org/10.1115/1.3153664>
- Heidari-Rarani, M., Shokrieh, M.M., Camanho, P.P., 2013. Finite element modeling of mode I delamination growth in laminated DCB specimens with R-curve effects. *Compos. Part B Eng.* 45, 897–903. <https://doi.org/10.1016/j.compositesb.2012.09.051>
- Higuchi, R., Okabe, T., Nagashima, T., 2017. Numerical simulation of progressive damage and failure in composite laminates using XFEM/CZM coupled approach. *Compos. Part A Appl. Sci. Manuf.* 95, 197–207. <https://doi.org/10.1016/j.compositesa.2016.12.026>
- Huiskes, R., Weinans, H., van Rietbergen, B., 1992. The relationship between stress shielding and bone resorption around total hip stems and the effects of flexible materials. *Clin. Orthop. Relat. Res.* 124–134. <https://doi.org/10.1097/00003086-199201000-00014>
- Isaza, E., García, L., Salazar, E., 2013. Determination of Mechanic Resistance of Osseous Element through Finite Element Modeling, in: *COMSOL Conference*. pp. 1–7.
- ISO, 1998. Fibre-reinforced plastic composites Determination of flexural properties.

<https://doi.org/10.1520/E0872-82R13.2>

- Kurtz, S.M., Devine, J.N., 2007. PEEK biomaterials in trauma, orthopedic, and spinal implants. *Biomaterials* 28, 4845–69. <https://doi.org/10.1016/j.biomaterials.2007.07.013>
- Lanzetta, M., Foucher, G., 1995. A comparison of different surgical techniques in treating degenerative arthrosis of the carpometacarpal joint of the thumb: A retrospective study of 98 cases. *J. Hand Surg. (British Eur. Vol. 20)*, 105–110. [https://doi.org/10.1016/S0266-7681\(05\)80027-0](https://doi.org/10.1016/S0266-7681(05)80027-0)
- Lessard, L.B., Chang, F., 1991. Damage Tolerance of Laminated Composites Containing an Open Hole and Subjected to Tensile Loadings: Patr II-Experiment. *J. Compos. Mater.* 25, 44–64. <https://doi.org/10.1177/002199839102500303>
- Li, C., Granger, C., Del Schutte, H., Biggers, S.B., Kennedy, J.M., Latour, R. a, 2002. Progressive failure analysis of laminated composite femoral prostheses for total hip arthroplasty. *Biomaterials* 23, 4249–62.
- Manteghi, S., Mahboob, Z., Fawaz, Z., Bougherara, H., 2017. Investigation of the mechanical properties and failure modes of hybrid natural fiber composites for potential bone fracture fixation plates. *J. Mech. Behav. Biomed. Mater.* 65, 306–316. <https://doi.org/10.1016/j.jmbbm.2016.08.035>
- McGarry, J.P., Ó Máirtín, É., Parry, G., Beltz, G.E., 2014. Potential-based and non-potential-based cohesive zone formulations under mixed-mode separation and over-closure. Part I: Theoretical analysis. *J. Mech. Phys. Solids* 63, 336–362. <https://doi.org/10.1016/j.jmps.2013.08.020>
- O’Brien, T.K., 1982. Characterization of Delamination Onset and Growth in a Composite Laminate. *Damage Compos. Mater. Basic Mech. Accumulation, Toler. Charact.* 140–167. <https://doi.org/10.1520/STP34325S>
- O’Higgins, R.M., McCarthy, M. a., McCarthy, C.T., 2008. Comparison of open hole tension characteristics of high strength glass and carbon fibre-reinforced composite materials. *Compos. Sci. Technol.* 68, 2770–2778. <https://doi.org/10.1016/j.compscitech.2008.06.003>
- Özkaya, N., Goldsheyder, D., Nordin, M., Leger, D., 2016. Fundamentals of biomechanics: Equilibrium, motion, and deformation, fourth edition, *Fundamentals of Biomechanics: Equilibrium, Motion, and Deformation, Fourth Edition*. <https://doi.org/10.1007/978-3-319-44738-4>
- Piitulainen, J.M., Kauko, T., Aitasalo, K.M.J., Vuorinen, V., Vallittu, P.K., Posti, J.P., 2015. Outcomes of cranioplasty with synthetic materials and autologous bone grafts. *World Neurosurg.* <https://doi.org/10.1016/j.wneu.2015.01.014>
- Polgár, K., Gill, H.S., Viceconti, M., Murray, D.W., O’Connor, J.J., 2003. Strain distribution within the human femur due to physiological and simplified loading: Finite element analysis using the muscle standardized femur model. *Proc. Inst. Mech. Eng. Part H J. Eng. Med.* 217, 173–189. <https://doi.org/10.1243/095441103765212677>
- Pozegic, T.R., Anguita, J. V., Hamerton, I., Jayawardena, K.D.G.I., Chen, J.-S., Stolojan, V., Balocchi, P., Walsh, R., Silva, S.R.P., 2016. Multi-Functional Carbon Fibre Composites using Carbon Nanotubes as an Alternative to Polymer Sizing. *Sci. Rep.* 6, 37334. <https://doi.org/10.1038/srep37334>

- Puck, A., Schürmann, H., 2002. Failure Analysis of FRP Laminates By Means of Physically Based Phenomenological Models. *Compos. Sci. Technol.* 62, 1633–1662. [https://doi.org/10.1016/S0266-3538\(96\)00140-6](https://doi.org/10.1016/S0266-3538(96)00140-6)
- Radcliffe, I.A.J., Taylor, M., 2007. Investigation into the effect of varus-valgus orientation on load transfer in the resurfaced femoral head: A multi-femur finite element analysis. *Clin. Biomech.* 22, 780–786. <https://doi.org/10.1016/j.clinbiomech.2007.03.011>
- Rae, P.J., Brown, E.N., Orlor, E.B., 2007. The mechanical properties of poly(ether-ether-ketone) (PEEK) with emphasis on the large compressive strain response. *Polymer (Guildf)*. 48, 598–615. <https://doi.org/10.1016/j.polymer.2006.11.032>
- Soden, P.D., Hinton, M.J., Kaddour, A.S., 2004. Lamina properties, lay-up configurations and loading conditions for a range of fibre reinforced composite laminates, in: *Failure Criteria in Fibre-Reinforced-Polymer Composites*. pp. 30–51. <https://doi.org/10.1016/B978-008044475-8/50003-2>
- Speirs, A.D., Heller, M.O., Duda, G.N., Taylor, W.R., 2007. Physiologically based boundary conditions in finite element modelling. *J. Biomech.* 40, 2318–2323. <https://doi.org/10.1016/j.jbiomech.2006.10.038>
- Tsai, S.W., Wu, E.M., 1971. A General Theory of Strength for Anisotropic Materials. *J. Compos. Mater.* 5, 58–80. <https://doi.org/10.1177/002199837100500106>
- Turon, A., Camanho, P.P., Costa, J., Renart, J., 2010. Accurate simulation of delamination growth under mixed-mode loading using cohesive elements: Definition of interlaminar strengths and elastic stiffness. *Compos. Struct.* 92, 1857–1864. <https://doi.org/10.1016/j.compstruct.2010.01.012>
- van der Meer, F., Sluys, L., Hallett, S., Wisnom, M., 2011. Computational modeling of complex failure mechanisms in laminates. *J. Compos. Mater.* 46, 603–623. <https://doi.org/10.1177/0021998311410473>
- Van Paepegem, W., De Baere, I., Degrieck, J., 2006. Modelling the nonlinear shear stress-strain response of glass fibre-reinforced composites. Part I: Experimental results. *Compos. Sci. Technol.* 66, 1455–1464. <https://doi.org/10.1016/j.compscitech.2005.04.014>
- Vigueras, G., Sket, F., Samaniego, C., Wu, L., Noels, L., Tjahjanto, D., Casoni, E., Houzeaux, G., Makradi, A., Molina-Aldareguia, J.M., Vázquez, M., Jérusalem, A., 2015. An XFEM/CZM implementation for massively parallel simulations of composites fracture. *Compos. Struct.* 125, 542–557. <https://doi.org/10.1016/j.compstruct.2015.01.053>
- Vogler, M., Rolfes, R., Camanho, P.P., 2013. Modeling the inelastic deformation and fracture of polymer composites-Part I: Plasticity model. *Mech. Mater.* 59, 50–64. <https://doi.org/10.1016/j.mechmat.2012.12.002>
- Wisnom, M.R., Hallett, S.R., 2009. The role of delamination in strength, failure mechanism and hole size effect in open hole tensile tests on quasi-isotropic laminates. *Compos. Part A Appl. Sci. Manuf.* 40, 335–342. <https://doi.org/10.1016/j.compositesa.2008.12.013>
- Wonderly, C., Grenestedt, J., Fernlund, G., Čěpus, E., 2005. Comparison of mechanical properties of glass fiber/vinyl ester and carbon fiber/vinyl ester composites. *Compos.*

Part B Eng. 36, 417–426. <https://doi.org/10.1016/j.compositesb.2005.01.004>

Wu, H.-Y.T., Springer, G.S., 1988. Measurements of Matrix Cracking and Delamination Caused by Impact on Composite Plates. *J. Compos. Mater.* 22, 518–532. <https://doi.org/10.1177/002199838802200602>

Xue, Z., Hutchinson, J.W., 2004. Constitutive model for quasi-static deformation of metallic sandwich cores. *Int. J. Numer. Methods Eng.* 61, 2205–2238. <https://doi.org/10.1002/nme.1142>

Zhao, L., Gong, Y., Zhang, J., Chen, Y., Fei, B., 2014. Simulation of delamination growth in multidirectional laminates under mode I and mixed mode I/II loadings using cohesive elements. *Compos. Struct.* 116, 509–522. <https://doi.org/10.1016/j.compstruct.2014.05.042>

## Appendix 4A

The laminate layups and specimen dimensions are listed in Table 4A1.

Table 4A1: Specimen dimensions and layups for all of the tests outlined in the main body of this text

			Test specimen dimensions		
Test	Standard	Layup	Length	Width	Thickness
Tension	ASTM 3039	$[0^\circ]_5$	250.0	15.0	1.0
		$[90^\circ]_{20}$	175.0	12.5	4.0
Compression	ASTM D6641	$[0^\circ]_{10}$	140.0	12.0	2.0
		$[90^\circ]_{10}$	140.0	12.0	2.0
		$[\pm 45^\circ]_5$	140.0	12.0	2.0
Flexure	ISO 14125	$[0^\circ]_{10}$	100.0	15.0	2.0
		$[90^\circ]_{10}$	60.0	15.0	2.0
		$[\pm 45^\circ]_5$	100.0	15.0	2.0
In-plane shear	ASTM D3518	$[\pm 45^\circ]_{s3}$	250.0	25.0	2.4
Fracture Toughness $G_{ic}$ & $G_{iic}$	ACEMA prEN6033 & prEN6034	$[0^\circ]_{16}$	250.0	25.0	3.2

Appendix 4B

The equations used to calculate the mode I fracture toughness,  $G_{ic}$ , and the mode II fracture toughness,  $G_{iic}$ , are given in Eqn. 4B1 and 4B2, respectively.

$$G_{ic} = \frac{A}{aw} \tag{4B1}$$

$$G_{iic} = \frac{9Pda^2}{2w\left(\frac{L^3}{4} + 3a^3\right)} \tag{4B2}$$

where,  $A$  is the area under the force-displacement curve,  $a$  is the initial crack length,  $w$  is the width of the specimen,  $P$  is the load at the onset of crack propagation,  $d$  is the crosshead displacement at the onset of crack propagation and  $L$  is the length of the span.

A parameter study was carried out in order to determine the mode I and mode II interface strengths and the normal and tangential characteristic lengths for the cohesive zone model. The results are presented in Figure 4B1.

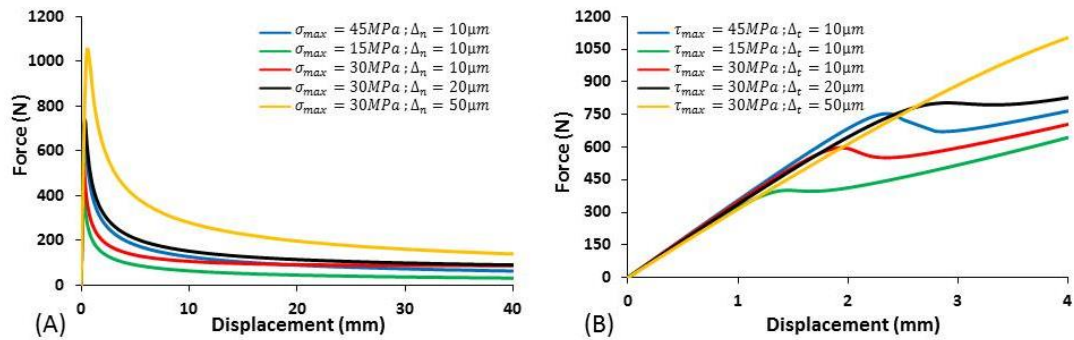


Figure 4B1: (A) Force-displacement curves for different mode I cohesive zone parameters.  
(B) Force-displacement curves for different mode II cohesive zone parameters.

Figure 4B1(A) shows the results of the parameter study performed to determine cohesive zone properties for the mode I inter-laminar strength ( $\sigma_{max}$ ) and the normal characteristic interface length ( $\Delta_n$ ). The peak force is governed by both  $\sigma_{max}$  and

$\Delta_n$ . The plateau in force that occurs after propagation is highly influenced by the value of  $\sigma_{max}$ . Increasing  $\sigma_{max}$  results in the plateau occurring at higher force and vice versa. Figure 4B1(B) shows the results of the parameter study performed to determine cohesive zone properties for the mode II inter-laminar strength ( $\tau_{max}$ ) and the tangential characteristic interface length ( $\Delta_t$ ). Examining the force-displacement relationships it is evident that the peak force is highly influenced by  $\tau_{max}$ , increasing  $\tau_{max}$  causes an increase in the max force. The slope of the curve and the drop in force after the crack has begun to propagate are primarily governed by  $\Delta_t$ .

## Appendix 4C

The technical drawings for the tensile and in-plane shear test specimens, taken from the ASTM standards, are displayed in Figure 4C1.

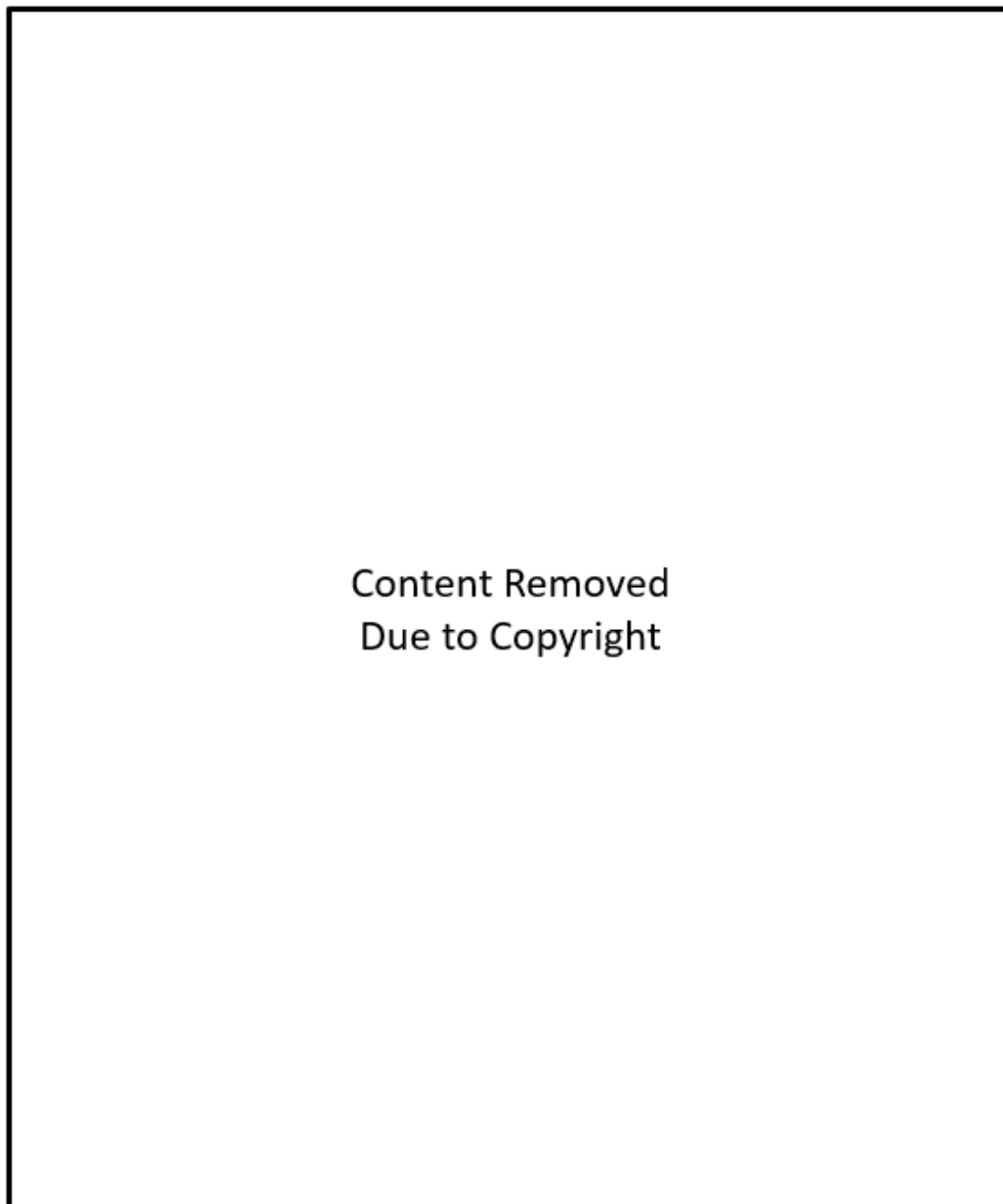
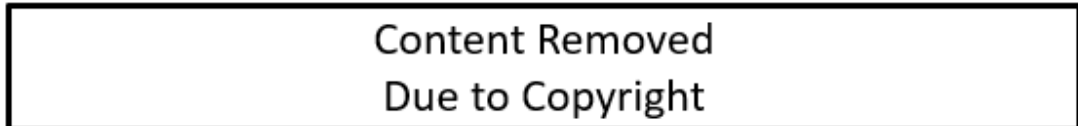


Figure 4C1: Technical drawings and technical notes for the tensile and in-plane shear test specimens ASTM D3039-07 (ASTM International, 2014).

The specimen dimensions are listed in Table 4C1 below, also taken from the ASTM D3039-07 (ASTM International, 2014) standards.

Table 4A1: Specimen dimensions and layups for all of the tensile tests outlined in the main body of this text



The technical drawings for the compression test specimens, taken from the ASTM standards, are displayed in Figure 4C2.



Figure 4C2: Technical drawings and technical notes for the compression test specimens ASTM D6641-14 (ASTM International, 2012).

The technical drawings for the Mode I fracture toughness test specimens, taken from the standards, are displayed in Figure 4C3. The Mode II fracture toughness test is performed on the same test sample after the Mode I test has completed.

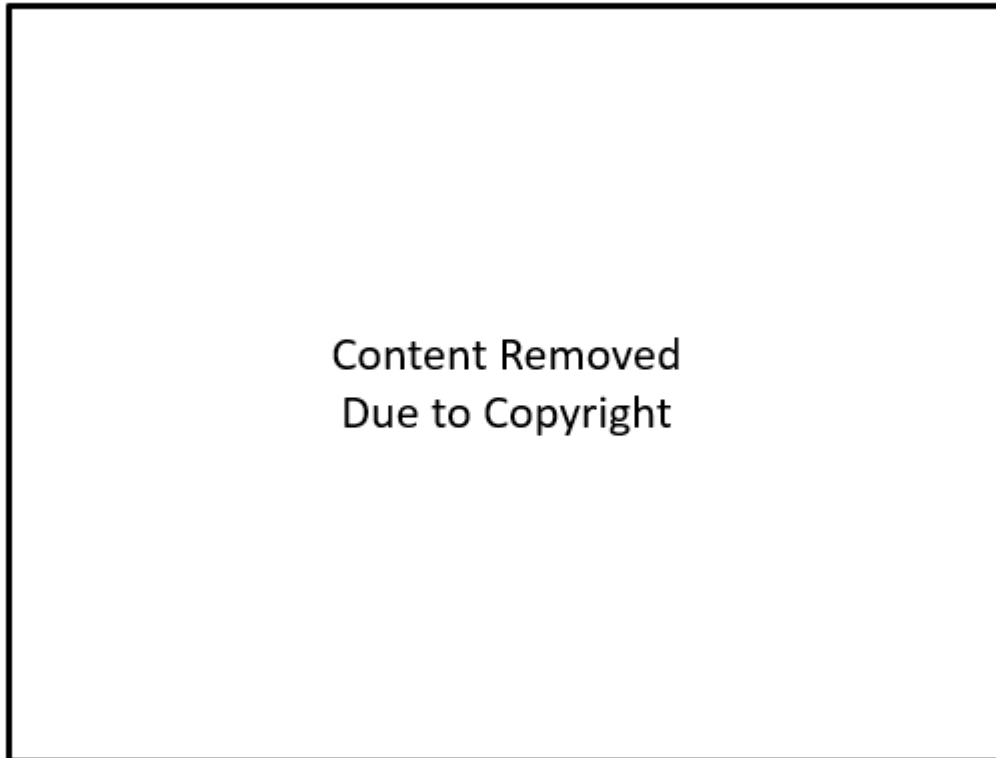


Figure 4C3: Technical drawings and technical notes for the compression test specimens EN6033-95 and EN6034-95 (AECMA Standard, 1995a, 1995b).

The test specimen dimensions for the four-point bend tests, taken from the ISO standards, are displayed in Table 4C2.

Table 4C2: Specimen dimensions for all of the flexure tests outlined in the main body of Chapter 4, ISO 14125-98 (ISO, 1998)



Content Removed  
Due to Copyright

**Appendix 4D**

Content Removed Due to Copyright

# Chapter 5

## Finite Element Investigation into CF/PEEK Laminates for Distal Radius Fracture Fixation Plates

---

### 5.1 Introduction

The stiffness of metallic orthopaedic implants, e.g. femoral stems or fracture fixation plates, is an order of magnitude greater than the stiffness of cortical bone. Furthermore, metal implants can cause problematic artefacts when subjected to MRI and CT imaging, resulting in a range of clinical complications in terms of correctly positioning the device and post-operative assessment (Rohner et al., 2005). A limited number of orthopaedic implants (e.g. vertebral cages used for spinal fusion) manufactured from short unaligned fibre reinforced poly-ether-ether-ketone (PEEK) have been investigated (Kurtz and Devine, 2007; Rhee and Shin, 2013; Steinberg et al., 2012; Tarallo et al., 2014). However, to date, carbon fibre reinforced composite

laminates (with multiple ply orientations) have not been widely used for orthopaedic applications. Such laminated composites exhibit, a high fatigue life, a high strength to weight ratio, are radiolucent and have anisotropic material properties that can be tailored simply by altering the layup of the angled plies in the laminate. A continuous carbon fibre reinforced PEEK composite material, PEEK-OPTIMA™ Ultra-Reinforced (Invibio Ltd., Thornton-Cleveleys, UK) hereafter referred to as CF/PEEK, has been cleared for implantation in humans by the FDA. This study will investigate the use of CF/PEEK laminates for fracture fixation plates, highlighting the requirement of multi-scale finite element modelling for identification of optimal ply layups and failure mechanisms.

The first part of this study entails a macro-scale analysis of CF/PEEK distal radius fracture fixation plates (DRP). All material properties and material damage and failure parameters are based on the recent multi-axial experimental characterisation of CF/PEEK by Gallagher et al. (Gallagher et al., 2018). Several layup designs are considered, and the mechanical performance of each design is computed under physiological loading conditions. In the second part of this study, multi-axial strain states, computed using the macro-scale DRP model, are applied to representative volume elements (RVEs) of the ply microstructure to obtain a new insight into the mechanisms of intra-ply failure. This study provides the first multi-scale analysis framework for CF/PEEK orthopaedic devices.

### **5.2 Model development**

The multi-scale modelling approach implemented in the current study entails: (i) the analysis of the stress-strain distribution in the macroscopic composite distal radius

fracture fixation plates under physiological loading; (ii) analysis of intra-ply micro-structural failure mechanisms.

### **5.2.1 Macro-scale model of distal radius fracture fixation**

A generic geometry of a distal radius fracture fixation plate is created based on commercially available compression type implants (Osada et al., 2003). The fixation plate is modelled in Abaqus 2017 (SIMULIA, Providence, RI, USA) using approx. 100,000 3D continuum elements (C3D8R). The plate is attached to an idealised bone geometry through rigid screw fixations at each screw hole. Boundary conditions that replicate the loading conditions induced during physiological movements of the wrist are applied to the plated bone. Unless otherwise stated physiological loading conditions will be torsion and bending moments of  $T_x=0.68\text{Nm}$  and  $M_y=1.05\text{Nm}$  (Christen et al., 2013; Gordon et al., 2006; Hirahara et al., 2003), respectively, are applied (see Figure 5.1).

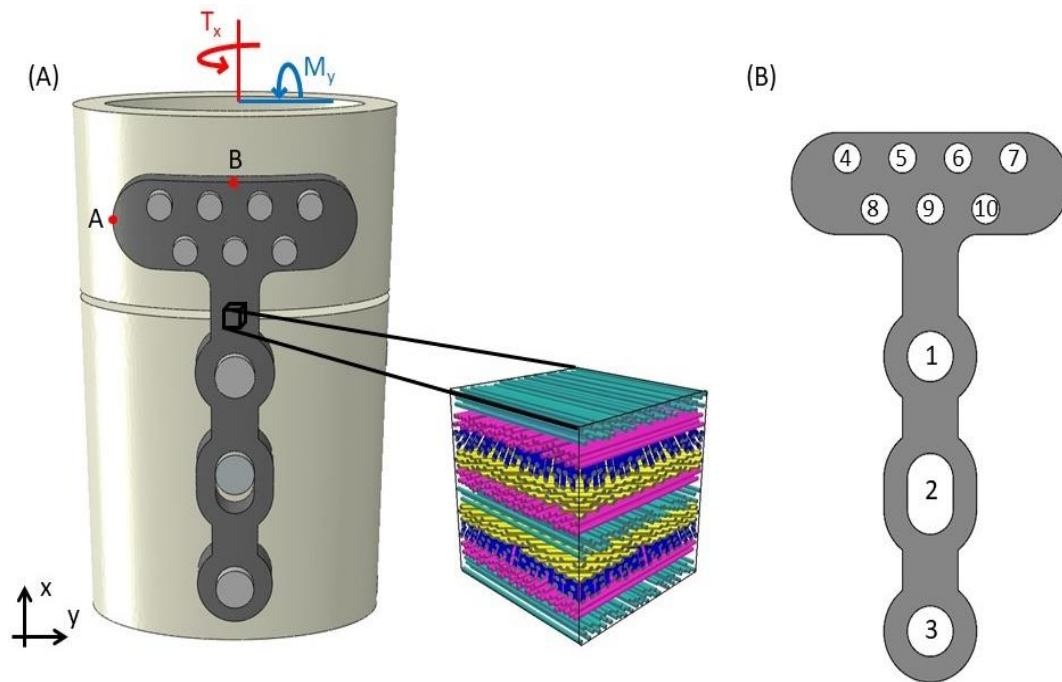


Figure 5.1: (A) Generic distal radius fracture plate geometry attached to an idealised model of a fractured distal radius. A schematic of a 3D ply layup is included for illustrative purposes (ratio of fibre diameter to ply thickness is not to scale). Boundary conditions applied to distal radius are shown. (B) Illustration of the numbering used to identify specific holes in the DRP.

To assess the design requirements of the implant and determine the optimum ply layup, five laminate layup configurations are considered:

Laminate 1: A unidirectional  $0^\circ$  CF/PEEK laminate  $[0^\circ_8]_s$ , hereafter referred to as ‘ $0^\circ$  laminate’;

Laminate 2: A unidirectional  $90^\circ$  CF/PEEK laminate  $[90^\circ_8]_s$ , hereafter referred to as ‘ $90^\circ$  laminate’;

Laminate 3: A CF/PEEK  $[\pm 45^\circ]_4s$  laminate, hereafter referred to as the ‘ $45^\circ$  laminate’;

Laminate 4: A CF/PEEK laminate with a ply layup of  $[\pm 45^\circ_2/0^\circ_4]_s$ ;

Laminate 5: A  $[0^{\circ}_2/\pm 45^{\circ}]_2$ s CF/PEEK laminate.

All laminates have an equal number of plies (16), each ply has a thickness of 0.2mm, and the fixation plates have an overall thickness of 3.2mm. The material properties for a unidirectional CF/PEEK ply are outlined in Table 5.1 from the results of Chapter 4. In addition to comparing the performance of the laminate designs above, a homogeneous and isotropic titanium plate is simulated (Table 5.1).

### 5.2.2 Laminate computational damage and failure model

Fibre reinforced composite materials can exhibit a number of damage and failure mechanisms, which depend on the mode of loading. Damage mechanisms reported in Chapter 4 include anisotropic plasticity, intra-laminar crack propagation and inter-laminar delamination. The calibrated and validated damage and failure model for CF/PEEK developed in Chapter 4 is used to analyse the performance of the composite implants described in Section 5.2.1.

The CF/PEEK material properties along with the calibrated material parameters for the damage and failure formulations previously described are listed in Table 5.1 below.

Table 5.1: Elastic material properties and tensile, compressive and shear strengths, inter-laminar CZM model parameters and anisotropic plasticity model parameters for macro-scale DRP simulations. Material properties for simulation of titanium DRP also presented.

CF/PEEK			
$E_{11} = 175.4 \text{ GPa}$	$X_T = 2882 \text{ MPa}$	$\sigma_y = 111 \text{ MPa}$	$\sigma_{max} = 49.5 \text{ MPa}$
$E_{22} = 9.4 \text{ GPa}$	$Y_T = 50 \text{ MPa}$	$R_{11} = 250$	$\tau_{max} = 37 \text{ MPa}$
$E_{33} = 9.4 \text{ GPa}$	$X_C = 1182 \text{ MPa}$	$R_{22} = 1.0$	$\delta_n = 10 \text{ }\mu\text{m}$
$\nu_{12} = 0.38$	$Y_C = 186 \text{ MPa}$	$R_{33} = 1.0$	$\delta_t = 10 \text{ }\mu\text{m}$
$\nu_{13} = 0.38$	$S = 96 \text{ MPa}$	$R_{12} = 0.64$	
$\nu_{23} = 0.46$	$G_{ic} = 1.44 \text{ kJ/m}^2$	$R_{13} = 0.64$	
$G_{12} = 5.2 \text{ GPa}$	$G_{iic} = 1.0 \text{ kJ/m}^2$	$R_{23} = 1.0$	
$G_{13} = 5.2 \text{ GPa}$			
$G_{23} = 1.9 \text{ GPa}$			
Titanium (Niinomi, 1998)			
$E = 112 \text{ GPa}$			
$\nu = 0.3$			
$\sigma_y = 847 \text{ MPa}$			

### 5.3 Micro-mechanical model of CF/PEEK micro-structure

Accumulations of micro-mechanical damage, such as fibre matrix debonding, can result in catastrophic failure of the laminate on a macro-scale. However, damage on

a micro-scale is not predicted by the macro-scale analysis of the DRPs. Therefore, a micro-scale damage model is developed to gain an enhanced understanding of the micro-failure mechanisms of the composite fracture fixation plate under physiologically relevant loads. Micro-scale representative volume elements (RVE's) with fibre volume fractions (FVF) of 62% are constructed (a sample RVE is shown in Figure 5.2(A)). A Python script is developed to implement a random sequential adsorption algorithm to randomly distribute the carbon fibres within the matrix. Generating the RVE in this manner leads to difficulties in FVFs greater than 54% as a result of fibres overlapping causing errors, and in generally it took several attempts to generate an RVE with 60% FVF. If a randomly generated fibre intersects the edge of the RVE another fibre is mirrored on the opposite face of the RVE to maintain periodicity. The RVE's used in this study have an overall size of  $50 \times 50 \mu\text{m}$  and a fibre diameter of  $5 \mu\text{m}$ .

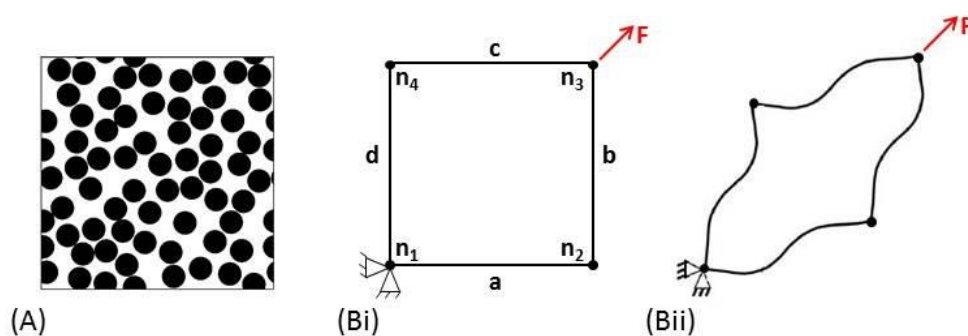


Figure 5.2: (A) Illustration of the micro-mechanical representative volume elements with a 62% fibre volume fraction. (B) Schematic of the periodic boundary conditions applied to the RVE.

Periodic boundary conditions (Dowling et al., 2013) are applied along the boundaries of the RVEs to ensure that opposing faces remain parallel. The equations have been expressed in terms of nodal displacements vectors,  $\mathbf{u}$ , in equations 5.1 and 5.2,

$$\mathbf{u}_a = \mathbf{u}_c - \mathbf{u}_{n4} \quad 5.1$$

$$\mathbf{u}_d = \mathbf{u}_b - \mathbf{u}_{n2} \quad 5.2$$

where, the subscripts  $a$ ,  $b$ ,  $c$  and  $d$  relate to nodes located on each face of the RVE and the subscripts  $n_2$ ,  $n_3$  and  $n_4$  correspond to the nodes located at the corners of the RVE, demonstrated in Figure 5.2 (Bi) and (Bii). The CZM model (equations 4.8-4.11) is used to simulate debonding of the matrix material from the embedded CFs. CZM characteristic lengths of  $1 \times 10^{-3} \mu\text{m}$  are applied at the fibre matrix interface (Cooper and Chyung, 1987; O'Dwyer et al., 2013). Tensile tests are simulated on the micro-structural RVEs to calibrate the interface strength between individual fibres and the surrounding PEEK matrix. The normal and transverse interface strengths are assumed to be equal. The fracture energy of the fibre-matrix interface, which is a commonly reported value for CZ interfaces, can be easily calculated once the interface strengths and characteristic lengths are calibrated. Results are validated using experimental data for aligned  $90^\circ$  tension tests from Chapter 4. Following calibration, the multi-axial strain state at the point of initial failure in a DRP is applied to the RVE to determine the microstructural failure mode under physiological loading.

Table 5.2: Material properties of the PEEK matrix material and the embedded carbon fibres used in micro-mechanical simulations of RVE micro-structure.

Carbon fibre (Banerjee and Sankar, 2014)	PEEK (Kurtz and Devine, 2007)
$E_{11} = 263 \text{ GPa}$	$E = 4 \text{ GPa}$
$E_{33} = E_{22} = 19 \text{ GPa}$	$\nu = 0.36$
$\nu_{12} = \nu_{13} = 0.2$	$\sigma_{y_t} = 108 \text{ MPa}$
$\nu_{23} = 0.35$	$\sigma_{y_c} = 142 \text{ MPa}$
$G_{12} = G_{13} = 27.6 \text{ GPa}$	
$G_{23} = 7.04 \text{ GPa}$	

Neat PEEK material has been shown to exhibit asymmetric yielding, with a higher yield stress in compression than in tension. Furthermore, the plastic yielding of PEEK has been shown to be rate dependent in both tension and compression (Rae et al., 2007). The strain sensitive extended Drucker-Prager model is used to simulate yielding of PEEK matrix material that surrounds the fibres in the micro-structural RVE model. The deviatoric stress measure is defined as:

$$t = \frac{q}{2} \left[ 1 + \frac{1}{K} - \left( 1 - \frac{1}{K} \right) \left( \frac{r}{q} \right)^3 \right] \quad 5.3$$

where  $K$  is the ratio of flow stress in triaxial tension to flow stress in triaxial compression,  $q$  is the Mises equivalent stress and  $r$  is the third invariant of deviatoric stress. This formulation allows for different yield values in tension and compression,

as is the case with PEEK (Rae et al., 2007). To ensure convexity of the yield surface  $0.778 \leq K \leq 1.0$ . The yield surface is defined as:

$$F = t - p \tan \beta - d = 0 \quad 5.4$$

where  $p$  is the equivalent pressure stress ( $p = -\frac{1}{3} \text{trace}(\sigma)$ ),  $\beta$  is the friction angle of the material and  $d$  is the hardening parameter which measures the cohesion of the material. The linear form of the Drucker-Prager model for tri-axial compression is outlined below:

$$\sigma_1 - \sigma_3 + \frac{\tan \beta}{2 + \frac{1}{3} \tan \beta} (\sigma_1 + \sigma_3) - \frac{1 - \frac{1}{3} \tan \beta}{1 + \frac{1}{6} \tan \beta} \sigma_c^0 = 0 \quad 5.5$$

The compressive and tensile yield strengths of unreinforced PEEK have been determined experimentally to be 108MPa and 142MPa, respectively (Rae et al., 2007). Using these yield strength values returns values of  $\phi = 7.82^\circ$  and  $c = 61.9\text{MPa}$  for the friction angle and the matrix cohesion, respectively and the following Drucker-Prager parameters are calculated for PEEK  $K = 0.913$ ,  $\beta = 15.9^\circ$  and  $\sigma_c^0 = 141.96\text{MPa}$ .

## 5.4 Results

### 5.4.1 Macro-scale model of composite fracture fixation plate

Bending, torsion, and combined bending-torsion loading are applied to all laminated fixation plates. Failure loads and failure modes for each of the laminate layups are listed in Table 5.3 - Table 5.5. A Factor of Safety (FoS) for each laminate is also

computed based on published physiological loads (0.68Nm torsion and 1.05Nm bending moment).

Table 5.3: Bending failure modes, applied moments at failure, and failure locations for all laminate layups.

Laminate layup	Mode of failure and location	Bending moment at failure (Nm)	Computed FoS
$[0^{\circ}_8]$	Intra-laminar transverse tensile crack Ply 1 ( $0^{\circ}$ ) at a screw hole 9	4.85	4.62
$[90^{\circ}_8]$	Intra-laminar transverse tensile crack Ply 1 ( $90^{\circ}$ ) (see Figure 5.3(A))	0.325	0.31
$[\pm 45^{\circ}]_4s$	Intra-laminar transverse tensile crack Ply 1 ( $45^{\circ}$ ) at a screw hole 8	1.20	1.14
$[\pm 45^{\circ}_2/0^{\circ}_4]s$	Intra-laminar transverse tensile crack Ply 1 ( $45^{\circ}$ ) at a screw hole 9 Ply 2 ( $-45^{\circ}$ ) at edge of implant where distal end joins the main shaft	3.51	3.34
$[0^{\circ}_2/\pm 45^{\circ}]_2s$	Intra-laminar transverse tensile crack Ply 1 ( $0^{\circ}$ ) at a screw hole 9	4.5	4.29

Examining the computed FoSs listed in Table 5.3, it is clear that the laminate layup has a significant effect on the strength and failure location of the DRP in bending. The  $0^{\circ}$  laminate, whose fibres are aligned in the x-axis parallel to the axis of the radius bone, has the highest predicted FoS in bending of 4.62. The  $0^{\circ}$  laminate is predicted to fail at an applied bending moment of 4.85Nm. The  $90^{\circ}$  laminate, which has fibres aligned along the y-axis, provides very little resistance to the applied bending moment. An intra-laminar matrix crack is predicted to initiate at an applied

bending moment of only 0.325Nm (see Figure 5.3(A)), more than ten times lower than the failure moment of the 0° laminate. The 45° laminate has a predicted FoS of 1.14, with the outermost plies predicted to fail due to a tensile matrix crack at an applied bending load of 1.2Nm. The predicted mode of failure for the  $[\pm 45^\circ_2/0^\circ_4]_s$  laminate is intra-laminar tensile matrix cracking of the outermost 45° and -45° plies (ply 1&2) at an applied bending moment of 3.51Nm. The  $[0^\circ_2/\pm 45^\circ]_2s$  laminate design is predicted to fail at an applied bending moment of 4.5Nm. Similar to the 0° laminate, the predicted mode of failure is an intra-laminar matrix crack of the outermost ply at the edge of a screw hole.

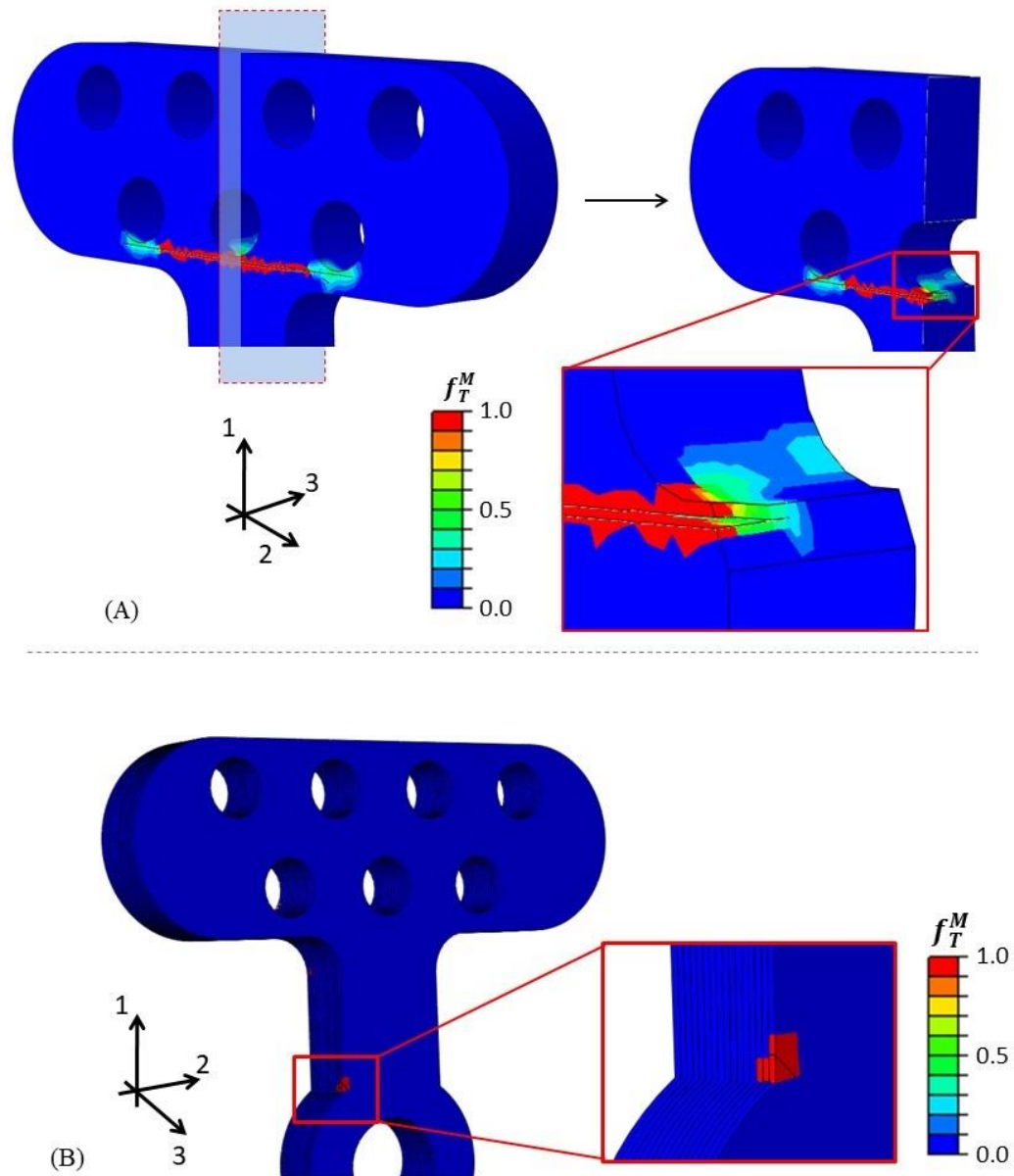


Figure 5.3: (A) Computed crack propagation in the  $90^\circ$  laminated fixation plate at an applied bending moment of 1.4Nm, where  $f_T^M$  is the tensile failure criterion (1.0 depicts an element that is fully cracked). (B) Computed crack propagation in the  $[\pm 45^\circ_2/0^\circ_4]_s$  laminated fixation plate at an applied torque of 1.78Nm.

All DRP designs fail at applied bending moments greater than physiological loads, apart from the  $90^\circ$  DRP. The  $[\pm 45^\circ_2/0^\circ_4]_s$  and  $[0^\circ_2/\pm 45^\circ]_2s$  laminates have an equal number of  $0^\circ$  and  $\pm 45^\circ$  plies in their layup. However, a higher FoS is predicted for the  $[0^\circ_2/\pm 45^\circ]_2s$  laminate. In the  $[\pm 45^\circ_2/0^\circ_4]_s$  laminate all the  $0^\circ$  plies are located near the centre of the DRP, whereas in the case of the  $[0^\circ_2/\pm 45^\circ]_2s$

laminate the  $0^\circ$  plies are positioned on the outer surfaces of the DRP, thus providing a higher bending strength (28% greater than the  $[\pm 45^\circ_2/0^\circ_4]_s$  design).

Table 5.4: Torsional failure modes, applied torques at failure, and failure locations for all laminate layups.

Laminate layup	Mode of failure and location	Torsional moment at failure (Nm)	Computed FoS
$[0^\circ_8]$	Intra-laminar transverse tensile crack Ply 16 ( $0^\circ$ ) at a screw hole 1	0.93	1.37
$[90^\circ_8]$	Intra-laminar transverse tensile crack Ply 1 ( $90^\circ$ ) mid-line of main shaft of implant	0.97	1.43
$[\pm 45^\circ]_4s$	Intra-laminar transverse tensile crack Plies 16 ( $45^\circ$ ), 14 ( $45^\circ$ ) & 2 ( $-45^\circ$ ) at laminate edge where main shaft meets hole 1	1.63	2.40
$[\pm 45^\circ_2/0^\circ_4]_s$	Intra-laminar transverse tensile crack Plies 16 ( $45^\circ$ ), 15 ( $-45^\circ$ ), 14 ( $45^\circ$ ), 3 ( $45^\circ$ ) & 2 ( $-45^\circ$ ) at laminate edge (see Figure 5.3(B))	1.78	2.62
$[0^\circ_2/\pm 45^\circ]_2s$	Intra-laminar transverse tensile crack Ply 16 ( $0^\circ$ ) at a screw hole 1	1.22	1.79

As shown in Table 5.4, all DRP designs fail at applied torsional loads greater than physiological value ( $T_x=0.68\text{Nm}$ ). However, despite its high FoS in bending, the  $0^\circ$  laminate has the lowest FoS (1.37) in torsion, failing at an applied torque of  $0.93\text{Nm}$ , demonstrating that a design consisting of only  $0^\circ$  fibres does not provide a high

resistance to torsional failure. In contrast, the predicted FoS of the 90° DRP in torsion is three times greater than the FoS predicted for the 90° plate in bending. The highest FoS for torsional loading is predicted for the 45° laminate design (FoS=2.4). Failure occurs due to an intra-laminar matrix cracking parallel to the fibres in the first 45° ply at an applied torque of 1.63 Nm. Failure in the  $[\pm 45^\circ_2/0^\circ_4]_s$  DRP is predicted to occur due to intra-laminar matrix cracking in the outermost 45° plies at an applied torque of 1.78Nm. The  $[0^\circ_2/\pm 45^\circ]_2s$  DRP is predicted to fail due to an intra-laminar matrix crack at an applied torque of 1.22Nm. The predicted torsional FoS for the  $[\pm 45^\circ_2/0^\circ_4]_s$  and the  $[0^\circ_2/\pm 45^\circ]_2s$  laminates, 2.62 and 1.79, respectively, are lower than the corresponding values of FoS in bending (3.34 and 4.29, respectively).

DRP failure under combined bending/torsion loading is reported in Table 5.5. A ratio of applied bending moment to applied torque of  $My/Tx = 1.54$  is maintained throughout each simulation, based on physiologically measured values (Christen et al., 2013; Gordon et al., 2006; Hirahara et al., 2003).

Table 5.5: Combined bending and torsion failure modes and failure locations for all laminate layups.

Laminate layup	Mode of failure and location	Combined moment at failure (Nm)	Computed FoS
$[0^{\circ}_8]$	Intra-laminar transverse tensile crack Ply 16 ( $0^{\circ}$ ) at a screw hole 1	$My = 1.50$ Nm, $Tx = 0.97$ Nm	1.43
$[90^{\circ}_8]$	Intra-laminar transverse tensile crack Ply 1 ( $90^{\circ}$ ) mid-line of main shaft of implant	$My = 0.30$ Nm, $Tx = 0.19$ Nm	0.29
$[\pm 45^{\circ}]_4s$	Intra-laminar transverse tensile crack Ply 2 ( $-45^{\circ}$ ) at laminate edge	$My = 1.34$ Nm, $Tx = 0.87$ Nm	1.28
$[\pm 45^{\circ}_2/0^{\circ}_4]s$	Intra-laminar transverse tensile crack Ply 2 ( $-45^{\circ}$ ) at laminate edge (Figure 5.4(A))	$My = 1.81$ Nm, $Tx = 1.17$ Nm	1.72
$[0^{\circ}_2/\pm 45^{\circ}]_2s$	Intra-laminar transverse tensile crack Plies 16 & 15 ( $0^{\circ}$ ) at hole 1 (Figure 5.4(B))	$My = 2.1$ Nm, $Tx = 1.36$ Nm	2.0

The highest FoS is computed for the  $[0^{\circ}_2/\pm 45^{\circ}]_2s$  laminate (FoS=2), followed by the  $[\pm 45^{\circ}_2/0^{\circ}_4]s$  laminate (FoS=1.72) are the only layups that will not fail within the allowable FoS under bending and torsional loading alone as well as under combined loading. In the case of the  $[\pm 45^{\circ}_2/0^{\circ}_4]s$  laminate, a crack is predicted in the outermost  $-45^{\circ}$  ply (ply 2) at the laminate edge (Figure 5.4(A)). In the case of the  $[0^{\circ}_2/\pm 45^{\circ}]_2s$  laminate, a crack is predicted in the outermost  $0^{\circ}$  plies (plies 16 & 15) at a screw hole (Figure 5.4(B)).

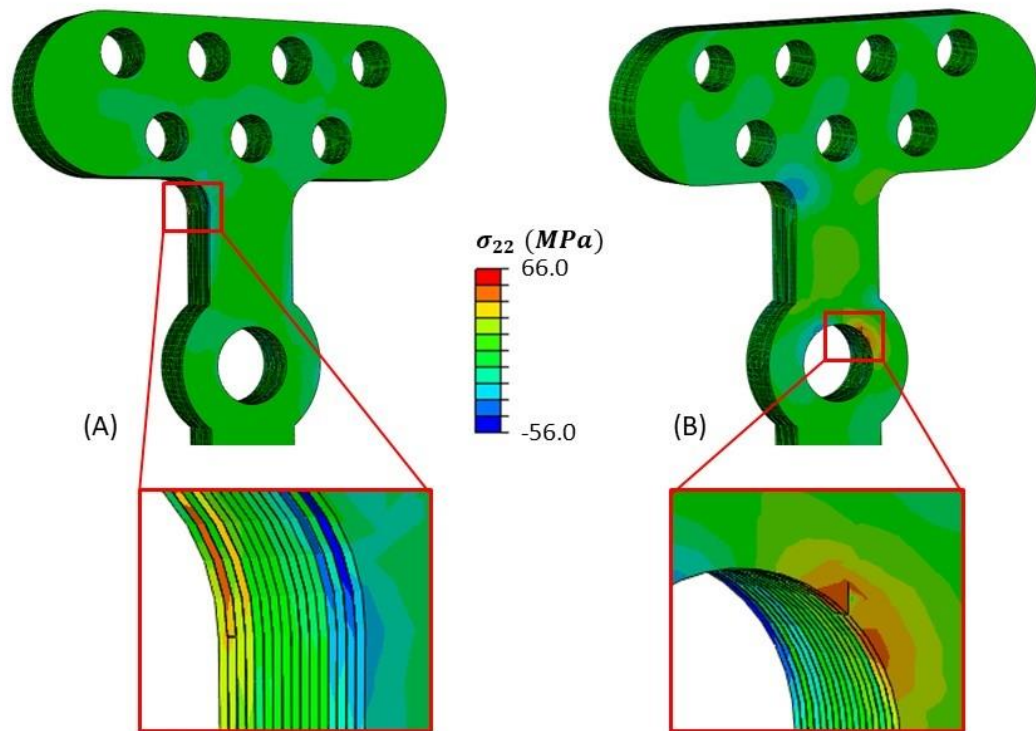


Figure 5.4: Predicted intra-laminar transverse tension cracks under combined bending-torsion loading for: (A) the  $[\pm 45^\circ_2/0^\circ_4]_s$  DRP; and (B) the  $[0^\circ_2/\pm 45^\circ]_s$  DRP. Contours depict the distribution of transverse stress ( $\sigma_{22}$ ) for an applied load of  $M_y = 1.81\text{Nm}$  and  $T_x = 1.17\text{Nm}$ .

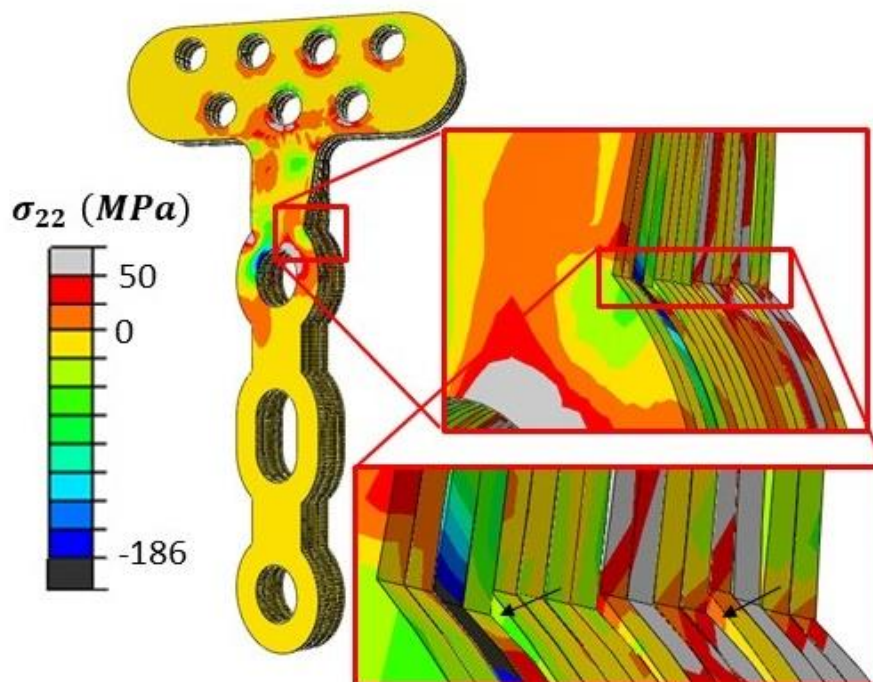


Figure 5.5: Contour plot of the transverse stress ( $\sigma_{22}$ ) distribution in the  $[0^\circ_2/\pm 45^\circ]_{2s}$  laminate at the point of inter-laminar failure under combined loads of  $M_y = 4.58\text{Nm}$ ,  $T_x = 2.96\text{Nm}$ , i.e. 4.4 times greater than physiological loading. Predicted mode II delamination is highlighted in the insert by black arrows.

The initial failure of each DRP design in bending, torsion and combined loading is computed to occur due to intra-laminar cracking. We next examine the required load to induce inter-ply delamination in the  $[0^\circ_2/\pm 45^\circ]_{2s}$  design. Figure 5.5 shows the transverse stress distribution ( $\sigma_{22}$ ) in the  $[0^\circ_2/\pm 45^\circ]_{2s}$  laminate at applied loads of  $M_y = 4.58\text{Nm}$ ,  $T_x = 2.96\text{Nm}$  (a factor of 4.4 times higher than physiological loading and 2.2 times higher than the load at initial intra-ply cracking). Significant levels of mode II delaminations are predicted in the shaft of the DRP around the first screw hole (highlighted in the insert). Under pure torsion the  $[0^\circ_2/\pm 45^\circ]_{2s}$  laminate undergoes mode II inter-ply delaminations at an applied load of  $3.0\text{Nm}$ , 2.5 times higher than the load at which intra-laminar cracking initiates. In the pure bending,

inter-ply delamination is not predicted in the  $[0^\circ_2/\pm 45^\circ]_2s$  laminate at applied bending moments of 7.4 Nm, more than seven times greater than physiological loads. A comparison of the stiffness and strength of the laminated DRP designs with a titanium implant of identical dimensions is shown in Figure 5.6. All laminated DRP curves are plotted up to the point of intra-laminar cracking, whereas the curve for the titanium plate is plotted up to the point at which the von Mises stress reaches the yield stress (825 MPa; see Table 5.1). As shown in Figure 5.6(A), the bending stiffness of a laminated plate is highly dependent on the layup design. For example, the  $0^\circ$  and  $[0^\circ_2/\pm 45^\circ]_2s$  DRP exceed the bending stiffness of a titanium plate. In contrast, the bending stiffness of the  $[\pm 45^\circ_2/0^\circ_4]s$  DRP is ~50% of the titanium DRP. In torsion, all laminated DRP designs are significantly more compliant than the titanium DRP. In general, Figure 5.6 illustrates the potential of laminated plate design to reduce stress shielding (associated with high stiffness metallic plates) while providing adequate strength to support physiological loading (see FoS values reported in Table 5.3-Table 5.5).

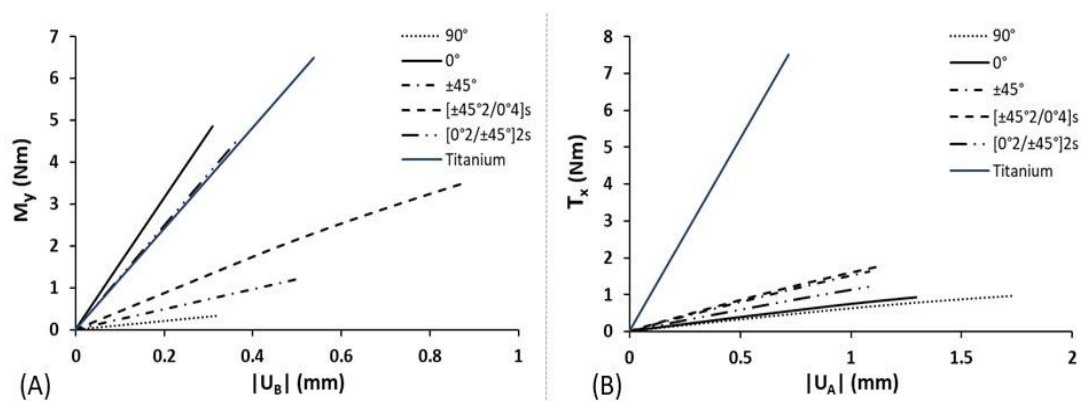


Figure 5.6: (A) Applied bending moment versus deflection of Point B (see Figure 5.1) for all laminate layups and for titanium DRP. (B) Applied torque versus deflection of Point A (see Figure 5.1) for all laminate layups and for titanium DRP. Curves are plotted up to the point of failure. Failure for the titanium plate is characterised by the onset of plastic deformation.

### 5.4.2 Micro-scale model of fibre-matrix debonding in RVE

As indicated in Table 5.3 - Table 5.5, intra-laminar tensile matrix cracking (equation 4.12) is the initial failure mode of every single laminate DRP. While the layup design and the mode of loading strongly influences the crack location and FoS, for all prototype layup designs intra-laminar matrix cracking is predicted as the initial failure mode. The model parameters,  $Y_T$  and  $S$ , associated with this failure mode were calibrated and validated in a recent experimental-computational analysis of CF/PEEK. However, such macro-scale damage modelling does not uncover the precise failure mechanism that results in intra-laminar tensile matrix cracking. Here we perform a micro-mechanical analysis of a micro-structural RVE (as described in Section 5.3) to determine if intra-laminar tensile matrix cracking results from (i) ductile failure of the PEEK matrix, or (ii) localised debonding of the PEEK matrix from CFs.

#### Micro-mechanical model calibration

The elastic plastic matrix material behaviour, including asymmetric yielding, has been experimentally characterised in Chapter 4 and Drucker-Prager material parameters are given in Section 5.3. However, the interface strength ( $\sigma_{max}$ ) between the matrix and the CFs has not previously been determined. Here we perform a parametric study to determine the interface strength, and consequently the failure mechanism, by comparing model predictions to experimental transverse tensile data from Chapter 4.

In Figure 5.7(A) the predicted RVE stress-strain behaviour is compared to experimental data for a range of interface strengths. For a high interface strength ( $\sigma_{max} = 500$  MPa) matrix-fibre debonding is not computed. The stress-strain curve

is stiffer than the experimental curve for strains greater than 0.001. A yield point is predicted at a stress of  $\sim 100$  MPa, followed by strain hardening. Such behaviour is not observed experimentally, specimen failure was observed at an ultimate strength of  $49.6 \pm 3.92$  MPa without any distinct yielding or strain hardening. An interface strength of  $\sigma_{max} = 110$  MPa results in the prediction of an ultimate strength of  $51.6 \pm 3.93$  MPa. Similar to experimental observation, the slope of the RVE stress-strain curve is predicted to reduce as a result of progressive fibre-matrix debonding as the strain applied to the RVE is increased. Reduction of the interface strength to a value lower than 110 MPa results in an under-prediction of the ultimate strength of the RVE. Figure 5.7(B) shows the predicted stress-strain curves and ultimate strength of five RVE geometries. Again, an interface strength of 110 MPa is used. Each RVE has a different randomly generated fibre distribution, with a fibre volume fraction of 62%. A reasonable match with experimental data is observed for all RVEs. A computed ultimate strength of  $51.6 \pm 3.93$  MPa at a strain of  $0.0058 \pm 0.0005$  is statistically similar ( $t(4) = -1.01$ ,  $p=0.37$ ) to the experimental ultimate strength of  $49.6 \pm 3.92$  MPa at a measured strain of  $0.0054 \pm 0.0005$ . Figure 5.7(C) shows that stress in the matrix material is reduced locally in region adjacent to a debonded surface. Figure 5.7(D) shows the significant levels of fibre-matrix debonding at the point of failure of the RVE. Furthermore, Figure 5.7(D) shows that the significant plastic deformation does not occur in the matrix during loading to failure. This further demonstrates that fibre-matrix debonding is the underlying failure mechanism in  $90^\circ$  tensile laminate tests, rather than plastic deformation or damage of the matrix material. In Figure 5.7(E) the jagged nature of the fracture surface of a transverse tensile experimental specimen is shown. The discontinuous nature of the

experimental crack shown is well described by the propagation of failure in the micro-mechanical RVEs.

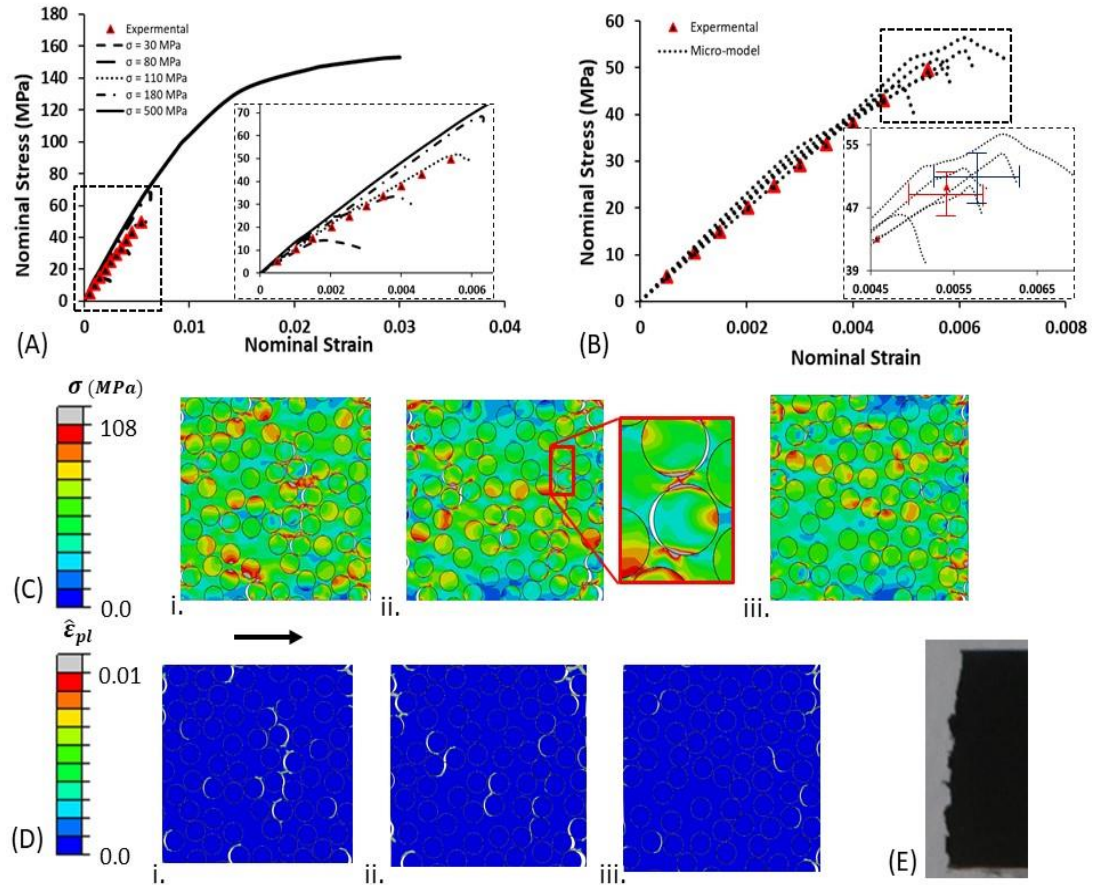


Figure 5.7: A) Computed RVE nominal stress-nominal strain curves for a range of interface strengths ( $\sigma_{max}$ ) for a single RVE geometry subjected to uniaxial tensile loading. Experimental uniaxial transverse tensile stress-strain curve (Gallagher et al., 2018) used to calibrate  $\sigma_{max}$ . B) Nominal stress-nominal strain uniaxial tension curves for five RVE geometries with interface strengths of  $\sigma_{max} = 110$  MPa. Insert shows the mean and standard deviations of failure stress and failure strain for experimental data (Gallagher et al., 2018) (red crosshairs) and the RVE predictions (navy crosshairs). C) Contour plots of the equivalent plastic strain ( $\hat{\epsilon}_{pl}$ ) distribution in three separate RVEs at the point of failure under uniaxial tension. (D) Contour plots of the von Mises stress ( $\sigma$ ) distribution in the RVEs at the point of failure under uniaxial tension. (E) Experimental image of crack propagation through  $90^\circ$  laminate from experiments carried out in Chapter 4 (Gallagher et al., 2018).

Micro-mechanical failure during macro-mechanical loading

We next use the micro-structural RVE to demonstrate that the failure mechanism of the laminated DRP is fibre-matrix debonding rather than plasticity or damage of the matrix material. Considering the  $[0^\circ_2/\pm 45^\circ]_2$ s laminated DRP, in Figure 5.8(A) we show the strain state in the outermost  $0^\circ$  ply under physiological loading levels. Recall that our macro-scale damage model predicts cracking at point A in this ply when the applied loading is increased to twice the physiological level. At physiological loading (prior to the macro-scale prediction of cracking) the in-plane strain state orthogonal to the fibre direction at point A is computed as  $\gamma_{23} = 0.0024$ ,  $\varepsilon_{22} = 0.0025$  and  $\varepsilon_{33} = 0.0014$  (corresponding to in-plane principal strains of 0.00327 and 0.00063). This strain state is applied to the micro-mechanical RVE, and the resultant micro-structural stress distribution is shown in Figure 5.8(Bi). No significant stress concentrations are observed in the matrix. Figure 5.8(Bii) shows that at physiological loading no significant plastic deformation of the matrix or debonding is computed. The macro-scale damage model predicts cracking at Point A when applied loading is increased to twice the physiological level. The corresponding strain state ( $\gamma_{23} = 0.0048$ ,  $\varepsilon_{22} = 0.005$  and  $\varepsilon_{33} = 0.0028$ ) at is applied to the RVE and the resultant micro-structural stress distribution is shown in Figure 5.8(Ci). While significant stress concentrations are computed, the matrix stress is relaxed adjacent to debonded surfaces. Significant levels of fibre-matrix debonding are computed, with 18 of the 76 fibres (24%) partially separating from the matrix. Highly localised plastic deformation of the PEEK matrix is computed in locations of stress concentrations. While higher areas of plastic deformation computed for this multi-axial loading than for uniaxial tensile loading (Figure 5.7(D)), the levels of plastic deformation in Figure 5.8(Cii) are not sufficiently high

(maximum  $\hat{\epsilon}_{pl} = 0.05$ ) to result in ductile failure of the matrix material (Rae et al., 2007), and fibre-matrix debonding is again the micro-structural failure mechanism.

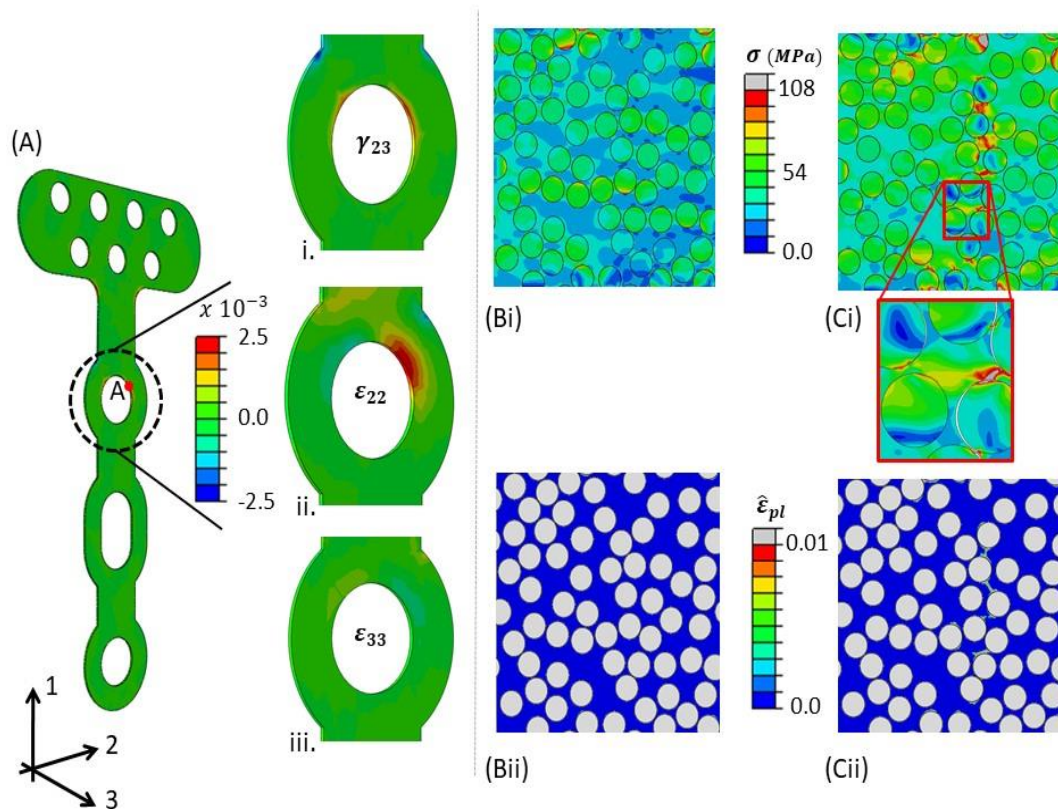


Figure 5.8: (A) Multi-axial strain state at Point A in the outermost ply of the  $[0^{\circ}_2/\pm 45^{\circ}]_2s$  laminated DRP under physiological loading ( $M_y = 1.05$  Nm,  $T_x = 0.68$  Nm). Computed strain-state is applied to micro-structural RVE. (B) Von Mises stress ( $\sigma$ ) and equivalent plastic strain ( $\hat{\epsilon}_{pl}$ ) distributions in RVE at physiological loading. (C) Von Mises stress ( $\sigma$ ) and equivalent plastic strain ( $\hat{\epsilon}_{pl}$ ) distributions in RVE at two times physiological loading. Inserts highlight matrix-fibre debonding. Macro-model predicts transverse tensile cracking at Point A at this level of applied loading.

## 5.5 Discussion

The current study demonstrates that CF/PEEK laminated DRPs can be designed with similar geometric dimensions to conventional metal plates while providing sufficient

structural strength to support physiological levels of loading. Macro-scale structural analysis of a distal radius fracture fixation plate highlights the importance of ply orientation. A high number of  $0^\circ$  plies near the outer surfaces results in a greater bending strength while the addition of  $45^\circ$  plies increases the torsional strength of the laminates. Ply layups design significantly influences the effective bending stiffness of the DRP.  $[0^\circ_2/\pm 45^\circ]_2$ s and  $0^\circ$  laminates exceed the effective bending stiffness of titanium DRP, whereas a  $[\pm 45^\circ_2/0^\circ_4]_s$  laminate provides a bending stiffness that is  $\sim 50\%$  that of a titanium DRP. All laminate designs provide an effective torsional stiffness that is significantly lower than that of a titanium DRP. However, it should be noted that the torsional stiffness of long bones is significantly lower than the bending stiffness; experiments carried out on adult femurs report a torsional stiffness of 5.0 Nm/deg, compared to a bending stiffness of 2.5 GPa (Cristofolini et al., 1996). The demonstrated potential of laminated DRPs to provide reduced bending and torsional stiffness, while still providing sufficient strength to support physiological loading, can be exploited to eliminate stress shielding associated with traditional metallic implants (Ganesh et al., 2005). While the current study does not determine an optimal device configuration, the detailed analysis of five ply layup configurations provides, for the first time, an outline of the key challenges and benefits of developing CF/PEEK laminated orthopaedic implants.

Macro-scale DRP simulations incorporate a multi-axial multi-mode damage model calibrated and validated in a recent experimental-computational study by the authors. This macro-scale damage model incorporates intra-laminar cracking, interlaminar delamination, and anisotropic plasticity. Implementation of this multi-mode damage framework for the simulation of DRPs under physiological loading predicts that intra-laminar transverse tensile crack is the primary mode of DRP failure under

physiological loading. We perform a multi-scale micro-mechanical analysis of the CF-PEEK microstructure to uncover the precise mechanism under-lying intra-laminar transverse tensile crack. Simulations reveal that this damage mechanism results from debonding of the PEEK matrix from CF fibres. Plastic strains in the matrix material are not sufficiently high to result in ductile failure of the matrix. The fibre-matrix interface strength of Optima UR is computed to be 110MPa. Reported experimental values for the fibre matrix interface strength of carbon fibre reinforced polymers have been as high as 202MPa (Sarasua et al., 1995). Fibre sizing, a process by which a film is dispersed onto the surface of the fibre in order to improve the surface chemistry, could be considered to increase the fibre-matrix adhesion (Blackketter et al., 1993; Wu et al., 2016). However to date, PEEK remains largely incompatible with most sizings, due to their low degradation temperatures ( $\sim 250^{\circ}\text{C}$ ), to overcome this new high performance thermoplastic sizing formulations are being developed (Giraud et al., 2015). Before including sizing in future CF/PEEK materials it must be taken into consideration that the lack of sizing in *CF/PEEK* has increased the materials toughness.

Through careful selection of the orientation of individual plies, the macro-scale effective anisotropy composite fracture plates can be matched to the anisotropic properties of bone, which is itself a self-assembling aligned long fibre reinforced composite material. Therefore, different laminate configurations can be designed for different areas in the body, as a function of both the physiological loading conditions and the density and anisotropy of the peri-prosthetic bone. Careful laminate design can also limit the stress concentrations near screw holes, minimizing the possibility of screw pull out. This is critically important if CF/PEEK laminates are to provide a clinically viable alternative to metal fixation plates. Laminate failure around the

screw hole will be examined in greater detail in a follow-on experimental and computational study.

## 5.6 References

- Banerjee, S., Sankar, B.V., 2014. Mechanical properties of hybrid composites using finite element method based micromechanics. *Compos. Part B Eng.* 58, 318–327. <https://doi.org/10.1016/j.compositesb.2013.10.065>
- Blacketter, D.M., Upadhyaya, D., King, T.R., King, J.A., 1993. Evaluation of fiber surfaces treatment and sizing on the shear and transverse tensile strengths of carbon fiber reinforced thermoset and thermoplastic matrix composites. *Polym. Compos.* 14, 430–436. <https://doi.org/10.1002/pc.750140510>
- Christen, P., Ito, K., Knippels, I., Müller, R., van Lenthe, G.H., van Rietbergen, B., 2013. Subject-specific bone loading estimation in the human distal radius. *J. Biomech.* 46, 759–66. <https://doi.org/10.1016/j.jbiomech.2012.11.016>
- Cooper, R., Chyung, K., 1987. Structure and chemistry of fibre-matrix interfaces in silicon carbide fibre-reinforced glass-ceramic composites: an electron microscopy study. *J. Mater. Sci.* 22.
- Cristofolini, L., Viceconti, M., Cappello, A., Toni, A., 1996. Mechanical validation of whole bone composite femur models. *J. Biomech.* 29, 525–535. [https://doi.org/10.1016/0021-9290\(95\)00084-4](https://doi.org/10.1016/0021-9290(95)00084-4)
- Dowling, E.P., Ronan, W., McGarry, J.P., 2013. Computational investigation of in situ chondrocyte deformation and actin cytoskeleton remodelling under physiological loading. *Acta Biomater.* 9, 5943–55. <https://doi.org/10.1016/j.actbio.2012.12.021>
- Feerick, E.M., Liu, X.C., McGarry, P., 2013. Anisotropic mode-dependent damage of cortical bone using the extended finite element method (XFEM). *J. Mech. Behav. Biomed. Mater.* 20, 77–89. <https://doi.org/10.1016/j.jmbbm.2012.12.004>
- Gallagher, E.A., Lamorinière, S., McGarry, P., 2018. Multi-axial damage and failure of medical grade carbon fibre reinforced PEEK laminates: Experimental testing and computational modelling. *J. Mech. Behav. Biomed. Mater.* 82, 154–167. <https://doi.org/10.1016/J.JMBBM.2018.03.015>
- Ganesh, V.K., Ramakrishna, K., Ghista, D.N., 2005. Biomechanics of bone-fracture fixation by stiffness-graded plates in comparison with stainless-steel plates. *Biomed. Eng. Online* 4. <https://doi.org/10.1186/1475-925X-4-46>
- Gordon, K.D., Kedgley, A.E., Ferreira, L.M., King, G.J.W., Johnson, J.A., 2006. Design and implementation of an instrumented ulnar head prosthesis to measure loads in vitro. *J. Biomech.* 39, 1335–1341. <https://doi.org/10.1016/j.jbiomech.2005.03.002>
- Hill, R., 1948. A Theory of the Yielding and Plastic Flow of Anisotropic Metals. *Proc. R. Soc. A Math. Phys. Eng. Sci.* 193, 281–297. <https://doi.org/10.1098/rspa.1948.0045>
- Hirahara, H., Neale, P.G., Lin, Y. Te, Cooney, W.P., An, K.N., 2003. Kinematic and torque-related effects of dorsally angulated distal radius fractures and the distal radial ulnar joint. *J. Hand Surg. Am.* 28, 614–621. [https://doi.org/10.1016/S0363-5023\(03\)00249-1](https://doi.org/10.1016/S0363-5023(03)00249-1)
- Kurtz, S.M., Devine, J.N., 2007. PEEK biomaterials in trauma, orthopedic, and spinal implants. *Biomaterials* 28, 4845–69. <https://doi.org/10.1016/j.biomaterials.2007.07.013>
- Máirtín, É.Ó., Parry, G., Beltz, G.E., McGarry, J.P., 2014. Potential-based and non-potential-

- based cohesive zone formulations under mixed-mode separation and over-closure—Part II: Finite element applications. *J. Mech. Phys. Solids* 63, 363–385. <https://doi.org/10.1016/J.JMPS.2013.08.019>
- McGarry, J.P., Ó Máirtín, É., Parry, G., Beltz, G.E., 2014. Potential-based and non-potential-based cohesive zone formulations under mixed-mode separation and over-closure. Part I: Theoretical analysis. *J. Mech. Phys. Solids* 63, 336–362. <https://doi.org/10.1016/j.jmps.2013.08.020>
- Niinomi, M., 1998. Mechanical properties of biomedical titanium alloys. *Mater. Sci. Eng. A* 243, 231–236. [https://doi.org/10.1016/S0921-5093\(97\)00806-X](https://doi.org/10.1016/S0921-5093(97)00806-X)
- O’Dwyer, D., O’Dowd, N., McCarthy, C., 2013. Numerical micromechanical investigation of interfacial strength parameters in a carbon fibre composite material. *J. Compos. Mater.* 48, 749–760. <https://doi.org/10.1177/0021998313477172>
- Osada, D., Viegas, S.F., Shah, M.A., Morris, R.P., Patterson, R.M., 2003. Comparison of different distal radius dorsal and volar fracture fixation plates: A biomechanical study. *J. Hand Surg. Am.* 28, 94–104. <https://doi.org/10.1053/jhsu.2003.50016>
- Rae, P.J., Brown, E.N., Orlor, E.B., 2007. The mechanical properties of poly(ether-ether-ketone) (PEEK) with emphasis on the large compressive strain response. *Polymer (Guildf)*. 48, 598–615. <https://doi.org/10.1016/j.polymer.2006.11.032>
- Rhee, P.C., Shin, A.Y., 2013. The rate of successful four-corner arthrodesis with a locking, dorsal circular polyether-ether-ketone (PEEK-Optima) plate. *J. Hand Surg. Eur. Vol.* 38, 767–773. <https://doi.org/10.1177/1753193413475962>
- Rohner, B., Wieling, R., Magerl, F., Schneider, E., Steiner, A., 2005. Performance of a composite flow moulded carbon fibre reinforced osteosynthesis plate. *Vet. Comp. Orthop. Traumatol.* 18, 175–182.
- Sarasua, J., Remiro, P., Pouyet, J., 1995. The mechanical behaviour of PEEK short fibre composites. *J. Mater. Sci.* 30, 3501–3508.
- Steinberg, E.L., Rath, E., Shlaifer, A., Chechik, O., Maman, E., Salai, M., 2012. Carbon fiber reinforced PEEK Optima-A composite material biomechanical properties and wear/debris characteristics of CF-PEEK composites for orthopedic trauma implants. *J. Mech. Behav. Biomed. Mater.* 17, 221–228. <https://doi.org/10.1016/j.jmbbm.2012.09.013>
- Tarallo, L., Mugnai, R., Adani, R., Zambianchi, F., Catani, F., 2014. A new volar plate made of carbon-fiber-reinforced polyetheretherketon for distal radius fracture: analysis of 40 cases. *J. Orthop. Traumatol.* 15, 277–283. <https://doi.org/10.1007/s10195-014-0311-1>
- Wu, Q., Li, M., Gu, Y., Wang, S., Yao, L., Zhang, Z., 2016. Effect of sizing on interfacial adhesion of commercial high strength carbon fiber-reinforced resin composites. *Polym. Compos.* 37, 254–261. <https://doi.org/10.1002/pc.23176>

**Appendix 5A**

In “Abaqus/Standard” implicit finite element schemes contact mechanics entails the definition of a master and a slave surface. Under finite-deformation large-sliding conditions and any given slave node may interact with any subset of master surface nodes. The subset of master surface nodes is identified by defining the nearest neighbour nodes to the point on the master surface closest to the slave node. Before defining this nodal subset, unit normal vectors for each node on the master surface must be computed. The unit normal vector is calculated by averaging the unit normal vectors of the two segments either side of a given node. As an example an interaction between master surface nodes (labelled 1, 2 and 3) and a slave surface is shown in Figure 5A1(A) and (B): The unit normal vector of node 2 is calculated by averaging the unit normal vectors of segments 1-2 and 2-3.

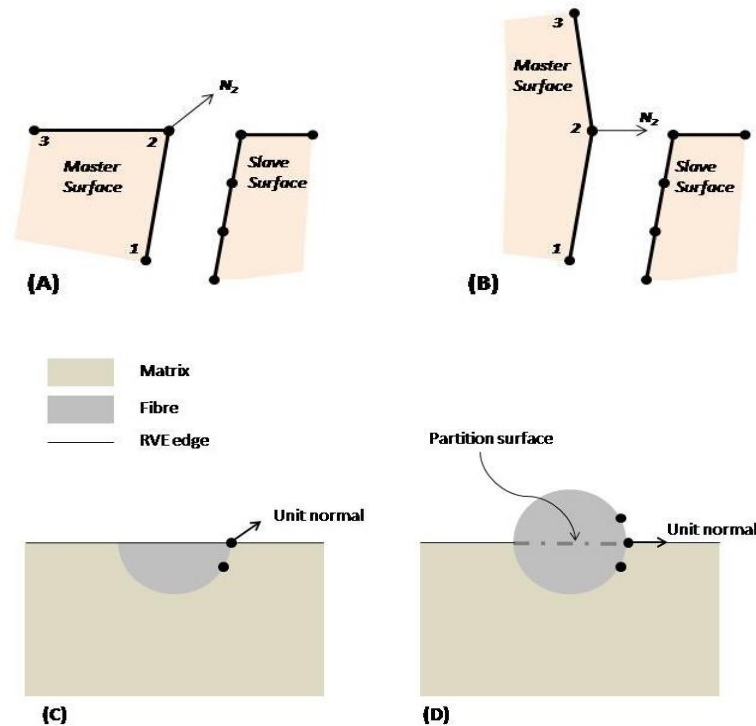


Figure 5A1: Schematic of the unit normal vector calculated for node 2 on two master surface geometries (A) and (B); illustration of the unit normal calculated for the corner node of a fibre crossing the boundary of the RVE for (C) a sectioned fibre and (D) a partitioned fibre

Examining Figure 5A1(A) and (C), it is clear that if a fibre crossing the boundary of the RVE is sectioned along the boundary edge a skewed unit normal vector will be calculated. As a result of the skewed unit normal vector numerical singularities occur on the corner nodes of the sectioned fibres. However, if the fibre is left whole, demonstrated in Figure 5A1(B) and (D), the correct normal vector is calculated. For this study the fibres crossing the borders of the RVE have not been sectioned but partitioned in line with the edge of the RVE, leaving a “dummy portion” of the fibre on the outside of the RVE. Such “dummy portions” do not provide any structural contribution to the model, but are merely used to define correct normal vectors for contact calculations at the face of the RVE. The periodic boundary conditions are applied along the fibre partition so that the periodic deformation of the RVE is correctly implemented.

**Appendix 5B**

Content Removed Due to Copyright

# Chapter 6

## Mechanical Response of CF/PEEK Laminates with Open Holes and Filled Holes

---

### 6.1 Introduction

As has been discussed in previous chapters, complex multi fragment fractures of human bone frequently occur after high impact traumas, such as a car accident or sporting injury. Large gaps between the bone fragments often result. Such complex fractures rarely heal properly with plaster cast alone and commonly result in a malunion and/or non-union of the fracture (El-Karef, 2005; Toivanen et al., 2001). With severely comminuted fractures, internal fixation of the fracture is the accepted clinical best practice. There are different types of commercially available fixation devices, including: compression plate systems, locked plate systems, and locking compression plate systems. A common feature of all such devices is that screws are

used to anchor the plates to the fractured bone. Depending on the fracture location (wrist, clavicle, femur etc.), and the design features of the fixation plate, the number of screws used to secure the implant to the bone can range from 4 to more than 20 (e.g. the 3.5mm curved LCP implant (DePuy Synthes, Raynham, MA, USA) contains 20 screw holes). When trauma and fracture fixation devices are implanted, the number of holes that are filled with screws is at the surgeon's discretion. However, the number of screws has been shown to have an effect on the stability of the fracture fixation and the rate of fracture healing (Nourisa et al., 2015; Stoffel et al., 2003). It is common for implanted fracture fixation plates to have both filled and open holes.

This thesis presents the first investigation of unidirectional carbon fibre reinforced poly-ether-ether-ketone (PEEK) laminates as a candidate material for the next-generation of fracture fixation plates. In Chapter 4, extensive experimental characterisation of the material properties of a medical grade unidirectional carbon fibre reinforced PEEK composite material PEEK-OPTIMA™ Ultra-Reinforced (Invibio Ltd., Thornton-Cleveleys, UK), hereafter called CF/PEEK, has been carried out. A comprehensive computational damage and failure model using a combined XFEM/CZM computational framework was calibrated and validated for CF/PEEK under multi-axial loading conditions. In chapter 5 key design insights were provided by this modelling framework for laminated CF/PEEK distal radius fracture fixation devices subjected to physiological loading.

It has been widely reported that drilling holes in fibre reinforced laminates has a direct effect on the laminate strength (Awerbuch and Madhukar, 1985; Panchagnula and Palaniyandi, 2017). The amount of damage prior to failure is influenced by the number and sequence of  $0^\circ$ ,  $90^\circ$  and  $\pm 45^\circ$  laminates in the laminate (O'Higgins et

al., 2008; Riccio et al., 2014). It is therefore imperative that the computational modelling framework developed in Chapter 4 should be further investigated using experimental test data for specimens containing drilled holes. In the current chapter, tensile and compressive tests are carried out on two laminate layups for both open hole and filled hole configurations. Digital image correlation (DIC) is carried out during the tests to accurately measure the strain distribution in the region of the hole throughout the experiment. The experiments are simulated using the previously developed combined XFEM/CZM computational model and the failure predictions are compared with the experimental results.

## 6.2 Materials and methods

### 6.2.1 Experimental methods

The material tested is a medical grade continuous carbon fibre reinforced poly-ether-ether-ketone (PEEK). The CF/PEEK prepreg (0.2mm thick) is consolidated into laminated panels with angled plies using the compression moulding method in accordance with the standards ASTM D5687 (ASTM D5687, 2002). The resulting thickness of the laminated plates is determined by the number of plies in the layup. The following laminates were prepared:

Laminate 1:  $[0^\circ / +45^\circ / -45^\circ / 90^\circ / 0^\circ / +45^\circ / -45^\circ / 90^\circ / 90^\circ / -45^\circ / +45^\circ / 0^\circ / 90^\circ / -45^\circ / +45^\circ / 0^\circ]$ , hereafter referred to as  $[0^\circ/\pm 45^\circ/90^\circ]_2s$ . Laminate 1 has a thickness of 3.2mm.

Laminate 2:  $[0^\circ / 90^\circ / 0^\circ / 90^\circ / 0^\circ / 90^\circ / 90^\circ / 0^\circ / 90^\circ / 0^\circ / 90^\circ / 0^\circ]$ , hereafter referred to as  $[0^\circ/90^\circ]_3s$ . Laminate 2 has a thickness of 2.4mm.

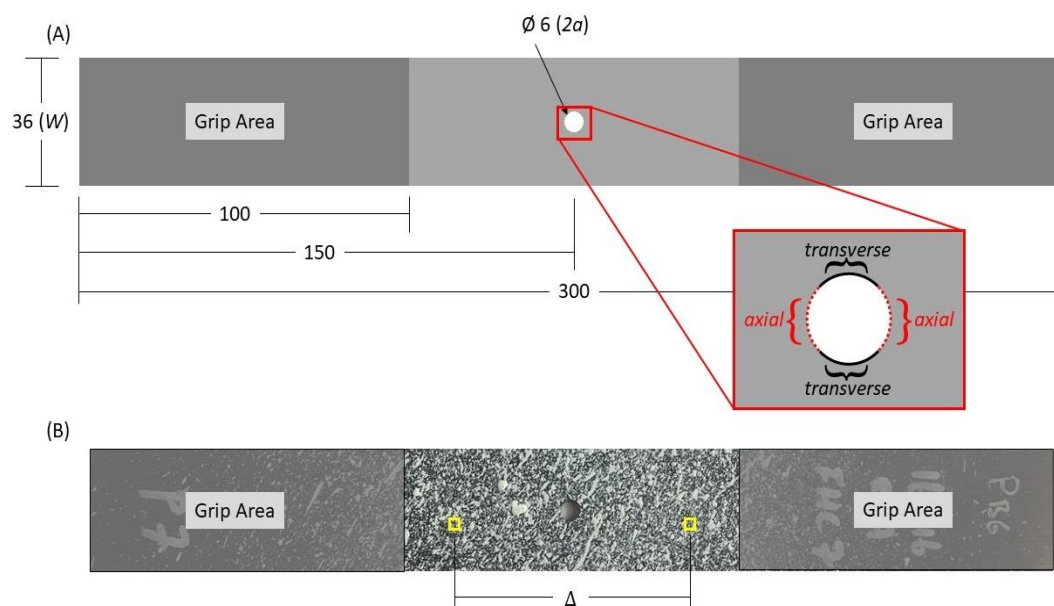


Figure 6.1: (A) Specimen dimensions for the open and filled hole tension and compression tests (all dimensions are in mm), insert demonstrates the transverse and axial sections of the hole. (B) Experimental image of sample showing the speckled paint pattern, the approximate marker positions for the nominal strain calculation are illustrated (in yellow).

Test specimens are cut from the laminate panels using a composite cutting machine with a diamond-coated cutting blade. The specimen geometry is outlined in Figure 6.1, conforming with the test standards (ASTM D5766, ASTM D6484 and ASTM D6742 (ASTM, 2014, 2012, 2002)). It is essential that high quality holes are machined in the test specimens, i.e. visual inspection of the machined hole should not reveal any delaminations, fibre pull-out, chip out, or micro-damage. Holes are drilled and then reamed to the final diameter using carbide tools so that processing induced damage is minimised. The hole radius  $a$  is chosen so that  $2a/W = 0.166$  for all specimens, where  $W$  is the width of the laminate. A stainless-steel pin (diameter 6mm) is inserted into the holes with a location/transition fit for the filled hole experiments.

Five specimens for each laminate layup are tested to failure for all four experimental investigations: open hole tension, open hole compression, filled hole tension and filled hole compression (hereafter referred to as OHT, OHC and FHC, respectively). The notched tensile ( $S_{OHT}$ ) and compressive ( $S_{OHC}$ ) strength of the laminates are determined from the OHT and OHC tests, respectively. The results of the OHC experiments will be compared with the results of the FHC experiments, to determine what effect, if any, the filled hole has on the progression of damage, crack propagation and failure point in the laminates. Digital image correlation (DIC) is implemented to measure the localised displacement in the vicinity of the hole up to the point of failure. The tension tests are carried out on a Denison Meyer (500kN) machine. The compression tests are carried out on a Zwick Z400 (250kN). All test specimens are quasi-statically loaded at a rate of 2mm/min.

### **6.2.2 Digital Image Correlation (DIC) method**

DIC is required to characterise the highly non-uniform distribution of strain in an anisotropic laminate containing holes. The DIC procedure developed in this study is summarised as follows. A speckled pattern of matt white paint is sprayed onto the front face of each test specimen. During the test a series of images of the speckled face of the laminate are taken. The strain distribution in each laminate in the region of the hole is determined from the series of images using a Matlab based DIC code. The displacements of the individual speckles of paint are tracked through each deformed image and compared with a reference image taken before the load is applied. Once the images are correlated, the Green-Lagrangian finite strain tensor is calculated by interpolating the displacements using finite element shape functions (explained in detail in Section 3.6 of this thesis). Because the DIC analysis is performed in two dimensions only, the strains do not take into account any out of

plane bending or buckling that may occur in the laminate during the experiment. While the stress state and strain state in each specimen is highly non-uniform due to the presence of a hole, for presentation of results we define a *specimen nominal stress* and a *specimen nominal strain*. *Specimen nominal stress* is plotted as a function of a *specimen nominal strain* from the onset of loading to the point of failure for each experiment. Effective compressive and tensile stiffness values for each experiment are taken as the slope of the *specimen nominal stress* versus *specimen nominal strain* plots. *Specimen nominal stress* is computed as  $F/A_o^f$ , where  $F$  is the measured force and  $A_o^f$  is the cross-sectional area of the specimen at a section that does not contain the hole. *Specimen nominal strain* is computed from the relative displacement of two points (see Figure 6.1) far from the hole.

To ensure the accuracy of the DIC method, the displacement distribution calculated for an open hole tensile specimen is compared with the predicted finite element distribution, see Figure 6.2. The DIC calculations show areas of increased displacement on the axial sides of the hole (Figure 6.2(A)). The magnitude of displacement calculated for this section of the test specimen is 9mm. Similar to the DIC calculations the computational model also predicts areas of increased displacement in the  $x$  direction on the axial sides of the hole (Figure 6.2(B)). The magnitude of displacement predicted by the computational model is in good agreement with the DIC calculations.

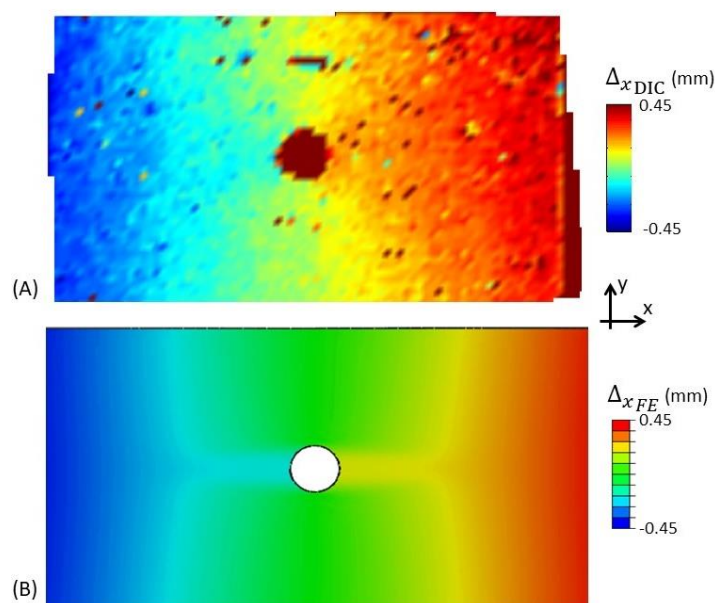


Figure 6.2: (A) DIC calculation of the displacement in the  $x$  direction ( $\Delta_{x_{DIC}}$ ) at a time point immediately prior to failure. (B) Finite element prediction of the displacement in the  $x$  direction ( $\Delta_{x_{FE}}$ ) at the same time point as (A).

### 6.2.3 Computational model

The previously developed computational model, calibrated and validated for CF/PEEK specimens without holes in Chapter 4 of this thesis, is here used to simulate the open and filled hole experiments. The CF/PEEK material properties along with the calibrated material parameters for the damage and failure formulations previously described are listed in Table 6.1 below.

Table 6.1: Elastic material properties and tensile, compressive and shear strengths, inter-laminar CZM model parameters and anisotropic plasticity model parameters for macro-scale DRFFP simulations.

CF/PEEK (Gallagher et al., 2018)			
$E_{11} = 175.4 \text{ GPa}$	$X_T = 2882 \text{ MPa}$	$\sigma_y = 111 \text{ MPa}$	$\sigma_{max} = 49.5 \text{ MPa}$
$E_{22} = 9.4 \text{ GPa}$	$Y_T = 50 \text{ MPa}$	$R_{11} = 250$	$\tau_{max} = 37 \text{ MPa}$
$E_{33} = 9.4 \text{ GPa}$	$X_C = 1182 \text{ MPa}$	$R_{22} = 1.0$	$\delta_n = 10 \mu\text{m}$
$\nu_{12} = 0.38$	$Y_C = 186 \text{ MPa}$	$R_{33} = 1.0$	$\delta_t = 10 \mu\text{m}$
$\nu_{13} = 0.38$	$S = 96 \text{ MPa}$	$R_{12} = 0.64$	
$\nu_{23} = 0.46$	$G_{ic} = 1.44 \text{ kJ/m}^2$	$R_{13} = 0.64$	
$G_{12} = 5.2 \text{ GPa}$	$G_{iic} = 1.0 \text{ kJ/m}^2$	$R_{23} = 1.0$	
$G_{13} = 5.2 \text{ GPa}$			
$G_{23} = 1.9 \text{ GPa}$			

All tests are modelled using the commercial finite element software Abaqus 6.13 (SIMULIA, Providence, RI, USA). Intra-laminar cracking is simulated through a user damage initiation (UDMGINI) subroutine in conjunction with the extended finite element method. Inter-laminar delamination is simulated through a cohesive zone model implemented in a user interface (UINTER) subroutine. Each ply contains approximately 9500 3D stress elements (C3D8). The  $[0^\circ/90^\circ]_3\text{s}$  laminate has 12 plies, i.e. 114,000 elements, while the  $[0^\circ/\pm 45^\circ/90^\circ]_2\text{s}$  has 16 plies, i.e. 152,000 elements. The pins are modelled as rigid analytical surfaces and a tie constraint is

placed between the rigid surface and the inside surfaces of each hole in the filled hole simulations.

## 6.3 Results

### 6.3.1 Open hole and filled hole compression: Experimental test results

The open hole compressive nominal failure stress of the  $[0^\circ/90^\circ]_3s$  laminate is  $322.56 \pm 6.69$  MPa and failure occurs at a nominal strain of  $0.0035 \pm 0.0002$ . Dependent student t tests are carried out to determine significance between the open and filled failure strengths and effective moduli of both laminates separately. There is a significant ( $p < 0.05$ ) increase in the compressive strength of the filled hole  $[0^\circ/90^\circ]_3s$  laminate compared to the open hole laminate. The failure stress of the filled hole laminate is  $457.18 \pm 30.04$  MPa, with a nominal strain of  $0.0046 \pm 0.0004$  at failure. The effective compressive stiffness of the open and filled hole  $[0^\circ/90^\circ]_3s$  laminates are  $91.22 \pm 2.18$  GPa and  $97.75 \pm 4.40$  GPa, respectively.

A similar trend is observed for the  $[0^\circ/\pm 45^\circ/90^\circ]_2s$  laminate. There is a significant ( $p < 0.05$ ) difference between the open hole compressive nominal failure stress of  $298.16 \pm 12.00$  MPa (failure occurs at a nominal strain of  $0.0046 \pm 0.0002$ ) and the filled hole compressive nominal failure stress of  $365.96 \pm 18.63$  MPa (failure occurs at a nominal strain of  $0.0053 \pm 0.0004$ ). The effective compressive stiffness of the open and filled hole  $[0^\circ/90^\circ]_3s$  laminates are  $63.93 \pm 1.23$  GPa and  $68.67 \pm 2.08$  GPa, respectively.

As shown in Figure 6.3, the  $[0^\circ/90^\circ]_3s$  laminate is significantly stronger than the  $[0^\circ/\pm 45^\circ/90^\circ]_2s$  laminate in filled hole axial compression (see Figure 6.3(A)) and significantly stiffer in both open and filled compression (see Figure 6.3(B)).

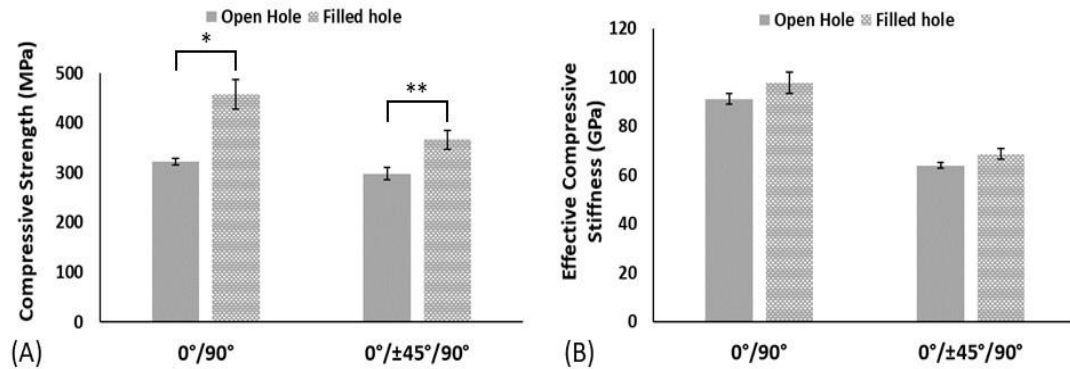


Figure 6.3: (A) Nominal compressive failure stress of the laminates ( $[0^\circ/90^\circ]_3s$  and  $[0^\circ/\pm 45^\circ/90^\circ]_2s$ ) comparing open and filled hole samples. \* $p < 0.05$  vs. open hole  $[0^\circ/90^\circ]_3s$  and \*\* $p < 0.05$  vs. open hole  $[0^\circ/\pm 45^\circ/90^\circ]_2s$ . (B) Effective compressive stiffness of the open and filled hole laminates ( $[0^\circ/\pm 45^\circ/90^\circ]_2s$  and  $[0^\circ/90^\circ]_3s$ ). Error bars denote standard deviation.

### 6.3.2 Open hole and filled hole compression: Experimental and computational failure modes

The experimental images of specimen failure modes, and corresponding computational predictions are presented in Figure 6.4 for  $[0^\circ/90^\circ]_3s$  laminates subjected to both open and filled hole compression tests.

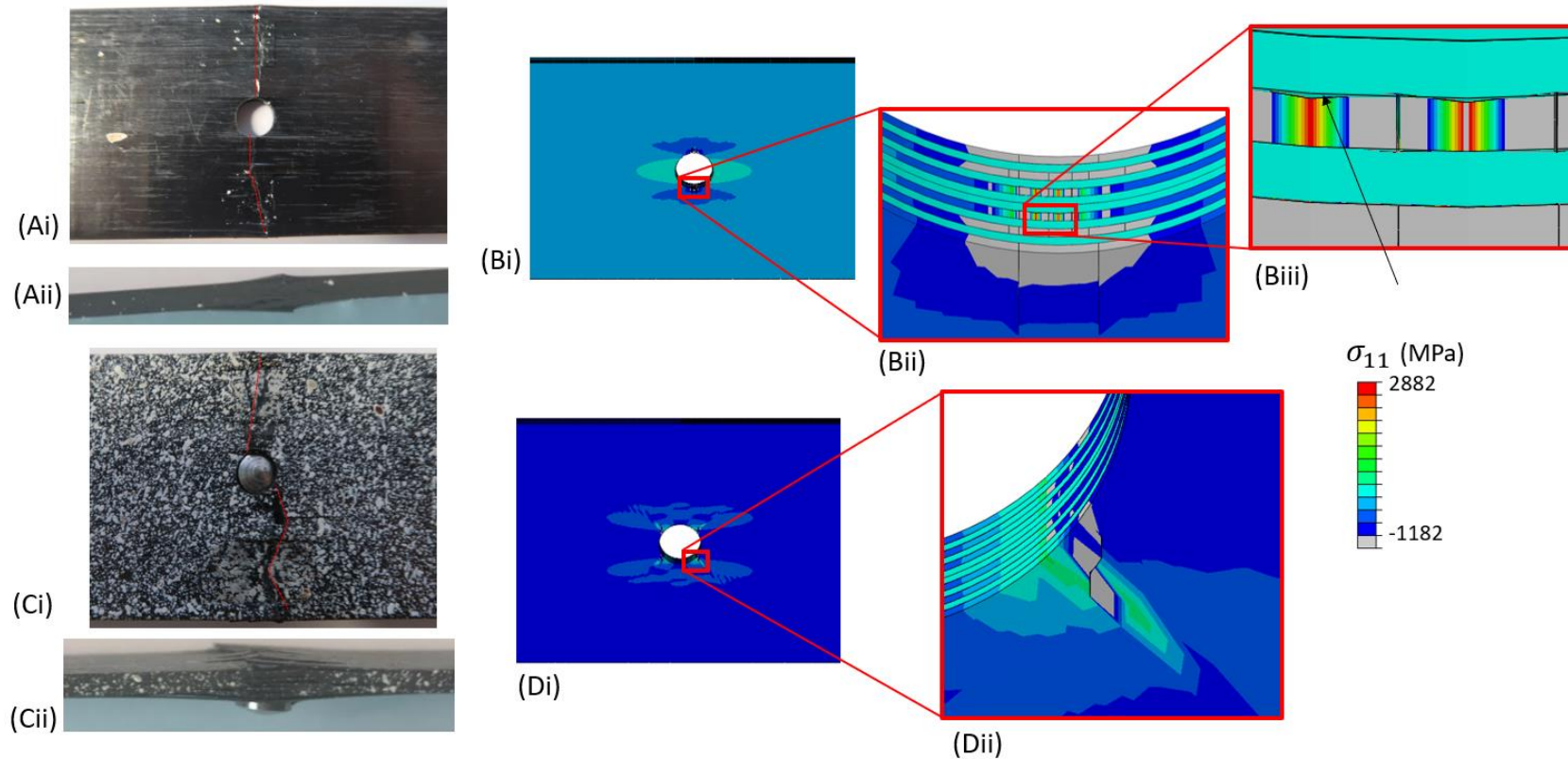


Figure 6.4: (Ai) Experimental images of the open hole  $[0^\circ/90^\circ]_3s$  specimens with crack path indicated by the dashed red line, (Aii) extensive delamination of outermost plies is visible. (Bi) Predicted longitudinal stress ( $\sigma_{11}$ ) distribution at failure, (Bii) extensive compressive longitudinal cracks of all  $0^\circ$  plies, (Biii) delaminations propagating from the crack are also predicted. (Ci) Experimental images of the filled hole  $[0^\circ/90^\circ]_3s$  specimens, crack path is indicated by the dashed red line, (Cii) extensive cracking and delamination of all plies occurs at failure. (Di) Predicted longitudinal stress ( $\sigma_{11}$ ) distribution at failure, (Dii) predicted location of cracking.

Figure 6.4(Ai) shows the experimental images of the failed laminate. A compressive intra-laminar crack initiates on the transverse sides (north and south sides of the hole in Figure 6.4(Ai)) of the open hole and propagates through all of the plies approximately perpendicular to the direction of loading. Significant inter-laminar delamination occurs in the  $0^\circ$  plies (Figure 6.4(Aii))

Figure 6.4(Bi) shows the predicted longitudinal stress ( $\sigma_{11}$ ) distribution in the open hole  $[0^\circ/90^\circ]_3$ s laminate at the point of failure. A reduced stress is predicted on the axial sides of the hole (north and south sides of the hole in Figure 6.4(Bi)), with the greatest stresses predicted on the transverse sides of the hole. Figure 6.4(Bii) shows the predicted longitudinal intra-laminar compressive fibre crack in the  $0^\circ$  plies. The model predicts the crack initiation on the transverse sides of the hole and propagating perpendicular to the direction of loading, which is in very good agreement with the experimental images of the open hole specimens. In Figure 6.4(Biii) the predicted inter-laminar delaminations propagating from the cracks in the  $0^\circ$  plies are highlighted by the black arrow.

Figure 6.4(C) shows experimental images for failed  $[0^\circ/90^\circ]_3$ s subjected to filled hole compression testing. Figure 6.4(Ci) shows the compressive longitudinal intra-laminar crack path, highlighted by a dashed red line. Unlike the open hole specimens, a longitudinal compressive crack is visible on the axial sides of the filled hole. Delamination is also observed in this region (Figure 6.4(Cii)). The inter-laminar delamination of the outermost  $0^\circ$  ply propagates axially through the laminate for approximately 50mm from the point of initiation at the edge of the hole. It should be noted that no inter- or intra-laminar failure is observed on the axial sides of the hole (east and west sides of the hole in Figure 6.4(Ci)).

The predicted stress distribution in the filled hole  $[0^\circ/90^\circ]_3$ s laminate is shown in Figure 6.4(Di). There is a significant difference between the predicted longitudinal stress ( $\sigma_{11}$ ) distribution in the open hole (Figure 6.4(Bi)) and the filled hole (Figure 6.4(Di)). In contrast to the open hole sample, the greatest stresses are predicted on the axial sides of the hole (east and west sides of the hole in Figure 6.4(Di)) where the compressed laminate is in contact with the stiff pin. Reduced stresses are predicted on the transverse sides of the hole. Figure 6.4(Dii) shows the intra-laminar crack is predicted to initiate at the boundary of the transverse and axial sides of the hole, propagating at approximately  $45^\circ$ . This is in good agreement with the experimental crack path, highlighted in Figure 6.4(Ci), which propagates at approximately  $45^\circ$  from the edge of the hole between the axial and transverse sides.

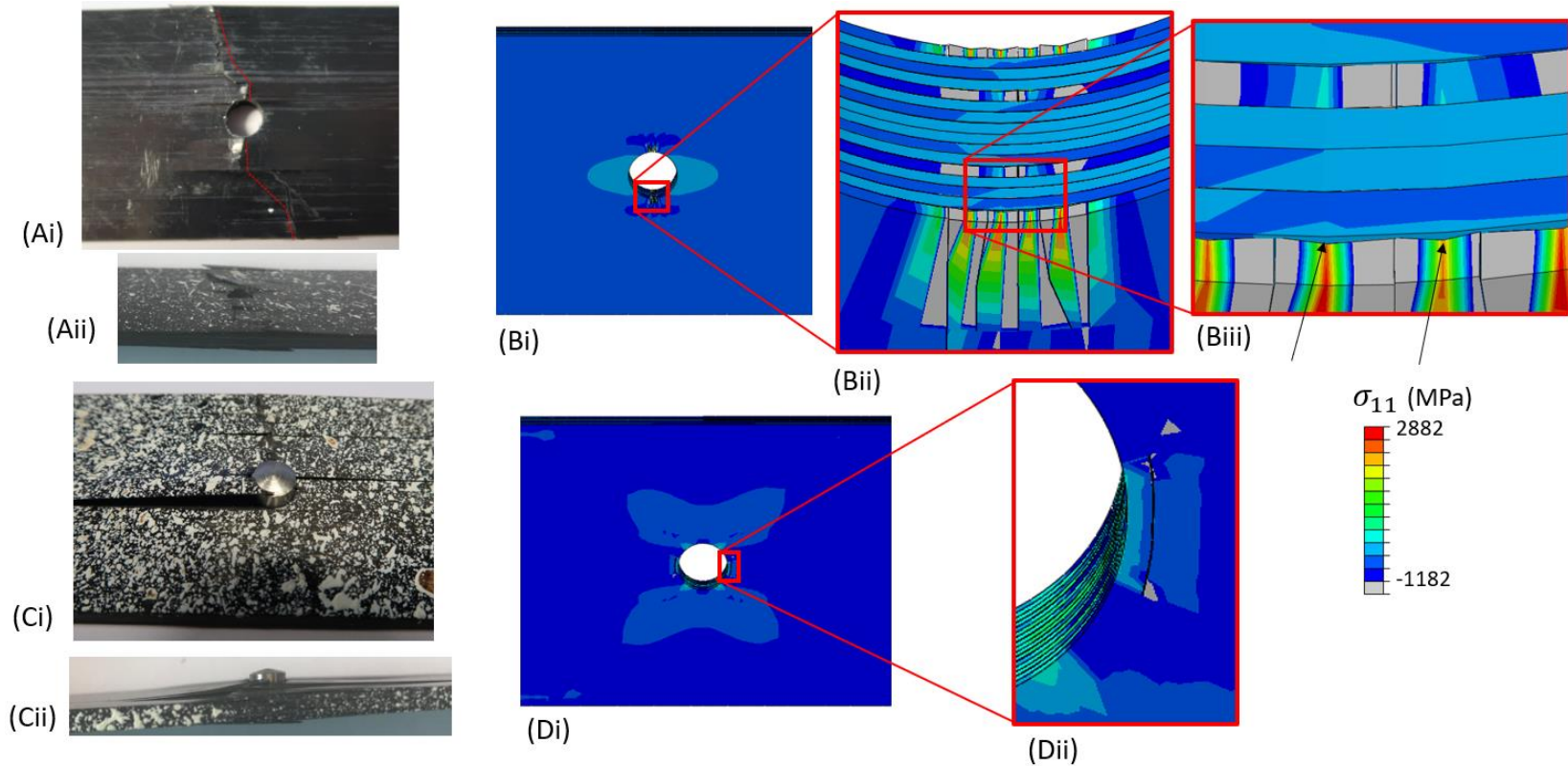


Figure 6.5: (A) Experimental images of the open hole  $[0^\circ/\pm 45^\circ/90^\circ]_2s$  specimens, (Ai) crack path is indicated by the dashed red line, (Aii) extensive delamination of outermost plies is visible. (Bi) Predicted longitudinal stress ( $\sigma_{11}$ ) distribution at failure, (Bii) extensive compressive longitudinal cracks of all  $0^\circ$  plies, (Biii) delaminations propagating from the crack are also predicted. (C) Experimental images of the filled hole  $[0^\circ/\pm 45^\circ/90^\circ]_2s$  specimens, (Ci) crack on axial side of hole clearly visible, (Cii) extensive cracking and delamination of all plies occurs at failure. (Di) Predicted longitudinal stress ( $\sigma_{11}$ ) distribution at failure, (Dii) predicted location of crack initiation.

Figure 6.5(Ai) shows an experimental image of a failed  $[0^\circ/\pm 45^\circ/90^\circ]_2s$  laminate subjected to open hole compression testing. The propagation of the crack in the outermost  $0^\circ$  ply has been highlighted by the dashed red line. Extensive cracking and delamination is also shown in Figure 6.5(Aii). Cracking and delamination occurs on the transverse sides (north and south in Figure 6.5(Aii)) of the hole, but not on the axial (east and west in Figure 6.5(Aii)) sides of the hole.

Figure 6.5(Ci) shows the computed stress distribution in the laminate at the point of failure in the open hole compression test. The greatest stresses are predicted on the transverse side of the hole, which is also the predicted location for the compressive intra-laminar cracks (Figure 6.5(Cii)). The propagation of the crack in a transverse direction from the screw hole is in good agreement with the experimental images. Inter-laminar delaminations propagating from the cracked  $0^\circ$  plies are also shown in Figure 6.5(Ciii).

Experimental images of a failed  $[0^\circ/\pm 45^\circ/90^\circ]_2s$  laminate subjected to filled hole compression testing are shown in Figure 6.5(Ci and Cii). The crack initiates at the hole and propagates at an angle to the edge of the laminate highlighted by the dashed red line (Figure 6.5(Ci)). Similar to the open hole experiments, significant delaminations occur along the crack path (Figure 6.5(Cii)). However, unlike the open hole specimens, an intra-laminar crack and delamination is observed on the axial side of the hole in the filled hole  $[0^\circ/\pm 45^\circ/90^\circ]_2s$  laminates.

The predicted stress distribution in the filled hole  $[0^\circ/\pm 45^\circ/90^\circ]_2s$  laminate is shown in Figure 6.5(Di). The areas of highest compressive stress are predicted on the axial side of the hole with lower compressive stresses predicted on the transverse side of the hole, in contrast to the computed stress distribution for open hole tests. The

model predicts that a compressive intra-laminar crack occurs on axial side of the hole Figure 6.5(Dii) which is in good agreement with the experimental images.

### 6.3.3 Longitudinal compressive strength

Figure 6.6 shows that the computational model accurately predicts the effective compressive stiffness for filled hole and open hole compression tests for both the  $[0^\circ/90^\circ]_3s$  and  $[0^\circ/\pm 45^\circ/90^\circ]_2s$  laminates. The computational model also correctly predicts that the compressive nominal failure stress is higher for the filled hole experiments than for the open hole experiments. However, the model under-predicts the magnitudes of the compressive failure stress for all cases. In all cases, laminates fail due to compressive fibre failure (equation 4.15, Chapter 4). The parameter  $X_C$ , longitudinal compressive strength, contributes exclusively to the compressive fibre failure criterion. This parameter relied on a single experimental test for calibration, namely a  $0^\circ$  compression test (see Chapter 4, Section 4.4), which resulted in a value of  $X_C = 1182$  MPa. However, during the experiment the tabs detached from the test samples prior to ultimate failure, as shown in Figure 6.7. After tab detachment the specimens failed due to a crushing of the laminate due to direct compression by the loading platen (see Figure 6.7). Such tab detachment may have resulted in an underprediction of  $X_C$ . Model predictions for a higher value of  $X_C = 1500$  MPa (this value has been previously reported for non-medical grades of carbon fibre reinforced PEEK composites (Du et al., 2016; Li et al., 2002)) are also shown in Figure 6.6. Such an increase results in a slight over-prediction of the nominal compressive failure stress for filled hole tests and a slight under-prediction of nominal compressive failure stress for open hole experiments.

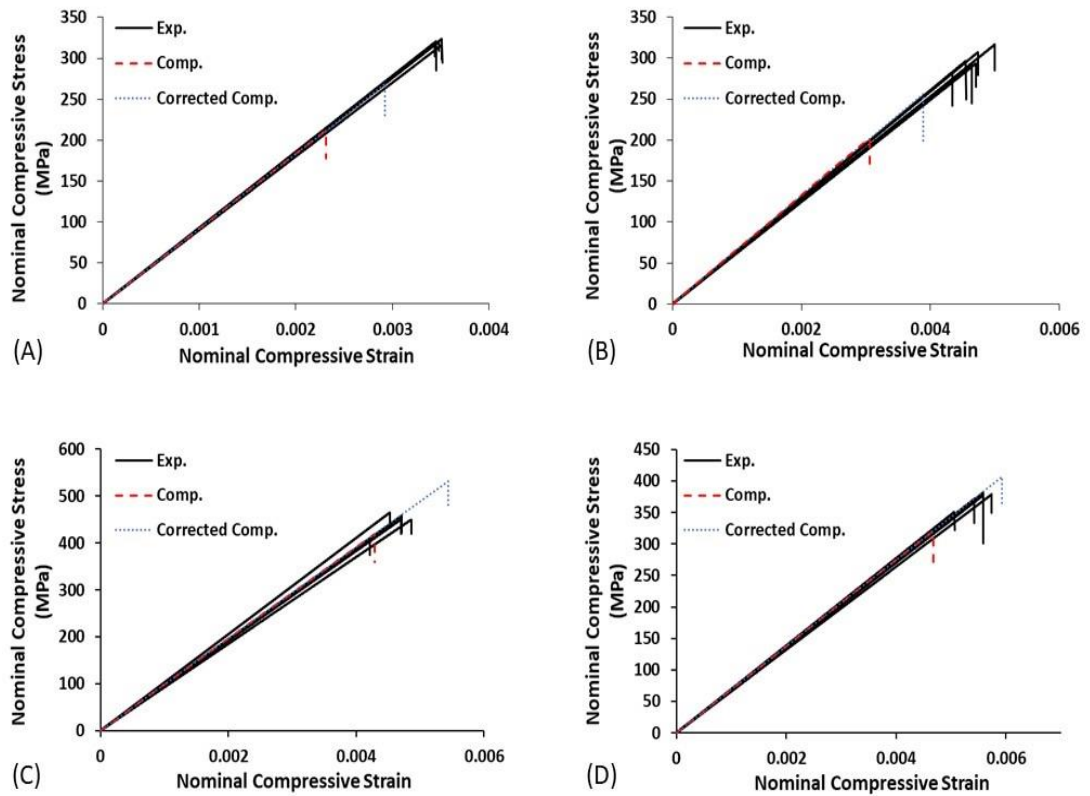


Figure 6.6: Compression stress-strain relationship, experimental (black), computational prediction for  $X_C = 1882\text{MPa}$  (red dashed) and  $X_C = 1500\text{MPa}$  (navy dotted line) for (A) Open hole  $[0^\circ/90^\circ]_3s$  laminate, (B) Open hole  $[0^\circ/\pm 45^\circ/90^\circ]_2s$  laminate, (C) Filled hole  $[0^\circ/90^\circ]_3s$  laminate and (D) Filled hole  $[0^\circ/\pm 45^\circ/90^\circ]_2s$  laminate.

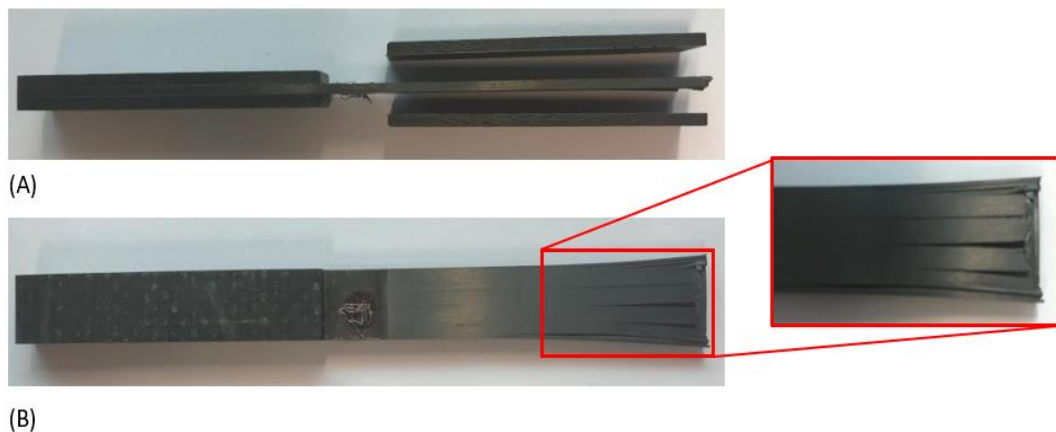


Figure 6.7: (A) Experimental image of a failed longitudinal compressive CF/PEEK specimen with broken tabs. (B) Experimental image of the crushed  $0^\circ$  laminate after the tabs debonded and final failure occurred.

### 6.3.4 Open hole tension

The experimental results and computational predictions for the open hole tensile tests performed on  $[0^\circ/90^\circ]_3s$  and  $[0^\circ/\pm 45^\circ/90^\circ]_2s$  laminates are presented in Figure 6.8(A) and Figure 6.8(B), respectively.

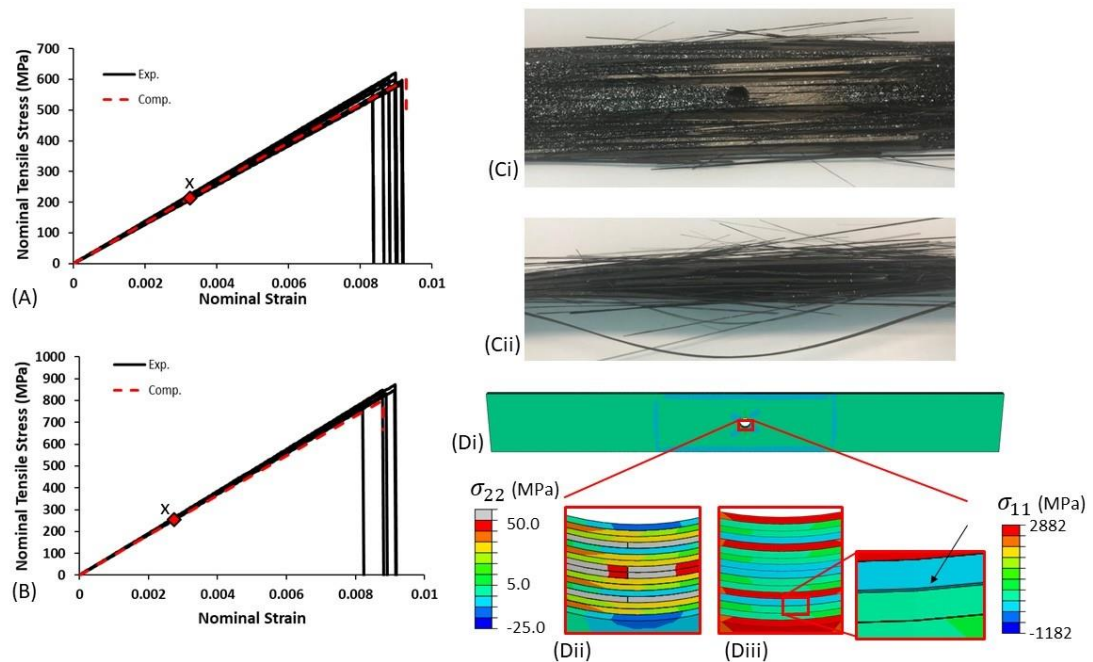


Figure 6.8: (A) Open hole tension nominal stress-strain relationship for the  $[0^\circ/\pm 45^\circ/90^\circ]_2s$  laminate, experimental (black) and computational prediction (red dashed), x indicates the predicted point of crack initiation. (B) Open hole tension stress-strain relationship for the  $[0^\circ/90^\circ]_3s$  laminate, x indicates the predicted point of crack initiation. (C) Experimental images of the failed specimens, (Ci) front view, (Cii) side view, shows the extensive cracking and delamination of all plies occurring at failure. (Di) Computational prediction of transverse stress ( $\sigma_{22}$ ) in the failure in the  $[0^\circ/\pm 45^\circ/90^\circ]_2s$  laminate at the point of crack initiation, (Dii) Predicted cracks in the  $90^\circ$  plies at the hole edge, (Diii) Predicted longitudinal stress distribution ( $\sigma_{11}$ ) and delamination (arrow) at the point of ultimate failure.

Figure 6.8(A) shows the stress-strain diagram for the  $[0^\circ/90^\circ]_3s$  open hole tension test. A linear elastic regime is observed up to the point of failure at a strain of  $0.0090 \pm 0.0005$ . The open hole tensile strength of the  $[0^\circ/90^\circ]_3s$  laminate is  $664.25 \pm 26.36$  MPa. The open hole tensile modulus of the laminate is  $93.23 \pm 2.57$  GPa. The

computational model provides a good prediction of the experimental stress strain behaviour. The ultimate strength of the open hole  $[0^\circ/90^\circ]_3s$  laminate is predicted to be 666 MPa and the strain at failure is 0.0088, both of which fall within the standard deviation of the experiments. The point of intra-laminar transverse tensile crack initiation in the  $90^\circ$  plies predicted computationally is indicated by point  $x$  in the stress-strain graph. The stress continues to increase in the laminate after these initial cracks occur, up to the point of ultimate failure due to extensive delamination.

Figure 6.8(B) shows the stress-strain diagram for the  $[0^\circ/\pm 45^\circ/90^\circ]_2s$  open hole tension test. Again, a linear elastic regime is observed up to the point of failure at a strain of  $0.0087 \pm 0.0002$ . The open hole tensile strength of the  $[0^\circ/\pm 45^\circ/90^\circ]_3s$  laminate is  $597.27 \pm 14.17$  MPa. The open hole tensile modulus of the laminate is  $67.00 \pm 4.23$  GPa. The strength of the open hole laminate and the strain at failure predicted by the computational model are 598.48 MPa and 0.0093, respectively, which are both in very good agreement with the experimental results. The point of crack initiation predicted computationally is indicated by point  $x$  in the stress-strain graph. The stress continues to increase in the laminate after these initial cracks occur, up to the point of ultimate failure due to extensive delamination.

In the experimental images shown in Figure 6.8(C) there is clear evidence of the explosive catastrophic failure that occurs in both the  $[0^\circ/90^\circ]_3s$  and the  $[0^\circ/90^\circ]_3s$  laminates. Extensive delamination and fibre breakages can be seen. It should be noted that during the test the distinctive ‘pinging’ of fibre breakages could be audible from very low applied strains. This observation is supported by the computational prediction of crack initiation (point  $x$ ) at a low strain in Figure 6.8(A) and Figure 6.8(B). Despite the initiation of fibre breakage at low strains, the stress

increases linearly up to the point of ultimate failure. The predicted location of the crack initiation is shown in Figure 6.8(Dii). The initial cracks occur in the 90° and the 45° plies at the hole. The delamination of all plies at the hole at the final failure of the laminate is shown in Figure 6.8(Diii).

## **6.4 Discussion**

PEEK-OPTIMA™ Ultra-Reinforced is intended to be used in the manufacture of laminated fibre reinforced orthopaedic implants, including fracture fixation devices and other trauma implants. One challenge presented by the use of fibre reinforced laminates in fracture fixation devices is the large number of screws and screw holes that are required to attach the implant to the bone fragments (Abrão et al., 2007; Nourisa et al., 2015). Significant stress concentrations occur at such screw holes, with an increased risk of damage initiation and failure at such locations. In this chapter we perform a thorough investigation of the failure mechanisms due to the presence of screw holes in PEEK-OPTIMA™ Ultra-Reinforced (Abrão et al., 2007; Davim and Reis, 2003; Ho-Cheng and Dharan, 1990). Two ply layups are considered, namely the  $[0^\circ/90^\circ]_3s$  and  $[0^\circ/\pm 45^\circ/90^\circ]_2s$  laminates. A series of experimental tests are performed: open hole compression tests; filled hole compression tests; open hole tension tests. Effective stiffness, failure stress, and failure modes are determined in all cases. The computational damage model developed in Chapter 4 is used to predict the experimentally observed failure mechanisms. A considerable number of studies have investigated the tensile and compressive behaviour of both open and filled notched laminates (Castanié et al., 2010; Morais, 2000; O'Higgins et al., 2008; Sawicki and Minguet, 1999; Wang et al., 2004). To date it is clear that predicting when and where damage is initiated in

notched laminates is extremely difficult (Bao and Liu, 2016; Leopold et al., 2017; Tan et al., 2017).

The open and filled hole compression experiments reveal extensive intra-laminar cracking initiating on the transverse side of the hole in the open hole tests and on the axial side of the hole in the filled hole experiments. The compressive strength of the filled hole specimens is significantly higher ( $p < 0.05$ ) than the open hole compressive strength; an increase in failure stress of approximately 30% is observed for both laminates when the hole is filled.

Experiments also reveal that the axial sides of the hole experience little to no intra-laminar cracking or inter-laminar delamination during open hole tension and compression. In the open hole samples all of the cracks initiate on the transverse side of the hole where a significant stress concentration occurs. In contrast, intra-laminar cracks and delaminations are observed on the axial side of the hole in the failed filled hole compression specimens. Contact between the stainless-steel pin and the axial side of the hole results in an increased stress in this region, ultimately resulting in crack formation. Failure mechanisms for open and filled hole tests are correctly predicted by the computational model.

The open hole tension tests reveal the explosive catastrophic nature of failure in notched laminates. Extensive inter-laminar delaminations and intra-laminar tensile fibre cracks are observed in failed samples of both laminates. The onset of fibre breakages occurs long before the final tensile failure of the laminate, the distinctive ‘pinging’ of fibre breakages can be heard at very low levels of applied strains, 0.2% nominal strain. Such acoustic emissions are very commonly noted during tensile failure of fibre reinforced laminates (Kim and Soni, 1984; Liu et al., 2012; Romhány

et al., 2017). It is not expected that the measured tensile stress required to cause such failure will occur due to even the most extreme physiological loading.

The computational model gives a very good prediction for the open hole tensile test. The fibre breakages that occurred at low strains, characterised by the tell-tale ‘pinging’ of fibres heard during the experiment was predicted by the computational model, which XFEM crack initiation occurring as early as 0.2% applied nominal strain in the  $[0^\circ/\pm 45^\circ/90^\circ]$  laminate. Extensive delaminations propagating from the edge of the hole where the initial cracks occur are predicted to cause catastrophic failure at stresses and strains within the experimental standard deviations.

Trauma implants and fracture fixation devices inevitably contain large numbers of screw holes. Therefore, fully characterising the open and filled hole failure mechanics of fibre reinforced laminates is essential. The results of this study present another key step in the development of next-generation unidirectional carbon fibre reinforced PEEK laminated orthopaedic devices. Future studies should consider multiple holes, with various combinations of filled and open holes, and bending and torsion loading should also be examined (Erhardt et al., 2012; Nourisa et al., 2015; Törnkvist et al., 1996). It is well established that the strength of fibre reinforced laminates is very sensitive to hole size or diameter (Camanho et al., 2007; Whitney and Nuismer, 1974). Size effects were not investigated in the current study but future work should experimentally investigate the response of *CF/PEEK* to different sized holes with a combined finite element investigation to determine if the computational model developed in Chapter 4 and implemented in the current chapter is capable of predicting size effects in notched laminates. Alternative methods to manufacture laminates with holes should also be investigated (Zitoune et al., 2011).

Chapter 7 will consider one such alternative manufacture method, namely moulded holes. A novel computational methodology for modelling moulded screw holes will be developed.

## 6.5 References

- Abrão, A.M., Faria, P.E., Rubio, J.C.C., Reis, P., Davim, J.P., 2007. Drilling of fiber reinforced plastics: A review. *J. Mater. Process. Technol.* <https://doi.org/10.1016/j.jmatprotec.2006.11.146>
- ASTM, 2014. D6484/D6484M – 14 Standard Test Method for Open-Hole Compressive Strength of Polymer Matrix Composite Laminates. *ASTM Int.* [https://doi.org/10.1520/D6484\\_D6484M-14](https://doi.org/10.1520/D6484_D6484M-14)
- ASTM, 2012. ASTM D6742/D6742M-12 Standard Test Method for Filled-Hole Tension and Compression Testing of Polymer Matrix Composite Laminates. *ASTM Int.* [https://doi.org/10.1520/D6742\\_D6742M-12](https://doi.org/10.1520/D6742_D6742M-12)
- ASTM, 2002. Standard Test Method for Open Hole Tensile Strength of Polymer Matrix Composite Laminates. *ASTM Stand. D5766/D5766M-02 03.*
- ASTM D5687, 2002. Standard Guide for Preparation of Flat Composite Panels with Processing Guidelines for Specimen Preparation. *Annu. B. ASTM Stand. 15.03*, 1–16. <https://doi.org/10.1520/D5687>
- Awerbuch, J., Madhukar, M.S., 1985. Notched Strength of Composite Laminates: Predictions and Experiments & mdash - A Review, *Journal of Reinforced Plastics and Composites of Reinforced.* <https://doi.org/10.1177/073168448500400102>
- Bao, H., Liu, G., 2016. Progressive failure analysis on scaled open-hole tensile composite laminates. *Compos. Struct.* 150, 173–180. <https://doi.org/10.1016/j.compstruct.2016.05.017>
- Camanho, P.P., Maimí, P., Dávila, C.G., 2007. Prediction of size effects in notched laminates using continuum damage mechanics. *Compos. Sci. Technol.* <https://doi.org/10.1016/j.compscitech.2007.02.005>
- Castanié, B., Crézé, S., Barrau, J.J., Lachaud, F., Risse, L., 2010. Experimental analysis of failures in filled hole compression tests of carbon/epoxy laminate. *Compos. Struct.* 92, 1192–1199. <https://doi.org/10.1016/j.compstruct.2009.10.008>
- Davim, J.P., Reis, P., 2003. Study of delamination in drilling carbon fiber reinforced plastics (CFRP) using design experiments. *Compos. Struct.* 59, 481–487. [https://doi.org/10.1016/S0263-8223\(02\)00257-X](https://doi.org/10.1016/S0263-8223(02)00257-X)
- Du, D., Hu, Y., Li, H., Liu, C., Tao, J., 2016. Open-hole tensile progressive damage and failure prediction of carbon fiber-reinforced PEEK-titanium laminates. *Compos. Part B Eng.* 91, 65–74. <https://doi.org/10.1016/j.compositesb.2015.12.049>
- El-Karef, E.A., 2005. Corrective osteotomy for symptomatic scaphoid malunion. *Injury* 36, 1440–1448. <https://doi.org/10.1016/j.injury.2005.09.003>
- Erhardt, J.B., Stoffel, K., Kampshoff, J., Badur, N., Yates, P., Kuster, M.S., 2012. The Position and Number of Screws Influence Screw Perforation of the Humeral Head in Modern Locking Plates: A Cadaver Study. *J. Orthop. Trauma* 26, e188–e192. <https://doi.org/10.1097/BOT.0b013e31823db922>
- Gallagher, E.A., Lamorinière, S., McGarry, P., 2018. Multi-axial damage and failure of medical grade carbon fibre reinforced PEEK laminates: Experimental testing and computational modelling. *J. Mech. Behav. Biomed. Mater.* 82, 154–167. <https://doi.org/10.1016/J.JMBBM.2018.03.015>
- Ho-Cheng, H., Dharan, C.K.H., 1990. Delamination During Drilling in Composite Laminates. *J. Eng. Ind.* 112, 236. <https://doi.org/10.1115/1.2899580>

- Kim, R.Y., Soni, S.R., 1984. Experimental and Analytical Studies On the Onset of Delamination in Laminated Composites. *J. Compos. Mater.* 18, 70–80. <https://doi.org/10.1177/002199838401800106>
- Leopold, C., Schütt, M., Liebig, W. V., Philipkowski, T., Kürten, J., Schulte, K., Fiedler, B., 2017. Compression fracture of CFRP laminates containing stress intensifications. *Materials (Basel)*. 10. <https://doi.org/10.3390/ma10091039>
- Li, C., Granger, C., Del Schutte, H., Biggers, S.B., Kennedy, J.M., Latour, R. a, 2002. Progressive failure analysis of laminated composite femoral prostheses for total hip arthroplasty. *Biomaterials* 23, 4249–62.
- Liu, P.F., Chu, J.K., Liu, Y.L., Zheng, J.Y., 2012. A study on the failure mechanisms of carbon fiber/epoxy composite laminates using acoustic emission. *Mater. Des.* 37, 228–235. <https://doi.org/10.1016/j.matdes.2011.12.015>
- Morais, A. de, 2000. Open-hole tensile strength of quasi-isotropic laminates. *Compos. Sci. Technol.* 60, 1997–2004.
- Nourisa, J., Baseri, A., Sudak, L., Rouhi, G., 2015. The Effects of Bone Screw Configurations on the Interfragmentary Movement in a Long Bone Fixed by a Limited Contact Locking Compression Plate. *J. Biomed. Sci. Eng.* 590–600. <https://doi.org/10.4236/jbise.2015.89055>
- O’Higgins, R.M., McCarthy, M. a., McCarthy, C.T., 2008. Comparison of open hole tension characteristics of high strength glass and carbon fibre-reinforced composite materials. *Compos. Sci. Technol.* 68, 2770–2778. <https://doi.org/10.1016/j.compscitech.2008.06.003>
- Panchagnula, K.K., Palaniyandi, K., 2017. Drilling on fiber reinforced polymer/nanopolymer composite laminates: A review. *J. Mater. Res. Technol.* <https://doi.org/10.1016/j.jmrt.2017.06.003>
- Riccio, A., Di Felice, G., Saputo, S., Scaramuzzino, F., 2014. Stacking sequence effects on damage onset in composite laminate subjected to low velocity impact, in: *Procedia Engineering*. pp. 222–229. <https://doi.org/10.1016/j.proeng.2014.11.148>
- Romhány, G., Czigány, T., Karger-Kocsis, J., 2017. Failure Assessment and Evaluation of Damage Development and Crack Growth in Polymer Composites Via Localization of Acoustic Emission Events: A Review. *Polym. Rev.* <https://doi.org/10.1080/15583724.2017.1309663>
- Sawicki, A.J., Minguet, P.J., 1999. Failure mechanisms in compression-loaded composite laminates containing open and filled holes. *J. Reinf. Plast. Compos.* 18, 1708–1728. <https://doi.org/10.1177/073168449901801805>
- Stoffel, K., Dieter, U., Stachowiak, G., Gächter, A., Kuster, M.S., 2003. Biomechanical testing of the LCP - How can stability in locked internal fixators be controlled? *Injury* 34. <https://doi.org/10.1016/j.injury.2003.09.021>
- Tan, J.L.Y., Deshpande, V.S., Fleck, N.A., 2017. The effect of laminate lay-up on the multi-axial notched strength of CFRP panels: Simulation versus experiment. *Eur. J. Mech. A/Solids* 66, 309–321. <https://doi.org/10.1016/j.euromechsol.2017.08.002>
- Toivanen, J.A.K., Honkonen, S.E., Koivisto, A.M., Järvinen, M.J., 2001. Treatment of low-energy tibial shaft fractures: Plaster cast compared with intramedullary nailing. *Int. Orthop.* 25, 110–113. <https://doi.org/10.1007/s002640000083>
- Törnkvist, H., Hearn, T.C., Schatzker, J., 1996. The Strength of Plate Fixation in Relation to the Number and Spacing of Bone Screws. *J. Orthop. Trauma* 10, 204–208. <https://doi.org/10.1097/00005131-199604000-00009>

- Wang, J., Callus, P., Bannister, M., 2004. Experimental and numerical investigation of the tension and compression strength of un-notched and notched quasi-isotropic laminates. *Compos. Struct.* 64, 297–306. <https://doi.org/10.1016/j.compstruct.2003.08.012>
- Whitney, J.M., Nuismer, R.J., 1974. Stress Fracture Criteria for Laminated Composites Containing Stress Concentrations. *J. Compos. Mater.* <https://doi.org/10.1177/002199837400800303>
- Zitoune, R., Crouzeix, L., Collombet, F., Tamine, T., Grunevald, Y.H., 2011. Behaviour of composite plates with drilled and moulded hole under tensile load. *Compos. Struct.* 93, 2384–2391. <https://doi.org/10.1016/j.compstruct.2011.03.027>

# Chapter 7

## Computational Modelling of Moulded Screw Holes

---

### 7.1 Introduction

The use of carbon fibre (CF) PEEK laminates as an alternative to metal in orthopaedic implants offers potential for the development of implants with customised anisotropic material properties to suit the specific loading conditions of the implant. However, it is a requirement of several orthopaedic implants, particularly trauma implants, that they include screw holes to facilitate attachment of the implant to the bone fragments to immobilise the fracture. When holes are machined in fibre reinforced laminates the continuous fibres are broken, promoting inter-laminar delamination and cracking at screw hole sites due to the non-homogeneous nature of the composite material (Panchagnula and Palaniyandi, 2017). An alternative approach is to mould the screw holes into the implant during

processing, eliminating the requirement of drilling holes following fabrication of the laminate structure. In this approach CFs are moulded around the holes during processing, so that fibres remain continuous in the laminate without broken exposed fibre ends at the site of the hole (Fujihara et al., 2003; Huang and Fujihara, 2005; Rohner et al., 2005).

Two methods exist for moulding holes in unidirectional laminates. The first method is composite flow moulding (CFM) where a unidirectional rod of fibres is heated and fed into an implant mould at high pressures. In this way the fibres are forced around the pins marking the location of the screw holes. CFM results in large concentrations of fibres around the perimeter of the holes (Kurtz and Devine, 2007). Trauma plates and pedical screws manufactured using CFM are commercially available (Icotec AG, Altstätten, Switzerland). A limitation of the CFM method is that complex laminates consisting of multi-directional ply layups cannot be manufactured. The second method for manufacturing moulded holes in unidirectional fibre reinforced laminates involves assembling the laminate layup in the usual manner, and then inserting pointed steel punches into the laminate to form the screw holes once the polymer matrix has melted. The insertion of the punch forces fibres to bend around the screw hole (Zitoune et al., 2011). This method offers the distinct advantage over the CFM method in that it facilitates the formation of moulded holes in complex multi-directional ply layups. Very few studies have considered moulded holes, and the majority of these have focused on woven fibre composites (Fujihara et al., 2003; Lin and Tsai, 1995). To the authors knowledge only one experimental study has been published experimentally investigating moulded holes in continuous unidirectional carbon fibres (Zitoune et al., 2011). The aforementioned studies, on woven and unidirectional laminates, report an increase in load bearing capacity for moulded

holes compared to drilled holes. However, to date no computational study has been published examining moulded screw holes in unidirectional fibre reinforced laminates. In this chapter we develop, for the first time, a finite element approach to analyse fracture fixation plates (FFPs) fabricated with moulded holes.

In the previous chapters, a computational investigation of idealised distal radius FFPs was performed. Physiological loading conditions were applied to finite element models of CF/PEEK laminated distal radius FFPs, with several laminate layup designs considered. Stress localisations are computed in the region of the screw holes on the shaft of the fixation plates for all layups. The reduction of stress concentrations through the use of moulded holes can potentially improve the mechanical performance of the device. This study will compare the response of idealised FFPs containing drilled and moulded holes under different loading configurations.

### **7.2 Development of the moulded fibre model**

The novel approach used to model the moulded hole in finite element is outlined in this section. The objective is to create a computational model where the fibres are moulded around the hole, and at a critical distance from the hole the fibres return to their straight/undeformed configuration. In macro-scale FE models of unidirectional fibre reinforced laminates fibres are not modelled individually, rather each ply is assigned transversely isotropic material properties.

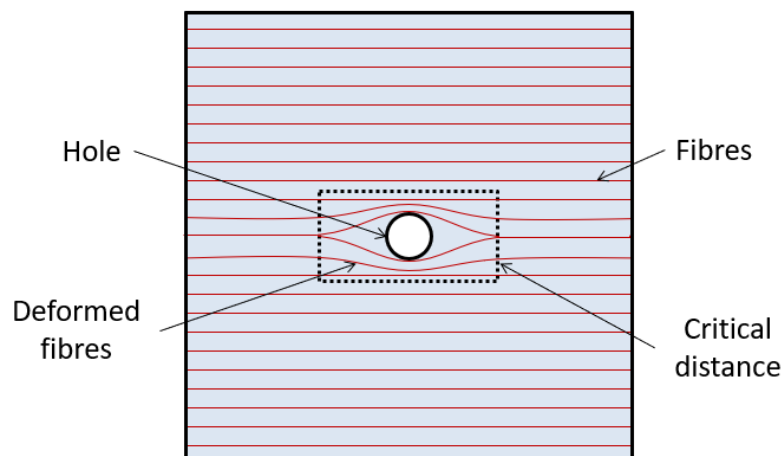


Figure 7.1: Schematic of the path of the unidirectional fibres moulded around the hole.

Orientations are assigned to individual plies which translate the material properties to match the local orientation of each ply. Therefore, in order to model the moulded continuous fibres which deform around the hole, rather than assigning a material orientation to the entire ply, each individual element within a critical distance of a hole (Figure 7.1) must be assigned a spatially dependent orientation. The following sections outline the approach used to determine the local element orientation within a ply, and a numerical method to implement such spatially varying orientations in the commercial FE programme Abaqus is presented.

### 7.2.1 Fibre bending model

The insertion of a punch into the laminate following melting of the matrix material results in a bending of fibres around the screw hole. Here we envisage that fibres deform as a cantilevered beam, with the symmetry boundary condition at the top of the punch also providing a constraint on the slope of the beam, as shown in Figure 7.2. The maximum deflection ( $\Delta$ ) between the two supported ends ( $A$  and  $B$ ) of the half-beam is equal to the radius of the hole. Point  $A$  lies on the edge of the hole and

point  $B$  is a critical distance from the hole. Beyond point  $B$  the fibre is assumed to return to its undeformed straight configuration.

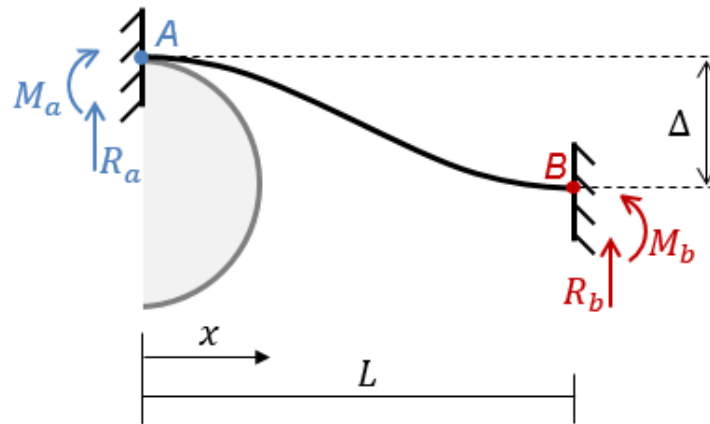


Figure 7.2: Schematic of the bending of a fibre around a punch/hole

The bending equation used is outlined below:

$$EI \frac{d^2y}{dx^2} = M_a + R_a x \quad 7.1$$

Integrating Eq.1 and letting  $R_a = 12EI\Delta/L^3$  and  $M_a = -6EI\Delta/L^2$  gives Eq. 2. The slope at any point ( $x$ ) on the bent fibre between the two supported ends ( $A$  and  $B$ ) can thus be calculated:

$$\frac{dy}{dx} = \frac{6\Delta x(x - L)}{L^2} \quad 7.2$$

At a critical vertical distance from the hole the fibres return to their undeformed straight configuration. For this fibre bending model we assume that the deflection of the fibre decreases linearly from, maximum deflection at the edge of the screw hole to zero deflection at the vertical limit of the critical box. Envisioning 25 fibres

evenly distributed along the vertical edge of the critical box (supported point  $B$ ), see Figure 7.3, the fibres remain evenly distributed at the point of maximum deflection (at the radius of the hole, supported point  $A$ ). The deflection of the fibre therefore becomes a function of the fibres position in the vertical direction, within the critical box, clearly illustrated in Figure 7.3. The vertical limit of the critical box is chosen such that the second last fibre in the box has a maximum deformation less than 0.01 of the maximum deformation of the first hole (i.e. the hole radius). The horizontal limit of the critical box is chosen such that the first fibre remains tangential to the end of the hole at supported end  $A$ .

Plotting the above bending equations in Matlab confirms that the fibres are bending around the hole as desired, see Figure 7.3.

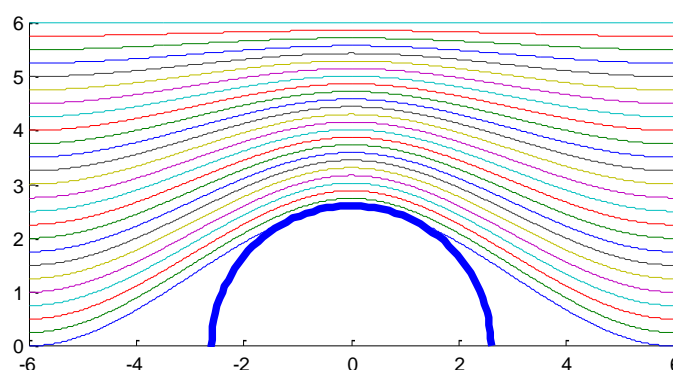


Figure 7.3: Illustration of the fibres deformed around the pin using the beam bending equations previously outlined

It should be noted that once the fibres have been moulded around the pin, there will be an area directly to the front and back of the hole that will have little to no reinforcing fibres. It is assumed that this unreinforced area (white area under the first fibre in Figure 7.3) has the same material properties as unreinforced PEEK.

### 7.2.2 Discretisation of spatially dependent fibre orientations

While fibres bending around the hole/punch are not explicitly represented in our finite element approach, a method must be developed to compute the discrete fibre orientation at each element in each ply based on element coordinates. A python script is developed in order to implement the following steps, ultimately providing the local orientations of each element in the mesh:

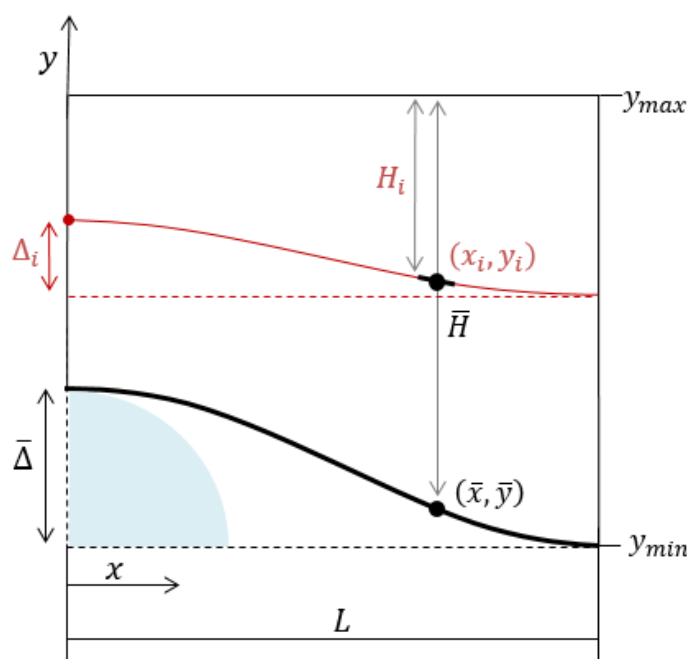


Figure 7.4: Illustration of the method used to assign separate orientations to each element within the critical box around the hole.

1. The location of each hole is identified.
2. A critical box is established around each hole.
3. All elements outside of the bounding box are assigned the global fibre orientation.
4. For every element within each critical box calculate the coordinates of the centroid  $(x_i, y_i)$ .
5. Recall that the fibre closest to the hole is the only fibre where the maximum

displacement (hole radius =  $\bar{\Delta}$ ) is known prior to any calculations. The next step is to calculate the y-coordinate ( $\bar{y}$ ) that corresponds to  $x_i$ , if  $x_i$  lay on the deformed fibre closest to the hole:

$$\bar{y} = \frac{-3\bar{\Delta}x_i^2}{L^2} + \frac{2\bar{\Delta}x_i^3}{L^3} + \bar{\Delta}$$

6. As  $\Delta$  decreases linearly from the first fibre ( $\Delta = \bar{\Delta}$ ) to the vertical limit of the critical box ( $\Delta = 0$ ) the maximum deflection ( $\Delta_i$ ) of the fibre passing through the centroid ( $x_i, y_i$ ) can be easily calculated:

$$\Delta_i = \bar{\Delta} \frac{H_i}{\bar{H}}$$

where  $H_i = y_{max} - y_i$ ,  $\bar{H} = y_{max} - \bar{y}$ , and  $y_{max}$  is the vertical limit of the critical box.

7. The slope of the centroid is next calculated and assigned as the orientation of that element:

$$\frac{dy}{dx} = \frac{6\Delta_i(x_i - L)}{L^3}$$

8. If the ratio of  $H_i/\bar{H}$  is less than 1 unreinforced PEEK is assigned as the material for that element, as the centroid falls between the centre of the hole and the first fibre.

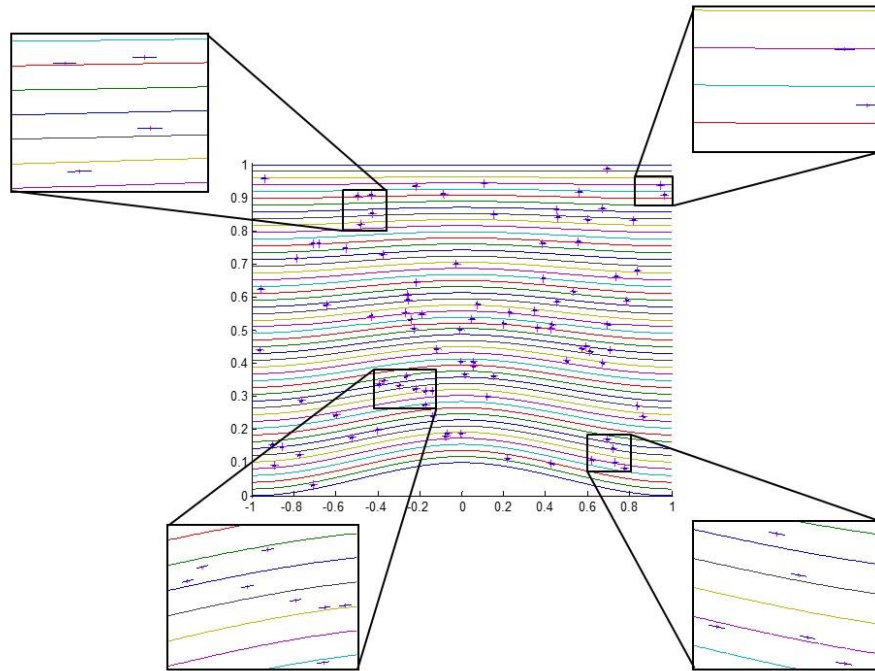


Figure 7.5: Accuracy check of methodology in Matlab

To confirm this method accurately assigns orientations to the chosen element, the steps above are implemented in a Matlab code and used to assign orientations to randomly selected coordinates within the critical zone. Orientations at randomly selected coordinates are plotted in Figure 7.5. A series of continuous bent fibres are superimposed for comparison. It is clear that the algorithm generates the correct relationship between spatial location and fibre orientation. In a finite element implementation of this algorithm in Abaqus, the fibre orientation is computed at the centroid of each element in the critical zone. This orientation is implemented through a separate *\*solid section* and *\*orientation* definition for each element in the critical zone. The python script to generate a moulded hole model is presented in Appendix 7.A.

### 7.3 Computational analysis of fixation plate with moulded and drilled holes

The python script described in the previous section is used to generate a finite element model of a generic FFP containing four moulded holes. The plate consists of 16  $0^\circ$  plies with an overall thickness of 3.2mm, (a length of 78mm, and a width of 10mm). Each hole has a diameter of 6mm. A schematic of the fibre orientations is shown in Figure 7.6(A). Analyses are also performed on a plate containing drilled holes for comparison. A schematic of the drilled-hole FFP is shown in Figure 7.6(B). Using rigid screws, the implant is fixed to a fractured bone. A gap of 1mm separates the fracture surfaces Figure 7.6(C). Three modes of loading are considered: axial compression, bending, and torsion, as shown in Figure 7.6(C). In all cases the applied loading is increased until cracking is computed in the FFP.

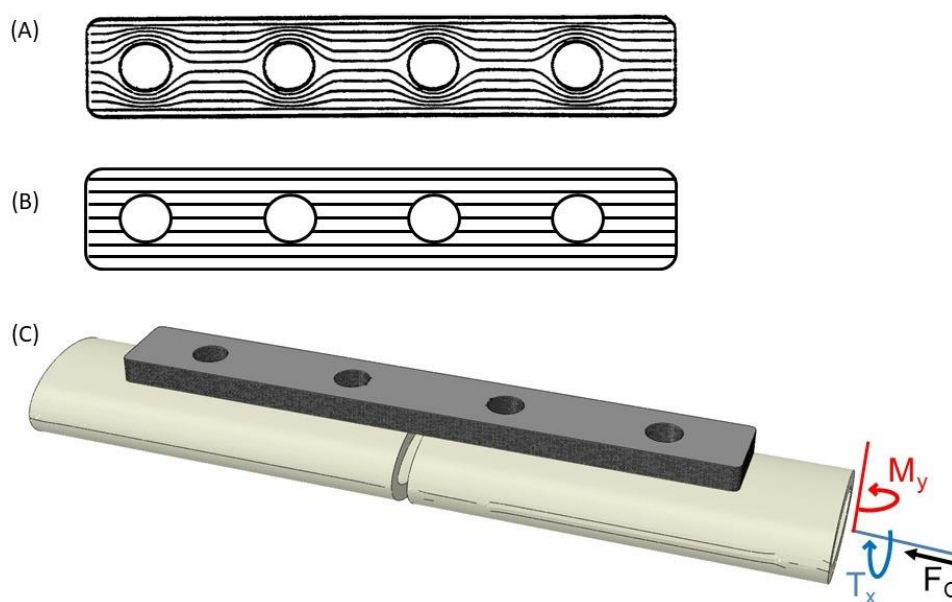


Figure 7.6: Schematic image of the fracture fixation plate (FFP) examined with (A) moulded holes and (B) drilled holes. (C) Computational assembly of the plate attached to the fractured bone with listed boundary conditions for the three loading conditions examined: compression ( $F_C$ ), bending ( $M_Y$ ) and torsion ( $T_X$ ).

## 7.4 Results

The longitudinal stress ( $\sigma_{11}$ ) distributions in the moulded and drilled hole FFP subjected to axial compression are shown in Figure 7.7(A) and (B), respectively. In both plates the areas of highest stress are concentrated in the centre of the implant. The moulded-hole FFP is predicted to fail due to transverse tensile intra-laminar cracks propagating from the edge of the hole on the lateral side of the implant (Figure 7.7 (A)). Cracks are predicted to initiate in the moulded-hole FFP at an applied compressive load of 1.703 kN (Figure 7.7(C)). In the case of the drilled-hole FFP, compressive intra-laminar fibre cracks are computed to propagating orthogonal to the loading direction in the centre of the implant on the medial side (Figure 7.7(B)). Cracking is predicted to occur at an applied compressive load of 4.345 kN (Figure 7.7(C)). As shown in Figure 7.7(C), the effective compressive stiffness of the drilled-hole FFP is approximately ~9% higher than that of the moulded-hole FFP. Localised areas of plastic deformation are predicted at each of the four holes in the drilled-hole FFP (Figure 7.7(D)), with the onset of yielding computed at an applied compressive load of 2.91kN. However, the load-displacement relationship remains approximately linear up to the point of cracking, despite such localised plastic yielding. In the case of the moulded-hole FFP, cracking is computed to occur prior to the onset of plastic yielding.

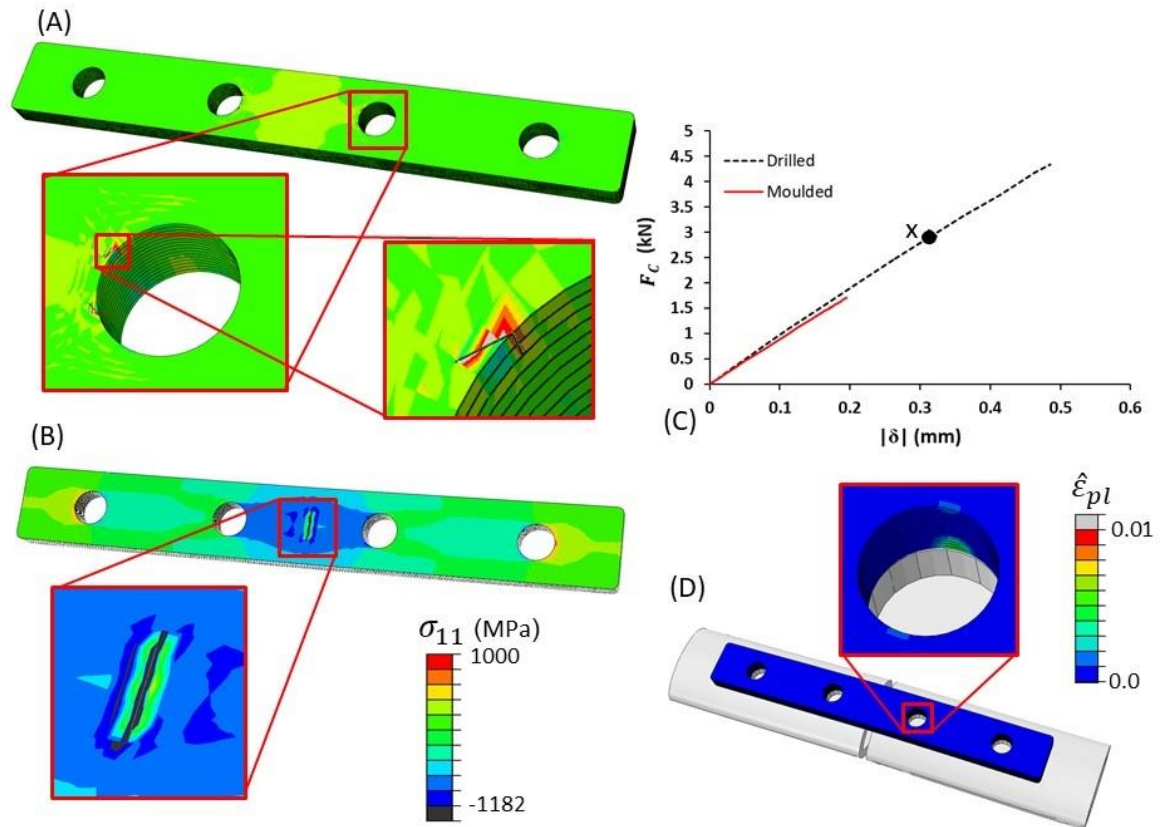


Figure 7.7: Longitudinal stress ( $\sigma_{11}$ ) distribution at the point of failure under applied axial compression ( $F_C$ ) in (A) the moulded and (B) the drilled FFP. (C) The relationship between applied compressive load ( $F_C$ ) and the magnitude of displacement ( $|\delta|$ ) between the proximal end of the fracture bone and the fixed distal end. The point “x” indicates the compressive load at which localised plastic deformation is computed in the drilled-hole FFP. (D) Predicted area of localised plastic deformation ( $\hat{\epsilon}_{pl}$ ) in the drilled-hole FFP.

The longitudinal stress ( $\sigma_{11}$ ) distribution in the moulded and drilled FFPs subjected to flexural loading is shown in Figure 7.8(A) and (B), respectively. The fixation plate with the moulded holes is predicted to fail due to transverse tensile intra-laminar cracks, initiating at the edge of the hole (Figure 7.8(A)). Figure 7.8(B) shows the predicted stress distribution in the drilled implant at an applied moment of 5kNm. The maximum stresses are predicted between the two centre holes on the lateral side of the FFP. In contrast to the drilled-hole FFP, cracking is computed in the moulded-hole FFP at an applied bending moment of 2.08Nm. The moulded-hole FFP is

predicted to fail due to transverse tensile intra-laminar cracks propagating from the edge of the hole on the lateral side of the implant (Figure 7.8(A)). The bending stiffness of the moulded-hole FFP is computed to be approximately ~18% lower than that of the drilled-hole plate.

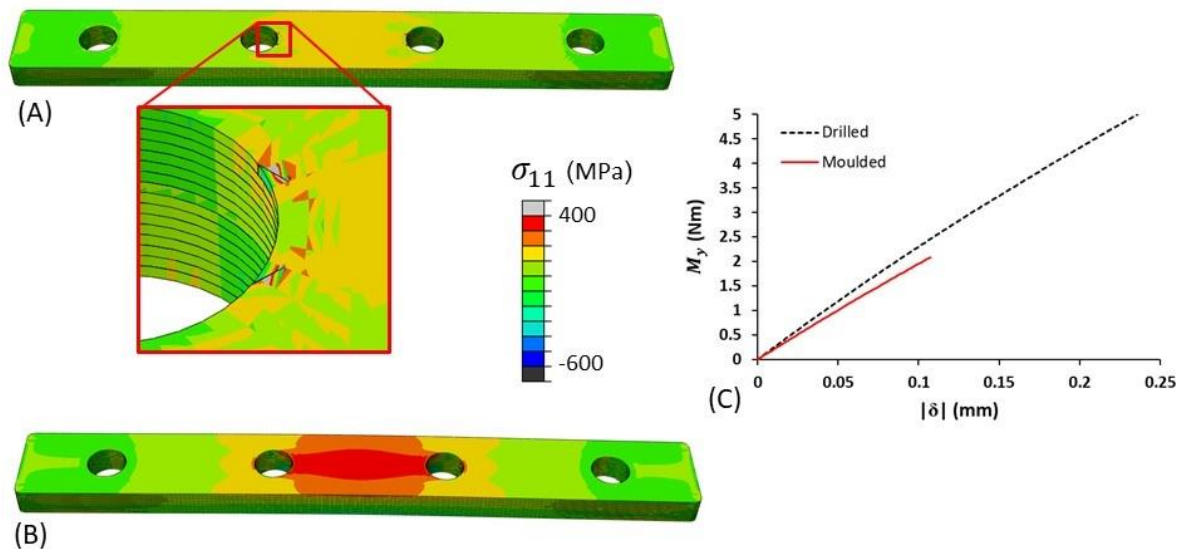


Figure 7.8: Longitudinal stress ( $\sigma_{11}$ ) distribution at the point of failure under applied bending moments ( $M_y$ ) in (A) the moulded and (B) the drilled FFP. (C) The relationship between applied torque ( $M_y$ ) and the magnitude of displacement between the proximal end of the fracture bone and the fixed distal end.

The longitudinal stress ( $\sigma_{11}$ ) distribution in the moulded and drilled hole FFPs under torsion ( $T_x$ ) is shown in Figure 7.9(A) and (B), respectively. Compressive intra-laminar matrix cracks are computed at the screw holes in the moulded-hole FFP at an applied torque of 0.697 Nm (Figure 7.9(A)). The cracks are computed to propagate along the local fibre directions. Tensile intra-laminar matrix cracking is computed at the screw holes in the drilled-hole FFP at an applied torque of 0.679 Nm. The torsional stiffness of the drilled-hole plate is slightly higher (~2.6%) than that of the moulded-hole plate.

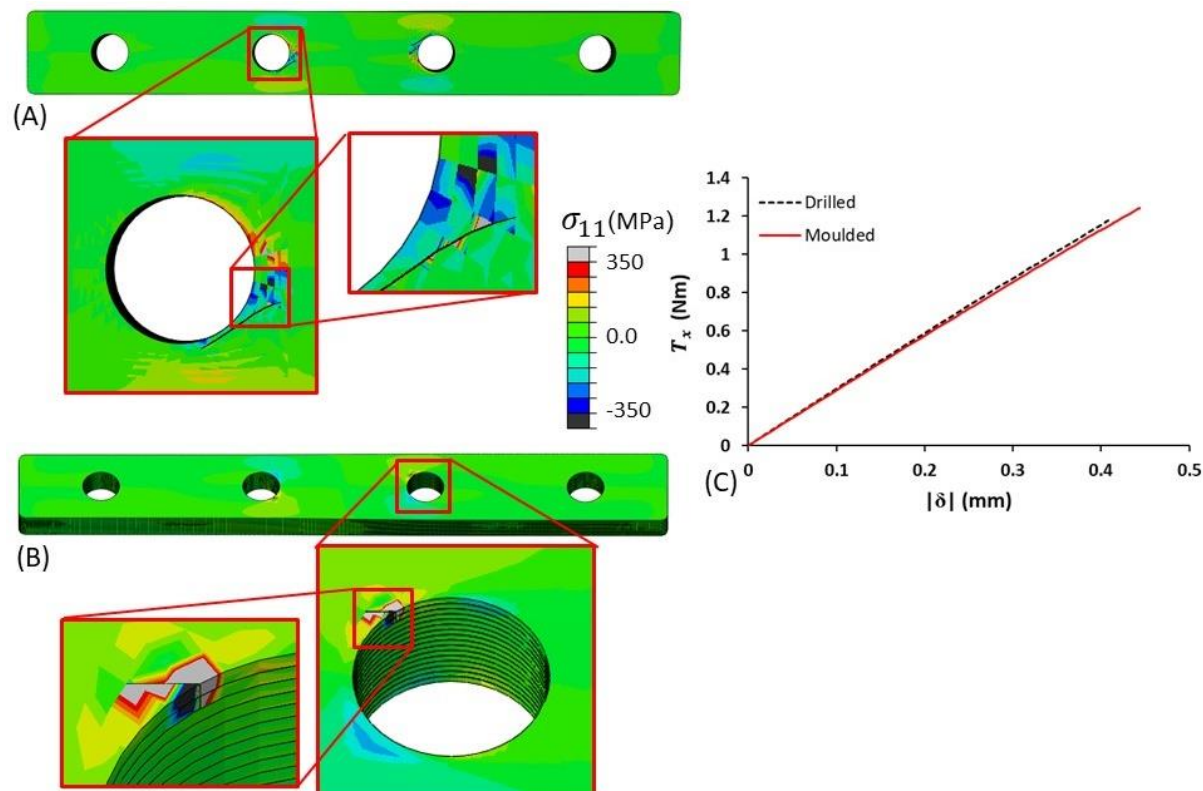


Figure 7.9: Longitudinal stress ( $\sigma_{11}$ ) distribution at the point of failure under applied torsional moments ( $T_x$ ) in (A) the moulded FFP and (B) the drilled FFP. (C) The relationship between applied torque ( $T_x$ ) and the magnitude of displacement between the proximal end of the fracture bone and the fixed distal end.

## 7.5 Discussion

Moulded holes have previously been proposed as an alternative to drilled holes in continuous fibre reinforced laminates (Lin and Tsai, 1995; Rohner et al., 2005; Zitoune et al., 2011). The current study presents for the first time a computational methodology for creating finite element models of moulded holes in continuous fibre reinforced laminated devices. Models of fracture fixation devices with moulded and drilled holes are constructed and the mechanical performance of the plates are compared for a variety of loading conditions. The drilled implant is predicted to have considerably greater failure strength in compression and bending. However, the

moulded hole plate is predicted to have a slightly higher failure strength in torsion. It should be noted that the current study assumes that the drilled-hole plate is undamaged prior to the onset of loading. However, several studies report that cracking, delamination and fibre pull-out can occur during the drilling process (Abrão et al., 2007; Davim and Reis, 2003; DiPaolo et al., 1996; Ho-Cheng and Dharan, 1990; Isbilir and Ghassemieh, 2011; Panchagnula and Palaniyandi, 2017). The occurrence of such damage to the plate during the manufacturing process will reduce the load bearing capacity of the plate and should be considered in future computational studies. Numerous studies have examined methods to reduce the damage caused by drilling laminates, including altering the drill tip, feed rate, step drill etc. (Abrão et al., 2008; Durão et al., 2010; Marques et al., 2009; Murphy et al., 2002; Shyha et al., 2010). However, to date fibre reinforced laminates with moulded holes have not been extensively studied (Lin and Tsai, 1995; Zitoune et al., 2011).

A novel modelling methodology for the generation of non-uniform fibre orientations in the region of moulded screw holes is developed in the current study. Fibres are assumed to bend around the hole, with a rotational constraint imposed both above the hole due to symmetry, and at a critical distance from the hole, where the fibre orientations smoothly transition to the axial direction. Experimental analysis of moulded hole fibre orientations should be performed in a follow-on study to determine the distance from the hole at which fibre orientations return to the axial direction. Such information has not been reported in the literature.

The work presented in this chapter is first attempt at modelling moulded holes in FE. The stepwise methodology presented has been successfully implanted to generate

moulded fracture fixation plates to compare to drilled plates. However, there are a number of steps that need to be completed in order to validate this methodology:

- In the current methodology the size of the critical box, used to determine at what distance from the hole the fibres return to their straight configuration, is chosen by the designer. Moulded holes should be manufactured in  $0^\circ$ ,  $90^\circ$  and  $45^\circ$  plies and accurate imaging of fibre orientations should be performed.
- The size of the area of neat PEEK, reduced fibre volume fraction, at the front and back of the hole must also be measured from images of the moulded experimental samples.
- The area at the top and bottom of the hole will have an increased fibre volume fraction. This should be reflected with the elements in this section of the mesh having an increased longitudinal strength (can be roughly determined from the rule of mixtures).
- Laminates with moulded holes should be manufactured in order to carry out extensive experimental testing on several laminate layups under uniaxial and multi-axial loading conditions in order to calibrate the model.

Moulded screw holes have the potential to solve a number of issues associated with drilling holes in laminates during post-processing. Manufacturing holes using the punch method allows moulded holes to be manufactured in laminates with any number of angled plies, and thus does not restrict the design of optimal laminate layups for specific locations in any way. The computational analyses of fracture fixation devices in chapters 4 and 5 of this thesis both predict high stress localisations and failures in the vicinity of the screw holes. If moulded holes can indeed increase the strength of laminates with holes, once calibrated, the stepwise

methodology presented in the current chapter will be a useful computational design tool for designers of next generation laminated CF/PEEK fracture fixation plates.

## 7.6 References

- Abrão, A.M., Faria, P.E., Rubio, J.C.C., Reis, P., Davim, J.P., 2007. Drilling of fiber reinforced plastics: A review. *J. Mater. Process. Technol.* <https://doi.org/10.1016/j.jmatprotec.2006.11.146>
- Abrão, A.M., Rubio, J.C.C., Faria, P.E., Davim, J.P., 2008. The effect of cutting tool geometry on thrust force and delamination when drilling glass fibre reinforced plastic composite. *Mater. Des.* 29, 508–513. <https://doi.org/10.1016/j.matdes.2007.01.016>
- Davim, J.P., Reis, P., 2003. Study of delamination in drilling carbon fiber reinforced plastics (CFRP) using design experiments. *Compos. Struct.* 59, 481–487. [https://doi.org/10.1016/S0263-8223\(02\)00257-X](https://doi.org/10.1016/S0263-8223(02)00257-X)
- DiPaolo, G., Kapoor, S.G., DeVor, R.E., 1996. An Experimental Investigation of the Crack Growth Phenomenon for Drilling of Fiber-Reinforced Composite Materials. *J. Eng. Ind.* 118, 104. <https://doi.org/10.1115/1.2803629>
- Durão, L.M.P., Gonçalves, D.J.S., Tavares, J.M.R.S., de Albuquerque, V.H.C., Aguiar Vieira, A., Torres Marques, A., 2010. Drilling tool geometry evaluation for reinforced composite laminates. *Compos. Struct.* 92, 1545–1550. <https://doi.org/10.1016/j.compstruct.2009.10.035>
- Fujihara, K., Huang, Z.M., Ramakrishna, S., Satknanantham, K., Hamada, H., 2003. Performance study of braided carbon/PEEK composite compression bone plates. *Biomaterials* 24, 2661–2667. [https://doi.org/10.1016/S0142-9612\(03\)00065-6](https://doi.org/10.1016/S0142-9612(03)00065-6)
- Ho-Cheng, H., Dharan, C.K.H., 1990. Delamination During Drilling in Composite Laminates. *J. Eng. Ind.* 112, 236. <https://doi.org/10.1115/1.2899580>
- Huang, Z.M., Fujihara, K., 2005. Stiffness and strength design of composite bone plates. *Compos. Sci. Technol.* 65, 73–85. <https://doi.org/10.1016/j.compscitech.2004.06.006>
- Isbilir, O., Ghassemieh, E., 2011. Finite Element Analysis of Drilling of Carbon Fibre Reinforced Composites. *Appl. Compos. Mater.* 19, 637–656. <https://doi.org/10.1007/s10443-011-9224-9>
- Kurtz, S.M., Devine, J.N., 2007. PEEK biomaterials in trauma, orthopedic, and spinal implants. *Biomaterials* 28, 4845–69. <https://doi.org/10.1016/j.biomaterials.2007.07.013>
- Lin, H.J., Tsai, C.C., 1995. Failure analysis of bolted connections of composites with drilled and moulded-in hole. *Compos. Struct.* 30, 159–168. [https://doi.org/10.1016/0263-8223\(94\)00040-9](https://doi.org/10.1016/0263-8223(94)00040-9)
- Marques, A.T., Durão, L.M., Magalhães, A.G., Silva, J.F., Tavares, J.M.R.S., 2009. Delamination analysis of carbon fibre reinforced laminates: Evaluation of a special step drill. *Compos. Sci. Technol.* 69, 2376–2382. <https://doi.org/10.1016/j.compscitech.2009.01.025>
- Murphy, C., Byrne, G., Gilchrist, M.D., 2002. The performance of coated tungsten carbide drills when machining carbon fibre-reinforced epoxy composite materials. *Proc. Inst. Mech. Eng. Part B J. Eng. Manuf.* 216, 143–152. <https://doi.org/10.1243/0954405021519735>
- Panchagnula, K.K., Palaniyandi, K., 2017. Drilling on fiber reinforced

polymer/nanopolymer composite laminates: A review. *J. Mater. Res. Technol.* <https://doi.org/10.1016/j.jmrt.2017.06.003>

Rohner, B., Wieling, R., Magerl, F., Schneider, E., Steiner, A., 2005. Performance of a composite flow moulded carbon fibre reinforced osteosynthesis plate. *Vet. Comp. Orthop. Traumatol.* 18, 175–182.

Shyha, I., Soo, S.L., Aspinwall, D., Bradley, S., 2010. Effect of laminate configuration and feed rate on cutting performance when drilling holes in carbon fibre reinforced plastic composites. *J. Mater. Process. Technol.* 210, 1023–1034. <https://doi.org/10.1016/j.jmatprotec.2010.02.011>

Zitoune, R., Crouzeix, L., Collombet, F., Tamine, T., Grunevald, Y.H., 2011. Behaviour of composite plates with drilled and moulded hole under tensile load. *Compos. Struct.* 93, 2384–2391. <https://doi.org/10.1016/j.compstruct.2011.03.027>

**Appendix 7 A**

Content Removed Due to Copyright

# Chapter 8

## Concluding Remarks and Future Perspectives

---

### 8.1 Summary of key contributions

The combined experimental-computational approaches implemented in this thesis provide new insights into damage progression and failure of carbon fibre reinforced PEEK materials. This section summarises the key contributions of this work to the field of advanced unidirectional fibre reinforced laminated materials for use in next generation trauma and fracture fixation devices.

#### **Chapter 4**

- The first experimental material characterisation of medical grade carbon fibre reinforced PEEK composite material PEEK-OPTIMA™ Ultra-Reinforced (Invibio Ltd., Thornton-Cleveleys, UK) is carried out.

- Three experimental failure mechanisms are uncovered in the extensive multi-axial suite of experiments performed: (1) inter-laminar delamination, (2) intra-laminar cracking and (3) anisotropic plasticity.
- A computational framework is developed such that, a cohesive zone model predicts inter-laminar delaminations, a Hashin-type XFEM failure criteria predicts intra-laminar cracking and anisotropic plasticity is modelled using the Hill potential function. Failure to include all three failure mechanisms will result in the inaccurate prediction of laminate failure. The computational damage and failure model is calibrated for CF/PEEK using the results of the experimental tests.

### **Chapter 5**

- A multi-scale computational analysis of damage progression and failure in laminated CF/PEEK distal radius fracture fixation plates reveal the importance of ply layup when designing laminated trauma and fracture fixation devices.
- The macro-mechanical model demonstrates that through careful layup design a CF/PEEK laminated device can support the physiological multi-axial loading of the distal radius, without excessive deformation.
- Transverse tension simulations performed on micro-mechanical RVEs demonstrate that fibre matrix debonding is the dominant mode of failure for in tension tests of 90° laminates.
- It is predicted that all of the laminates examined in this study failure due to cracks propagating after the transverse tensile strength of the CF/PEEK is exceeded.

### Chapter 6

- Experimental tests performed on open and filled hole laminates reveal the complex failure, crack propagation and extensive delamination that occur in laminates with drilled holes.
- It is demonstrated that filled hole compression samples have an increased failure strength compared to open hole compression. Experiments also reveal that filled holes experience cracking and delamination across the full width of the specimen while open hole specimens have no visible damage directly above and below the hole.
- Computational simulations (implementing the damage and failure model) give very good predictions of the experimental stress-strain relationships. An excellent agreement with the tensile open hole tests strength is predicted. However, the initial strength predictions for the open and filled hole compression strengths under predicted the experimental values.

### Chapter 7

- A novel computational methodology for creating finite element models of moulded holes is presented.
- The punch hole technique described will allow for moulded holes to be manufactured in laminated devices with several angles plies in the layup.
- Computational analyses of a generic fracture fixation device comparing drilled and moulded holes demonstrate that moulded holes do not increase the strength of the laminate under the various loading conditions examined.

## **8.2 Future perspectives**

The current thesis has addressed some of the key topics in the development of unidirectional carbon fibre reinforced laminated orthopaedic implants. Section 8.1 has already summarised the novel contributions of this thesis. This section will discuss the implications of this work and outline future studies that may address them.

A calibrated damage and failure computational model for fibre reinforced laminates is presented in Chapter 4. Several previously developed computational damage models have simulated only intra-laminar failure (Ballo et al., 2007; Duarte et al., 2017) or inter-laminar failure (Heidari-Rarani et al., 2013; Turon et al., 2010; Zhao et al., 2014), combined inter- and intra-laminar failure (Bouhala et al., 2015; Grogan et al., 2015a, 2015b; Viguera et al., 2015), and combined inter- and intra-laminar failure with isotropic plasticity (Higuchi et al., 2017; van der Meer et al., 2011). These studies should be re-run using the combined intra- laminar, inter-laminar and anisotropic plasticity presented in Chapter 4. The findings in Chapter 4 and 6 demonstrate that all three failure mechanisms must be included in the computational model to accurately simulate a full multi-axial suite of experiments. Correct prediction of damage progression and failure in unidirectional fibre reinforced laminates is vital for the design of next generation laminated fracture fixation devices. However, the model is not limited to laminated medical devices, and can be implemented for a variety of applications including turbine blades (Fagan et al., 2016, 2015; Grogan et al., 2013) and aerospace (Grogan et al., 2015b; Murray et al., 2017, 2016) among others. Future experimental and computational studies should investigate the laminates response to cyclic loading (Blanco et al., 2004; Liakat and

Khonsari, 2016; Scarselli et al., 2015), fatigue failure (Degrieck and Paepegem, 2001; Hashin and Rotem, 1973; Rotem and Hashin, 1975) and strain rate hardening (Gates and Sun, 1991; Gilat et al., 2002; Ochola et al., 2004).

In Chapter 5 a computational multi-scale study of predicted failure in laminated DRFFPs is presented. The key findings of Chapter 5 provide motivation for further investigation of laminated CF/PEEK DRFFPs. Future simulations on different DRFFP geometries are currently on the market (Osada et al., 2003), will help to determine the effect of implant geometry on the failure of laminated DRFFPs. A patient specific fracture distal radius generated in Materialise Mimics (Leuven, Belgium) from CT images with applied joint and muscle forces would provide a more accurate prediction of the damage progression and failure in laminated DRFFPs under physiological loading conditions.

The open and filled hole compressive and tensile strengths are examined in Chapter 6. It is demonstrated that the computational damage and failure model, presented in Chapter 4, accurately predicts the failure of notched laminates. Future experimental studies on the strength of notched laminates under bending and torsion will be most beneficial for the design of laminated implants as these loading conditions are commonly experienced throughout by all long bones in the body. Experiments reveal a potential issue with the results of the  $0^\circ$  longitudinal compression tests presented in Chapter 4. Further  $0^\circ$  compression tests performed on CF/PEEK will affirm the inaccurate value of longitudinal compressive strength ( $X_C$ ) reported in Chapter 4.

Finally, in Chapter 7 a stepwise methodology for creating finite element models of moulded holes is presented. Future experimental tests should manufacture moulded hole samples in  $0^\circ$ ,  $90^\circ$  and  $45^\circ$  plies. These samples will be examined to determine

at what distance from the hole the fibre return to their straight configuration. These values will then determine the size of the critical box in the methodology. The precise area of unreinforced PEEK at the front and back of the moulded hole should also be experimentally measured from the images of polished moulded hole experimental samples. Both will allow for more accurate simulation of the deformation and failure of laminates with moulded holes. To date unidirectional laminates have only been examined in tension (Zitoune et al., 2011), a more comprehensive multi-axial suite of experiments including compression, torsion, bending and combined loading cases should be performed to fully characterise the damage progression and failure of moulded hole laminates. Finally, a parameter study should be carried out in conjunction with measurements from the polished experimental images to determine in percentage increase in fibre volume fraction at the top and bottom of the hole (where the fibres are at peak deformation). Any change in fibre volume fraction will affect longitudinal and transverse material properties of the CF/PEEK and this should be reflected in the moulded hole computational model.

### 8.3 References

- Ballo, A.M., Lassila, L. V., Vallittu, P.K., Närhi, T.O., 2007. Load bearing capacity of bone anchored fiber-reinforced composite device. *J. Mater. Sci. Mater. Med.* 18, 2025–2031. <https://doi.org/10.1007/s10856-007-3159-6>
- Blanco, N., Gamstedt, E.K., Asp, L.E., Costa, J., 2004. Mixed-mode delamination growth in carbon–fibre composite laminates under cyclic loading. *Int. J. Solids Struct.* 41, 4219–4235. <https://doi.org/10.1016/j.ijsolstr.2004.02.040>
- Bouhala, L., Makradi, A., Belouettar, S., Younes, A., Natarajan, S., 2015. An XFEM/CZM based inverse method for identification of composite failure parameters. *Comput. Struct.* 153, 91–97. <https://doi.org/10.1016/j.compstruc.2015.02.035>
- Degrieck, J., Paepegem, W. Van, 2001. Fatigue damage modeling of fibre-reinforced composite materials: review. ... *Rev.* 54, 279–300.
- Duarte, A.P.C., Díaz Sáez, A., Silvestre, N., 2017. Comparative study between XFEM and Hashin damage criterion applied to failure of composites. *Thin-Walled Struct.* 115, 277–288. <https://doi.org/10.1016/j.tws.2017.02.020>
- Fagan, E.M., Kennedy, C.R., Leen, S.B., Goggins, J., 2016. Damage mechanics based design methodology for tidal current turbine composite blades. *Renew. Energy* 97, 358–372. <https://doi.org/10.1016/j.renene.2016.05.093>
- Fagan, E.M., Leen, S.B., Kennedy, C.R., Goggins, J., 2015. Finite element based damage assessment of composite tidal turbine blades, in: *Journal of Physics: Conference Series*. <https://doi.org/10.1088/1742-6596/628/1/012106>
- Gates, T.S., Sun, C.T., 1991. Elastic/Viscoplastic Constitutive Model for Fiber Reinforced Thermoplastic Composites. *AIAA J.* 29, 457–463. <https://doi.org/10.2514/3.59922>
- Gilat, A., Goldberg, R.K., Roberts, G.D., 2002. Experimental study of strain-rate-dependent behavior of carbon/epoxy composite. *Compos. Sci. Technol.* 62, 1469–1476. [https://doi.org/10.1016/S0266-3538\(02\)00100-8](https://doi.org/10.1016/S0266-3538(02)00100-8)
- Grogan, D.M., Leen, S.B., Kennedy, C.R., Ó Brádaigh, C.M., 2013. Design of composite tidal turbine blades. *Renew. Energy* 57, 151–162. <https://doi.org/10.1016/j.renene.2013.01.021>
- Grogan, D.M., Ó Brádaigh, C.M., Leen, S.B., 2015a. A combined XFEM and cohesive zone model for composite laminate microcracking and permeability. *Compos. Struct.* 120, 246–261. <https://doi.org/10.1016/j.compstruct.2014.09.068>
- Grogan, D.M., Ó Brádaigh, C.M., McGarry, J.P., Leen, S.B., 2015b. Damage and permeability in tape-laid thermoplastic composite cryogenic tanks. *Compos. Part A Appl. Sci. Manuf.* 78, 390–402. <https://doi.org/10.1016/j.compositesa.2015.08.037>
- Hashin, Z., Rotem, A., 1973. A Fatigue Failure Criterion for Fiber Reinforced Materials. *J. Compos. Mater.* 7, 448–464. <https://doi.org/10.1177/002199837300700404>
- Heidari-Rarani, M., Shokrieh, M.M., Camanho, P.P., 2013. Finite element modeling of mode I delamination growth in laminated DCB specimens with R-curve effects. *Compos. Part B Eng.* 45, 897–903. <https://doi.org/10.1016/j.compositesb.2012.09.051>
- Higuchi, R., Okabe, T., Nagashima, T., 2017. Numerical simulation of progressive damage

- and failure in composite laminates using XFEM/CZM coupled approach. *Compos. Part A Appl. Sci. Manuf.* 95, 197–207. <https://doi.org/10.1016/j.compositesa.2016.12.026>
- Liakat, M., Khonsari, M.M., 2016. Analysis and life prediction of a composite laminate under cyclic loading. *Compos. Part B Eng.* 84, 98–108. <https://doi.org/10.1016/j.compositesb.2015.08.015>
- Murray, B.R., Doyle, A., Feerick, P.J., Semprinoschnig, C.O.A., Leen, S.B., Ó Brádaigh, C.M., 2017. Rotational moulding of peek polymer liners with carbon fibre/peek over tape-placement for space cryogenic fuel tanks. *Mater. Des.* 132, 567–581. <https://doi.org/10.1016/j.matdes.2017.07.026>
- Murray, B.R., Leen, S.B., Semprinoschnig, C.O.A., Brádaigh, C.M.Ó., 2016. Helium permeability of polymer materials as liners for composite overwrapped pressure vessels. *J. Appl. Polym. Sci.* 133. <https://doi.org/10.1002/app.43675>
- Ochola, R.O., Marcus, K., Nurick, G.N., Franz, T., 2004. Mechanical behaviour of glass and carbon fibre reinforced composites at varying strain rates. *Compos. Struct.* 63, 455–467. [https://doi.org/10.1016/S0263-8223\(03\)00194-6](https://doi.org/10.1016/S0263-8223(03)00194-6)
- Osada, D., Viegas, S.F., Shah, M.A., Morris, R.P., Patterson, R.M., 2003. Comparison of different distal radius dorsal and volar fracture fixation plates: A biomechanical study. *J. Hand Surg. Am.* 28, 94–104. <https://doi.org/10.1053/jhsu.2003.50016>
- Rotem, A., Hashin, Z., 1975. Failure Modes of Angle Ply Laminates. *J. Compos. Mater.* 9. <https://doi.org/10.1177/002199837500900209>
- Scarselli, G., Castorini, E., Panella, F.W., Nobile, R., Maffezzoli, A., 2015. Structural behaviour modelling of bolted joints in composite laminates subjected to cyclic loading. *Aerosp. Sci. Technol.* 43, 89–95. <https://doi.org/10.1016/j.ast.2015.02.017>
- Turon, A., Camanho, P.P., Costa, J., Renart, J., 2010. Accurate simulation of delamination growth under mixed-mode loading using cohesive elements: Definition of interlaminar strengths and elastic stiffness. *Compos. Struct.* 92, 1857–1864. <https://doi.org/10.1016/j.compstruct.2010.01.012>
- van der Meer, F., Sluys, L., Hallett, S., Wisnom, M., 2011. Computational modeling of complex failure mechanisms in laminates. *J. Compos. Mater.* 46, 603–623. <https://doi.org/10.1177/0021998311410473>
- Vigueras, G., Sket, F., Samaniego, C., Wu, L., Noels, L., Tjahjanto, D., Casoni, E., Houzeaux, G., Makradi, A., Molina-Aldareguia, J.M., Vázquez, M., Jérusalem, A., 2015. An XFEM/CZM implementation for massively parallel simulations of composites fracture. *Compos. Struct.* 125, 542–557. <https://doi.org/10.1016/j.compstruct.2015.01.053>
- Zhao, L., Gong, Y., Zhang, J., Chen, Y., Fei, B., 2014. Simulation of delamination growth in multidirectional laminates under mode I and mixed mode I/II loadings using cohesive elements. *Compos. Struct.* 116, 509–522. <https://doi.org/10.1016/j.compstruct.2014.05.042>
- Zitoune, R., Crouzeix, L., Collombet, F., Tamine, T., Grunevald, Y.H., 2011. Behaviour of composite plates with drilled and moulded hole under tensile load. *Compos. Struct.* 93, 2384–2391. <https://doi.org/10.1016/j.compstruct.2011.03.027>